2020

Tribochemical Reaction on Alkali Phosphate Lubricant at Sliding Interface in Hot Rolling of Steel

Manh Ha Le

UNIVERSITY
OF WOLLONGONG
AUSTRALIA

Tribochemical Reaction on Alkali Phosphate Lubricant at Sliding Interface in Hot Rolling of Steel

Manh Ha Le

Principal supervisor: Dr. Hongtao Zhu
Co-supervisor: Senior Professor Anh Kiet Tieu

This thesis is presented as part of the requirement for the conferral of the degree:
Doctor of Philosophy

University of Wollongong
School of Mechanical, Materials, Mechatronic and Biomedical Engineering

April 2020

Certification

I, Manh Ha Le, declare that this thesis submitted in fulfilment of the requirements for the conferral of the degree Doctor of Philosophy, from the University of Wollongong, is wholly my own work unless otherwise referenced or acknowledged. This document has not been submitted for qualifications at any other academic institution.

_____

Manh Ha Le

4th April 2020

Acknowledgments

I am greatly grateful to my supervisors Senior Professor Anh Kiet Tieu and Dr. Hongtao Zhu for the sincere guidance and support during my Ph.D journey.

I would like to thank my theoretical team members: Dr. Dinh Thi Ta, Ms. Thi Thuy Huong Ta, Mr. Van Nam Tran, which provide lots of help and assistance as well as heaps of fruitful discussion on my work in particular and on theoretical knowledge in general.

I would like to show my appreciation to the staffs and students within the School of Materials, Mechanical, Mechatronics and Biomedical Engineering for all the help and assistance given. In particular, I wish to thank A. Prof. Buyung Kosasih, Mr. Le Quang Phan, Mr. Do Xuan Vinh Nguyen, Mr. Ba Hieu Nguyen, and Mr. Dinh Tri Vo for their valuable advices in Ph.D work and life.

I would like to express my gratitude to the Information Management & Technology Services (IMTS) at the University of Wollongong and Australian National Computational Infrastructure (NCI) for high performance computing. I would like to thank the University of Wollongong and Australian Research Council for providing the HDR scholarships.

Personally, I would like to thank my friends at Crown Street. You guys are my second family which bring beautiful colors into my life. I also thank my friends in Australia, in Vietnam and around the world, thank you for helping me when I needed you.

Finally, I would like to thank my family in Vietnam: my father Kim Ba Le, my mother Thi Hong Dau, my sister Lan Vy Le, my brother-in-law Hoang Vu Nguyen, and my super lovely nephew Le Minh (Jack) Nguyen. Thank you, from the bottom of my heart. However, it truly has no bottom for you.

For beloved J, whenever I feel alone, you find a way to sneak in. Thank you for always making my life more complete and for making my 28th birthday precious.

It such a long journey until this moment and I really appreciate every landscape I saw, every person I met and every moment I got. I am also really excited about my next journey and can wait to start it. Thank everyone for everything. Love you all!!!

Manh Ha Le

Wollongong, April 2020

List of Publications

1. **Manh Ha Le,** Anh Kiet Tieu, Hongtao Zhu, Dinh Thi Ta, Haibo Yu, Thi Thuy Huong Ta, Van Nam Tran and Shanhong Wan, "Depolymerization of sodium polyphosphates on an iron oxide surface at high temperature", *Physical Chemistry Chemical Physics*, 2018. 20(11): p. 7819-7835.
2. **Manh Ha Le,** Anh Kiet Tieu, Hongtao Zhu, Dinh Thi Ta, Haibo Yu, Thi Thuy Huong Ta and Van Nam Tran, "Surface transformation and interactions of iron oxide in glassy lubricant: An ab initio study", *Chemical Physics*, 2020. 538: p. 110919.
3. Dinh Thi Ta, **Manh Ha Le,** Anh Kiet Tieu, Hongtao Zhu, Thi Thuy Huong Ta, Van Nam Tran, Shanhong Wan and Adri van Duin, "Reactive molecular dynamics study of hierarchical tribochemical lubricant films at elevated temperatures", *ACS Applied Nano Materials*, 2020. 3(3): p. 2687-2704.
4. Dinh Thi Ta, Anh Kiet Tieu, Hongtao Zhu, **Manh Ha Le,** Thi Thuy Huong Ta, Van Nam Tran, and Shanhong Wan, "Physical and chemical insights into molecular adsorption of copolymer's monomers on rutile surface", *Chemical Physics*, 2019. 520: p. 8-20.
5. Thi Thuy Huong Ta, Anh Kiet Tieu, Hongtao Zhu, Haibo Yu, Dinh Thi Ta, Shanhong Wan, Van Nam Tran and **Manh Ha Le,** "Chemical origin of sodium phosphate interactions on iron and iron oxide surfaces by first principle calculations", *The Journal of Physical Chemistry C*, 2018. 122(1): p. 635-647.
6. Thi Thuy Huong Ta, Anh Kiet Tieu, Hongtao Zhu, Haibo Yu, Van Nam Tran, **Manh Ha Le,** and Dinh Thi Ta, "Structural response of alkali metal borates at Fe_2O_3 sliding interface: The effect of alkali cations", *Computational Materials Science*, 2020. 184: p. 109930.
7. Van Nam Tran, Anh Kiet Tieu, Hongtao Zhu, Thi Thuy Huong Ta, Dinh Thi Ta and **Manh Ha Le,** "First-principles study of the adsorption and depolymerization mechanisms of sodium silicate on iron surfaces at high temperature", *The Journal of Physical Chemistry C*, 2018. 122(36): p. 20827-20840.
8. Van Nam Tran, Anh Kiet Tieu, Hongtao Zhu, Thi Thuy Huong Ta, **Manh Ha Le** and Dinh Thi Ta, "An ab initio study on the effects of Na passivation on friction reduction of an iron oxide surface", *Journal of Applied Physics*, 2020. 127(6): p. 065305.
9. Van Nam Tran, Anh Kiet Tieu, Hongtao Zhu, Thi Thuy Huong Ta, The Sang Pham, **Manh Ha Le** and Dinh Thi Ta, "Insights into the tribochemistry of sliding iron oxide surfaces lubricated by sodium silicate glasses: An ab initio molecular dynamics study", *Applied Surface Science*, 2020. 528: p. 147008.

List of Names or Abbreviations

2D	Two Dimensions
3D	Three Dimensions
AFM	Atomic Force Microscopy
AIMD	Ab Initio Molecular Dynamics
B3LYP	mixing of Becke exchange potential and Lee–Yang–Parr correlation potential
BO	Bond Order
BOP	Bond Overlap Population
CDD	Charge Density Difference
COOP	Crystal Orbital Overlap Population
DDEC	Density Derived Electrostatic and Chemical
DFT	Density Functional Theory
DFT+U	Density Functional Theory with on-site Coulomb interaction of localized electrons correction
DOS	Density of States
ELF	Electron Localization Function
EoS	Equation of State
GA	Genetic Algorithm
GGA	Generalized Gradient Approximation
GGA+U	Generalized Gradient Approximation with on-site Coulomb interaction of localized electrons correction
HF	Hartree-Fock
HSAB	Hard Soft Acid Base Theory
IAP	Inorganic Alkali Polyphosphate
LAMMPS	Large-scale Atomic/Molecular Massively Parallel Simulator
LDA	Local Density Approximation
LOBSTER	Local-Orbital Basis Suite Towards Electronic-Structure Reconstruction
MD	Molecular Dynamics
ML	Monolayer
MSD	Mean Square Displacement
MTP	Metathiophosphate

$NaPO_3$	Sodium Polyphosphate Glass $(-NaPO_3-)_n$
NEMD	Non-Equilibrium Molecular Dynamics
NPT	Number of molecules N, Pressure P, and Temperature T
NVE	Number of molecules N, Volume V, and Energy E
NVT	Number of molecules N, Volume V, and Temperature T
µVT	Chemical potential µ, Volume V, and Temperature T
O_b	Bridging Oxygen
O_l	Linkage Oxygen (O_{nb} connected to iron from oxide surface)
O_{nb}	Non-bridging Oxygen
O_s	Oxide Surface Oxygen
O_t	Terminal Oxygen (O_{nb} connected to sodium)
PAW	Project Augmented Wave
PBE	Perdew, Burke and Ernzerhof
PDOS	Projected Density of States
QM	Quantum Mechanics
ReaxFF	Reactive Force Field
SBO	Sum of Bond Order
SCF	Self-Consistent Field
TCP	Tricresyl Phosphate
TMP	Trimethyl Phosphite
VASP	Vienna Ab-initio Simulation Package
vdW	van der Waals
ZDDP	Zinc Dialkyldithiophosphate

Table of Contents

List of Tables

List of Figures

Abstract

Inorganic sodium phosphate glass has been proposed as a potential lubricant in hot rolling processes. Previous experimental works have demonstrated the outstanding tribological performance of this glass lubricant under the extreme condition of temperature, load and shear. The lubricity mechanism of sodium phosphate glass has also been revealed in the laboratory tests. However, the detailed picture of the mechano-tribochemical reaction of sodium phosphate glass lubricant on iron oxide surfaces is still not complete due to a number of missing pieces, for example, how the role of elements/compounds in reducing friction, lubrication and wear. This thesis applies various theoretical methods to unveil the tribochemical behavior of different sodium phosphate compounds with iron-based interfaces at the atomistic scale and the resulting lubrication effect of this inorganic glass. Firstly, the bond nature of the system, effect of surface and effect of chain length on depolymerization of phosphate-based lubricant have been analyzed with density functional theory (DFT) calculations and ab initio molecular dynamics (AIMD) simulations at 1100K. In general, the tribo-system contains medium covalent P-O bond, pure ionic Na-O interaction and moderate Fe-O ionic/covalent bond. The bridging P-O_b is the weakest bond targeted for the depolymerization which is induced by sodium - bridging oxygen interaction. The iron oxide surface plays a dual role in promoting/inhibiting the phosphate depolymerization. On one hand, the phosphate adsorption of oxide surface generates stable configurations and the partial anchoring of phosphate chain on substrates supports P-O_b depolymerization due to the effect of temperature. On the other hand, the oxide surface captures sodium cation which reduces the sodium attack on P-O_b bond and obstructs the depolymerization. The monodentate complex (one atom such as O, P linked to one atom of Fe) structures is dominant in all adsorption cases regardless of the chain length. The chain length of phosphate has little effects on the P-O bridging dissociation. The monodentate structures create the deformed FeO_4 tetrahedra on the oxide surface which allow the flexibility of phosphate network but still maintains the strong adherence lubricant film. Moreover, the small chain length structure is preferable at the lubricant-surface interfaces for the full phosphate coverage and all linkages are monodentate, which are related to the good lubricity of short-chain Na_3PO_4 and the depolymerized products of long-chain $NaPO_3$ in some experimental studies.

Secondly, DFT calculations and AIMD simulations are also used to investigate the surface transformation and interactions of iron oxide in glassy lubricant. Among three main interlayer interactions between phosphate networks with iron oxide, Fe-O_{glass} is the most stable linkage which can weaken the outermost Fe-O layer of oxide surface. $O_{surface}$-P interaction is observed under high load conditions and Fe-P direct bond occurs under severe conditions of high temperature, with an exposure of considerable number of iron atoms and a presence of under-coordinated phosphorus atoms. The Fe-P linkage can strengthen the Fe-O bonds of the iron oxide surface but has low probability to form in the system. Sodium cations in the glass network also reduce the Fe-$O_{surface}$ stability through generated O-terminated iron oxide surfaces. The iron oxide structure deformation can occur at normal temperatures with an excess concentration of sodium. In addition to thermal and mechanical factors, phosphate glass itself has a combined chemical/electronical effect on the deformation of the iron oxide surface, which supports the abrasive particle digestion theory in anti-wear mechanism of phosphate lubricant.

Last but not least, a comprehensive reactive force field (ReaxFF) has been developed for sodium phosphate/iron oxide system using a robust genetic algorithm (GA) and a consistent reference data from quantum mechanics (QM) calculation. This force field shows a significant improvement in the prediction of the heat of formation, mechanical properties, lattice constants, bulk modulus, and density of Fe, Na, and P, as well as their binary oxides compared to previous ReaxFFs. Additionally, the new parameters of ternary and quaternary oxides of $Na_xP_yO_z$, $Fe_xP_yO_z$, and $Na_xFe_yP_zO_n$ were also developed and validated against QM calculation at static and elevated-temperature dynamic conditions. This new ReaxFF not only predicts well the crystalline properties of these oxides, but it also predicts the most stable configuration and the order of energies of the intermediate states. The application of the new developed ReaxFF for the system of $Na_4P_2O_7$ lubricant confined between Fe_2O_3(0001) surface reveals a hierarchical tribochemical layers in which a sodium layer was formed at lubricant-surface interface to improve the system tribological performance which is in agreement with previous experimental work.

Introduction

Tribology is a study of friction, lubrication, and wear and it involves multi-disciplinary science of interacting surfaces in relative motion. This field attracts much attention due to the adverse impact of friction and wear which accounts for 23% world's energy consumption.[1] Lubricants are usually introduced into the tribosystem to reduce friction and wear effect, thus saving energy from high friction, extending service life of tools and improve the reliability of manufacturing processes. There are different types of lubricants but they are usually sorted into oil-based group, solid lubrication and aqueous one. Aqueous lubricants are mostly natural-based and more environmentally friendly among all. Even so, the performance of aqueous lubricants at high temperature has some limitation due to the high volatility and oxidative reactivity with water.[2]

Before the hot rolling process, steel slabs are heated in the reheating furnace for several hours at 1250^{o}C which produces an oxide scale layer of 3 to 5mm thickness. Then this oxide layer is descaled by high pressure water jet before going to the first rolling mill. However, due to the effect of temperature and the high humidity environment, the secondary oxide scale always forms on the steel strip during the rolling process. Then the steel stock goes through several reduction passes (up to 40% thickness reduction) through many rolling stands to achieve a desired thickness. The hot rolling for a variety of steel products is normally carried out between 700 to 1100°C at pressures between 500 MPa - 1 GPa. The process cost can be high due to high friction between strip-roll contact, significant roll wear (which affects roll life) and intense oxidation (that affects the product yield). Hence in our hot metal manufacturing, the lubricant plays a critical role in cost reduction.[3-5] However, developing a suitable lubricant for steel hot rolling at an elevated temperature condition can be quite challenging. Not only that, the interface of high temperature tribological process experiences a complex change in thermo-physical and tribochemical behaviors, bulk material and surface reactivity.[6]

Phosphate glass has been widely used in sealing material, solid state electrolytes, bioactive glass, optical fiber and radioactive immobilizer has been reported.[7-11] However, this inorganic glass, especially the water-soluble sodium polyphosphate glass, has attracted attention recently as a potential high-temperature lubricant due to the good properties of low friction and wear, thermal stability, chemical durability and oxidation resistance.[12-14] The phosphate lubricant has produced remarkable results in reducing

rolling force, friction, and wear at rolling steel condition. At lower temperature up to 200°C, the mechanism of phosphate-based lubricity has been studied for 40 years in zinc dialkyldithiophosphate (ZDDP) additive in automobile engine oil.[15, 16] ZDDP generally can generate a thick film of the decomposed zinc phosphate and react to abrasive iron oxide particles to protect the rubbing surfaces.[17, 18] Nevertheless, there is an abundant debate on what drives the ZDDP film formation. The flash temperature, pressure-induced reaction, tribo-emission, and recently the mechano-chemistry have been investigated.[19, 20] With advanced characterization techniques, scientists gradually unveil the nature of lubrication mechanism at high temperature with modern equipment but questions about the mechanism for friction and wear of the polyphosphate glass lubricant still remain unclear. Molecular modelling and atomic simulation are the notable approaches that will help to unlock the tribochemistry of the thin lubricant film and overcome the limitations of experimental approaches.

This thesis aims to unveil the mechanism and tribochemical reaction of sodium phosphate glass as a lubricant for metal forming process at high temperatures. Different behaviors of alkali phosphate glass on iron/iron oxide surface such as the adsorption, the depolymerization, and the surface transformation have been considered in the atomistic scale by Quantum Mechanics (QM). Finally, a reactive force field has been developed for the Molecular Dynamics (MD) model of the sheared lubricating thin film to reveal the lubricity performance of phosphate glass in a more realistic sliding interface of the contact in metal forming system.

Chapter 1 Literature review

1.1 High temperature inorganic glass lubricants

Throughout the history of centuries of hot metal forming, many research & development efforts have been made to improve the process productivity. Especially, there is a growing interest in the academia and industrial fields for a hot rolling process of steel. In the process, steel is preheated at 800-1200ºC before entering rolling stands with high speed (1-10 m/s) and high loading condition (~0.5-1 GPa). At the interface between cold work tool and heated work piece, heat transfer, friction and wear behavior has been considered in the system.[21] During the pre-heating stage in the reheat furnace , the oxidation accumulated on the steel work piece surface, forming a thick oxide layer with several millimetres thickness.[22] After the process, even the oxide layer has been descaled, there is always a secondary scale formed on the steel surface due to the effect of temperature and the humid ambient environment. This oxide scale is the cause of high friction and wear, and the surface fatigue.[6] Moreover, the oxide scale on the final rolled products requires costly removal processing to meet desired product specification. Hence, the optimum lubrication should be achieved for hot rolling processes to reduce energy consumption, excessive oxidation and roll maintenance cost.

Many lubricants in gaseous, liquid and solid forms have been developed and applied in practice. However, when the operational temperature of these conventional lubricants reaches the metal forming condition, the desired tribological behaviors cannot be obtained. For example, the oil-based and other liquid lubricants usually decompose beyond 250°C. Meanwhile, the solid lubricants such as metal oxides or graphite derivatives have the working condition below 650°C. The temperature of the steel slab/strip in the hot rolling process varies between 700ºC to 1100ºC.[23] Thus it is imperative that suitable lubricants with an optimum tribological performance should be selected for these applications.

Inorganic glass has been explored as a lubricant because of its molten phase behavior in the above elevated temperature. Borate, silicate and phosphate are the typical glass compounds which have boron oxide, silicon oxide and phosphorus oxide as the network former skeleton.[24] These glasses can achieve a good tribological performance in their molten state from 500 to 1200°C, which exceed the working conditions of conventional liquid lubricant.[25] Different glass composition containing the basic network former

elements (boron, silicon, and phosphorus) and the addition of metal oxide from alkaline, alkaline earth oxide to aluminum or transition metal oxide have been reported.[26] With regards to the tribological behavior, polyphosphate glass has produced a strong adhesion to the iron oxide surface which has less oxidation and lower friction and wear,[27] while silicate and borate can produce low friction and anti-oxidation properties.[28, 29] Nevertheless, the individual role of each element contributing to the glass tribological performance is not fully understood.

1.1.1 Borate

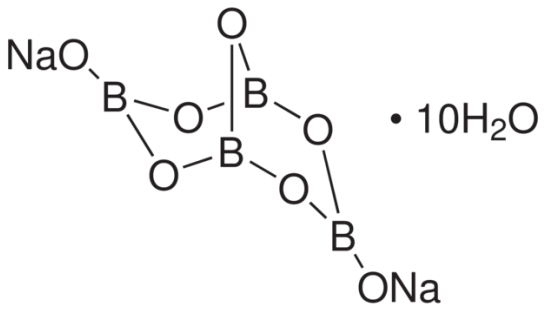

Figure 1-1. The structure of sodium borate $Na_2B_4O_7.10H_2O$

Due to suitable chemical properties and heat resistance, inorganic borate-based network has wide applications as a thermal-resistant glass and fiber glass. Sodium borate $Na_2B_4O_7.10H_2O$ and several borate-based compounds are also applied in tribological processes as an additive or lubricant.[30] The borate compounds can perform several tribological functions in automotive engines such as anti-wear additives, friction modifier, corrosion inhibitors and antioxidants. Walsh et al.[31] demonstrated the rust truncation ability of boric acid esters. However, this compound also has a poor hydrolytic stability. Subsequently, different candidates such as boron nitride, borate amines, and metal borides were found capable to reduce friction and wear in engine oils.[32, 33]

At room temperature, borate compounds have been reported to form the planar framework on metal surfaces which played an important role on their anti-wear and anti-oxidation properties.[34, 35]. The application of borate in tribology was reported in some early patents. For example, Peeler et al. [36] discussed the wear inhibition and huge load reduction with alkali borate additive. The mixture of hydrated sodium and potassium borate dispersed in oil has been used as an automobile lubricant which performed very well in extreme-pressure tests, dispersion tests, wear tests, and gear performance tests at

about 150°C. In another patent, Georg et al. [37] proposes a lubricant contained alkali borate and alkali phosphate for metal forming processes such as rolling, drawing, and pressing metal with the temperature range from 800°C to 1000°C. The aqueous lubricant showed the good adherence to metal surface, corrosion resistance, and obtained the excellent scale-loosening effect for those processes. Besides, Henricks [38] considers the molten borate as a lubricant which can digest, remove the scale and also can be anti-oxidants. The lubricant has been designed for processes such as metal machining, drawing and metal forming process.

Recently, the lubrication performance of borate-based glass has been studied on the ball-on-disc test at the hot rolling steel condition of 800°C.[39] In the study, borate-based lubricant obtained the coefficient of friction of 0.12 which is even better than phosphate lubricant at the same condition test. The author also studied the role of alkali elements in the system when both B_2O_3 and $Na_2B_2O_4$ lubricants were compared. The network without sodium cannot generate the efficient lubrication which results in a higher friction, higher wear loss and more surface damages than the sodium borate lubricant.[39] However, the performance of borate glass decreased with an increase of load due to the delamination of the lubricant network. Noticeably, without sodium, B_2O_3 produced an excessive wear loss compared to $Na_2B_2O_4$ lubricant due to its weak affinity to steel surface. Thus, the B_2O_3 layer could not attach to the contact area and squeezed out of the wear track.[39] With the addition of sodium, a tribofilm with the thickness of 50 – 60mm was formed,[39] which was twofold smaller than alkali phosphate lubricant.[13] The sodium borate glass also generated a Na-rich layer near the iron oxide surface which reduced the friction of tribosystem as well as mitigated the oxidation process of the steel surface by obstructing the reaction pathway between oxygen and iron ions.[13]

The lubricating mechanism of borate-contained compounds depends on the adsorption interaction between lubricants and metal-based surfaces.[40] The borate film has a weak affinity to the substrates which explains why there is no detection of boron on the steel surfaces after a tribological test. Thus, the physical adsorption has been adopted as a behavior of borate on metal surface and the solid protective borate film contributes on the functions of load-carrying and anti-wear.[41] In a contradictory view, the tribological performance of borate induced by the diffusion of free boron on the iron surface to form Fe_2B or FeB has been proposed by researchers. The coefficient of friction reduced by 33% and the mean wear scar diameter reduced by 35% in the four-ball scar test at 54.4°C [42, 43] Therefore, the precise behavior of borate-based compound on a metal surface

needs to be understood to explain the different behaviors outlined previously.

In an attempt to unveil the interaction between the sodium borate glass and the iron oxide surface, Ta et al. simulated the tribosystem with ab-initio molecular dynamics (AIMD) at the temperature of 1073 K.[44] The simulation result showed the strong adsorption of $Na_2B_4O_7$ on iron oxide and the lubricant decomposed at 1073 K due to the transformation of BO_4 structures into BO_3 and non-bridging oxygen. At the compression phase, the borate film rearranged and layered at low pressure of 1.8 GPa and the polymerization occurred at the pressure up to 4.3 GPa.[45] A transformation from BO_3 group into BO_4 tetrahedra occurred during compression, whereas this process was irreversible during decompression.[45]

The dispersion of borate additives in lubricant solution effects their tribological performance. It is quite difficult to deliver boron-based compound equally into surface active sites because of poor hydrolytic stability. The dispersion can be improved by connecting boron with long chain hydrocarbons, functional groups or soluble polymer substance.[46, 47]

1.1.2 Silicate

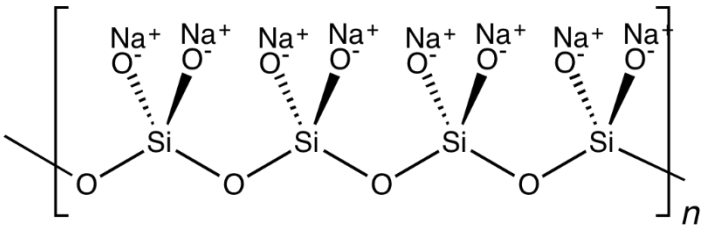

Figure 1-2. The structure of polymeric sodium silicate $(-Na_2SiO_3-)_n$

The inorganic silicate polymer, especially sodium silicate (Na_2SiO_3) is the popular lubricant used in high temperature metalworking, as well as a corrosion inhibitor for steel.[48, 49] The repeated structure of this polymer contains tetrahedral SiO_4^{4-} anions linked together through covalent bridging oxygen atoms.[50] In addition, the cations play the role of network modifier or charge balance in the polymer matrix. For instance, some high valence cations such as Al^{3+}, Fe^{3+}, Ti^{4+} can connect with SiO_4^{4-} tetrahedral to increase the network connectivity.[51, 52] Generally in silica melts at molten temperature, the depolymerization of glass network has been induced by the interaction between mono- or bivalent cations such as Na^+, K^+, Ca^{2+} with non-bridging oxygen atoms. The final structure depends on the glass composition and the working temperature but it is usually observed as polyhedral with 4 coordinated sites of silicon [53].

Silicate-based aqueous solution has been used as the lubricant for bearings or gear boxes.[54] The composition includes sodium silicate and/or potassium silicate. Under extreme temperature and load, a metallic silicate tribofilm has been generated due to the reaction between metal substrates and silicate lubricant.[54] Besides, this silicate-based film is good at thermal stability because of the high latent heat and high specific heat of aqueous alkaline silicate.[54]

Moreover, the silicate compounds have been examined as a lubricant additive with the aim to reduce friction and wear and protect surfaces. Zhang et al. [55] used $Al_4[Si_4O_{10}](OH)_4$ as an oil-additive for the pin-on-disc tester and confirmed the self-repair behavior of silicate at the contact areas. Besides the self-repair property, silicate-based powder additive can improve the sliding surface according to Yue et al [56]. Additionally, the silicate additive induced the generation of carbon-rich layer to protect the automotive engine cylinder surface as well as repairing the pits and cracks on the worn surfaces.

In steel hot rolling application, the sodium silicate melts and experiences a redox reaction with metal oxide debris. The alkali cations diffuse through molten silicate, and contribute to the kinetics of the reaction while oxygen diffusion controls the redox reaction.[3] The redox reaction mechanism of silicate melts has been explained by Neuville et al.[57, 58]. In the molten mixture of SiO_2, MgO, CaO, Na_2O, Li_2O and Fe_3O_4, the ratio of $Fe^{3+}/\Sigma Fe$ depended strongly on temperature. The addition of single valent cations can increase the redox reaction kinetics.[57] In the work of iron sodium borosilicate glass, Neuville et al. studied the network modifier role of Fe^{2+} with a fourfold and a sixfold oxygen interaction while Fe^{3+} played the role of a network former with tetrahedral oxygen coordination.[58] Recently, Tran et al. studied the tribochemical reaction of silicate lubricant with iron surface using dynamic QM methods.[59] With sodium silicate lubricant, the silicate cluster chemically adsorbs on the iron surface by forming multiple Fe – non-bridging oxygen (O_{nb}) bonds which have a strong covalent characteristic compared to the Si–O bonds. This strong covalent bond confirms the adhesion capability of the sodium silicate to the metal surface. However, the strength of $Si–O_{nb}$ bond within the molecule was reduced significantly at high temperature. This influences its bond dissociation and results in the instability of the tribofilm with a higher wear and friction.[59] In fact previous experiment reported an increase in coefficient of friction of sodium silicate lubricant when the temperature rose above 1000 °C.[60]

1.1.3 Phosphate

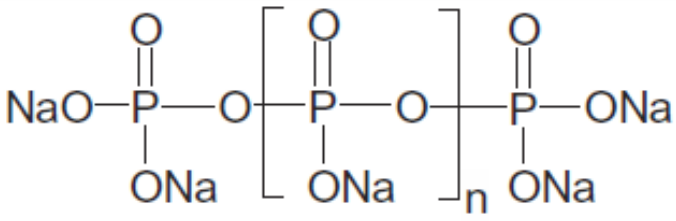

Figure 1-3. The structure of sodium polyphosphate $(-NaPO_3-)_n$

Glassy polyphosphate has a low melting temperature and good stability at the molten phase. It has the potential to replace conventional lubricant such as hydrocarbon, graphite, MoS_2, and even traditional ZDDP, which rapidly decompose at temperatures beyond 300°C. At high temperature, alkali metal phosphate glass not only possesses the excellent tribological behaviors of ZDDP but can also be used in aqueous lubricant which is more environmentally-friendly. The phosphate glass can melt without decomposing and the viscous molten liquid can form a stable matrix with abrasive metal oxides from the substrate. As a result it reduces friction, promotes the adhesion to the surfaces and protect surfaces from excessive wear.

Some early patents of Talley et al. and Gililland have been mentioned about the effective performance of aqueous alkali polyphosphate lubricant in metal working processes such as metal cutting, drilling and drawing.[61, 62] At the temperature of hot rolling process, water evaporates from phosphate aqueous lubricant and produces a dry phosphate layer onto the surface. This layer melts and provides a viscous liquid at the glass transition temperature.[12] De Barros-Bouchet et al. showed that the Fe-P bonding was formed during the chemical adsorption of tribofilm on the metal surface at room temperature [63]. Pawlak et al. indicated the cross-linking Fe/Zn-O-P bonds which replace amorphous P-O-P bonds in order to promote the chemical durability and mechanical strength of the tribofilm.[64]

Table 1.1. Comparison of borate, silicate, phosphate-based lubricant **[26]**

Inorganic polymer	**Friction**	**Wear**	**Adherence**
Borate	Good	Poor	Fair

Silicate	Fair	Good	Poor adhesion between 900 to 1170°C
Phosphate	Good	Good	Good

Although the molten phase of phosphate-based glass has been investigated, the application of this glass for tribology at high temperature still remains unclear. Our group took the initial steps to study the potential performance of molten polyphosphate as a lubricant for metal working process and the results will be discussed in the next section.

1.2 Polyphosphate glass

1.2.1 Phosphate glass structures and applications

Phosphorus oxide P_2O_5 is a typical glass forming oxide mentioned in classic Zachariasen's work (along with B_2O_3, SiO_2, and GeO_2).[65] The fundamental block of phosphate glass structure is the PO_4 tetrahedron even though phosphorus is a pentavalent element. The vitreous phosphoric oxide v-P_2O_5 is a basic phosphate-based glass with the PO_4 block which has 3 bridging oxygen and 1 double-bond oxygen surrounding P^{5+}. The v-P_2O_5 has a similar structure as vitreous silica v-SiO_2 but acquires the vitreous boric oxide v-B_2O_3 connectivity. Thus v-P_2O_5 has an easy-disrupted structure with a low glass transformation temperature compared to the silicon-based and boron-based glass.[66] The tetrahedral structure has been classified by Q^i expression which applied to silicon glasses [67] and then to phosphate glasses [68] (Figure 1-4). The structure of simple phosphate glass was also reviewed by Brow's study.[10]

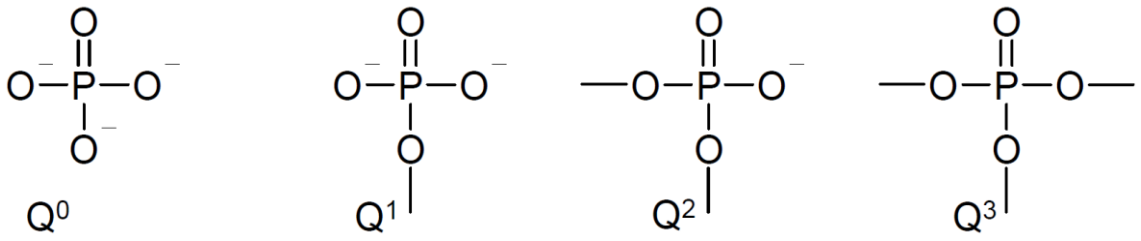

Figure 1-4. Tetrahedral structure classification Q^i in phosphate glass

In the expression, i indicates the number of bridging oxygen atoms per tetrahedron. Thus the phosphate glasses structure can vary from cross-linked phosphate network Q^3 (in v-P_2O_5) to polymer-like phosphate chain Q^2 (in the addition of metal cations) to pyrophosphate Q^1 (in $P_2O_7^{4-}$ compounds) and orthophosphate Q^0 (in PO_4^{3-}). The polymer

morphology of phosphate glass can exist in chains, branched or rings structures.

The tetrahedral structure is a result of sp^3 orbital hybridization of phosphorus electron configuration $3s^2 3p^3$. In the addition of metal oxide into the phosphate glass, the fifth electron of P is promoted to unoccupied d-orbital which forms the shared π-bond among non-bridging oxygen of the tetrahedral.[69, 70] The metal cations (M) form the chelate structure in the phosphate glass with non-bridging oxygen (O_{nb}).[68] The alkali and alkaline earth cations such as Na^+, K^+, Ca^{2+} usually play a role of network modifier along with the ionic M-O_{nb} interaction while the higher field strength cations such as Fe^{2+}, Fe^{3+}, Al^{3+} are well-known as the network former or the intermediate when featured with mixed ionic-covalent M-O_{nb} bond. The interaction with cations can influence the covalency of P-O_{nb} bond, which is often mentioned as the inductive effect.[71, 72]

1.2.2 Phosphate lubrication properties at low temperature

In the tribology field, polyphosphate zinc dialkyldithiophosphate (ZDDP) has been considered to be the most effective lubricant-additive to protect the rubbing surface from friction and wear at ambient temperatures up to 230^{o}C.[17] First appeared in the late 1930s, there is little change in the applications of ZDDP until now - it has been applied as an additive for engine lubricants and industrial oils. In the history of 80 years, there have been numerous studies which investigated the properties of ZDDP in the view of antiwear mechanism and tribological behaviors.

There are three main ways have been mainly discussed about ZDDP antiwear behavior [17]:

- Forming mechanically protective film which can reduce the stresses from asperities to metal surfaces.
- Removing corrosive peroxides or peroxy-radicals, thus protecting the substrate from corrosive wear.
- Digesting abrasive iron oxide particles which can reduce the harmful wear effects.

ZDDP decomposes in oil at 150°C into zinc polyphosphate and mixed alkyl sulphides. ZDDP does not directly adsorb on the iron surface but its decomposition products have provided tribological functions such as anti-wear and anti-oxidation [16]. Zinc phosphate, especially zinc polyphosphate as the decomposed compounds form a low melting glassy fluid on the oxide surface. The mixture after tribological process contain zinc phosphate and thiophosphate with different configurations such as ortho (PX_4^{3-}), pyro ($P_2X_7^{4-}$) and

poly (PX_3^-) with X represents S or O. The polymerization of phosphate is possible after the decomposition with a chain length of seven phosphorus atoms. The Zn-O bond in ZDDP molecules can be described as ionic or covalent interaction. Another product mixed-alkyl sulphide reacts with the iron oxide to produce elemental sulphur which can generate iron sulphide FeS when interacting with iron element after that. Under tribological conditions, the primary reactions of ZDDP are the hydrocarbon alkyl group dissociation and the sulphur--oxygen interchange in the ZDDP molecules. The S-O exchange reaction can replace the RS group (R represents alkyl groups) by a phosphonyl group in order to form polyphosphate. Watkins et al.[15] showed the presence of bivalent sulphur (sulphide), bivalent oxygen (oxide, phosphate), pentavalent phosphorus (phosphate, not phosphide), and bivalent zinc (zinc cations) in the lubricant system. The fusible glass layer of polyphosphate combined with ternary eutectic mixture of Fe-Fe_2O_3-FeS has been considered to provide the antiwear function of ZDDP. The ZDDP tribofilm performance is determined by two counter processes: chemical enhancement in tribofilm generation rate and mechanical removal of tribofilm which reduces its thickness.

Furthermore, So et al.[73] have investigated the formation mechanism and layer structure of ZDDP chemical film in three steps. Firstly, the ZDDP in the based oil starts decomposing at the 150°C. Then, the decomposed products absorbs on the surfaces to generate the chemisorbed film. Finally, the chemisorbed film reacts with the iron-based substrates. The layer structure has been described as a chemical reaction film which appears at the interface and reacts with iron substrate. The next layers in the film structure are chemisorbed layer and the gel-like material which is disputed about their nature.[17]

Yin and co-workers [74] proposed that the ZDDP film on the steel surface also has a patchy structure with the thickness of approximately 50 – 100 nm. The P/S ratio of the film is higher than the initial ZDDP compound. The structure attains the flat, plateau-like pads separated by deep valleys. In the composition of the pads, the short-chain phosphate exists at the interface of the steel substrate while the bulk of the pads contains mostly long-chain polyphosphate. The short-chain polyphosphates are inter-grown within the iron oxide layer.

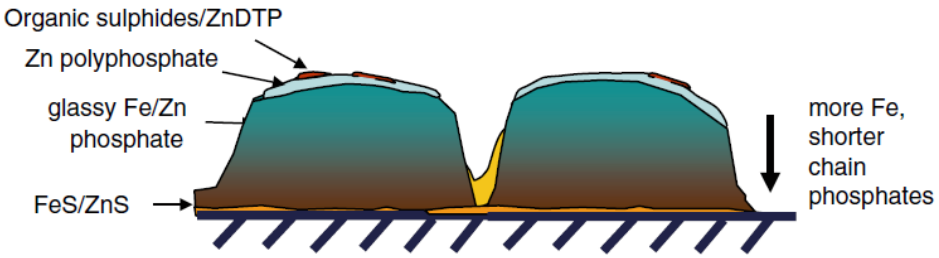

Figure 1-5. Pads structure and gradient composition of phosphate tribofilm [17]

The film from the rubbing process (tribofilm) has the same chemical properties with the film created thermally (thermal film) but the mechanical characteristics are stronger [75]. The tribofilm can be formed at a lower temperature than the thermal film but it requires tribological conditions of pressure, shear and temperature. Moreover, the antiwear performance of ZDDP depends on the alkyl group structure with the ranking of secondary alkyl > primary alkyl > aryl [76]. As for aryl tribofilm, no short-chain polyphosphate has been detected when compared with alkyl tribofilm. As the decomposed products of ZDDP cannot interact effectively with chromium, stainless steel or aluminum alloy, the antiwear behavior of ZDDP will be less effective with these material surfaces.[77]

Martin et al.[18, 78] proposed that the tribofilm contained zinc(II)/iron(III) phosphate glass with the octahedral Fe(III). The iron oxides have been digested by phosphate according to the Hard Soft Acid Base (HSAB) theory of Persson and this process has been considered as an important mechanism to reduce wear through removing abrasive iron oxide particles. This digestion process results in the gradient composition of the tribofilm – the proportion of iron to zinc increases continuously towards the iron-based substrate. The authors also suggested that the unbalance charge when exchanging Zn^{2+} with Fe^{3+} can reduce the chain length of polyphosphate. Besides, the sulphur reacts with the nascent iron to form iron sulphide in the tribofilm. The polyphosphate has been named as smart material as the hardness increases with the loading force.[78] The center of the pads is stiffer than other region due to the composition of long-chain polyphosphate. [79]

By using quantum calculation, Mosey et al.[80, 81] introduced the pressure-induced cross-linking theory of antiwear performance of ZDDP and zinc polyphosphate. The authors showed that the zinc coordination has changed from tetrahedral configuration to hexa-coordinate geometry, which modifies the linear chain of polyphosphate to the 2D or 3D matrix of zinc and phosphate ions. The coordination of zinc can be reverted to tetrahedral but the planar structure still remains. This irreversible pressure-induced

formation of cross-links of the zinc atoms contributes to the "smart" properties of antiwear tribofilm of phosphate. As the pad in Figure 1-5 is exposed to the high contact load, the cross-linking occurs and induces a rapid growth of stiff pad and the formation of long-chain polyphosphate. Mosey also discussed the contribution of each element to the antiwear behavior of ZDDP. Zinc with a flexible coordination plays a role as a cross-link agent; phosphorus also gets various covalent coordinations and acts as both glass former and cross-linking agent.

In tribological contact area, phosphates in different configuration such as ortho [17, 82], pyro [83, 84], and metaphosphate with a variable chain-length [17, 83, 85] possessed an anti-wear potential because of a similar ZDDP-derived tribofilm formation. In general, these three different types of phosphate contribute synergistically to reduce friction and wear.[86] Among many ZDDP research, the effect of phosphate chain length has been considered as an important factor that affects the antiwear efficiency. Based on HSAB principle, Martin et al.[18] proposed that the long chain polyphosphate could digest abrasive iron oxide particles and form short chain mixed iron/zinc phosphate glasses. Supporting the Martin's study, Wan and co-workers [87] considered that the ZDDP detergent combination containing short chain polyphosphates produces a poor antiwear performance with the tribofilm formed during pin on disc experiments. Nevertheless, there are still disagreements on these ideas. A review by Nicholls [79] suggested that the lubricant tribofilm is composed of antiwear patches in the direction of rubbing. At the contact area with high pressure, severe depolymerization took place and resulted in the short chain polyphosphate with iron oxide located at the center of the pads. Heuberger et al. [88] also found a thicker short chain polyphosphate film in the tribo-stressed area at higher contact loads with the ball-on-disc tribotest at the temperature up to 150°C. Crobu et al [86] obtained a lower friction coefficient and antiwear behavior at room temperature for short chain polyphosphate compared to longer chain lubricant with the same tribotest. For the non-contact areas, the long chain configuration is still maintained in the thermal film, the film created outside the wear track and effected by the temperature only.

Recently, Gosvami et al.[89] applied mechano-chemistry to explain ZDDP tribofilm formation mechanism. Under single-asperity contacts, the tribofilm formation rate was grown exponentially with pressure and temperature. The pressure and temperature can reduce the activation energy of the polymer degradation reaction which induced the formation of the tribofilm. Spikes then reviewed the idea of stress-promoted thermal activation in tribology and the application of this model in describing the friction

coefficient and tribofilm formation.[19] The recent work of Spikes's group reconfirmed the stressed induced and thermal activated theory on ZDDP tribofilm formation reaction. The formation rate depends on the applied stress and temperature under elasto-hydrodynamic lubrication (EHL) conditions.[90] The decomposition of ZDDP compounds was mechano-chemically driven by the shear stress instead of pressure due to the fact that the tribofilm formed in the high EHL viscosity test rather than the lower viscosity case. Moreovers, the tribofilms formed in the full-film EHL condition, which removed the effect of direct asperity contact in the tribological process. The rate of tribofilm growth was independent of ZDDP concentration, thus it is concluded to follow the zero-order kinetics. This state-of-the-art approach provided a valuable tool in studying mechanochemical processes which are the innovative theories to explain different engineering phenomena. [90]

The use of ZDDP with sulphur and zinc has a deleterious effect on the exhaust through the catalytic converter. Besides, the performance of ZDDP at 600°C to 1200°C for metal forming is also questionable. Thus, there is a demand to reduce ZDDP in engine oil and/or replacing the conventional additives by more environmentally friendly ones.

For other phosphorus-based compounds, Holbert et al. [91] in 1998 conducted a study of the reaction between trimethyl phosphite $P(OCH_3)_3$ with Fe(110) surface in order to study the ZDDP performance. Trimethyl phosphite decomposed through P-O bond breaking, released methoxy $–OCH_3$ group and formed phosphide film on the surface. This Fe-P film has been supported by Philippon and co-workers.[92, 93] The authors discussed the spontaneous growth of iron phosphide film by investigating the thermodynamics process. The formation mechanism was also proposed with the methoxy decomposition and iron phosphide formation by friction. The high hardness of iron phosphide layer is considered as an important factor of antiwear and lubricating under friction condition. Recently, this group investigated further into the trimethyl phosphite by a combined first-principle calculation and experiments.[63, 94, 95]

1.2.3 Phosphate lubrication properties at high temperature

Sodium polyphosphate glass $(-NaPO_3-)_n$ ($NaPO_3$ for short) is a potential candidate for high temperature lubricant for hot rolling processes as this inorganic glass reduces the usage of heavy metal while producing the phosphate network lubricity and achieving the good aqueous solubility. With the use of sodium polyphosphate ($NaPO_3$) and potassium

dihydrogen phosphate (KH_2PO_4), Tieu et al.[12, 13] reported the friction and wear reduction by 60% at the temperature from 600 to 800°C. A 200 to 300nm thick tribofilm has been generated with the composition of Na, K, P and O elements. With the same lubricant in the rolling mill tests, Kong et al.[14] confirmed the digestion of iron oxide into polyphosphate. Fe_2O_3, $FePO_4$ and $NaFeP_2O_7$ have been observed in the tribofilm as products of tribochemical reactions. The layered structure and gradient composition of polyphosphate film is also confirmed. The tribofilm contains a 5 nm short-chain polyphosphate layer on the top and a 5 nm long-chain polyphosphate layer underneath the top layer which adheres to the oxide surfaces through another short-chain layers from 50 – 200 nm. The reaction between iron ions with polyphosphate film shortens the polymer chain and produces more Fe-O-P strong bonds and $P_2O_7^{4-}$ group. The gradient composition of alkali phosphate tribofilm was also mentioned in Wan's work [27], thus reconfirming the tribochemical reaction between abrasive oxide particle with polyphosphate glass.

In order to unveil the working mechanism of phosphate lubricant in hot rolling condition, Cui et al.[96] tested different chain-length sodium phosphate compounds at 800°C. The long chain sodium polyphosphate $NaPO_3$ achieved a more stable friction coefficient during the test compared to sodium pyrophosphate $Na_4P_2O_7$ and sodium orthophosphate Na_3PO_4 even though the smallest coefficient of friction was obtained with the orthophosphate. In hot rolling processes, reducing friction close to zero is not a priority as the process still need friction to have to work piece drawn into the rolling stands.[21] Thus the stable and sufficiently low value of friction is preferable in the hot rolling process. The dissolution of Fe atom was observed in the trace of $NaFePO_4$ in the wear debris after tribological tests in later experiments.[97, 98]

The alkali cations also play an important role on tribological performance of polyphosphate. However, the detailed tribochemical reaction, the exact role of alkali cation, and the tribological performance of sodium polyphosphate lubricant at high temperature are not fully understood nor can they explain all experimental results.

1.2.4 Theoretical approach to tribology of phosphate-based compounds

The laboratory tests have been developed throughout time to study most of the main issues in hot metal forming processes: friction, wear, heat transfer, and lubrication.[6] However, the industrial process, especially hot rolling steel, is difficult to replicate at

laboratory scale due to the complexity of the real process such as the high contact speed of work piece and tool, complex oxidized surface, and the coolant water used during the process.[21] Thus, since 1998, Beynon suggested that a computer-based model is an effective source for tribologists to study and tackle the interfacial events in hot rolling process.[21] With the presence of lubricant in the process, many chemical reactions have been occurred in the confined interface of tool – lubricant – work piece under arduous working conditions. The computer simulation at atomistic scale has been proven to be an effective method to investigate the molecular nature of these reactions. Many common methods have been used currently to investigate the lubricant/surface tribochemical reaction are: density functional theory (DFT), ab initio molecular dynamics (AIMD) and reactive molecular dynamics (reactive MD).

Due to the complexity of tribological system which involves temperature, pressure, shear, multi-element compounds, the application of computer simulation into tribology is quite limited including the phosphate-based system. Mosey et al. studied the thermal decomposition of ZDDP monomer, dimer and isomers in relation to their antiwear performance at different temperature of 700K and 1500K.[99, 100] DFT calculation was used to discuss the structures and energetics of ZDDP compounds while AIMD was performed to investigate the decomposition pathway for those compounds at 700K and 1500K. ZDDP monomer underwent the Zn-S dissociation path while the dimer and isomer went through different decomposition pathway of radicals, olefins and sulfides removal depending on the substituents species. All pathways created the thiophosphate compounds which are the precursor of ZDDP tribofilm. However, the aryl-substituted ZDDP lost the alkoxy radicals during the decomposition which reduced the quality of tribofilm as well as its antiwear performance.[99] Mosey's group also used DFT and AIMD to investigate the metathiophosphate (MTP) formation in the process and its ability to generate phosphates chain at the high load contact area, which is well-known as the smart ZDDP film.[101, 102] MTP dissociation has been proven to be energetically favorable at high temperature and the phosphate chain can be polymerized from certain type of MTP in the system.[101] The reaction pathway from MTP molecules to phosphate chain was also developed which provided the insight of tribofilm formation mechanism as well as the lubricant design of ZDDP.[102]

The lubrication performance of other phosphorus-based compounds also received attention to the theoretical studies. De Barros-Bouchet et al. investigated the trimethyl phosphate $(CH_3)_3PO_4$/trimethyl phosphite $(CH_3)_3PO_3$ absorbed on Fe(110) surface in a

combination of experiments and DFT method.[63] The friction reduction behavior of phosphate/phosphite lubricant was observed with the experiment and was reconfirmed by DFT calculation. Phosphorus was efficient in reducing the sliding resistance between iron surfaces compared to the same concentration oxygen. This observation led to the explanation of different lubricity between phosphate and phosphite. With a higher amount of phosphorus, phosphite could generate an iron phosphide with native iron surfaces at extreme tribological condition and contributed to its friction reduction.[63] Righi's group then focused on the adsorption and dissociation mechanism of trimethyl phosphite $(CH_3)_3PO_3$ (TMP) on iron surface with DFT and AIMD simulations.[94, 95, 103] The mechanism of phosphorus released on iron surface was proposed with the completed reaction pathway. The activation energy of 0.75 eV was stated as an essential energy to start the TMP dissociation.[95] In the simulation comparison between P-passivated and S-passivated iron surface, the resistance for sliding compared to cleaned iron surface reduced 60% for phosphorus and 70% for sulfur which predicted the more efficient friction reduction in S-based lubricant.[94] Recently, the interfacial chemistry of tricresyl phosphate (TCP) additive has been studied using theoretical methods of DFT method.[104] The comprehensive comparison between different thermodynamics reaction pathways based on different environment conditions of TCP anti-wear film formation on iron surface has been conducted. The pathway of TCP decomposition including C-O bond breakage, toluene removal, and the final tribofilm of phosphate showed a strong binding of phosphate group to the iron surface. However, this mechanism need thermal and mechanical energies to overcome the high barrier energy of the dissociation reaction.[104] DFT and AIMD have their advantages in capturing the tribochemical reaction in the landscape of energy, temperature, pressure, and shear. However, the system size is limited up to 200 atoms due to the huge computational cost and small time scale. This problem restrain the simulation model to the ideal condition of structures, time, and space domains.

In order to expand the system to observe more realistic tribological behavior, Koyama et al. conducted the phosphoric trimethyl $(CH_3)_3PO_4$ on Fe surfaces simulation with 45 molecules of phosphoric trimethyl between two Fe substrates.[105] One molecule of phosphoric trimethyl and a layer of nine Fe atoms had been treated in a QM space with the tight-binding quantum chemical calculation to reveal the tribochemical reaction between the lubricant additive and the nascent Fe surface while the rest was described with classical MD at 423K, pressure of 1 GPa, and shear rate of 100 m/s. The combination

approach can deal with the large complex system with proper computational cost and still remain the chemical behavior of the system. The combination code provided the result of lubricant – surface interaction through oxygen from P=O and P-O-CH_3. The interaction then dissociated under boundary lubrication condition via the monitoring of bond overlap population during simulation which was the initial step of tribofilm formation process.[105] In the comparison of sliding and non-sliding cases, the study showed the strong effect of the friction on the dissociation reaction of phosphoric trimethyl on Fe surface.[105] Onodera et al. simulated Fe_2O_3/Cr_2O_3/MnO nanoparticle inside zinc metathiophosphate ($Zn(PS_{0.5}O_{2.5})_2$) and zinc metaphosphate ($Zn(PO_3)_2$) network confined by Fe surfaces with the in-house QM-MD combination code which increased the system size up to 3315 atoms.[106, 107] With the boundary lubrication condition and temperature of 353K, oxide particles were digested by phosphate-based network in the combined effect of pressure and shear. The process was also thermodynamically favorable. The calculations confirmed the ability of zinc polyphosphate to react with abrasive metal oxides nanoparticles under pressure and shear which contributed to the good anti-wear performance of phosphate-based lubricant or additive.[106, 107]

Martin et al. used classical MD to investigate the tribochemical reaction of zinc phosphate and iron oxide surface in various tribological condition: temperature range 300K – 2500K, pressure from 1 MPa to 1 GPa, sliding rate from 0.1 m/s to 100 m/s.[78] The series of calculations confirmed the abrasive particle digestion based on HSAB theory.[78] However, the detailed reaction cannot be depicted by normal MD. This can be overcome with a Reactive MD with reactive force field (ReaxFF) which can deal with the realistic tribological system size and describe accurately the behavior of the reaction inside the system. This method is drawing attention in various physics/chemistry/biology fields, especially the growing number of studies using this force field in tribology. Thus, ReaxFF will be carefully reviewed in section 2.3. With the improvement of computational resources, the simulation approaches gradually catch up with the space and time domain of tribological processes. Different methods have been used recently in the tribology field such as quantum mechanics, ab initio molecular dynamics, reactive molecular dynamics, etc. which are able to reveal the atomistic to molecular behavior of lubricant during the complicated tribological procedures, especially our focus on hot rolling.

1.3 Main aims of thesis

As seen in the literature review, much knowledge about tribological properties of

phosphate as a lubricant has been obtained, especially for zinc dialkyldithiophosphate. With the history of 80 years, the mechanism of ZDDP under boundary condition has been unveiled. However, the demand of new green lubricant is becoming more significant because of the modern standard of friendly environmental and non-toxic additive. The non-zinc and non-sulfur phosphate compounds have attracted attention recently but there are few studies considering the detailed tribological properties of this material. Not only that, the trending approach of atomistic simulation receives even less attention in the academic world. Few attempts have been made to study the mechanism of sodium polyphosphate glass as a lubricant for hot rolling processes. However, the experimental approaches cannot reveal the deeper understanding of this lubricant mechanism and many questions still remain unclear. Which phenomena occur between oxide surfaces with lubricant surface? Adsorption, desorption, chemical reaction, or physisorption? How temperature affects these phenomena? What is the key factor which mainly contributes to the lubricity performance? What is the chemical viewpoint of the lubricity process? And other questions need to be answered. Hence, this thesis applies different multiscale theoretical approaches to provide novel solutions for a deep insight into the tribochemical reaction and the tribological performance between sodium polyphosphate with iron-based interfaces for hot rolling steel.

In this thesis, chapter 3 studies the depolymerization of sodium polyphosphate on iron oxide surface which includes the bond nature of the system and the effect of chain length and temperature on the depolymerization reaction. The depolymerization of phosphate-based lubricant was reported in several experimental studies but there is no theoretical studies about this phenomenon has been done previously for sodium polyphosphate glass. The depolymerization of phosphate glass is also considered as a core behavior which helps this glass lubricant to achieve a low and stable coefficient of friction. Chapter 4 completes the tribochemical mechanism of sodium phosphate lubricant with the surface transformation effect due to lubricant adsorption. The contribution of every interaction on surface also unveils, e.g -Fe-O-P- linkage, Fe-P direct bond, and Na-O interaction. The surface transformation behavior contributes to the good anti wear performance of phosphate glass lubricant as well as reconfirms the well-known abrasive particle digestion theory for ZDDP. Finally, chapter 5 develops the reactive potential for sodium phosphate and iron oxide system, then applied in the reactive MD to study the tribological behavior of this inorganic glass lubricant at the realistic molecular dynamics scale. The novel force field is newly developed and can be used for systems which include Na/Fe/P/O elements.

Chapter 2 Methodology

2.1 Quantum mechanic

In recent years, theoretical approaches by using computational simulation has a considerable development and remarkable impact on the material engineering field. This computational methods have been used to develop, identify, optimize, and design new materials, especially in nanotribology [108-110]. Current experimental analysis techniques cannot investigate the tribochemical reactions and the products at the interface of sliding surfaces at high temperature and pressure, nor the detailed nature of the contacts at the sub-nano scale; thus they cannot explain how the tribo-contacts behave nor what determine the achieved level of friction and wear between the surfaces. Computer simulations on a model can be carried out to perform a parametric study to gain insights into the mechanics that achieves an optimum tribological performance of the interface in the end. With this method, it is possible to vary the atomic structures, sliding conditions, and interactions between atoms. Therefore, both theoretical approach and experimental studies are needed to explore completely nano-tribological phenomena, especially the tribofilm behavior. The theoretical simulation can unveil the dynamical and electronical behaviors at molecular level and be employed in the nano-tribological field. However, the practical length scale and the time scale pose as a drawbacks for all engineering problems, although they can provide much needed insights into the contact interface.

Among different computational methods, quantum mechanics (QM) is considered to be the most accurate tool to investigate the energy and structure of a system of atoms and molecules at the atomic scale. QM also has the capability to describe the chemical reactions in complex systems. The method determines energy and geometry of system by solving the Schrodinger equation:

$$H\psi(\vec{r}) = E\psi(\vec{r}) \qquad (2.1)$$

where H is the Hamiltonian operator which contains kinetic energy T and potential energy V of the system. ψ is the wave function and E the energy of the system. However, from atoms with more than one electron, the Hamiltonian operator become very complex and cannot be solved analytically. The well-known approximation Hartree - Fock and Density Functional Theory has been proposed to solve the equations with much reduced computational cost.[111]

2.1.1 Hartree-Fock method

Hartree-Fock method (HF) provides an ab initio approach which writes wave function as a simple product of single particle states. It was originally formulated by D.R. Hartree and then accomplished by V. Fock and J.C. Slater [112, 113]. This method also named as self-consistent field method (SCF) which contains the following iteration steps:

- Initial guess at the orbitals
- Construction of all the operators
- Solution of the pseudo-Schrodinger equations for single particle
- Reconstruction of Hartree operators with the new set of orbitals
- Iterations convergence is achieved

Even though the HF method helps to achieve the solution iteratively, it neglects the important contribution of the electron correlation energy, and thus it has to be adjusted by using Møllet - Plesset perturbation theory. However, the solution by this ab initio method is complicated due to the integral operator in the equation, spin contamination effect and huge computational cost. Therefore, it has been superseded by the density functional theory.

2.1.2 Density Functional Theory method

An alternative to the HF methods is the density functional theory (DFT) [114] which offers a good compromise between accuracy and computational expense for many systems. Nowadays, DFT has become the method of choice for exploring electronic structure and reaction mechanisms in chemical, biological, material and solid-state systems. The basic idea of DFT method is to derive properties of a system through the electron probability density. The original concept of a density functional for the energy came from L.H. Thomas and E. Fermi work in the late 1920s. After that, the correspondence between ground-state energy and its electron density was formalized by P. Hohenberg, W. Kohn and L.J. Sham [115, 116]. Instead of solving directly the Schrodinger equation, the Kohn-Sham equation reduces the computational complexity from order of n^4-n^7 to an order of n^3 where n is the number of basis functions used. However, the exchange-correlation potential in the Kohn-Sham equation still needs to be approximated further. Based on the type of exchange-correlation approximations, DFT has been classified into the local density approximation (LDA), generalized gradient

approximation (GGA) and the hybrid one.

- **Local density approximation (LDA):** LDA is a poor approximation in practice because the electron density tends to be inhomogeneous with the presence of the nuclei. The most common LDA functional is S-VWN5, which use Slater's expression for the exchange [117] and Vosko, Wilk and Nusair's expression for the correlation [118].
- **Generalized gradient approximation (GGA):** The GGA functional such as PBE [119] usually provides a significant increase in the accuracy of predicted energies and structures, but with an additional cost compared to LDA.
- **Hybrid functional:** The hybrid functional such as B3LYP [120, 121] uses the Hartree-Fort correction in conjunction with DFT correlation and exchange. The method consumes more computational cost than GGA and LDA.

The quantum calculations to elucidate the tribological reaction behavior under boundary lubrication state have been performed by Mosey et al. with the Car-Parrinello first-principles molecular dynamics simulation [81, 102, 122, 123]. With the method, the author can reveal the nature of tribochemical reaction under pressure. However, more quantum studies are needed to investigate the realistic tribological system with shear rate which is absent in Mosey's works. In the study of chemical processes, quantum calculation cannot represent the tribological systems which usually cover 10,000 to 1,000,000 atoms in many nanoseconds running time due to the extremely large computational cost [124, 125]. Quantum method can hardly represent the tribochemical reaction dynamics, which covers not only the friction process but also complex substrates and interfaces as well. Therefore, the conventional molecular dynamics has been proposed to deal with complex tribology systems at the atomistic level. However, the accurate energy system and the nature of many-body interaction acquired by QM, especially DFT still have to be used to optimize empirical force fields which require fewer computational resources [126]. These empirical methods, including reactive force field (ReaxFF) in molecular dynamics, can consider tribochemical reactions with much improved simulation scale and a considerable accuracy [127].

2.2 Molecular dynamics

Molecular dynamics (MD) is a simulation technique which investigates the time dependent motion of molecular system under specific conditions. MD simulation assumes that the classical Newton's equation of motion hold true at the molecular level and treats the nuclei as point charges in the same way as quantum mechanics but does not explicitly model electron density. MD calculation can potentially be used as a possible replacement for experiments with appropriate interaction potential between the particles which include bonds, valence angles, torsion, van der Waals interactions, etc. [128, 129].

Molecular dynamics manages the trajectories of atoms by solving Newton's classical equation of motion on all interacting atoms in the molecular system:

$$F = ma \qquad (2.2)$$

The relationship between force F and potential energy U is

$$F = -\nabla U \qquad (2.3)$$

From the knowledge of the force on each atom, the atom trajectories such as positions, velocities and accelerations can be obtained. Thus, the molecular dynamics determine the evolution of a system of atoms through time such as structure, dynamics and thermodynamics. This powerful numerical method can provide not only the information in steady state but also the behavior of the system in non-equilibrium process.

2.2.1 Integration methods

The original Verlet algorithm provides a direct solution of Newton's equation of motion [129]. To calculate atomic position of next step, the current position, current acceleration and previous position of atom have been used:

$$r(t + \delta t) = 2r(t) - r(t - \delta t) + \delta t^2 a(t) \qquad (2.4)$$

The velocity is calculated with the next and the previous step atom position as follow:

$$v(t) = \frac{r(t+\delta t) - r(t-\delta t)}{2\delta t} \qquad (2.5)$$

The positions have the error of the order δt^4 and velocities of the order δt^2. The velocity Verlet algorithm is one of the most popular modifications to minimize the velocity errors and improve the stability. Thus, the velocity Verlet algorithm [130, 131] has been used in order to obtain the position and the velocity of every atom. The periodic boundaries are also applied in our model to represent the infinite system in a specific directions.

2.2.2 Types of ensemble

Ensemble is a collection of all possible systems which have different microscopic state but share an identical macroscopic or thermodynamic state. The different types of ensemble have been discussed as follow [132]:

- **Micro-canonical ensemble (NVE):** The thermodynamic state is identified with a fixed number of atoms (N), a fixed volume (V), and a fixed energy (E). This ensemble represents an isolated system. The internal energy is conserved in the simulation.
- **Canonical ensemble (NVT):** This ensemble is defined by a fixed number of atoms (N), a fixed volume (V), and a fixed temperature (T).
- **Grand canonical ensemble (μVT):** This ensemble is composed of large number of open, isothermal systems of particles, each of which has same chemical potential (μ), same volume (V) and same temperature (T). The number of atoms (N) is not necessarily constant.
- **Isobaric-Isothermal ensemble (NPT):** This is a collection of systems which have thermodynamic state characterize by a fixed number of atoms (N), a fixed pressure (P), and a fixed temperature (T).

The MD simulations use the thermostat to maintain a constant temperature, while barostat has been used for pressure consideration. The barostat rescales the system volume each time step to maintain pressure. Some common barostats were introduced by Anderson [133], Rahman-Parinello [134] and Berendsen [135]. The thermostats will be discussed in the following sections.

2.2.3 Thermostat models

Tribological MD simulations require an accurate temperature control. When shearing is applied on two surfaces, the work done on the atoms is finally transformed into random thermal motion which raise the temperature of the system because the heat is not totally dissipated. To simulate the experimental conditions, the system should be coupled with the heat reservoir to produce the heat flow from the system into the surrounding. The most common algorithm is Nose-Hoover [136-138]. In order to retain the temperature of system, the heat is transferred back and forth between the heat reservoir and our system. In Nose-Hoover algorithm, the Newton's equation has been modified as follow:

$$a_i(t) = \frac{F_i(t)}{m_i} - \zeta(t)v_i(t) \qquad (2.6)$$

Where the friction coefficient ζ is defined as:

$$\frac{d}{dt}\zeta(t) = \frac{N_F}{Q}(k_B T(t) - k_B T_0) \qquad (2.7)$$

Where N_F is the number of degrees of freedom which equals $3N + 1$, N is number of particles. $T(t)$ is the instantaneous temperature, T_0 is the reservoir temperature, k_B is the Boltzmann constant.

The fictitious mass parameter Q represents the heat transfer rate. It should be adopted to a proper value to control the system temperature. If Q is too large, the system will decouple from the heat reservoir and make the algorithm ineffective, whereas if Q is small, the high heat transfers between the heat reservoir and the system can turn the system into a non-physical model.

In MD simulation of confined shear tribological system, the confined fluid atoms are not thermostatted and the walls are maintained at the constant temperature. This thermostating approach proves to be an efficient method that closely resembles experimental conditions.[139, 140]

2.2.4 Force field

The key component in a molecular dynamics model is the force field which is a functional set of parameters that expresses the potential energy of molecular systems as a function of atomic positions. The parameters of a force field represent the bonded and non-bonded interaction between atoms. These parameters include the inter-molecular and intra-molecular linkage, electrostatic Coulombic attraction and van der Waals force.

The conventional force fields ignore the electronic motions and calculate the energy of a system based on the atom coordinates. Hence, in general, the conventional molecular dynamics is inadequate to deal accurately with atom connectivity, for instance bond forming and breaking among atoms as well as chemical reactivity and transition state [141]. An exception is the Brenner potential [142] which can obtain accurate ground state structure of hydrocarbon and represent the bond breaking. However, the van der Waals and Coulomb interaction are not included in this potential. In addition, the Brenner potential describes poorly the actual potential energy curves which produce very high reaction barriers in the bond breaking reaction. The modification of Brenner potential has included non-bond forces [143] but still suffer some problems on reactive potential curves. Other methods which use bond order concept such as Bond Energy Bond Order

(BEBO) and VALBOND are notable. However, these methods do not fully provide the chemical reactivity of breaking and forming bonds.

The ReaxFF [144] which upgrades the Brenner potential concept is a state-of-the-art reactive force field with the bond order/bond distance relationship. This advanced force field bridges the gap between the conventional molecular dynamic and the empirical quantum calculation with a reliable accuracy and simplification of the chemical interaction.[125] Thus ReaxFF is our choice to solve the tribological system of sodium polyphosphate with iron oxides surface and it will be discussed later.

Even though conventional MD simulation cannot yield the bond behavior of atoms, it can provide representative details of confined shear process in term of mechanical and tribological properties. For instance, the results of MD calculation usually includes molecular arrangement, layering behavior, temperature profile, film thickness and so on. The molecular dynamics simulation has been conducted on LAMMPS code [145] and then the results visualized with VMD [146] and OVITO [147] software.

2.2.5 Non-equilibrium molecular dynamics

Non-equilibrium molecular dynamics (NEMD) simulations in tribology normally involve shear forces with a conventional MD system. These systems can help tribologists understand the behavior in both dry friction (no separation between sliding surfaces) and lubricated friction (or wet friction in which sliding surfaces are covered by lubricant). Urbakh et al. reviewed the fundamental understanding of friction in 2004.[2] In the review, atomistic MD simulation has wide range of tribological applications and reaches a certain degree of accuracy even though its limitation in timescale and length scale. In 2008, Szlufarska et al. summarized experimental and theoretical researches in dry and wet friction in the focus of nanotribology.[148] The authors discussed the usage of atomic force microscopy (AFM) in the experimental method and atomistic simulation in a theoretical approach in the context of single-asperity contact studies. In 2013, Vanossi et al.[149] reviewed advances of nanoscale to mesoscale friction modelling and Dong et al.[150] focused on NEMD simulations of AFM experiments. Sawyer et al. in 2014 organized advances in dry friction understanding with the contribution of NEMD.[151] In 2018, Ewen et al. provided an overview of recent innovation in using NEMD to study lubricated friction systems.[152] Thanks to the fast development of simulation algorithms, force fields, experimental advances and computation resources, NEMD can

begin to compare directly to experiment and unveil the fundamental understanding of tribological phenomena from the atomic scale.

2.3 Reactive force field (ReaxFF)

Reactive force field (ReaxFF) is a MD potential parameterized from quantum mechanics calculations which is developed by van Duin and colleagues [144]. In recent year, ReaxFF has become the most advanced potential which is able to accurately model chemical reaction with the MD computational expense.

The main function for the chemical activity in ReaxFF is the bond order which derived from the basis of interatomic distances and updated every iterative time step. The value of bond order will be reduced to zero when the atomic distance goes beyond the cutoff radius. The correct bond order is subsequently adjusted with over-coordination and under-coordination penalty energies. The reactive force field also obtained multi-body interaction effects such as 3-body valence angle terms or 4-body torsional terms [125].

The overall system energy has been described as a sum of different individual energy terms which vanished smoothly as the bonds are broken.

$$E_{system} = E_{bond} + E_{lp} + E_{over} + E_{under} + E_{val} + E_{pen} + E_{coa} + E_{C2} + E_{triple} + E_{tors} + E_{conj} + E_{H-bond} + E_{vdWaals} + E_{Coulomb} \quad (2.8)$$

The partial energies introduced in Equation 2.8 include bond energy, lone pair energy, over-coordination energy, under-coordination energy, valence angle energy, torsion energy, hydrogen bond energy, van der Waals, and Coulomb interaction. The detailed functions for each partial term can be found from ReaxFF User Manual updated and expanded on March 2013 [153] or in the supplementation document of reference [154]. All terms except van der Waals and Coulomb are bond-order dependent and they change continuously between single, double, and triple bonds and gradually go to zero as the distance increases. The Coulombic energy is computed using the electronegativity equalization method (EEM) [155], which allow charge transfer during the chemical reactions. The van der Waals term is derived using Morse potential and the excessive close range non-bonded contacts are avoided by shielding function. With bonded and non-bonded terms, ReaxFF can be used to predict the reaction rate and activation energies for covalent, ionic, metallic and intermediate materials. It is designed to include bond dissociation, bond formation and other higher order effects with the acceptable accuracy

compared to DFT methods but at significantly less computational expense.[141]

The parameters of the ReaxFF potential are optimized from a training set which is obtained from experiment and quantum mechanics derived data. Therefore, the accuracy of ReaxFF method depends on the quality of the training set, which gives the empirical optimization for the potential parameters. The training set usually contains geometry configuration (bond length, angle, torsion, etc.), atomic charges, heat of formation, and different types of energy (bond dissociation, transition state, heat of reactions, etc.). In order to make a transferable force field, the training set needs to cover the element information for a wide range of structure diversity and various phase of compositions. The weighting factors are also included in the training set which helps the optimization to focus on the critical parameters. Normally the single-parameter parabolic extrapolation method introduced by van Duin [156] has been applied to find the optimal parameters. However, there is no guarantee that the global optimum is reached in the optimization. Selecting an efficient and accurate minimization steps can be quite difficult with many local minimum valley of parameters.[157, 158] Thus, many studies have focused on multi-object global optimization methods for ReaxFF parametrization using genetics algorithms (GA) which surpass the conventional single-parameter one.[157, 159-161] Besides GA, many other advanced ReaxFF parameter optimization techniques have been developed such as multiple objective evolutionary strategies (MOES),[162] metropolis Monte Carlo with simulated annealing (MMC),[158] covariance matrix adaptation evolutionary strategy algorithm (CMA-ES),[163] etc. Among the robust methods for comparison, GA presented the lowest probability being trapped in a local minimum.[164] Hence, an advance GARFfield package using multi-object GA optimization was applied for ReaxFF parametrization.[160] The procedure for parametrizing a reactive force field is presented in Figure 2-1. More detailed calculations for ReaxFF optimization of our tribological system is discussed in Chapter 5. ReaxFF parameter sets are usually published in a standard text file which can be read by LAMMPS or ReaxFF program. The ReaxFF program is a standalone FORTRAN code which can be used to run MD simulation as well as parameter optimization. This FORTRAN code was provided privately by Prof. van Duin [144].

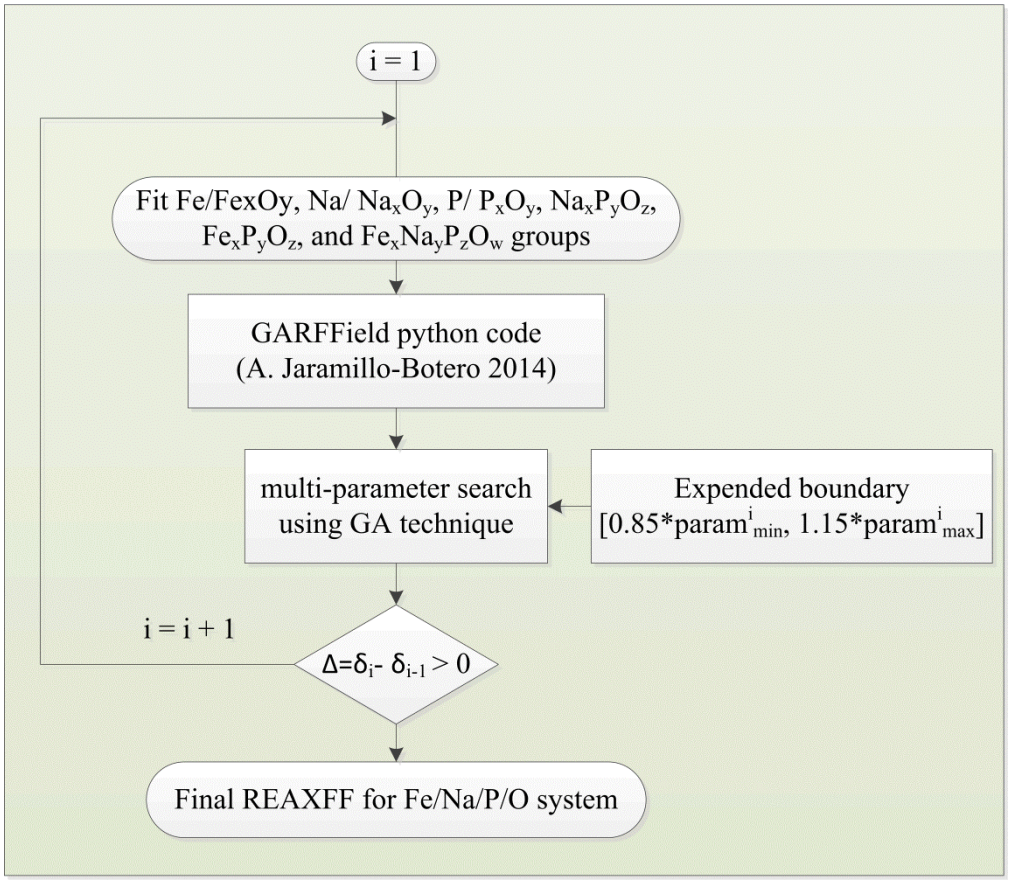

Figure 2-1. Optimization strategy our current ReaxFF development for Fe/Na/P/O systems

Recently, ReaxFF can successfully describe the majority of the periodic table. The general ReaxFF procedure to determine energies and available elements will be described in Figure 2-2. The references for most ReaxFF publications can be found in reference [127].

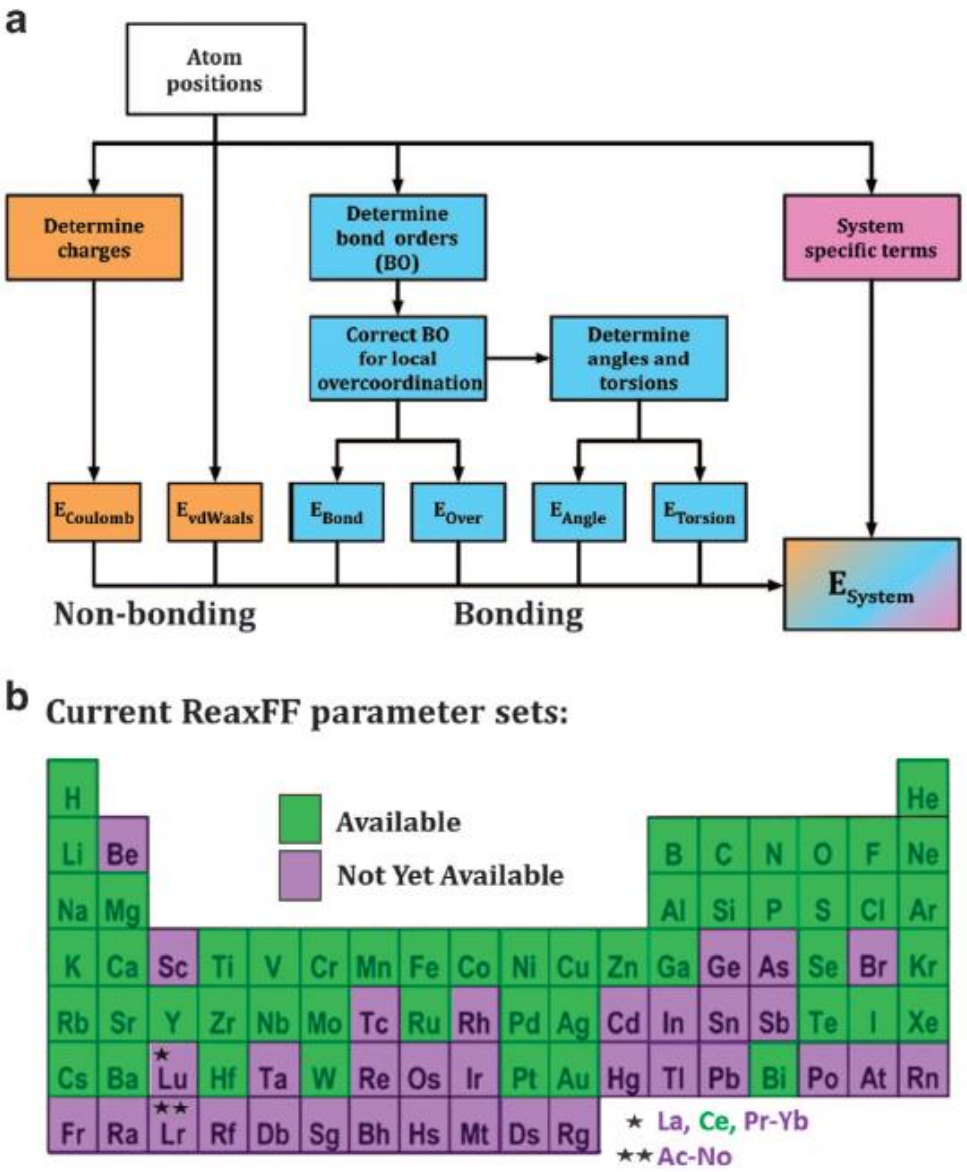

Figure 2-2. (a) General ReaxFF energies component and (b) Available elements in the ReaxFF publications [127]

In tribology, the application of reactive MD using ReaxFF is trending in recent years.[165] Since 2013, the works of Yue et al. are the typical studies of tribological thin film.[166, 167] Reactive MD has been utilized to investigate the tribochemical reaction of phosphoric acid on silica surfaces. During the sliding condition, the friction behavior depended on temperature. Below 600K, the rotational and translational movement of phosphoric acid dominated the tribological performance, whereas the polymerization of this acid and slip plane of water created due to the polymerization are the controlling phenomenon above 800K. Wen et al.[168] studied the nanoscale wear of silicon/amorphous silica system in aqueous environment with reactive MD. The Si-O-Si

and Si-Si dissociation was spotted during the tribochemical process which was responsible for Si-surface removal. The dual role contribution of water to the wear process was also observed as promoting-inhibiting Si removal. The reactive MD can combine with the novel mechano-chemical theory to explain the mechanical-induced reaction pathway. Yeon et al.[169] explored the polymerization of allyl alcohol sheared between amorphous silica surfaces. Allyl alcohol in the polymeric form can provide the lubrication effect and the polymerization reaction was mechanically induced by the alcohol molecules anchoring to surface then undergoing molecular distortion. The tribological simulations on iron-based surface has recently received some attention. Mohammadtabar et al.[170, 171] investigated the chemisorption as well as thin film formation of di-tert-butyl disulfide on Fe(100) surfaces. The reactive MD simulations demonstrated the comparable results to ab initio calculations in the thermal film growth process. The ReaxFF simulation also reconfirmed the thermal and mechanical-induced driving force of the tribochemical reactions in the system. More relevantly, the reactive MD simulation for wear performance of inorganic sodium silicate glass on amorphous silica has been conducted by Hahn et al.[172] In the presence of water, the mechano-chemical wear has been suppressed. The role of Na^+ cation was also discussed in the study which showed its contribution in the hydrolysis and dissociation of Si-O-Si linkage. Although the applications of reactive MD in tribology are potentially significant, the number of ReaxFF works in this field is still limited due to the unavailability of relevant force fields. The tribological systems usually contains many elements and a proper ReaxFF for that system has to be newly developed which is challenging and time consuming. The new ReaxFF developed in Chapter 5 is the first reactive force field for the inorganic sodium phosphate glass/iron oxide system. The most related ReaxFF is the force field development work on tricresyl phosphate on iron oxide which has no parameters for sodium element [173]. With this recent developed tricresyl phosphate force field, Ewen et al. studied the thermal decomposition effect of phosphate esters on different ferrous surfaces.[174] The simulation on Fe_3O_4 (001) and α-Fe(110) observed the chemisorption of phosphate esters even at the room temperature while the physisorption occurred on the hydroxylated amorphous Fe_3O_4-OH. The simulated temperature order for C-O bond dissociation is consistent with the experimental observation of different substituents of phosphate esters decomposition on the Fe_3O_4 (001) surface.

Chapter 3 Depolymerization of sodium polyphosphates on an iron oxide surface at high temperature [1]

3.1 Introduction

An effective lubricant is essential in a hot metal manufacturing process due to vast of adverse effects at elevated temperatures such as high friction, considerable wear and severe oxidation. Phosphate glass lubricants have received more attention recently due to the excellent tribological behavior of zinc diakyldithiophosphate (ZDDP) at the temperature below 250°C and also its environmentally friendly and thermal stability nature. In the harsh working condition of hot rolling of steel, alkaline polyphosphates can provide the good antiwear property, friction reduction and oxidation inhibition.[12-14] In previous studies on tribological tests [26, 27], a polyphosphate film has been observed to have layered structure and gradient composition which makes it a very effective lubricant.[17, 18] However, the working mechanism of inorganic phosphate glasses as a promising lubricant at elevated temperature needs more in depth understanding. Besides the potential lubricant functionality, the glassy compounds contained polyphosphate are also well-known for their bioactivity,[7] optical technology application,[9] and radioactive waste immobilization.[8]

For the well-known ZDDP, Ito et al.[175] proposed the mechanism of physical adsorption on iron oxide surface and the dissociation of lubricant molecules at ambient temperature. The phosphate adsorption on the oxide surface at ambient temperature has been investigated in soil mechanics from both experiments [176-180] and simulations.[181-185] The phosphate anion $H_nPO_4^{3-n}$ has been usually used as an adsorbate on metal hydr(oxide) surface. However, the complex formation and lubricant-oxide interaction in these studies are still controversial. Either monodentate or bidentate have been generated during the adsorption under different pH conditions.[185, 186] The iron-phosphate interaction has been considered as both ionic bonding[187] and covalent nature.[105] Recently, we have examined the adsorption of sodium ortho- and pyrophosphate clusters on iron and iron oxide surface.[188] The initial phase of tribochemical reaction of phosphate glass lubricant has been investigated with in-depth analysis in electronic

[1] Based on **Manh Ha Le,** Anh Kiet Tieu, Hongtao Zhu, Dinh Thi Ta, Haibo Yu, Thi Thuy Huong Ta, Van Nam Tran and Shanhong Wan, "Depolymerization of sodium polyphosphates on an iron oxide surface at high temperature", *Physical Chemistry Chemical Physics*, 2018. 20(11): p. 7819-7835.

structures.

Besides, the depolymerization of polyphosphate lubricant during the tribological process has been widely reported and it plays a crucial role in the molten phosphate lubricity. At ambient temperature, Martin et al.[18] showed that the long-chain zinc polyphosphate glass enhanced the antiwear property by digesting abrasive iron oxide and formed the short-chain iron/zinc phosphate glasses. Nicholls et al.[79] proposed the antiwear pad structure in the ZDDP tribofilm which composed of long-chain polyphosphate and was stiffer to withstand intense loads than nearby short-chain areas. Crobu et al.[86] mentioned that the initial short-chain phosphates exposed the lower wear and friction compared to long-chain polyphosphate case. For tribological behavior of phosphate at elevated temperature, Tieu et al.[13, 27] employed alkaline phosphate glasses and noted the reduction of phosphate chain length with increasing temperature. Short-chain length orthophosphate structures were observed in the whole tribofilm. The digestion of iron oxide into polyphosphate film which shortens the polyphosphate chain was observed. Cui et al.[96] conducted works on different chain length phosphates such as ortho- (Na_3PO_4), pyro- ($Na_4P_2O_7$) and long chain meta-phosphate $(NaPO_3)_n$. The short chain tribofilm obtained from the depolymerization of metaphosphate produced a better tribological performance compared to the anti-oxidation orthophosphate case. Even though the experimental studies have shown the effect of depolymerization of polyphosphate lubricant on tribological properties, there is still limited understanding on the detailed mechanism and the influence of the oxide surface on this process.

In recent years, the theoretical methods have a remarkable growth and considerable impact on the academic and application field. These computational approaches have been used for exploiting the potential materials as well as studying the unexplored properties, especially in nanotribology.[108] Among all, quantum mechanics (QM) is a suitable tool to describe bond breaking and formation in a chemical reaction at atomic scale and the tribochemical reaction of phosphate gets no exception. Mosey et al.[100] conducted density functional theory (DFT) calculation for the unimolecular decomposition of ZDDP. Righi et al.[95] proposed the mechanism of the dissociative adsorption of phosphite additive on Fe(110) surface. Ta et al.[188] discussed the sodium phosphate clusters adsorbed on iron-based substrates. Recently, the development of advanced computational resources allows more realistic tribological conditions to be considered by the ab initio molecular dynamics (AIMD).[101, 123, 189] Compared to the productive applications, limited number of theoretical studies using phosphate is available due to its

complex structure and various behavior involvements inside the glassy system.

In this study, both DFT and AIMD calculations have been carried out to understand the depolymerization of sodium polyphosphates on iron oxide surface at high temperatures which is an important phenomena observed in experimental work.[96] The bridging bond dissociations of $Na_4P_2O_7$ and $Na_5P_3O_{10}$ cluster with and without iron oxide surface have been conducted. The detailed results about the bond nature of the system, effect of surface, chain length and temperature on depolymerization reaction will be presented.

3.2 Computational details

3.2.1 Static DFT calculation

DFT calculations have been conducted in order to investigate the structure optimization of phosphate clusters and their decomposed products on iron oxide surface. All spin-polarized calculations have been performed with Vienna Ab-initio Simulation Package (VASP).[190] The Projector Augmented Wave (PAW) method [191] has been chosen with the Generalized Gradient Approximation (GGA) of Perdew−Burke−Ernzerhof (PBE) exchange and correlation functional [119] as it has been acknowledged as a reasonable compromise among other functionals when representing dynamic decomposition on a metallic surface. [192] The energy cutoff of 400 eV has been applied for all calculations to truncate the expansion of plane wave basis set. Fe_2O_3(0001) facet has been chosen as the adsorption surface with the dimension of a = b = 10.07 Å, c = 23.98 Å for $Na_4P_2O_7$ adsorption and a = 15.11 Å, b = 10.07 Å, c = 23.98 Å for $Na_5P_3O_{10}$ adsorption in order to minimize lubricant periodic image interaction. A vacuum region of 20 Å is included in the system to avoid the effect of nearby Fe_2O_3 layers in the z-direction. For static calculations, a Γ-point only sampling has been used for super-cell geometry optimization and a denser Monkhorst-Pack mesh [193] of 9x9x1 has been employed for total energy calculations of slab models. The geometry optimizations are conducted using the conjugate gradient algorithm along with a first order Methfessel-Paxton scheme [194] until the energy convergence criterion of 10^{-4} eV has been reached. For more accurate energetic properties, the single point calculation use tetrahedron smearing technique with Blöchl corrections and the energy converged within 10^{-4} eV.

The adsorption energy E_{ads} is defined as:

$$E_{ads} = E_{total} - (E_{surface} + E_{mol}) \qquad (3.1)$$

where, E_{total}, $E_{surface}$, and E_{mol} are the total energy of the adsorbed molecules on substrate,

bare Fe_2O_3 substrate and isolated gas-phase lubricant, respectively. Hence, the negative value of E_{ads} indicates a thermodynamically favorable adsorption. Besides, the dissociation of separated molecule in the gas phase has also been considered in order to investigate the effect of the iron oxide surface on phosphate decomposition process. This process focuses mainly on depolymerization of linear polyphosphate chain.

The dissociation pathway of P-O bond on Fe_2O_3 surface was investigated with constrained minimization approach.[195-197] P-O distance has been fixed and all remaining degrees of freedom have been optimized to minimize the Hellmann-Feynman forces.[198] The P-O distance is then varied to monitor the energy profile of the reaction with these conditions: (a) all forces on atoms vanish and (b) the energy is a maximum along the reaction coordinate (P-O distance) but it is a minimum for all other degrees of freedom. The geometry relaxation of the constrained systems has been performed with external optimizer GADGET,[199] which uses the VASP output, computes the optimal steps of internal coordinates and starts the new VASP run. The relaxation stopped when the variation of the energy is less than 10^{-4} eV and the force less than 10^{-2} eV/A.

To investigate the bonding characteristic, both Electron Localization Function (ELF) and Bond Overlap Population (BOP) have been employed in the high-accuracy single point calculations. The ELF (η) evaluates the probability of finding the same spin electron in the surrounded area of reference electron.[200, 201] The maxima $\eta = 1$ has been found in C-C covalent single bond of diamond crystal while $\eta = 0.5$ shows the homogeneous electron gas in some metal structure.[202] The BOP has been computed by the integration of crystal orbital overlap population (COOP) using the Local-Orbital Basis Suite Towards Electronic-Structure Reconstruction (LOBSTER) package.[203] The BOP, which represents the shared electron density between two atoms, can measure the covalency of the system. It provides the information about bonding, antibonding and non-bonding nature of a covalent interaction when the BOP is over zero, below zero or close to zero, respectively.[204]

3.2.2 AIMD simulation procedure

AIMD simulations have been implemented for dynamics depolymerization process of sodium polyphosphates on iron oxide surface at elevated temperature. Due to the high computational expense, only the Γ-point sampling is applied in these simulations. Based on the compromise between computational efficiency and integration error, 0.5 fs time

step has been chosen. With this time step, the total energy deviation of less than 0.02 eV has been observed during a 500-step MD run which has assured the stability of the system.[192] Three bottom layers of iron oxide have been fixed while the top three and lubricant coordinates have been optimized. Three preliminary AIMD simulations at 300 K include one $Na_4P_2O_7$ cluster on Fe_2O_3 surface; one $Na_5P_3O_{10}$ cluster on Fe_2O_3 surface; one Na_3PO_4 unit and one $NaPO_3$ unit on Fe_2O_3 surface. The main simulations use the same structures and have been heated to 1100 K. These simulations run for 20 ps which suggested stable ground-state or intermediate configurations for static calculation. The snapshots will be captured in the Appendix A. Then, seven structures of each system have been chosen and subjected to energy minimizations. The lowest energy conformer of each case has been reported here as ground-state structures. Next, each decomposed unit, Na_3PO_4 and $NaPO_3$ have been optimized separately on the Fe_2O_3 surface in order to capture stable adsorption configurations. The active adsorption sites of the surface are Fe atoms which strongly link to oxygen atoms of the lubricant compound. On top of the Fe-terminated oxide surface, iron atoms form equilateral triangles with 5.04 Å side. The stable adsorption sites of decomposed products are usually inside these triangles. Finally, both decomposed units have been relaxed on top of the surface with different relative positions of triangles (shown in Figure A-2 in Appendix A). In order to distinguish the different types of non-bridging oxygen (O_{nb}), we denoted the ionic-bonding Na-O as terminal oxygen (O_t), and the Fe-O-P as linkage oxygen (O_l). Thus, the oxygen types in the system include (1) bridging oxygen (O_b) in P-O-P, (2) terminal oxygen (O_t) in P-O-Na, (3) linking oxygen (O_l) in P-O-Fe linkage between lubricant and surface, and (4) surface oxygen (O_s) on Fe_2O_3 surface.

3.3 Results

3.3.1 Structure of $Na_4P_2O_7$ and $Na_5P_3O_{10}$ clusters

For lubricant compounds, tetrasodium pyrophosphate $Na_4P_2O_7$ has been chosen as a model for polyphosphate $(NaPO_3)_n$ according to reference [205]. Pyrophosphate is also one of the most stable structures of condensed phosphates which has been reported by Van Wazer.[68] Another linear phosphate compound sodium triphosphate $Na_5P_3O_{10}$ has been included to investigate the chain length effect. Triphosphate is a main product of thermal decomposition phosphate glass up to 828 K.[206] These substances contain the oxygen sites of the same properties as in polyphosphate which are bridging oxygen (O_b)

and non-bridging oxygen (O_{nb}). O_{nb} will be categorized into O_t and O_l as the oxide surface included in the system. In order to validate the geometry optimization of the sodium phosphates by DFT, we analyzed the structure of both $Na_4P_2O_7$ and $Na_5P_3O_{10}$ clusters. Calculated bonding and angular properties were compared with the experimental data of $Na_4P_2O_7$ and $Na_5P_3O_{10}$ (Table 3.1). The geometric properties of $Na_4P_2O_7$ and $Na_5P_3O_{10}$ cluster agree very well with crystalline structures reported by Larsen et al.[207], MacArthur and Beevers [208] and Cruickshank.[209] The distance difference of ~ 0.1 Å between P-O_b and P-O_{nb} has been observed in previous experimental work [210] which is consistent with our results (Table 3.1).

Moreover, we calculated the bond overlap population (BOP) and electron functional localization (ELF) to provide detailed information of chemical bonding in our system. The optimized structures of $Na_4P_2O_7$ and $Na_5P_3O_{10}$ clusters with BOP and ELF data have been presented in Figure 3-1 and Figure 3-2.

Table 3.1. The geometrical parameters of $Na_4P_2O_7$ and $Na_5P_3O_{10}$ clusters

	$Na_4P_2O_7$		$Na_5P_3O_{10}$	
	Current DFT	Expt.[a]	Current DFT	Expt.[b]
P-O_b (Å)	1.66	1.63	1.63 (inner) 1.72 (outer)	1.61 (inner) 1.67 (outer)
P-O_{nb} (Å)	1.54	1.45 - 1.52	1.53	1.49 – 1.51
Na-O_{nb} (Å)	2.15	2.47 - 2.63	2.20	2.25 – 2.76
P-O_b-P (degree)	139.5	128.7 - 133.5	132.5	122.2
O_b-P-O_b (degree)	-	-	99.1	98.7
O_b-P-O_{nb} (degree)	106.3	99.0 – 109.6	105.7	100.1 – 110.1
O_{nb}-P-O_{nb} (degree)	112.4	113.0 – 116.0	115.4	113.4 – 116.4

[a] Data obtained by Larsen et al.[207] and MacArthur and Beevers [208]

[b] Data obtained by Cruickshank [209]

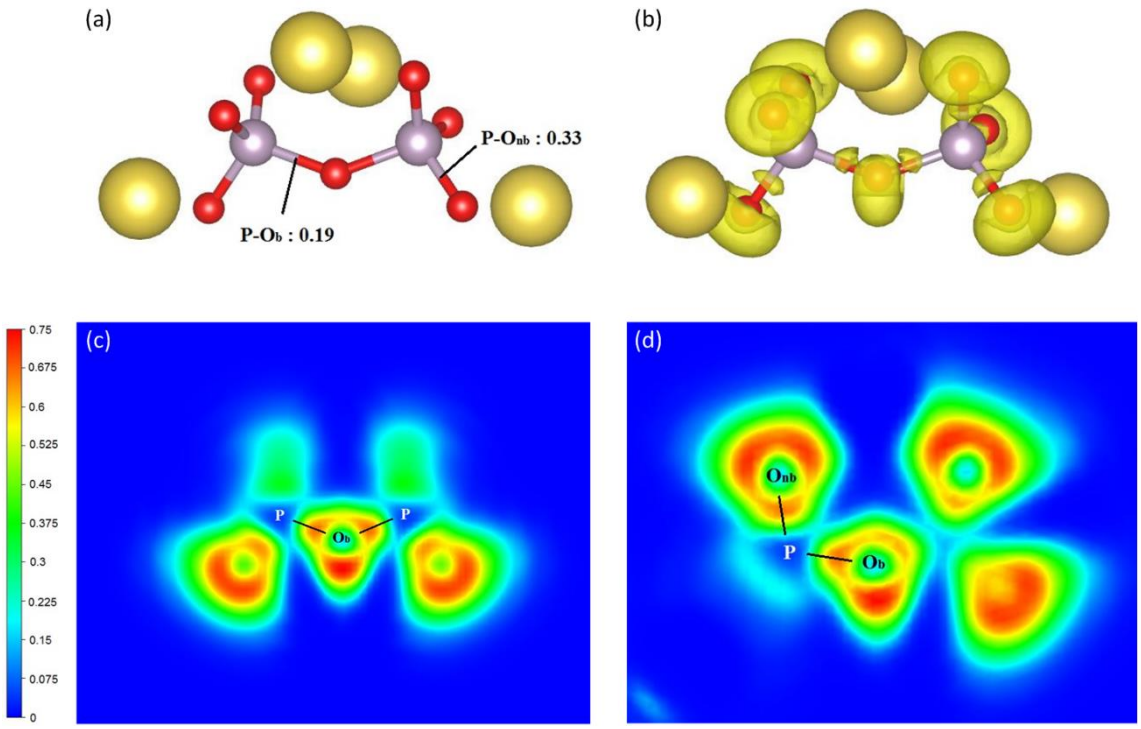

Figure 3-1. Optimized structure of $Na_4P_2O_7$ cluster with (a) average BOP of P-O_b and P-O_{nb} bond; (b) ELF isosurface (yellow regions) at $\eta = 0.62$; ELF contours of (c) P-O_b-P slice, (d) O_b-P-O_{nb} slice. Red, purple and yellow spheres represent oxygen, phosphorus and sodium atoms, respectively.

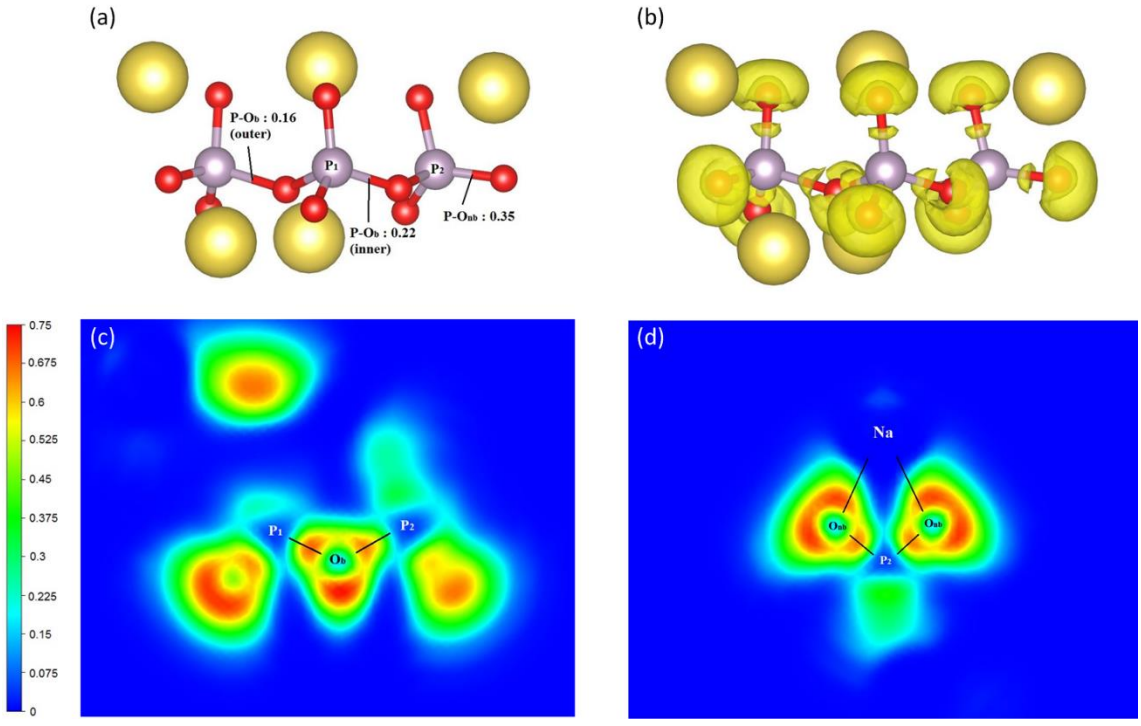

Figure 3-2. Optimized structure of $Na_5P_3O_{10}$ cluster with (a) average BOP of P-O_b inner, P-O_b outer and P-O_{nb} bond; (b) ELF isosurface (yellow regions) at $\eta = 0.62$; ELF contours of (c) P_1-O_b-P_2 slice, (d) O_{nb}-Na-O_{nb} slice. Red, purple and yellow spheres represent oxygen, phosphorus and sodium atoms, respectively.

Besides the consistent geometric properties of phosphate cluster, the BOP ratio P-O bridging bond/non-bridging bond of 0.16-0.22e / 0.33-0.35e agrees well with the COOP curve of $P_2O_7^{4-}$ by Le Beuze et al.[211] The P-O non-bridging bonds are twice stronger than bridging ones. In Figure 3-1 and Figure 3-2, the maximal ELF value is 0.75 which represents a moderate degree of electron pairing and covalent bonding. Most of electron pairs are localized around oxygen atoms as electron receivers with different shapes and concentration. For bridging oxygen atom, three explicit regions have been observed in Figure 3-1b and Figure 3-2b. Two electron-localized areas appear in the middle of phosphorus and oxygen which indicates the modest covalent interaction of P-O_b. Another region on the bridging oxygens depicts the lone pair area which avoids the phosphorus-oxygen bond direction. In terms of non-bridging oxygen atoms, a P-O electron-pair localized area for each O_{nb} is also spotted in the middle of the bond in Figure 3-1d and Figure 3-2d. Thus, the P-O interaction in general is the strongest covalent bond among all. The mushroom-like localized lobe of lone pair electron gets no deformation toward sodium and is located in the opposite of covalent P-O area as seen in Figure 3-1b and Figure 3-2b. Besides, the BOP for Na-O bond is 0.01 to 0.02e, which indicates no overlap area between sodium and oxygen. Thus, the interaction between sodium and non-bridging oxygen is purely ionic interaction. For $Na_5P_3O_{10}$ cluster, the non-bridging P-O_{nb} bonds have the average BOP of 0.35e which is nearly identical to this bond type in $Na_4P_2O_7$ (BOP = 0.33e). We show two bridging P-O_b bonds as inner and outer of the $Na_5P_3O_{10}$ cluster in the Figure 3-2. The BOPs for these bonds are 0.22e and 0.16e, respectively. The bond distances are also matching with the BOPs: 1.63 Å for inner bond, and 1.72 Å for outer bond. With the difference of the BOP values and the distances of P-O_b inner and P-O_b outer bonds in $Na_5P_3O_{10}$ cluster, the ELF also shows that the electron localized area between P_1-O_b (inner) and P_2-O_b (outer) has a slightly distinct shape. P_1-O_b has a larger and more intense area of electron pair possibility which indicates that the covalent bond of inner P-O_b bond is stronger than the outer bridging bond. In conclusion, the bridging P-O bond is the most fragile site in the phosphate chain and has the topmost possibility to be detached in the working environment of hot metal forming process.

3.3.2 Dissociation of $Na_4P_2O_7$ and $Na_5P_3O_{10}$ clusters

Isolated phosphate clusters

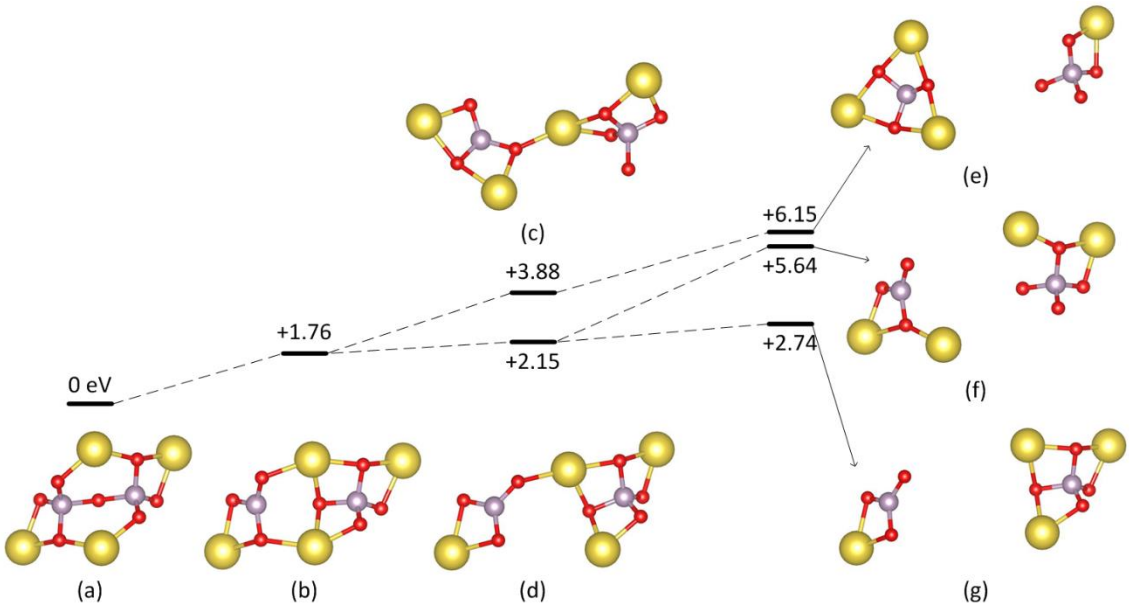

Figure 3-3. Structure evolution of sodium atoms during P-O-P bridging bond dissociation: (a) $Na_4P_2O_7$ cluster, (b) PO_3 and PO_4 units sharing two Na ions, (c, d) PO_3 and PO_4 units sharing one Na ion, (e) Na_3PO_3 and $NaPO_4$ structures, (f) Na_2PO_3 and Na_2PO_4 structures, (g) $NaPO_3$ and Na_3PO_4 structures. Red, purple and yellow spheres represent oxygen, phosphorus and sodium atoms, respectively. The energies are in eV.

In Figure 3-3a of small $Na_4P_2O_7$ cluster, the number of oxygen atoms around sodium cation is two so the position between two PO_4 tetrahedra includes two sodium atoms. For alkali polyphosphates, there are some discrepancies in the reported oxygen coordination around Na atom in the literature, i.e. 5 by Hoppe et al.[212, 213], 2 by Uchino and Ogata [214] and 2.4 by Musinu et al.[215] This variation comes from different experimental and theoretical structures of alkali phosphate glass. Thus, the two-oxygen coordination around sodium ions in our study is feasible.

In Figure 3-3, the Na-O bonds have been visualized with the cutoff distance of 2.4 Å during P-O bridging bond dissociation. Non-directional ionic Na-O interaction allows sodium atoms to move freely toward PO_3 unit or PO_4. Three different structures generated by three schemes with different sodium complexation have been optimized without constrains (shown in Figure 3-3d, 3-3e and 3-3f). Along these schemes, P-O_b distance has been elongated from 1.66 Å to ~7.0 Å. Seven converged configurations have been depicted in Figure 3-3. At the initial phase of the dissociation, PO_3 and PO_4 units have two shared sodium ions at the distance of ~2.72 Å (Figure 3-3b) or have one shared sodium ion at the distance of ~4.25 Å (Figure 3-3c). These structures indicate that sodium

ions can be distributed between two different phosphate chains. This means that sodium ions also have a weak network forming role besides the dominant modifier function as proposed by Uchino and Ogata.[216] The relative stabilities of three decomposed configurations are shown in Figure 3-3d, 3-3e, and 3-3f. In these configurations, two phosphate units are separated by a distance about 7 Å. The optimized results show that the structure in Figure 3-3f reaches the lowest total energy among the three configurations; therefore it has been used for the optimization of decomposed products on the Fe_2O_3 surface in the following steps. Remarkably, the relative energies yield positive values which mean the decomposition of P-O_b bridging bond in the isolated $Na_4P_2O_7$ cluster is not thermodynamically preferable. The energy of +2.74 eV is taken into account for the dissociation energy of P-O bridging bond in the isolated cluster as it follows the minimum energy path of the decomposition.

The ground-state structure and energy differences of $Na_4P_2O_7$, $Na_5P_3O_{10}$ and their decomposition products from isolated cluster and on iron oxide surface have been presented in the upper part of Figure 3-4a and Figure 3-4b. Besides, geometric parameters and bond overlap population (BOP) between them have been listed in Table 3.2.

Firstly, different complexation forms of sodium ions have been considered for the ground state of $Na_4P_2O_7$ decomposition. As a result, the structure including one Na_3PO_4 cluster and one $NaPO_3$ unit has reached the lowest total energy as shown at Figure 3-3f. Correspondingly, the products of $Na_5P_3O_{10}$ decomposition are optimized as $NaPO_3$ unit and $Na_4P_2O_7$ cluster. In Table 3.2, P-O_b bridging bond becomes P-O_{nb} non-bridging bond after decomposition. For $Na_4P_2O_7$ cluster, the P-O_b distance varies from 1.66 Å to 1.60 Å and the BOP increases from 0.19e to 0.26e. Another P-O_b distance is elongated up to 7.02 Å and the BOP becomes 0.00e, indicating that this P-O_b bond is completely broken. One covalent sharing area of O_b atom in Figure 3-1b merges with the lone pair area of that bridging atom and is located opposite to the remaining covalent localized area during the decomposition. At the end, the PO_4 unit contains four non-bridging oxygens with four P-O covalent electron-localized areas and four mushroom-like electron lobes of oxygen lone pair which interact ionically with sodium.

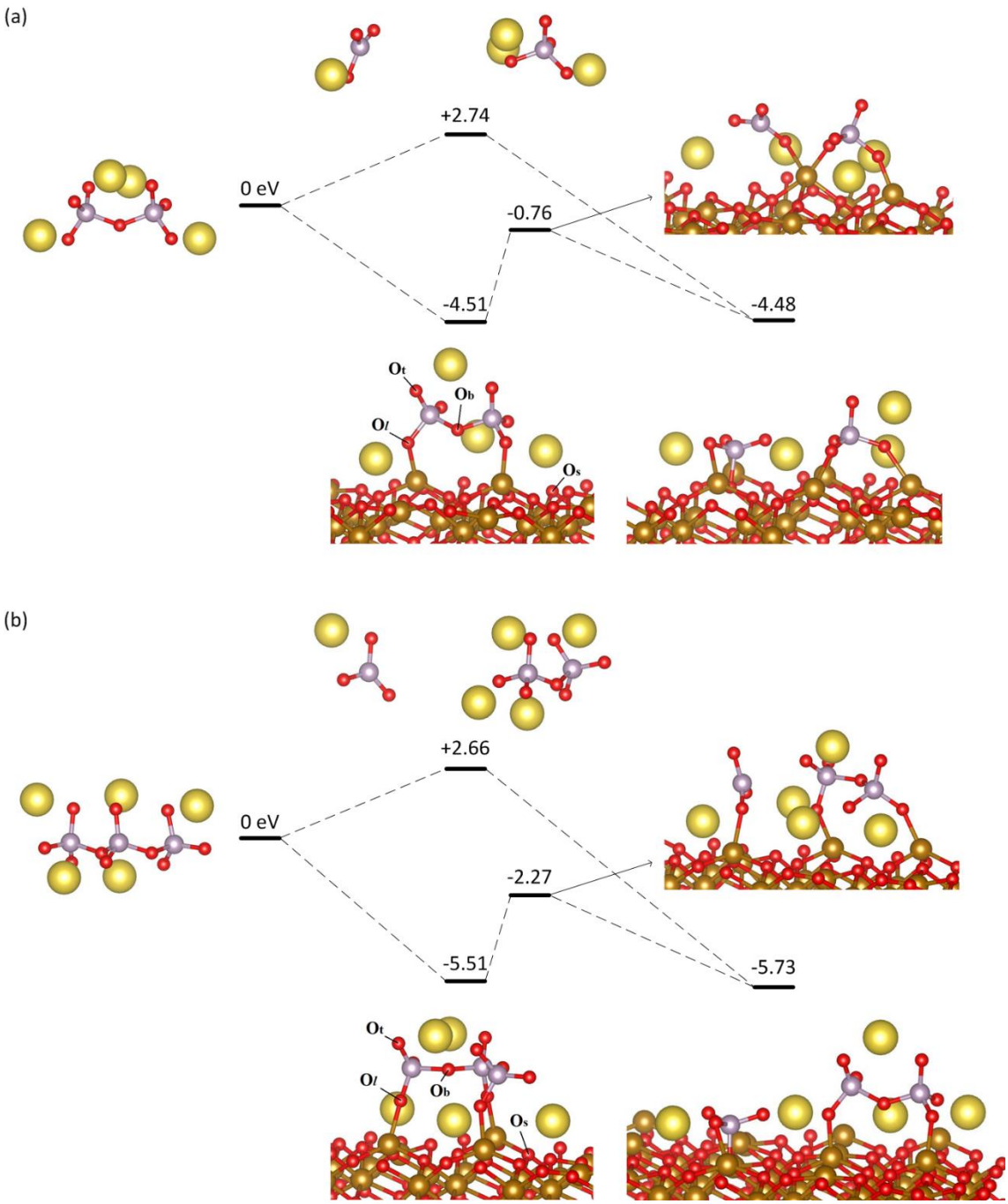

Figure 3-4. The bridging bond dissociation of (a) isolated $Na_4P_2O_7$ cluster and its interactions with $Fe_2O_3(0001)$ surface, (b) isolated $Na_5P_3O_{10}$ cluster and its interactions with $Fe_2O_3(0001)$ surface. Red, gold, purple and yellow spheres represent oxygen, iron, phosphorus and sodium atoms, respectively. The energies are in eV.

Table 3.2. Geometric parameters and BOP of phosphate clusters and their decomposition products. Values of BOP (|e|) from integrated crystal orbital overlap population (COOP) are shown in parenthesis.

	Isolated $Na_4P_2O_7$ cluster	Decomposed isolated $Na_4P_2O_7$	Isolated $Na_5P_3O_{10}$ cluster	Decomposed isolated $Na_5P_3O_{10}$
P-O_b (Å) (outer)	1.66 (0.19)	1.60 (0.26) 7.02 (0.00)	1.72 (0.16)	1.85 (0.10) 7.41 (0.00)
P-O_b (Å) (inner)			1.63 (0.22)	1.60 (0.27) 1.61 (0.23)
P-O_{nb} (Å)	1.54 (0.33)	1.53 (0.33)	1.53 (0.35)	1.52 (0.35)
Relative energy (eV)	0.00	+2.74	0.00	+2.66

In terms of longer chain length cluster, one outer P-O_b bond has increased to 7.41 Å and BOP reduces to 0.00e in the decomposition process of $Na_5P_3O_{10}$ cluster (Figure 3-4b). The inner bridging bond connects to the broken outer bridging has shortened from 1.63 Å to 1.60 Å and the BOP has risen from 0.22e to 0.27e, which is close to that of a typical non-bridging bond. Another inner bond slightly reorganizes the bond distance and BOP due to the alteration of outer bridging bond nearby. This outer bond is extended to 1.85 Å and reduces the BOP to 0.10e. The decomposed-like variation is caused by an imbalanced distribution of sodium atoms around P_2O_7 unit as seen in the top structure of Figure 3-4b. In particular, the bridging oxygen of P_2O_7 unit is surrounded by three sodium ions with the distances of 3.26 Å, 2.50 Å and 2.42 Å and the corresponding BOP values of -0.01e, 0.02e, and 0.01e, respectively. In comparison with $Na_4P_2O_7$ cluster in the left structure in Figure 3-4a which has the typical bridging P-O bond of 1.66 Å (BOP 0.19e), two Na-Ob interactions produced an identical distance (BOP) of 2.98 Å (-0.01e). The negative value of BOP represents the antibonding interaction. Thus, the bridging oxygen of P_2O_7 unit from $Na_5P_3O_{10}$ cluster decomposition has been attacked by nearby sodium atoms and causes the elongation of outer bridging P-O bond. This phenomenon confirms the network modifier function and induced-depolymerizing effect of alkali metal on phosphate glass.[217]

Both $Na_4P_2O_7$ and $Na_5P_3O_{10}$ dissociation are not thermodynamically favorable in the gas due to the positive energy difference up to 2.74 eV for $Na_4P_2O_7$ and 2.66 eV for $Na_5P_3O_{10}$. There is a difference between two P-O breakage energies but it is not considerable. The

difference is mainly based on the sodium distribution around breakage bond. Moreover, the P-O_b split energy of P_2O_7 unit in Figure 3-4b is 2.87 eV while this energy of outermost P-O_b on $Na_6P_4O_{13}$ is 2.78 eV. Hence, the P-O_b bond dissociation energy of sodium phosphate is about 2.6 – 2.9 eV and is affected to a minor degree by the chain length.

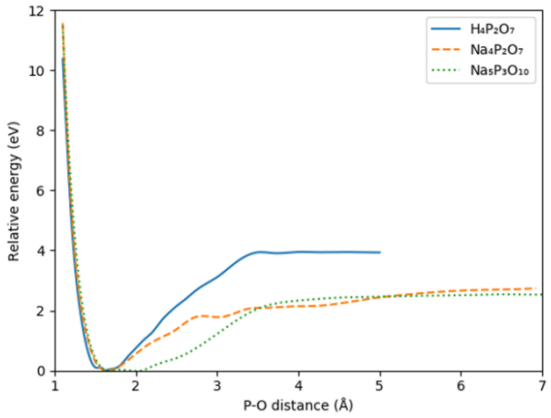

Figure 3-5. Relative energies of P-O bond dissociation of isolated $H_4P_2O_7$, $Na_4P_2O_7$, and $Na_5P_3O_{10}$ clusters.

The energy profiles of P-O bridging bond dissociation for the isolated $Na_4P_2O_7$ and $Na_5P_3O_{10}$ clusters have been showed in Figure 3-5. The result of $H_4P_2O_7$ cluster has also included in the figure in order to investigate the effect of cations on bridging bond dissociation. The energy at the equilibrium P-O distance of the three clusters has been chosen as the reference energy. For $Na_5P_3O_{10}$ cluster, the P-O outer bond is selected. In the figure, 3.5 Å is the cut off of the bond dissociation process, and the stable dissociation energy appeared after this distance. Compared among three clusters, the dissociation energies of $Na_4P_2O_7$ and $Na_5P_3O_{10}$ are steady around 2.7 eV while much higher dissociation energy of 4.0 eV from $H_4P_2O_7$ result has been observed. Four hydrogen atoms of $H_4P_2O_7$ can play a role as dangling bonds in the network,[214, 216] thus the dissociation energy of $H_4P_2O_7$ can represent the dissociation of 3-D network of polyphosphate without cation, i.e. P_2O_5 glass structure. Hence the modifier cation like sodium helps reduce the P-O bridging dissociation energy.

Sodium phosphates dissociation on Fe_2O_3 surface

For the oxide substrate, we conduct the study on the iron termination of Fe_2O_3(0001) surface which has been reported as the most stable facet in many experimental and theoretical studies.[218, 219] Six atomic layers of Fe_2O_3(0001) surface have been used and the number of atoms in the surface is up to 60 atoms. Three bottom atomic layers of the surface have been fixed in order to represent the bulk behavior of iron oxide while all above layers have gone through relaxation. For the iron oxide surface, the obtained charge of Fe_2O_3(0001) is in agreement with the model by Ta et al.[220] The results have been provided in Appendix A.

The most stable configurations of $Na_4P_2O_7$ cluster adsorption and $Na_5P_3O_{10}$ cluster adsorption have been described in the bottom structures of Figure 3-4a and 3-4b, respectively. $Na_4P_2O_7$ adsorption structure has been obtained from the study by Ta et al.[188] A variety of oxygen types have been noted in Figure 3-5a. The geometry parameters and bond overlap population (BOP) in those configurations have been listed in Table 3.3.

Table 3.3. Geometric parameters and BOP of phosphate clusters and their decomposition products adsorbed on Fe_2O_3 surface. The BOP values (|e|) from integrated crystal orbital overlap population (COOP) are shown in parenthesis.

	Absorbed $Na_4P_2O_7$[a]	Decomposed $Na_4P_2O_7$	Absorbed $Na_5P_3O_{10}$	Decomposed $Na_5P_3O_{10}$
P-O_b (Å) (outer)	1.66 (0.21)	1.57 (0.30) 4.04 (0.00)	1.71 (0.17)	1.65 (0.22) 4.40 (0.00)
P-O_b (Å) (inner)			1.61 (0.24)	1.58 (0.26) 1.66 (0.21)
P-O_t (Å)	1.52 (0.36)	1.51 (0.39)	1.51 (0.38)	1.51 (0.37)
P-O_l (Å)	1.59 (0.27)	1.58 (0.29)	1.55 (0.31)	1.58 (0.27)
P-O_s (Å)		1.70 (0.18)		1.78 (0.15)
O_l-Fe (Å)	1.91 (0.24)	2.09 (0.18)	1.98 (0.22)	1.91 (0.24)
Fe-O_s near P-O-Fe linkage (Å)	1.89 (0.21)	1.89 (0.21)	1.90 (0.21)	1.91 (0.20)
Fe-O_s on surface (Å) [b]	1.86 (0.23)	1.89 (0.20)	1.88 (0.21)	1.90 (0.20)
Relative energy (eV)	0.00	0.03	0.00	-0.22

[a] Data obtained by Ta et al.[188]

[b] The Fe atoms on the top layer of the surface only

In terms of the phosphate – iron oxide adsorption, Atkinson et al.[180] proposed P-O-Fe monodentate structure of iron phosphate complex as one of the most stable linkages observed during the adsorption of phosphate on goethite interface which is observed in Figure 3-4a and b. The adsorbed structure of $Na_5P_3O_{10}$ is also in line with Kubicki et al.[183] which mentioned P-O_l bond 1.56 Å and P-Fe distance 3.42 Å. In addition, these values are also observed in the studies of Belelli et al.[181] and Acelas et al.[182]. When $Na_5P_3O_{10}$ clusters adsorb on the Fe_2O_3 surface, some P-O_t bonds change into P-O_l interaction. The bond distance and bond overlap population change from 1.53 Å, 0.35e into 1.55 Å, 0.31e. The Fe_2O_3 surface will reduce the strength of P-O terminal bond if the terminal oxygen atom contributes to P-O-Fe linkage which is consistent with Ta et al.[188] for short chain length sodium phosphate cluster $Na_4P_2O_7$. In the case of adsorbed cluster structures, one oxygen atom of each PO_4 tetrahedron forms an interaction with one iron atom on the substrate. These O_l-Fe bonds are 1.91 – 1.98 Å long and have the BOP of 0.22 - 0.24e, which are similar to the distance and BOP of Fe-O_s on the surface in both clusters. Thus, we categorize the bond type into three strength levels and their order based on BOP after adsorption is as follow:

$$P\text{-}O_b \approx Fe\text{-}O_s \approx Fe\text{-}O_s \text{ near linkage} \approx Fe\text{-}O_l < P\text{-}O_l < P\text{-}O_t$$

For iron-oxygen interaction, Fe-O_l bond is as strong as Fe-O_s next to linkage and the normal Fe-O_s on top of the surface which have BOP of 0.21 – 0.24e. With the system contained phosphate clusters and iron oxide surface, P-O_b is still one of the most feeble bond and has a strong chance for dissociation. The finding is supported by the study of $Na_4P_2O_7$ adsorption on Fe_2O_3.[188] In additional, the ELF value of cluster adsorption has been displayed in Figure 3-6 for more information about Fe-O-P linkage interactions.

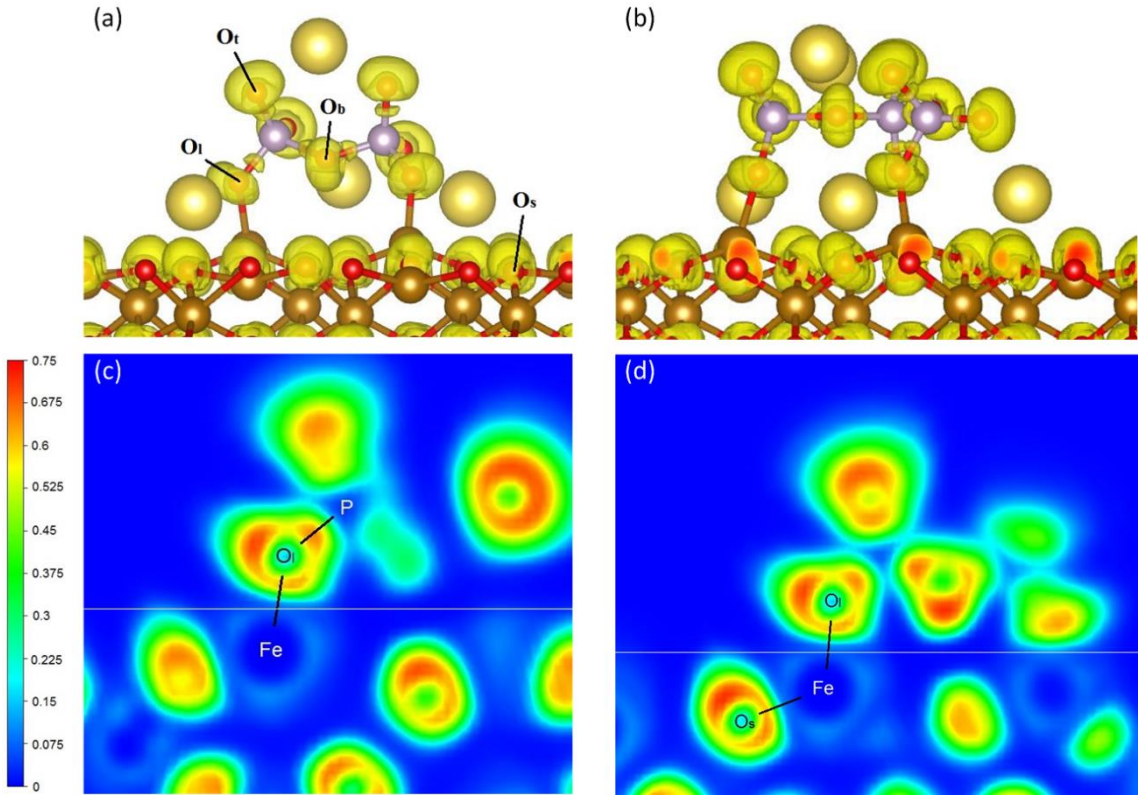

Figure 3-6. Electron localization function (ELF) isosurfaces (yellow regions) at η = 0.62 of (a) adsorbed $Na_4P_2O_7$ cluster on Fe_2O_3 surface, (b) adsorbed $Na_5P_3O_{10}$ cluster on Fe_2O_3 surface. Red, gold, purple and yellow spheres represent oxygen, iron, phosphorus and sodium atoms, respectively; ELF contour of (c) P-O_l-Fe slice (d) O_l-Fe-O_s slice in adsorbed $Na_5P_3O_{10}$ cluster on Fe_2O_3 surface. The Fe_2O_3 surface is below the horizontal white lines.

When the $Na_5P_3O_{10}$ adsorption occurs, terminal oxygens link with iron atom on the surface and create linkage oxygens as mentioned in Figure 3-6a. There are three electron pair regions observed from linkage oxygen atoms: one medium covalent bond between P-O, one partial mushroom-like electron region for ionic interaction with sodium, and one small deformed area in the direction towards Fe surface atom which can be observed in Figure 3-6c. The third has a similar contour to the Fe-O bond on the top of the oxide surface in Figure 3-6d, hence this Fe-O bond has been considered to be a mixed ionic/covalent bond with the same nature as the iron oxide interconnection. The adsorption energy of isolated $Na_5P_3O_{10}$ clusters on Fe_2O_3 surface is -5.51 eV for $Na_5P_3O_{10}$, which is thermodynamically favorable and is as strong as the chemical adsorption. The adsorption of short chain length sodium phosphate cluster on iron oxide substrate also has the same trend.[188] It is worth noting that most references data on the adsorption energies were from the study of phosphate adsorption in the soil industry. Thus, the models from these references will be more complicated than this work because

of the contribution of proton, the dissociation of OH- group or H_2O molecules from mineral surface. And the adsorbates are usually $H_nPO_4^{3-n}$ with one or two bridges with metal atoms on the surface. However, the adsorption energy per PO_4 tetrahedron about -1.83 eV for $Na_5P_3O_{10}$ is still comparable to previous studies of phosphate adsorption on goethite α-FeO(OH) or gibbsite $Al(OH)_3$ which have the listed energy from -3.44 to -0.66 eV [181, 221].

With the forming of strong chemical adsorption linkage, the alkali phosphate network can create a durable layer which provides a lower friction, significant wear reduction and significant oxidation prevention for steel/steel contact in metal forming process [12, 13]. The adsorption energy of the system goes down from -4.51 eV of $Na_4P_2O_7/Fe_2O_3$ to -5.51 eV of $Na_5P_3O_{10}/Fe_2O_3$ (Figure 3-4). Thus, for longer chain length of phosphate cluster, the absorbed structure is more stable. However, the absorbed energy per PO_4 tetrahedron or per Fe-O-P bond has a reverse trend. The absolute value rises from -2.25 eV of $Na_4P_2O_7$ cluster to -1.83 eV of $Na_5P_3O_{10}$ cluster. Additionally, the average Fe-O_l bond distance stretches by 0.07 Å and the mean BOP slightly lessens by 0.02e. Although the variation of linkage bond strength is minute, the small phosphate chain is preferable if the full coverage monodentate complex of phosphate spreads over iron oxide surface.

The ground-state structures of decomposed products adsorption are shown in the bottom right of Figure 3-4a and 3-4b. Due to previous energy minimizations of $NaPO_3$ and Na_3PO_4 on the surface, the most stable configurations have been chosen. The PO_3 unit in both decomposition cases forms one or two P-O-Fe linkages and one P-O_s bond. This adsorption contains a FeO_4 tetrahedron and a PO_4 tetrahedron which share one edge. The P-O_s distances are 1.70 Å for $Na_4P_2O_7$ and 1.78 Å for $Na_5P_3O_{10}$ which are the longest P-O interaction and the BOP is 0.18e and 0.15e respectively which are the weakest bond type of the system. Meanwhile, the PO_4 unit in the $Na_4P_2O_7$ decomposition creates three linkages with the Fe atoms on the surface through three oxygen vertices of tetrahedron. And P_2O_7 unit in $Na_5P_3O_{10}$ breakage generates the monodentate complex as a full $Na_4P_2O_7$ cluster.

During the P-O-P cleavage, P-O_b bridging bond can become P-O_t terminal or P-O_l linkage bond depended on the relative position of O_b on the surface. The ELF of decomposed products of $Na_4P_2O_7$ cluster on the Fe_2O_3 surface has been depicted in Figure 3-7.

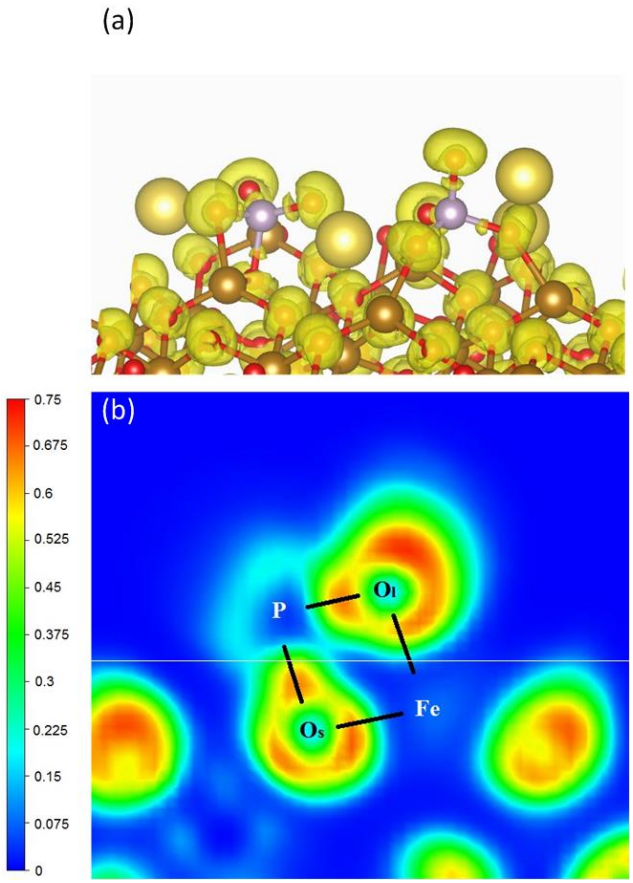

Figure 3-7. (a) Electron localization function (ELF) isosurfaces (yellow regions) at η = 0.62 of decomposed products of $Na_4P_2O_7$ cluster on Fe_2O_3 surface. Red, gold, purple and yellow spheres represent oxygen, iron, phosphorus and sodium atoms, respectively; (b) ELF contour of O_s-P-O_l plane in $NaPO_3$ unit adsorbed on Fe_2O_3 surface. The Fe_2O_3 surface is below the horizontal white lines.

The ELF of $Na_5P_3O_{10}$ degradation is very similar (data not shown). As no bridging oxygen exists, all oxygens have mushroom-like electron lobe of terminal atoms for isolated molecule decomposition. When these products are absorbed on oxide substrate, the P-O_s bond formed and PO_3 unit becomes a PO_4 tetrahedron with the help of one surface oxygen atom. The localized electron regions have been found along the P-O_s direction in Figure 3-6b. These regions have the same shapes to other covalent P-O bridging, terminal or linkage bonds but have smaller bond overlap population values. This bond is a weak covalent bond and is the weakest P-O interaction in the system. This phenomenon is also observed in the $Na_5P_3O_{10}$ case and can be explained by an abundance of O_s coordination up to three before the P-O_s bond initiation. The maximum P-O coordination of four has been maintained in the phosphate glass network as reported by Hoppe et al.[222]

The energy profiles of P-O bond dissociation of $Na_4P_2O_7$ and $Na_5P_3O_{10}$ clusters on Fe_2O_3 surface have been displayed in Figure 3-8 and Figure 3-9, respectively.

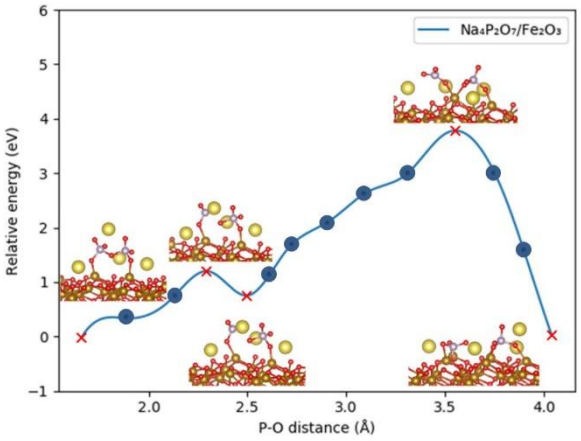

Figure 3-8. Energy profile of P-O bridging dissociation of $Na_4P_2O_7$ cluster on Fe_2O_3(0001) surface. Some maxima and minima have been marked with red crosses. Sample points have been marked with blue dots.

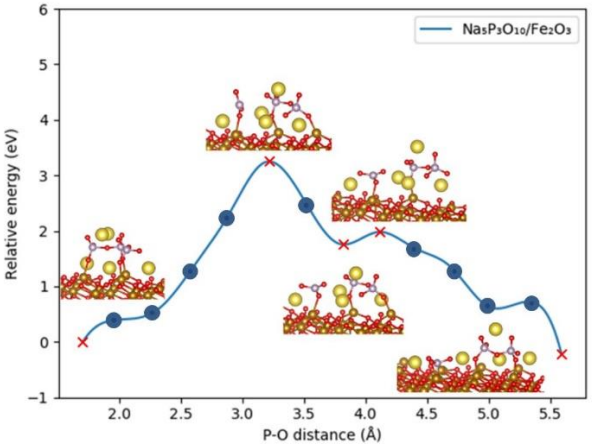

Figure 3-9. Energy profile of P-O bridging dissociation of $Na_5P_3O_{10}$ cluster on Fe_2O_3(0001) surface. Some maxima and minima have been marked with red crosses. Sample points have been marked with blue dots.

The origins at 0 eV have been set for the adsorption of two clusters on iron oxide surface. The relative energies of structures which have different P-O bridging distances are related to the origins. In Figure 3-8 and Figure 3-9, there are some maxima and minima due to the simultaneous contribution of P-O bond stretch and mobile movement of sodium which can stabilize and destabilize our system. The energy barriers for the dissociation on the surface are 3.75 eV for $Na_4P_2O_7$ and 3.24 eV for $Na_5P_3O_{10}$ which are spotted from the highest relative energies. The beginning, the highest maximum and the end of Figure 3-8 and Figure 3-9 have been simplified and displayed in Figure 3-4. As can be seen in Figure 3-4, Fe_2O_3 surface can reduce the bridging bond dissociation reaction energy from +2.74 eV to +0.03 eV for $Na_4P_2O_7$ and from +2.66 eV to -0.22 eV for $Na_5P_3O_{10}$. Even though

the energy barriers are quite high, around 3.3 – 3.8 eV, the structures at the top of the hill still have negative energy values compared to the total energy of isolated clusters, -0.76 eV in Figure 3-4a and -2.27 eV in Figure 3-4b. Thus, the decomposition reaction is more feasible on the iron oxide surface. The lower schemes in Figure 3-4a and 3-4b are preferable in both cases. Phosphate chains will adsorb on the surface and then undergo the bridging bond dissociation. This mechanism has been proposed before by Zhang et al.[223] when studying the tribofilm formation of ZDDP. The iron oxide surface plays a crucial role to help the system to achieve the lower energy states for cluster and decomposed products. However, when comparing the bridging bond dissociation reaction of the isolated clusters and the adsorbed clusters on surface, the barrier energies for the latter case are higher (~3.5 eV compared to ~2.7 eV). The barrier energy around 3.5 eV is also comparable with the bond dissociation energy of $H_4P_2O_7$. Hence, the Fe_2O_3 surface also has both positive and negative effects on the P-O bridging dissociation process. For the chain length effect, the higher chain length cluster $Na_5P_3O_{10}$ formed a more stable absorbed complex with Fe_2O_3 surface and had a lower energy barrier for bond dissociation as shown in Figure 3-4. However, this effect will not be much significant in the real polyphosphate system because of the extreme mobility of modifier metal like sodium. Besides, with a harsh environment of the metal forming process, all barriers in our system will be overtaken. The energy difference between absorbed clusters and their decomposition is rather small which infers that there is a co-existence of breaking and non-breaking chains during the process. The chain and the decomposed products can be observed simultaneously due to the reciprocity of polymerization and depolymerization. In the following section, first principle molecular dynamics simulations were undertaken in order to investigate the nature of lubricant depolymerization/polymerization at elevated temperatures.

3.3.3 Ab initio molecular dynamics simulations at high temperatures

This section will discuss the behavior of $Na_4P_2O_7$ and $Na_5P_3O_{10}$ phosphate cluster during interaction of iron oxide surface at 1100 K which is the working temperature of the hot rolling process.[224]

$Na_4P_2O_7$ cluster on iron oxide surface

Figure 3-10 exhibits the trajectory of sodium pyrophosphate cluster on iron (III) oxide surface at 1100K. Sodium atoms have been hidden for clarity. Iron sites on top of the surface have been introduced by gold spheres. The bridging oxygen has been noted as O_b, while the non-bridging oxygens which have interacted with surface have been marked from O_1 to O_4.

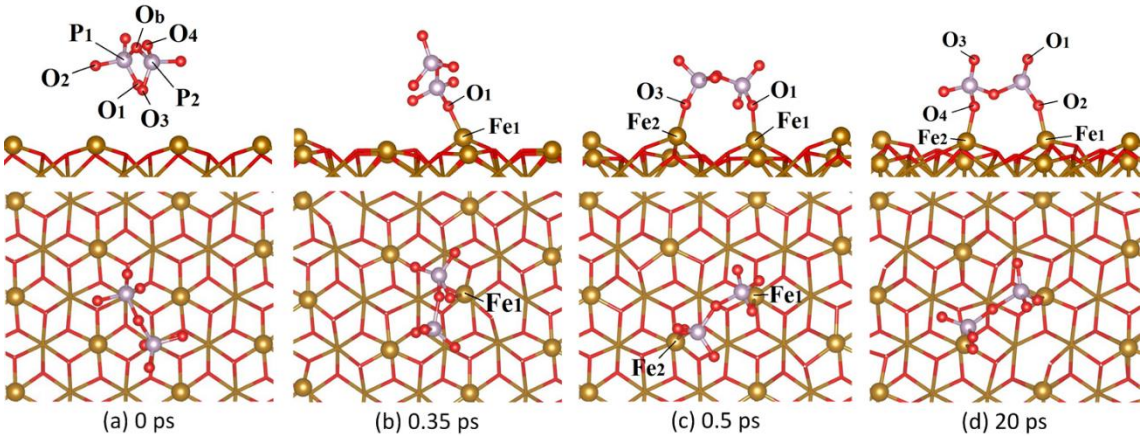

Figure 3-10. Snapshots of AIMD at 1100 K of $Na_4P_2O_7$ cluster on Fe_2O_3 surface at 0 ps (a), 0.35 ps (b), 0.5 ps (c), and 20 ps (d). Structures have been displayed in side view (upper) and top view (lower). Red, gold, and purple spheres represent oxygen, iron, and phosphorus atoms, respectively. Sodium, surface oxygen and lower-layered iron atoms have been removed for apparent visualization.

In the starting configuration, P_2O_7 cluster was placed randomly at 3 Å above the iron oxide substrate (Figure 3-10a). As the cluster gradually moved closer to the surface to explore the favorable adsorption site, it rotated and formed the first linkage between Fe_1 and O_1 at 0.35 ps (Figure 3-10b). The dangling part of cluster quickly went down and created the second linkage Fe_2-O_3 at 0.5 ps (Figure 3-10c). After that, the cluster anchored stably on the surface through two linkages with Fe_1 and Fe_2. During 20 ps of the simulation time, no bridging bond dissociation or depolymerization was observed. The evolution of the two bridging P-O bonds as a function of simulation time is shown in Figure 3-11.

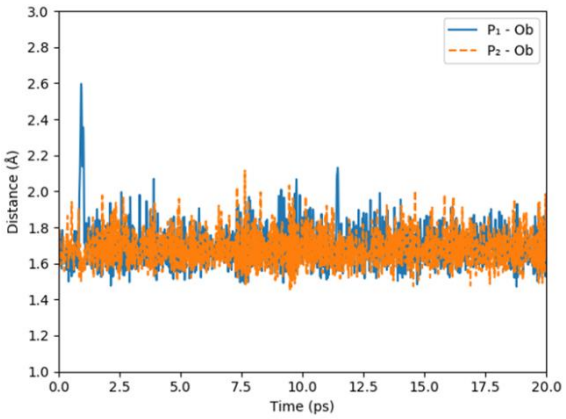

Figure 3-11. Distances of P-O bridging bonds in the AIMD of $Na_4P_2O_7$ cluster on Fe_2O_3 surface at 1100 K.

Under the impact of elevated temperature, both bridging bonds fluctuated around an average value of 1.69 Å, which was 0.02 Å longer than the equilibrium bridging P-O bond in the isolated $Na_4P_2O_7$ and the adsorbed one on the surface. At ~1.0 ps, P_1-O_b distance extended up to 2.6 Å then quickly got back to the average value. At 1100K, the thermodynamic movement of atoms increased and weakened the bridging bond to a slight degree. The thermal effect is expected to be more intense at a higher temperature. In fact, an additional simulation of $Na_4P_2O_7$ cluster on oxide surface at 1500 K produced the dissociation of P-O bridging bond. The snapshots have been shown in Figure A-6 in Appendix A. Although there was no breakage occurred, the linkages Fe-O-P evolved over the simulation time.

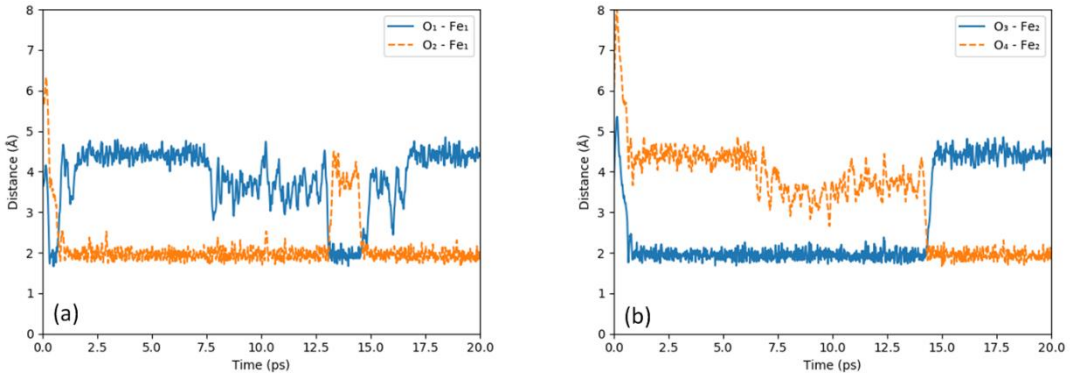

Figure 3-12. Distances of Fe-O linkage bonds in the AIMD of $Na_4P_2O_7$ cluster on Fe_2O_3 surface at 1100 K.

The interatomic distances between different O_{nb} with Fe_1 and Fe_2 have been presented in Figure 3-12. As shown in Figure 3-10 and 3-12, the Fe adsorption sites had been competed by various non-bridging oxygens from one PO_4 tetrahedron. In particular, O_1 and O_2 interacted with Fe_1 (Figure 3-12a), O_3 and O_4 connected to Fe_2 (Figure 3-12b). From 0 ps to 0.5 ps, the adsorption of P_2O_7 cluster has been observed with a decrease of Fe-O distances in both PO_3 groups. After that, the linkage distances remain steady at 1.95 Å in Figure 3-12a and 3-12b which is the equilibrium distance of Fe-O_l or Fe-O_s obtained from static DFT calculation in the previous section. Despite the fact that O_1 and O_2, O_3 and O_4 replaced each other to form linkage with Fe, monodentate configurations between the $Na_4P_2O_7$ cluster and oxide surface were always maintained. This indicates that one Fe-O-P linkage per PO_4 unit is the most stable structure for the interaction between phosphate and iron oxide substrate, which has an agreement to the previous conclusion in previous section and the study of Atkinson et al.[180] Fe atoms at the adsorption site usually created a deformed FeO_4 tetrahedron which connected to a PO_4 tetrahedron through the linkage oxygen which has been mentioned in the structure of the iron phosphate crystal.[225] This was different from the rigid FeO_6 octahedra in the bulk of Fe(III) oxide crystal. The deformed FeO_4 tetrahedra allowed the phosphate chain to be mobile but still strongly adhere to the surface. The oxygen atom at the bridging state did not form any stable bonds with iron from surface but being attacked by the floating sodium. The sodium atoms, which were not represented in the snapshots, were moving and terminated the non-bridging oxygen atoms or three oxygens on the oxide surface.[226]

$Na_5P_3O_{10}$ cluster on iron oxide surface

The snapshots of $Na_5P_3O_{10}$ cluster on the iron oxide surface during AIMD simulation at 1100 K are shown in Figure 3-13. Sodium, lower layer of irons and surface oxygens were also removed for better visualization. The bridging oxygens were noted as O_I and O_{II}, the important non-bridging oxygens were counted from O_1 to O_5, and three phosphorus atoms were P_1 to P_3.

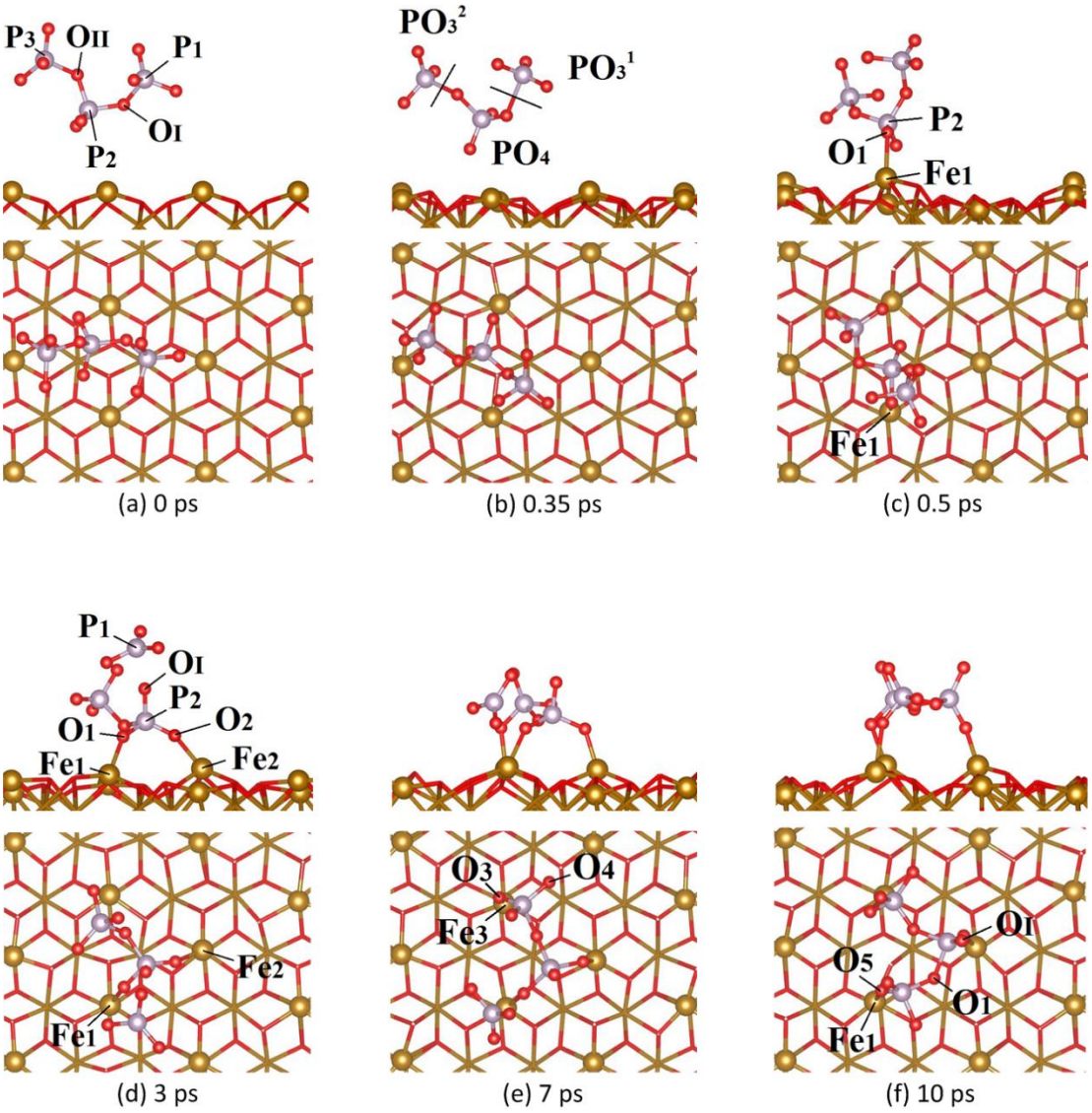

Figure 3-13. Snapshots of AIMD at 1100 K of $Na_5P_3O_{10}$ cluster on Fe_2O_3 surface at 0 ps (a), 0.35 ps (b), 0.5 ps (c), 3 ps (d), 7 ps (e), and 10 ps (f). Structures have been displayed in side view (upper) and top view (lower). Red, gold, and purple spheres represent oxygen, iron, and phosphorus atoms, respectively. Sodium, surface oxygen and lower-layered iron atoms have been removed for apparent visualization

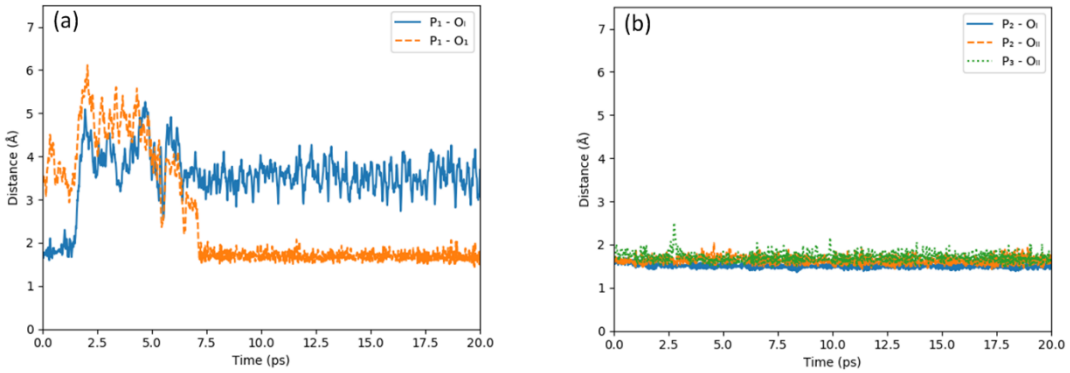

Figure 3-14. Distances of P-O bridging bonds in the AIMD of $Na_5P_3O_{10}$ cluster on Fe_2O_3 surface at 1100 K.

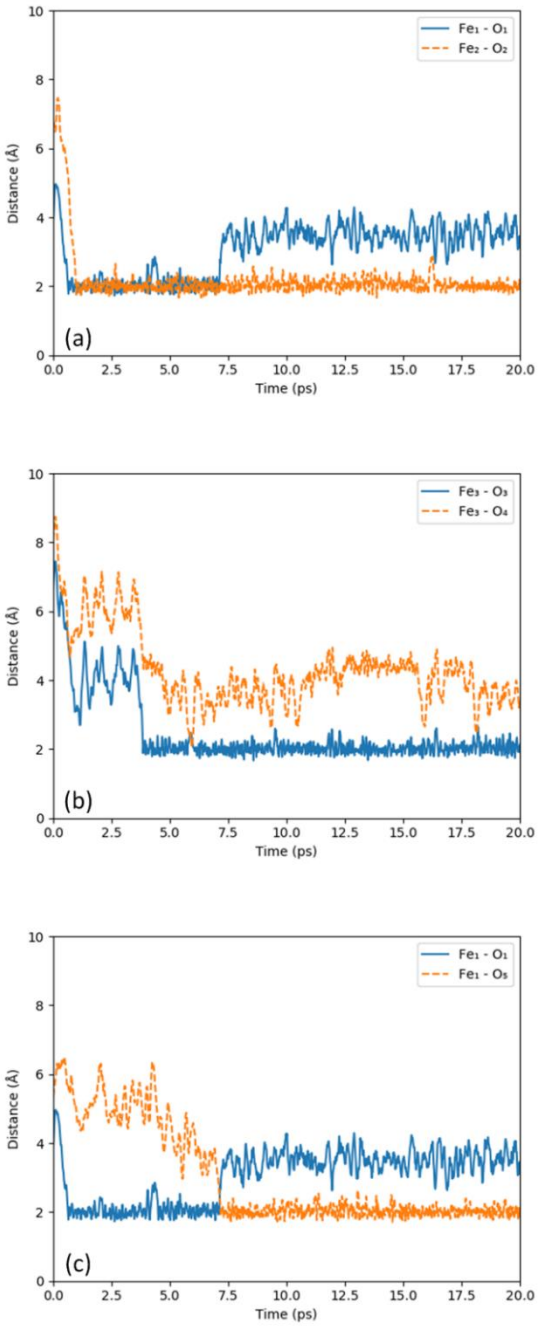

Figure 3-15. Distances of Fe-O linkage bonds in the AIMD of $Na_5P_3O_{10}$ cluster on Fe_2O_3 surface at 1100 K.

The trajectory of P_3O_{10} cluster is more complicated than the P_2O_7 due to the occurrence of the bridging bond dissociation between P_1-O_I-P_2. Thus, the P_3O_{10} cluster could be divided into PO_3^1 which contained P_1 and three O_{nb}; PO_4 which contained P_2, two O_b and two O_{nb}; and PO_3^2 for the rest (Figure 3-13b). At the beginning, the cluster also stayed above the surface 3 Å. The first linkage between O_1 from PO_4 with Fe_1 of surface appeared at 0.5 ps (Figure 3-13c). The second linkage from PO_4 continuously generated between O_2 and Fe_2 at 0.9 ps. Following the connection of the middle unit of P_3O_{10} cluster,

the P_1-O_I bridging bond was broken at 1.5 ps and PO_3^1 unit moved far away from adsorbed phosphate chain. These steps can be observed in Figure 3-14a and Figure 3-15a. The snapshot at 3 ps showed the stable adsorption with two linkages from PO_4 unit and also the dissociation of P_1-O_I bond. The distance of P_1-oi was about 4 Å at 3 ps (Figure 3-13d). The linkage between PO_3^2 and Fe_3 was observed at 3.5 ps until the end of the simulation. After moving above adsorbed P_2O_7 unit, P_2O_7 and PO_3^1 reunited to form the initial P_3O_{10} cluster at 7 ps (Figure 3-13e). Firstly, P_1 approached O_1 atom, which was already bonded with Fe_1. Then the O_5 from PO_3^1 competed with O_1 in order to connect with Fe_1 and interrupted the Fe_1-O_1 linkage. This process finished at 7.5 ps. The stable P_3O_{10} cluster reformed and attached itself to the oxide substrate through three monodentate linkages. No significant changes were observed after 10 ps. The detailed bond evolution during the adsorption and dissociation process has been illustrated in Figure 3-14 and Figure 3-15. The bridging bonds related to P_1 were described in Figure 3-14a while others bridging P-O were shown in Figure 3-14b. P_1-O_I bridging bond started to increase at 1.5 ps and confirmed the bond dissociation. Besides, the P_1-O_1 varied from 3 – 6 Å at the beginning because two atoms belonged to two groups, O_1 is the member of PO_4 unit which has center P_2. After 7.5 ps, O_1 became a bridging oxygen between P_1 and P_2 with the average distance of 1.7 Å. All other bridging bonds such as P_2-O_I, P_2-O_{II}, and P_3-O_{II} showed no significant variations and maintained at a distance of 1.71 Å. With the bridging bond breaking and forming during the simulation run, the adsorbed cluster and decomposed products can coexist in the system as mentioned in the static DFT calculation. Therefore, the depolymerization and polymerization of phosphate chain can occur simultaneously in the hot rolling process. Moreover, the Fe-O linkages had some interesting rearrangements which were shown in Figure 3-15. Figure 3-15a showed two linkages of PO_4 unit formed after the adsorption at 0.5 and 0.9 ps with the average distance of 2.05 Å. The first linkage Fe_1-O_1 was then broken at 7.5 ps due to the competition of O_5 atom in Figure 3-15b during the bridging bond forming process. Besides, the linkage between PO_3^2 with Fe was stable after 7.5 ps with some exchanged interactions between Fe-O_3 and Fe-O_4 in Figure 3-15c. In conclusion, one monodentate linkage per PO_4 tetrahedron is the most observed structure in the AIMD simulations of $Na_5P_3O_{10}$ cluster on the Fe_2O_3 surface at 1100K.

In general, both sodium phosphates $Na_4P_2O_7$ and $Na_5P_3O_{10}$ tend to adsorbed on the surface regardless bond dissociation. In the comparison between different phosphate chains, at 1100 K bond dissociation has been recorded in $Na_5P_3O_{10}$ by cleaving P-O_b bonds while $Na_4P_2O_7$ remains as a stable chain. A higher temperature is needed to break

$P\text{-}O_b$ bonds of $Na_4P_2O_7$. This observation agreed with the study by Cui et al.[96] that the tribofilm observed after the pin-on-disk test with sodium pyrophosphate lubricant which showed a slight degree of polymerization and the depolymerization for longer phosphate chains.

3.4 Discussion

Polyphosphate glass has been built up from a network of PO_4 tetrahedra linked through P-O-P bridging bonds. With the metal addition which is a network modifier such as alkali or alkali earth metal, three-dimensional structures of polyphosphate can degrade into polymer-like metaphosphate chains, rings, short-chain pyrophosphate glass or isolated orthophosphate molecules. These structures are related to the ratio of bridging and non-bridging oxygen in the glass.[227] In P-O interactions of PO_4 tetrahedron, phosphorus atom promotes its fifth valence electron into its 3d orbital which creates a π-bond with a 2p orbital of oxygen. This π-bond has been shared equally to all $P\text{-}O_{nb}$ through resonance effect.[10] In comparison between bridging and non-bridging P-O bond overlap populations, the interaction of $P\text{-}O_b$ is weaker than $P\text{-}O_{nb}$ which has been studied by Boyd.[228] The electrons of non-bridging oxygens are more likely to fill the molecular orbital $P\ 3d_\pi + O\ 2p_\pi$ than do the bridging oxygens. Because of the electron sharing with two nearby phosphorus atoms, the bridging bond cannot be strengthened by "back-bonding" effect from 3d orbital as strong as the non-bridging bond. According to the bond overlap population in Table 3.3, one of the non-bridging P-O bonds is weakened by Fe atoms from surface and becomes $P\text{-}O_l$ link. The $P\text{-}O_l$ bond is weaker than normal $P\text{-}O_t$ terminal bond because the oxygen atom in the $P\text{-}O_l\text{-}Fe$ linkage has to share 2p orbital to both P and Fe, which reduces the effect of back-bond d-p orbital from terminal oxygens to phosphorus atoms. However, $P\text{-}O_b$ is still the weakest bond in both the isolated cluster and the adsorbed phase. This conclusion has been supported by our AIMD simulations which observed no $P\text{-}O_{nb}$ dissociation either at ambient temperature or elevated temperature but the bridging bond cleavage of phosphate cluster has been spotted at extremely high temperatures.

For iron-oxygen interactions, $Fe\text{-}O_l$ bond is as strong as $Fe\text{-}O_s$ next to linkage and the normal $Fe\text{-}O_s$ on the top of the surface as indicated by similar bond overlap population and electron localization function. The iron-oxygen bond in iron oxide structure is well-known for its strong ionic nature and decent covalent property. The 2p orbitals of oxygen can hybridize with e_g 3d orbitals of iron to form σ-bonds, with t_{2g} 3d orbitals of iron to

form π-bonds, and can weakly hybridize with 4sp orbitals of iron atom also.[229] As Fe(III) octahedral structure has been considered in Table 3.3 with an Fe(III)-O distance of 1.86 – 2.09 Å, the covalent nature of this bond is considerable when comparing a pure ionic Fe(II)-O bond distance of 2.16 Å and a covalent-metallic Fe(II)-O 2.01 Å.[230] Hence, the Fe-O_l bond is an ionic/covalent resonance bond which has a similar strength as Fe-O_s on the surface.[231] However, the BOP difference of four weakest bonds P-O_b, Fe-O_s, Fe-O_s near linkage, and Fe-O_l is rather minor, being 0.03e. Comparing P-O_b bonds with Fe-O interactions, the bridging oxygen bond has the same covalent strength but less ionic nature than Fe-O. Therefore, the P-O bridging bond has the highest tendency to break during the tribological shearing test. The O_s-Fe bond can also be cleaved and form iron oxide nanoparticles which will be digested by phosphate lubricant. The digestion of iron oxide by polyphosphate tribofilm at 800°C has been proposed by Cui et al.[98] As the structure of iron/iron oxide nanoparticle is different from standard crystalline oxide [232], the interactions of alkali phosphates and iron-based nanoparticles are worth further investigation, particularly the competition between alkali and iron ions inside phosphate tribofilm.

Generally, the alkali metal plays a role as a network modifier which reduces the P-O-P bridging bonds and ionically interacts with terminal oxygen atoms. Thus, the metaphosphate long chain structure has been commonly mentioned in alkali phosphate glass studies instead of 3D-network of vitreous P_2O_5.[233] The energy profile in Figure 3-5 also supported this point. When adding iron oxide into alkali phosphate glass, the P-O-P chain will be substituted by durable Fe-O-P bonds.[234] The introduction of transition metal oxide intensifies the depolymerization degree of phosphate chain in condensed glass.[235] The mixed alkali iron phosphate glass gets high durability due to the rigid octahedral sites of Fe(III) which reinforce the cross-linking between short phosphate chains.[236] The Fe-O coordination value in iron phosphate glass is mixed from four to six.[222, 237, 238] The abovementioned studies indicate the effect of iron/iron oxide to alkali phosphate in the bulk phase. In our study, the iron oxide plays quite a different role for the depolymerization as an adsorption surface. Firstly, the surface helps phosphate chain achieve low energy status through chemical adsorptions. The chemical bonds between non-bridging oxygens and iron atoms on top of surface contribute to the favorable adhesion of phosphate glass lubricant during the tribological process. Secondly, the dissociation scheme will attach with the surface adsorption then conducted the depolymerization. Last but not least, we propose that the oxide surface

does not contribute directly to P-O_b dissociation but indirectly through partially immobilize the phosphate chain. In that way, the non-adsorbed units under harsh environment will get intense fluctuation and suffer the bridging bond decomposition. Besides the indirect P-O_b dissociation induction of the surface, it also has an inverse impact. As mentioned in previous section, the attacking of sodium or any cations on bridging oxygen will result in bridging bond dissociation. Iron oxide surface easily attracts flexible sodium atoms through the most top oxygen, which retards the approaching of sodium to the oxygen from phosphate chain then lessens the decomposition.[226] It is noted from our static result that the barrier energy for bond dissociation reaction by iron oxide increases up to the value of $H_4P_2O_7$ which is related to non-modifier metal phosphate system. The sodium attraction by oxide surface has been also observed in all AIMD simulations. The snapshots with sodium atoms can be reached at Figure A-3 to Figure A-5 in Appendix A. Even though iron oxide substrate reduces the appearance of sodium, the introduction of iron into phosphate glass induces the depolymerization because the higher field strength and a larger coordination number of Fe compared to Na which help iron approach oxygen better, especially bridging oxygen atoms.[227] Therefore, the diffusion of iron from oxide substrate into the phosphate layer plays an important role on reducing the chain length of phosphate structure.

According to P-O bridging bond dissociation energy, the chain length has a minor effect on the P-O_b decomposition. The static calculations of $Na_5P_3O_{10}$ barrier energy showed a lower value of 0.5 eV than that of the shorter $Na_4P_2O_7$ cluster. At 1100 K of AIMD run, $Na_5P_3O_{10}$ cluster decomposed while the $Na_4P_2O_7$ did not. This result compares well with the study by Cui et al.[96], which found that the pyrophosphate lubricant slightly polymerized whilst polyphosphate experienced depolymerization. We suggest the steric effect has a contribution to the surface interaction of phosphate chain. Longer chain length $Na_5P_3O_{10}$ cannot fully adsorb on the surface when thermal movement of other free atoms are more intense at 1100 K. As partial cluster anchored on the surface, the free atoms experienced large movement which can terminate the weakest bond – bridging P-O.

It is worth noting that our study has some limitations which make it not fully comparable to experimental study of hot rolling lubricant. The important effect of pressure and shear rate haven't been included in the current study. Besides, the lubricant coverage should be higher to mimic the higher chain length and the behavior of lubricant at bulk stage. Finally, the interactions between iron oxide nanoparticles with condensed phosphate cluster should be considered. These shortcomings will be the foci in a subsequent work.

3.5 Conclusions

DFT calculations and AIMD simulations at 1100 K have been performed with the $Na_4P_2O_7$ and $Na_5P_3O_{10}$ cluster on iron oxide surface. The BOP and ELF analyses as well as AIMD simulations provided detailed insights into the bond nature of the system, effect of surface and effect of chain length on depolymerization of phosphate-based lubricant. The conclusions have been summarized below:

- The system contains medium covalent P-O bond, pure ionic Na-O interaction and moderate Fe-O ionic/covalent bond. The bridging P-O_b is the weakest bond targeted for the depolymerization. The interactions of sodium or any modifier metal with bridging oxygens induces the P-O_b separation. Elevated temperature is also a trigger factor for this process.
- Iron oxide surface supports phosphate clusters and their dissociation products to achieve more stable configurations. The adsorption then depolymerization phosphate on the surface is the most thermodynamically favorable pathway. Deformed FeO_4 tetrahedra observed in the phosphate-iron oxide linkage allows the mobility of phosphate but still maintains the strong adherence. Due to the equivalent ground states, structures of phosphate cluster and the decomposed products coexist. The substrate not only promotes the P-O_b breakage through partially immobilizing phosphate chain but also obstructs the depolymerization due to the interaction between modifier alkali metal and surface oxygen.
- The monodentate complex structures have been observed in all phosphate clusters adsorption regardless to the chain length. The chain length of phosphate clusters has little effect on the P-O bridging dissociation. However, the small chain will be preferable when the surface gets full phosphate coverage and all linkages are monodentate.

Chapter 4 Surface transformation and interactions of iron oxide in glassy lubricant [2]

4.1 Introduction

In metalworking processes, particularly the hot rolling of steel at high contact load and temperature, the wasted energy and low production efficiency caused by friction, wear, and oxidation is a significant concern.[6] Hence, an effective lubricant should be applied in the rolling process to address these issues. Recently, inorganic alkali polyphosphate glass has been proposed as a promising lubricant which not only works well in elevated temperature but also is less harmful to environment.[26, 27] The polyphosphate film formed during the tribological tests with the glass lubricant can provide an effective lubricity due to its gradient composition and layered structure.[27] In particular, Kong et al.[14] investigated the mixture of sodium polyphosphate ($NaPO_3$) and potassium dihydrogen phosphate (KH_2PO_4) as a water-based lubricant in the rolling mill test. The phosphate lubricant melted and covered the steel surface in the range 650 - 850°C, thus the reduction of the rolling force by 24.7% compared to unlubricated tests is observed across the temperature range. Tieu et al.[12, 13] further explored the tribological properties of the same phosphate lubricant in the balls and discs test. The molten glassy polyphosphate generated a hierarchical tribofilm which reduced 60% friction and 59% wear volume compared to the dry condition. The author also proposed the functions of each layers of tribofilm in lubrication, anti-wear, stress relief, and anti-oxidation. Nevertheless, the working mechanism of polyphosphate lubricant at high temperature is not totally understood, especially the performance of the glassy state.

Some attempts have been made in order to clarify the working mechanism of the potential phosphate lubricant at high temperature. Cui et al.[96] studied different chain-length compounds of sodium phosphate on ball-on-disk tribometer at 800°C. The short-chain sodium orthophosphate (Na_3PO_4) was better in reducing friction and wear but long-chain sodium polyphosphate ($NaPO_3$) provided more stable friction coefficient which was considered as the most suitable compound for hot rolling processes among the candidates. Moreover, the depolymerization and polymerization of phosphate lubricant was

[2] Based on **Manh Ha Le,** Anh Kiet Tieu, Hongtao Zhu, Dinh Thi Ta, Haibo Yu, Thi Thuy Huong Ta and Van Nam Tran, "Surface transformation and interactions of iron oxide in glassy lubricant: An ab initio study", *Chemical Physics*, 2020. 538: p. 110919.

monitored in the study without detailed explanation. Wan et al.[27] revealed the gradient composition of alkali phosphate tribofilm, in which the tribochemical reaction occurred between iron oxide layer and abrasive oxide particle with molten glass network. In this study, the alkaline elements Na^+ and K^+ were mentioned as the charge compensators and the viscosity modifier in the lubricant tribofilm. Cui et al.[97, 98] then reaffirmed the dissolution of Fe atom into molten glass by the observation of $NaFePO_4$ in the wear debris and the iron oxide layer above lubricant layer after tribo-tests but no more explanation provided.

It is worth noting that the tribological mechanism of phosphate compounds has been widely studied for the well-known zinc dialkyldithiophosphate (ZDDP) additive at normal temperature. The general working mechanism of the decomposed tribofilm of ZDDP on surface includes four main steps [17, 79]: (i) the adsorption of phosphate film on the substrate, (ii) the depolymerization of phosphate glass, (iii) the diffusion of Fe from substrate into lubricant layer above, and (iv) the interaction between Fe with lubricant network. Ito et al.[175] suggested the mechanism of ZDDP adsorption is based on the adsorption of thermal dissociation product of ZDDP, and this process contributes to the formation of the precursor of the tribofilm. Besides, soil industry studies also mentioned the phosphate adsorption on iron/iron oxide surface at ambient temperature.[177, 180, 183] Crobu et al.[86] linked the phosphate chain length to the friction and wear performance in which the long-chain phosphate was induced to polymerize by the tribochemical reaction with iron oxide under shear sliding and temperature. The short-chain length compositions showed enhanced mechanical properties and anti-wear performance of the tribofilm. Berkani et al.[239] studied the role of the iron/iron oxide surface on the depolymerization process which indicated that the depolymerization occurred under the effect of the iron oxide surface but not the aluminum surface. The micro-particle dispersion of goethite also induces the lubricant depolymerization on a sapphire substrate. For the last two steps of ZDDP tribofilm mechanism, Martin et al.[78] proposed the "digestion" mechanism in which abrasive iron oxide particles were absorbed in the tribofilm to produce an anti-wear function. However, the Fe dissolution in the glass network is not thermodynamic favorable so the final tribofilm contains a gradient of Fe content. The outer and inner diffusion of network modifier cations in phosphate, silicate and borate glass were also studied along with the redox reaction of multivalent cations in glass forming field. [240-243] In step (iii) of tribofilm mechanism, the removal of iron/iron oxide from the surface occurred first. This phenomenon was generally

considered a result of mechanical abrasive wear of metal-metal interaction, but no study has yet to focus on this topic. The contribution of lubricant compounds to the removal of iron/iron oxide as an outcome of wear is still questionable. The same pattern for the tribological mechanism of phosphate compounds has been recognized in both normal and high temperature. However, the experimental studies cannot complete the view on the tribo-reaction due to the complexity of the system under operating conditions.

As quantum mechanics (QM) has an ability to describe a chemical reaction in general and a tribochemical reaction specifically, it is well suited to investigate the structure and electronic properties at the atomistic scale to obtain a deeper understanding of the tribological process. Recently, Righi et al.[103, 244] studied the tribochemical reaction and the chemisorption of phosphite P(III) additives on Fe(110) surface using density functional theory (DFT) and ab initio molecular dynamics (AIMD) method. In these systems, the iron phosphide tribofilm was observed with the network of covalent P-P at high lubricant coverage, which explained the high adhesion and friction reduction of the P-rich iron tribofilm on the sliding steel condition. For system using phosphate glass P(V) lubricant, Ta et al.[188] investigated the adsorption of different alkali phosphate compounds Na_3PO_4 and $Na_4P_2O_7$ on iron-based surfaces which compared their adherence on the surface. The stronger binding of short-chain phosphate compounds, which was investigated through the bond order population, density of states and other electronic properties, contributed to the lubricant's anti-wear performance. Le et al. [245] went through the process of phosphate depolymerization at the iron oxide surface. The effect of the iron oxide surface on long-chain phosphate molecules was pointed out but the reverse process, the influence of phosphate glass on the surface remained unclear. Moreover, no theoretical work using full coverage of glass model on the surface has been available for the tribological field.

In order to fulfill the tribological mechanism of alkali phosphate glass lubricant, the full coverage $(NaPO_3)_x$ glass model with different compounds/fragments such as -(PO_3)-, -(PO_4)- in the depolymerization stage has been used in the theoretical DFT simulations to determine the glass effect on iron oxide surface. Each interaction pair of compound-surface has also been studied separately for more detailed analysis. Finally, the cluster models have been used in AIMD to develop a comprehensive understanding of the behavior of Fe/Fe_2O_3 particles in the interaction with phosphate network. The pure iron cluster has been considered in order to represent the nascent Fe surface formation which is a popular phenomenon during wear processes.[175] This work continues the previous

experimental and theoretical studies [96, 188, 245] to provide more insight into the above-mentioned step (iii) the diffusion of Fe from substrate into lubricant layer above the surface, and (iv) the interaction between Fe with lubricant network.

4.2 Computational details

4.2.1 Static DFT simulations

DFT + U calculations have been performed in an effort to study the iron oxide surface behavior under $(NaPO_3)_x$ glass adsorption. Vienna Ab-initio Simulation package (VASP) was used for the spin-polarized calculations [190] with projector augmented wave (PAW) method [191] and generalized gradient approximation (GGA) of Perdew−Burke−Ernzerhof (PBE) exchange and correlation function.[119] The plane-wave expansion has been truncated at 400 eV, and the energy convergence criteria of 10^{-4} eV and 10^{-3} eV are used for the electronic self-consistent loop and ionic relaxation, respectively. A Hubbard (U − J = 4 eV) with the scheme of Dudarev [246] has been added to handle the strongly-correlated Fe 3d orbitals. This U correction yields a band gap of 1.98 eV for α-Fe_2O_3, which agrees well with the experimental range of 1.9 − 2.2 eV. [218, 247] For static adsorption, the geometry relaxations are performed using the conjugate gradient algorithm along with a first order Methfessel-Paxton method [194] and Γ-point sampling. Moreover the electronic calculations use tetrahedron smearing technique with Blöchl corrections and a denser Monkhorst-Pack mesh [193] of 3 x 3 x 1 for more accurate energy values.

The single Fe-terminated α-Fe_2O_3(0001) facet has been chosen with the system dimension of a = 17.44 Å, b = 10.07 Å, and c = 26.27 Å. A vacuum region of 15 Å is included in the system to avoid the effect of nearby Fe_2O_3 layers in the z-direction while the periodic boundary conditions are set up in the x and y directions. The single Fe-terminated slab of 9 atomic layers including 3 fixed bottom layers were used, as the termination of the single Fe layer proved its stability at room temperature and the number of layers is sufficiently thick to present the accurate surface adsorption behavior. [218, 247, 248] The slab system was optimized before going to the adsorption process and it achieved good agreement in term of surface structure. [218, 247, 249] The results are provided in Table B.1 of the Appendix B. The glass layer has been prepared by the "melt and quench" procedure which will be explained later in the dynamics method section. Other simple adsorbates such as H_2PO_3, H_3PO_4, and the cluster models are also relaxed separately in order to achieve an

equilibrium structure. Equilibrium structures are used as the input of the dynamics process.

The adsorption energy E_{ads} has been defined as follows:

$$E_{ads} = E_{sur+lub} - (E_{sur} + E_{lub}) \qquad (4.1)$$

In the above equation, $E_{sur+lub}$, E_{sur}, and E_{lub} are the total energies of the adsorption system, the pure iron oxide surface, and the lubricant, respectively. Thus, the negative value of E_{ads} describes a thermodynamically favorable adsorption process.

The electronic properties of the systems have been revealed by studying the partial charge, bond order (BO), charge density difference (CDD), electron localization function (ELF), and density of states (DOS). The atomic charges of selected atoms and the BO of interesting interactions in the system are obtained using the refinement of the Density Derived Electrostatic and Chemical approach (DDEC6) developed by Manz and Limas.[250-252] DDEC6 BO has the interesting application of chemical nature bond quantifiers for transition metal and transition metal oxide.[253, 254] The sum of bond order (SBO) is the summation of the abovementioned BO for a particular atom with the limit bond print threshold goes to 0 and the bond cutoff radius goes to infinity.[250] Charge density difference ($\Delta\rho$) has been calculated based on the electron density of adsorption systems ($\rho_{sur+lub}$) and the isolated surface and adsorbates (ρ_{sur} and ρ_{lub}):

$$\Delta\rho = \rho_{sur+lub} - (\rho_{sur} + \rho_{lub}) \qquad (4.2)$$

The ELF (η) estimates the same spin electron probability in the vicinity of the volume of the reference electron. [200, 201] The regions close to $\eta = 1$ represent many electrons, which are localized around a nucleus or in a very strong covalent interaction, e.g. C-C single bond in diamond crystal, while $\eta = 0.5$ indicates a homogeneous electron gas which has the metallic character.[202]

4.2.2 AIMD calculations

In the preparation of AIMD calculations of the glass layer, the "melt and quench" method, which is a well-known procedure to create glassy states in general and phosphate-based glass in particular,[255, 256] was applied. Firstly, a box of $NaPO_3$ crystal (the ratio of Na/P/O atoms is 1/1/3) with the dimension of a = 17.44 Å, b = 10.07 Å, c = 9.62 Å was heated to 4000K for 20ps with the time step of 0.5 fs in order to achieve a full melted structure. The system was then cooled down to room temperature, 300K with the cooling rate about 30 K ps^{-1}. The system size and the cooling rate has been considered with the

aim to present good local- and medium-range glass structure and minimal defects.[256] Moreover, the radial distribution function of the glassy state was in good agreement with previous experimental and theoretical works (Figure B-1 in Appendix B). [212, 256, 257] The phosphate glass was then cleaved for two phosphate backbone chain in the z-direction, in order to reduce computational cost and generate different compounds in the depolymerization stage of the system, such as: long chain, short chain phosphate, PO_4 tetrahedra and PO_3 fragments. The cleaved glass surface was stacked on $Fe_2O_3(0001)$ surface at different distances (from 1.5 to 3.5 Å) for repeated adsorption simulation.

The AIMD simulations for the dynamics interaction between phosphate clusters with iron/iron oxide clusters at different temperatures have also been performed in order to represent the behaviour of iron-based compound in the glass network. Three cases considered by AIMD are: (i) tetrasodium pyrophosphate cluster $Na_4P_2O_7$ with iron oxide cluster $(Fe_2O_3)_3$, (ii) rich-Na pyrophosphate cluster $Na_{15}P_2O_7$ with iron oxide cluster $(Fe_2O_3)_3$, and (iii) normal pyrophosphate cluster $Na_4P_2O_7$ with pure iron cluster Fe_7. Γ-point sampling, with 0.5 fs time steps for each 20ps run was used in the simulations. With this time step, the total energy change of the system of less than 0.02 eV has been observed during 500 steps which confirms the system stability.[192] Every cluster has been optimized separately before proceeding with the contact dynamics simulation at 300K. After stabilizing 20ps at 300K, the system will be heated to 1100K and 1500K. The trajectory will be captured and analysed for the behaviour of pure iron and iron oxide cluster in the normal phosphate and rich-Na phosphate network.

4.3 Results

4.3.1 Full coverage phosphate glass adsorption

To unveil the effect of adsorbed phosphate glass to iron oxide surface, the adsorption simulations are carried out. Previously, work by Le et al.[245] observed some surface reconstruction when studying the depolymerization of phosphate cluster model adsorbed on iron oxide surface (Figure 4-1a). Some atoms in Fe layer 1 have been dragged inward below O layer 2 to create O-terminated sites. The unadsorbed oxide surface has been depicted in Figure B-2 in Appendix B for comparison. However, the partial coverage adsorption of a single $Na_4P_2O_7$ cluster on Fe_2O_3 surface cannot represent the realistic situation in which the glass lubricant melted and covered the whole surface.[14] Thus, we consider the full coverage of $(NaPO_3)_x$ glass adsorbed on iron termination of $Fe_2O_3(0001)$

surface (x = 16 after the cleaving). For convenience; $(NaPO_3)_x$ glass will be named as $NaPO_3$ for short. After geometry relaxation (Figure 4-1b), all Fe sites have been occupied by O or P atoms and the structure of Fe-terminated surface remains. It is worth noting that the cleavage surface of the glass layer already contains possible fragments such as long chain, short chain phosphate, PO_4 tetrahedra and PO_3 fragments which can represent the normal depolymerization stage of the lubricant. As we focus on the surface-lubricant interface and near surface behavior, the partial charge, SBO, BO and bond distance of the bottom half of the glass layer were considered.

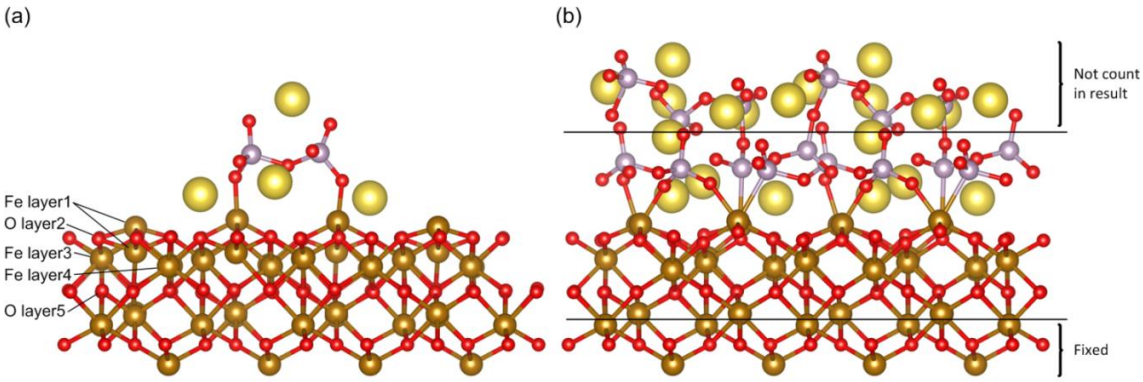

Figure 4-1. Adsorption structure on $Fe_2O_3(0001)$ surface of (a) one $Na_4P_2O_7$ cluster in Le et al.[245] and (b) $NaPO_3$ glass layer (this work). O atoms are colored in red, Fe in gold, P in purple and Na in yellow.

In the relaxed structure, the glass layer adsorbed on most Fe sites of the Fe_2O_3 surface through monodentate linkage (one atom such as O, P linked to one atom of Fe) as mentioned in the previous study [245]. Some less common structures such as mononuclear bidentate complex (two glass oxygen atoms connected to one iron site of the surface) or oxygen bridging linkages have been reported in Figure B-3 in Appendix B. The density of the glass layer is 2.292 g/cm^3 which is in the range of the $NaPO_3$ crystal (2.54 g/cm^3)[258, 259] and the molten glass $NaPO_3$ at 950°C (2.142 g/cm^3).[260] The lubricant-oxide interface has been enlarged, tilted and removed sodium atoms for clearer visualization in Figure 4-2b. Three types of Fe-adsorption sites have been observed, as seen in Figure 4-2b: Fe_O – the linkage between the glass and the surface is Fe-O bonds only (at Fe_A and Fe_B sites, Fe_O-O average distance 2.024 Å); Fe_P – only P atoms adsorbed on these Fe sites (at Fe_C site, Fe_P-P average distance 2.518 Å); Fe_{OP} – at these Fe sites, both O and P are adsorbed (at Fe_D site).

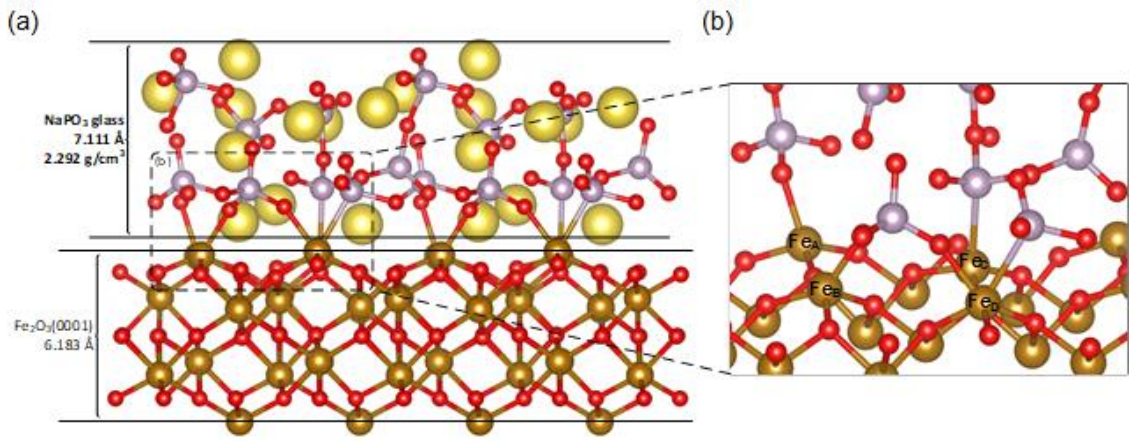

Figure 4-2. (a) $NaPO_3$ glass layer and $Fe_2O_3(0001)$ surface dimension; (b) enlarged and tilted structure of glass – oxide interface, sodium atoms have been removed for clear visualization. O atoms are colored in red, Fe in gold, P in purple and Na in yellow.

The atomic partial charge, SBO, BO and bond distance of the glass-oxide system before and after adsorption is presented in Table 4.1. Different types of oxygen atom have been marked as: $O_{bridging}$: bridging oxygen in -P-O-P- network; $O_{terminal}$: oxygen atoms of glass terminated by modifier cation; $O_{linkage}$: glass oxygen atoms connected to oxide layer through -P-O-Fe- linkage; O_{glass}: oxygen atoms of glass layer; $O_{surface}$: oxygen atoms belonging to the top surface of the oxide layer (or O_{layer2}).

The partial charge adjusts among Fe sites after adsorption. The Fe_O has increased charge (from +1.436 |e| to +1.475 |e|) whilst the Fe_P gets its charge reduced (from +1.436 |e| to +1.094 |e|). The charge of Fe_{OP} is in between, but since P is the electronically dominant effect, the net charge still decreases. Hence, P adsorption makes the Fe partial charge less positive, and creates less electrostatic attraction to other anions while O adsorption increases the Fe positive charge and electrostatic connection. For O_{layer2}, there is also a variation of atomic partial charge but it does not have a particular tendency due to the influence of sodium on oxygen sites. On average, O_{layer2} receives negative charge (from -0.952 |e| to -0.971 |e|).

Table 4.1. The average partial charge, SBO of different atoms, BO and bond distance of different bonds before and after the adsorption.

Atom		Partial charge (|e|)		Sum of bond order	
		Before adsorption	After adsorption	Before adsorption	After adsorption
$O_{linkage}$			-0.838		
Fe_{layer1}	Fe_P	+1.436	+1.094	2.575	3.123
	Fe_{OP}		+1.272		2.910
	Fe_O		+1.475		2.669
O_{layer2}		-0.952	-0.971		
around Fe_P			-0.957		
around Fe_{OP}			-0.914		
around Fe_O			-0.996		
Fe_{layer3}		+1.448	+1.475	2.930	2.866

Bond	Bond order		Bond distance (Å)	
	Before adsorption	After adsorption	Before adsorption	After adsorption
$P - O_{bridging}$		1.076		1.637
$P - O_{terminal}$		1.645		1.507
$P - O_{linkage}$		1.363		1.532
$Na - O_{glass}$		0.076 – 0.081		2.351 – 2.539
$Na - O_{surface}$		0.077 – 0.080		2.387 – 2.502
$Fe_P - P$		0.444		2.575
$Fe_{OP} - P$		0.299		2.533
$Fe_{OP} - O_{glass}$		0.426		2.037
$Fe_O - O_{glass}$		0.429		2.036
$Fe_{layer1} - O_{layer2}$	0.765	0.684	1.813	1.864
$Fe_P - O_{layer2}$		0.790		1.847
$Fe_{OP} - O_{layer2}$		0.650		1.880
$Fe_O - O_{layer2}$		0.647		1.863
$Fe_{layer3} - O_{layer2}$	0.528	0.527	1.932	1.928
$Fe_{layer3} - O_{layer5}$	0.360	0.350	2.079	2.083
$Fe_{layer4} - O_{layer2}$	0.374	0.361	2.043	2.076
$Fe_{layer4} - O_{layer5}$	0.422	0.430	2.012	2.002

Regarding SBO, Fe atoms on the surface increase their SBO because of the new bond formation between the glass layer and the oxide layer. However, different sites of Fe experience different changes. The Fe_P has the largest change in SBO after adsorption (+0.548) while Fe_O gets a slight increase from 2.575 to 2.669. This increment indicates that Fe_P has more interactions with surrounding atoms after adsorption compared to other Fe_{layer1} sites. In the Fe_P sites with P directly adsorbed only, the BO of Fe_{layer1}-O_{layer2} increases from 0.765 before adsorption to 0.790 after adsorption. Moreover, there is also a strong BO of Fe-P (0.444). These BO increments result in the largest SBO value of 3.123 among Fe_{layer1} sites a.

After adsorption, the P-O bond is a pure covalent bond inside the glass layer, with the BO greater than 1 and the P-$O_{bridging}$ bond is the weakest P-O bond with the longest distance of 1.637 Å and the smallest BO of 1.076. The bond distance of these interactions also correlates with the bond order, as shorter bond lengths result in a greater bond strength. However, it is worth noting that even among the covalent bonds the bond length–bond strength rule is not always true when comparing different types of bond due to orbital delocalization, depopulation or so called bond anomaly, especially when the elements with lone pair electrons such as P, N, F are involved.[261] The stable position of Na atoms is either at the interstitial space of glass or on O adsorption sites of the iron oxide surface. Na-O is an ionic interaction with the BO in the range of 0.076 – 0.081 which is close to the value of ionic solid from Manz's study [250] (BO 0.09 for Na-F and Na-Cl). When comparing the Na-O_{glass} and Na-$O_{surface}$, the bond order is identical even if the Na-$O_{surface}$ distance has a tighter range than the Na-O_{glass}. Hence, the Na-O interaction is indistinguishable at the interface between glass and iron oxide surface. There are two other important interface interactions along with the Na-$O_{surface}$: direct bond Fe-P and Fe-O_{glass}. Fe_O-O_{glass} with a BO of 0.429 is in the range of Fe-O interaction in the bulk (i.e. 0.422 Fe_{layer4}-O_{layer5} before adsorption). Fe_P-P direct bond is slightly higher in BO with the value of 0.444. These are the medium mixed ionic-covalent bonds.

Besides the connection between glass and oxide surface, the adsorption also has an impact on the top layer interaction of iron oxide surface Fe_{layer1}-O_{layer2}. The main aim of this study is whether the Fe_2O_3 surface endures the destruction, deformation or transformation by the interaction with polyphosphate. As monodentate the linkage was the most dominant structure in the system, thus the Fe_{OP}-O_{layer2} was not considered while the Fe_P-O_{layer2} and Fe_O-O_{layer2} interactions were analyzed in the results. For the outermost layer of Fe_2O_3 surface, an extension of Fe-O_{layer2} distance (from 1.813 Å to 1.864 Å) and a decrease of

BO in average (from 0.765 to 0.648) were observed. However, at Fe_P sites, the Fe-O_{layer2} BO increased up to 0.790 despite the increased distance. This abnormality at Fe_P sites may be caused by the effect of lone-pair electrons from phosphorus as mentioned above. Lower layer interactions maintained their properties after adsorption.

In order to unveil more detail about the electronic structure of the current system, the visualization of CDD and ELF has been depicted in Figure 4-3. PDOS has been depicted in Figure 4-4.

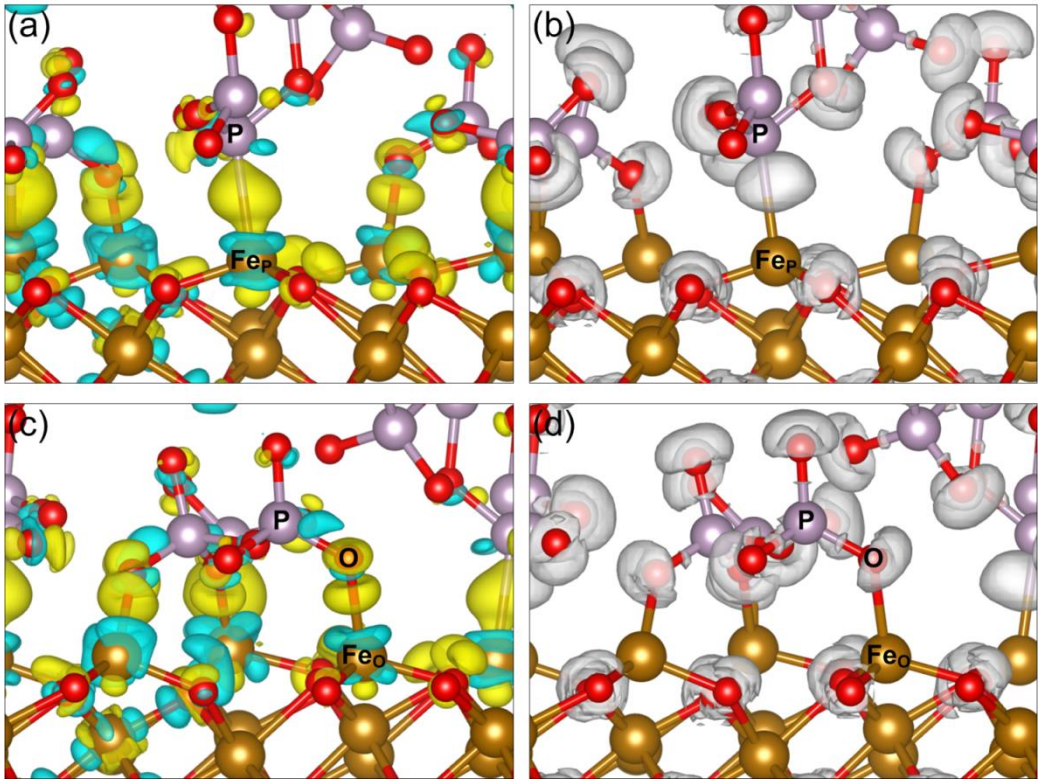

Figure 4-3. Charge density different (CDD – left column) of (a) Fe_P – P bond and (c) Fe_O – O – P linkage, the yellow areas depict the electron accumulation and cyan areas depict electron depletion regions respectively, isosurfaces are 0.005 e/Å^3. Electron localization function (ELF – right column) isosurfaces (silver regions) at $\eta = 0.65$ of (b) Fe_P – P bond and (d) Fe_O – O – P linkage. O atoms are colored in red, Fe in gold, P in purple. Na atoms have been removed for clear visualization.

The typical Fe_P-P is shown in Figure 4-3a and b; the Fe_O-O_{glass} bond is depicted in Figure 4-3c and d. In terms of CDD for both cases, the Fe sites at the interface between the glass layer and oxide surface are subjected to the electron depletion. However, the partial charge in Table 4.1 mentioned the charge reduction of Fe_P and the charge increase of Fe_O. This phenomenon can be explained by the yellow electron accumulation areas found in the middle of the Fe_P-P and Fe_O-O_{glass} bonds. In the case of Fe_P-P, this area is a

combination of two separated electron build-up regions (Figure 4-3a). The major region is located at the center of Fe_P-P bond while the minor one occurs around the Fe site. The cross-section in Figure B-4 in Appendix B clearly reveals the separation. On the other side, the accumulation area in Fe_O-O_{glass} is the one region that is smaller than Fe_P-P at the same isosurface value and is positioned near the O atom. Besides, the ELF visualization shows that the Fe_P-P involves an-electron-pair area between two atoms, which indicates the contribution of the phosphorus lone pair in this bond (Figure 4-3b). While the visualization of the Fe_O-O_{glass} bond displays the same nature as the Fe-$O_{surface}$ and other Fe-O bonds. The ELF observation of this bond has been reported previously [245, 262]. Both electronic analysis methods unveil the nature of these two notable bond types in our system. Fe_P-P is generally considered as a metal – ligand synergetic bonding which has the mixed contribution of σ-donation and π-back donation [263-265]. The Phosphorus → Metal σ-donation has been created by the lone pair donation from P into the empty 3d orbital of Fe while Metal → Phosphorus π-back bonding has been constructed of the 3d donation from Fe into σ* molecular orbital of $P(OR)_3$ ligand instead of 3d or 3d phosphorus orbital. Phosphite-based ligand has been considered as a good σ-donor and medium π-acceptor [266-268]. On the other hand, Fe_O-O_{glass} has the nature of a Fe-O bond in pure iron oxide with the inductive effect commonly mentioned in iron phosphate compounds [269, 270]. The Fe-O bond is usually expressed as the hybridization Fe 3d and O 2p states. However, in the inductive effect, the Fe atom is affected by the P atom when bonding to O in the Fe-O-P linkage which reduces the bond strength of Fe-O. As a result, the BO of Fe_O-O_{glass} is 0.429 compared to 0.684 of normal bonds in the oxide surface Fe_{layer1}-O_{layer2}.

For the Fe-O in the oxide layer, the first bond pair Fe_{layer1}-O_{layer2} endures a significant variation after the adsorption compared to lower bond pairs, e.g. Fe_{layer3}-O_{layer2}, Fe_{layer4}-O_{layer5}. In general, this bond pair reduces BO from 0.765 to 0.684. This a consequence of increasing Fe coordination and an aim to achieve a stable configuration at the bulk Fe sites. The sharing connection and bond transformation do not have the same effect for every Fe site. The Fe_{layer1}-O_{layer2} BO increases at Fe_P sites and reduces at Fe_O sites which was mentioned before. However, this difference cannot be clearly observed on CDD and ELF graphs.

Hence the PDOS of 3d states of Fe atoms before and after phosphate adsorption was investigated and presented in Figure 4-4.

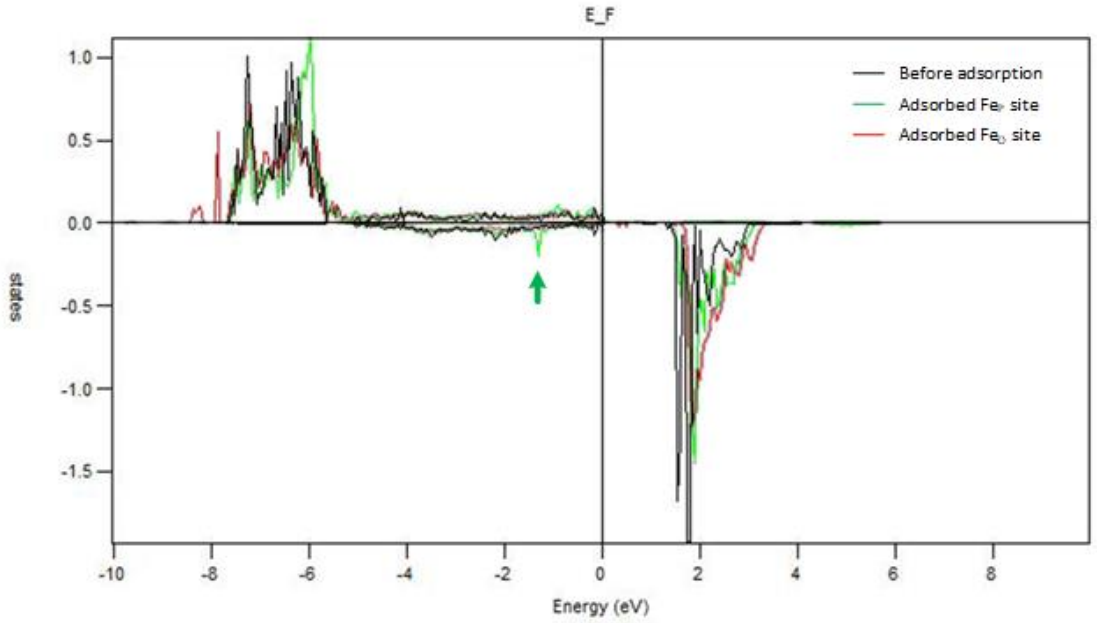

Figure 4-4. Projected density of state (PDOS) for Fe 3d states before adsorption (black line), Fe_P after adsorption (green line), and Fe_O after adsorption (red line). The Fermi level is indicated at zero. The positive and negative values on vertical axis represent different spin states. Note the valence state change of Fe_P after adsorption.

Before adsorption, the PDOS of Fe 3d states show a good agreement with previous studies of α-Fe_2O_3 structure [247, 271]. The major spin channel with positive values of states have been occupied whilst the minor spin channel is empty which indicates a $3d^5$ configuration of an Fe^{3+} ion. After the adsorption, at Fe_P sites, an additional peak has been observed in the minor spin channel just below the Fermi level. This peak was related to the sixth electron and the reduction of Fe^{3+} to Fe^{2+} $3d^6$ occupation [272, 273]. Thus the Fe_P atom changes from valence state +3 to +2 due to the direct interaction of Fe-P. Moreover, the difference of 0.3 – 0.4 |e| of partial charge has been expected between Fe^{3+} to Fe^{2+} [274], which reaffirms that the electron accumulation of Fe_P sites is based on the reduction. At the same time, Fe_O sites remain +3 valence state with a slight electron depletion.

In general, the direct Fe-P bond reduces the electrostatic attraction of the surface, but it strengthens the top surface's interaction eventually, through the covalent part. In contrast, the Fe-O_{glass} bond weakens the Fe-O bond of the surface and can promote Fe_2O_3 surface deformation.

4.3.2 Single interaction adsorption on Fe_2O_3 surface

Interlayer phosphate – iron oxide interaction

In the context of full coverage phosphate glass adsorption, the interactions such as Fe-O, Fe-P, and Na-O are influenced by other bonds. Thus, with the general view of full adsorption, we determine these important interactions in the system, and break down the system into single interaction adsorption which considers Fe-O, Fe-P, O-P, and O-Na separately. For the first 3 interaction types, we look at 6 cases which include 4 types of adsorbate and 2 adsorption sites on the oxide surface. The stable adsorption configuration is depicted in Figure 4-5.

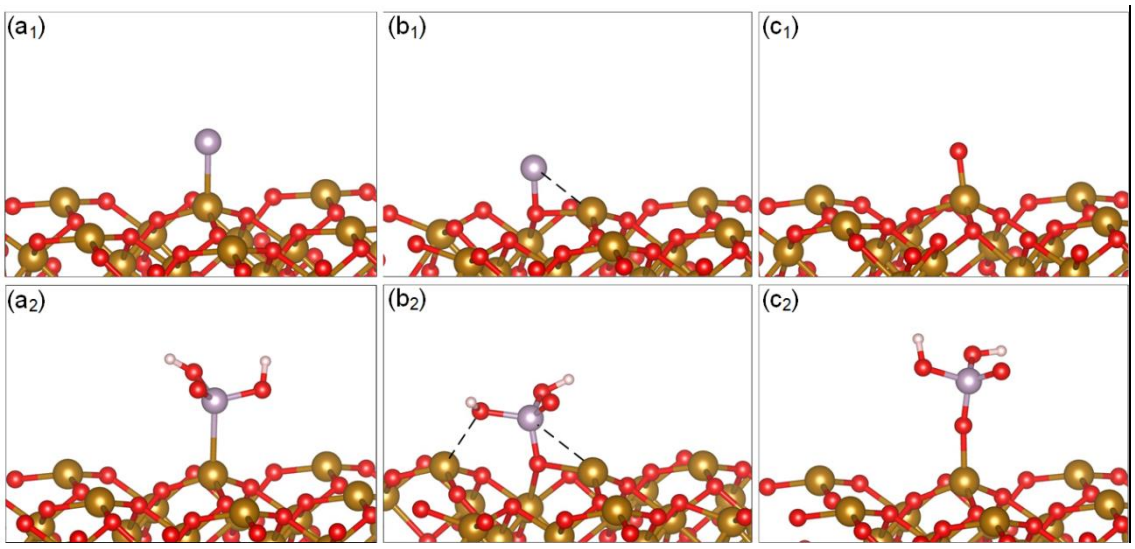

Figure 4-5. Stable adsorption configuration on Fe_2O_3(0001) surface of (a_1) P atom on Fe site, (a_2) H_2PO_3 on Fe site, (b_1) P atom on O site, (b_2) H_2PO_3 on O site, (c_1) O atom on Fe site, and (c_2) H_2PO_4 on Fe site. O atoms are colored in red, Fe in gold, P in purple and H in white. The undesirable interactions have been depicted in black dash lines.

In order to isolate the interaction inside the current system, simple adsorbates have been used such as P atom, O atom, H_2PO_3, and H_3PO_4. Hydrogen is used to terminate the oxygen with the aim of removing sodium effects. The configuration has been carefully relaxed and made sure no hydrogen bond formation between $H_{adsorbate}$ and $O_{surface}$. It is worth noting that only monodentate configuration has been considered as this is the dominant structure in the phosphate adsorption on iron oxide surface in previous studies.[245, 275] For example, the most stable configuration for the P atom adsorption is a hollow position between 3 oxygen atoms of the surface, which is not a monodentate structure. The monodentate structure of one P atoms linked to one O is the desired one (Figure 4-5b_1). In the different structures of full coverage glass adsorption, when the input

thickness between glass and oxide layer is as low as 1.5 Å, the $O_{surface}$-P bond takes place and remains in the relaxed structure. The detail relaxed structure of this case is visualized in Figure B-5 in Appendix B. Thus the $O_{surface}$-P cases (Figure 4-5b_1 and b_2) have also been studied here because this bond may appear in the high compression condition such as extreme load in rolling steel processes. Even though the interlayer hydrogen bonds were completely avoided (the BO of all interlayer hydrogen interactions is nearly 0), some other interactions can only be partly minimized because of the configuration of Fe-terminated oxide surface (black dash lines in Figure 4-5b_1 and b_2). It is believed that those bonds are too weak to affect the considered main interaction. In particular, $Fe_{surface}$-P_{glass} BO of 0.463 in Figure 4-5b_1 (compared to $O_{surface}$ – P BO of 1.48), $Fe_{surface}$-O_{glass} BO of 0.214 and $Fe_{surface}$-P_{glass} BO of 0.076 in Figure 4-5b_2 (compared to $O_{surface}$ – P BO of 1.34).

Table 4.2. Adsorption energy (eV), BO of different adsorbates on Fe- and O- sites of Fe_2O_3(0001) surface, BO of Fe_{layer1}-O_{layer2}, and barrier energy of Fe_{layer1}-O_{layer2} dissociation (E_{bar}) of these cases. Energy is in eV unit.

Bond	Adsorbate	Site	E_{ads}	BO	Fe_{layer1}-O_{layer2}		Figure
					BO	E_{bar}	
Fe_P – P	P atom	Fe	- 1.20	0.823	0.760	2.932	Figure 4-5a1
	H_2PO_3	Fe	- 1.32	0.464	0.751		Figure 4-5a2
$O_{surface}$ – P	P atom	O	- 3.46	1.480			Figure 4-5b1
	H_2PO_3	O	- 3.92	1.340			Figure 4-5b2
Fe_O – O_{glass}	O atom	Fe	- 4.44	1.134	0.726	2.188	Figure 4-5c1
	H_2PO_4	Fe	- 8.47	0.618	0.615		Figure 4-5c2

As presented in Table 4.2, the adsorption energies for different Fe_P-P, $O_{surface}$-P, Fe_O-O_{glass} configurations are -1.2 to -1.3 eV, -3.4 to -3.9 eV, and -4.4 to -8.4 eV, respectively. These values are in good agreement with the sodium pyrophosphate cluster and sodium triphosphate cluster adsorption on the iron oxide surface [245] and the trimethyl phosphite

on steel [276]. The results indicate that the popular linkage -P-O_{glass}-Fe- is more thermodynamically favorable than other interaction types and the adsorption from P-direct bond to Fe site is rarely observed in this system. In conclusion, the -P-O_{glass}-Fe-linkage will dominate the system even at the ambient temperature. Many studies pointed out the strong affinity between phosphate and iron oxide at room temperature in soil mechanics [181, 183]. In the compression condition, the second-best stable interaction of $O_{surface}$-P will occur due to the closeness between the two layers. Lastly, Fe_P-P will form when the system contains more Fe exposure such as nascent Fe surface or an iron oxide cluster.

Fe-O interaction at the outermost oxide layer

The effect of a single interaction on the outermost iron oxide layer was also analyzed. The BO of Fe_{layer1}-O_{layer2} has been reported in Table 4.2. The data reaffirms that the BO of Fe_{layer1}-O_{layer2} is smaller at Fe_O sites than others at Fe_P. In terms of energy, the energy profile of the first Fe_{layer1}-O_{layer2} bond dissociation with different adsorbate-attached systems was studied and depicted in Figure 4-6.

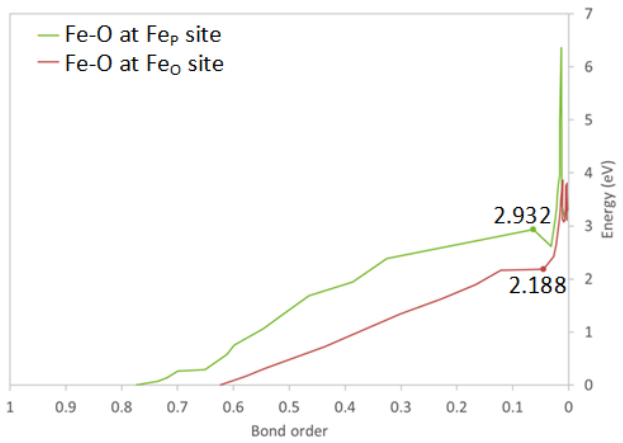

Figure 4-6. Energy profile (eV) of the first Fe-O bond dissociation in the respect of Fe-O BO for P-adsorbed system (blue line) and O-adsorbed system (red line)

In the simulation of Fe_{layer1}-O_{layer2} dissociation, the simplest configurations of P atom and O atom adsorbed on the iron oxide surface at Fe sites were used. The starting configurations are geometry optimized structures as seen in Figure 4-5a1 and Figure 4-5 c1. Then the adsorbed Fe atom has been displaced upward and has been fixed in the z-direction and relaxed in other directions. Thus, among the three Fe_{layer1}-O_{layer2} bonds of that Fe atom, the BO of the first bond dissociation, which has the Fe-O distance exceeded

3 Å, was monitored. The result in Table 4.2 and Figure 4-6 indicate that barrier energy of the first Fe_{layer1}-O_{layer2} dissociation in the P-adsorbed system is 2.932 eV while in the O-adsorbed system is 2.188 eV. The energy values increase sharply for the BO below 0.05 in both cases due to the second and third Fe_{layer1}-O_{layer2} dissociation. With a higher barrier energy, the dissociation of Fe_{layer1}-O_{layer2} in the P-adsorbed system is more difficult than in the O-adsorbed system. It is worth noting that the linkage -P-O_{glass}-Fe- creates a more stable adsorption configuration and gets a lower barrier energy for Fe_{layer1}-O_{layer2} bond dissociation, which promotes the iron or iron oxide removal in the tribological system. We also try to conduct the abovementioned dissociation by fixing the adsorbate–surface distance instead of the Fe atom. However, the adsorbate – surface dissociation occurs before the Fe_{layer1}-O_{layer2} dissociation, which is expected when comparing BO of adsorbate–Fe and Fe_{layer1}-O_{layer2}.

Effect of sodium

The effect of sodium on the Fe-terminated iron oxide surface was explored with the monolayer (ML) sodium adsorption at different coverages. Initial coverage of 1/16, 3/16, 6/16, 8/16, 16/16 ML sodium was used, which has Na atoms placed at the hollow position between three O_{layer2} atoms. The stable configuration is shown in Figure 4-7.

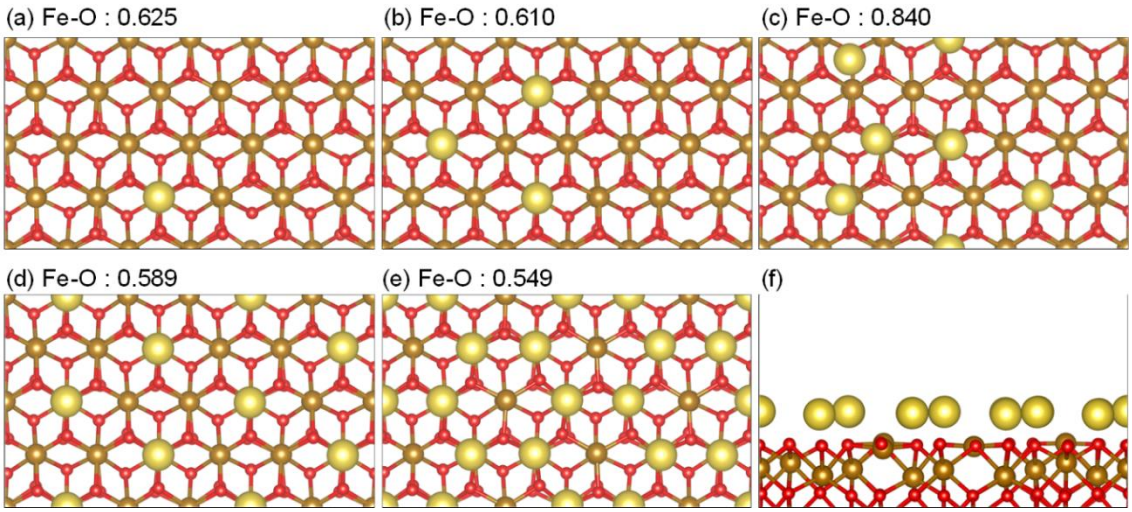

Figure 4-7. Stable adsorption configuration of sodium monolayer adsorption on Fe_2O_3(0001) surface at different coverage (a) 1/16 ML, (b) 3/16 ML, (c) 6/16 ML, (d) 8/16 ML, and (e) 16/16 ML; (f) side view of 16/16 ML. O atoms are colored in red, Fe in gold, and Na in yellow. The BO of Fe_{layer1}-O_{layer2} near sodium adsorption sites has been labelled for each configuration.

After adsorption, Na atoms stay at the hollow sites of the oxygen triangle on the surface as it is the most stable configuration of sodium adsorption which is observed in the full coverage glass adsorption and the single interaction cases. Moreover, the Fe-terminated oxide surface has been transformed by sodium adsorption. The Fe atoms near the targeted oxygen shrink down and expose the oxygen atoms to the outermost layer, which reconstructs the Fe-terminated surface into the O-terminated surface. This transformation creates a partially O-terminated surface in the 1/16 ML and the fully O-terminated surface in the full sodium ML coverage case (Figure 4-7f). The BO of Fe_{layer1}-O_{layer2} is also reported for the sodium adsorption cases. The results indicate that the sodium adsorption reduces the BO of Fe_{layer1}-O_{layer2} thus these adsorptions play an important role in weakening the oxide surface and promote Fe removal in the system. The outlier is the 6/16 ML case which has the most significant sodium rearrangement between the initial and the optimized structures. This is because six Na atoms inside six oxygen triangles around one Fe atom is too packed and cannot create a stable structure. As Na atoms move around, the BO of Fe_{layer1}-O_{layer2} receives abnormal values. The result of Fe_{layer1}-O_{layer2} BO in all cases is accounted for the Fe-O bond which O atoms belong to Na-adsorbed oxygen triangles.

4.3.3 Ab initio molecular dynamics of phosphate cluster with iron oxide cluster

In order to study the oxide deformation and behavior of Fe/Fe_2O_3 particles in the interaction with phosphate network, the AIMD simulations of phosphate clusters with iron/iron oxide clusters were conducted at 300K, 1100K and 1500K. The cluster models have been chosen to investigate the behavior of iron/iron oxide inside the network of sodium phosphate glass in general, and the interaction between phosphate monomer of glass with the nanoscale wear particle of iron/iron oxide, which has more Fe or O exposure than the typical surface. The simulation was performed at ambient temperature to stabilize the system first then the simulation proceeded to 1100K and 1500K, which are the working temperature of hot rolling processes and the possible temperatures reached at the impact points [224]. Three cases were considered for the AIMD such as pyrophosphate cluster $Na_4P_2O_7$ with iron oxide cluster $(Fe_2O_3)_3$, rich-Na pyrophosphate cluster $Na_{15}P_2O_7$ with iron oxide cluster $(Fe_2O_3)_3$, and normal pyrophosphate cluster $Na_4P_2O_7$ with pure iron cluster Fe_7, which are displayed in Figure 4-8, Figure 4-9, and

Figure 4-10 respectively. The structure of iron oxide was optimized from Reference [277], while the iron cluster was optimized from Reference [278].

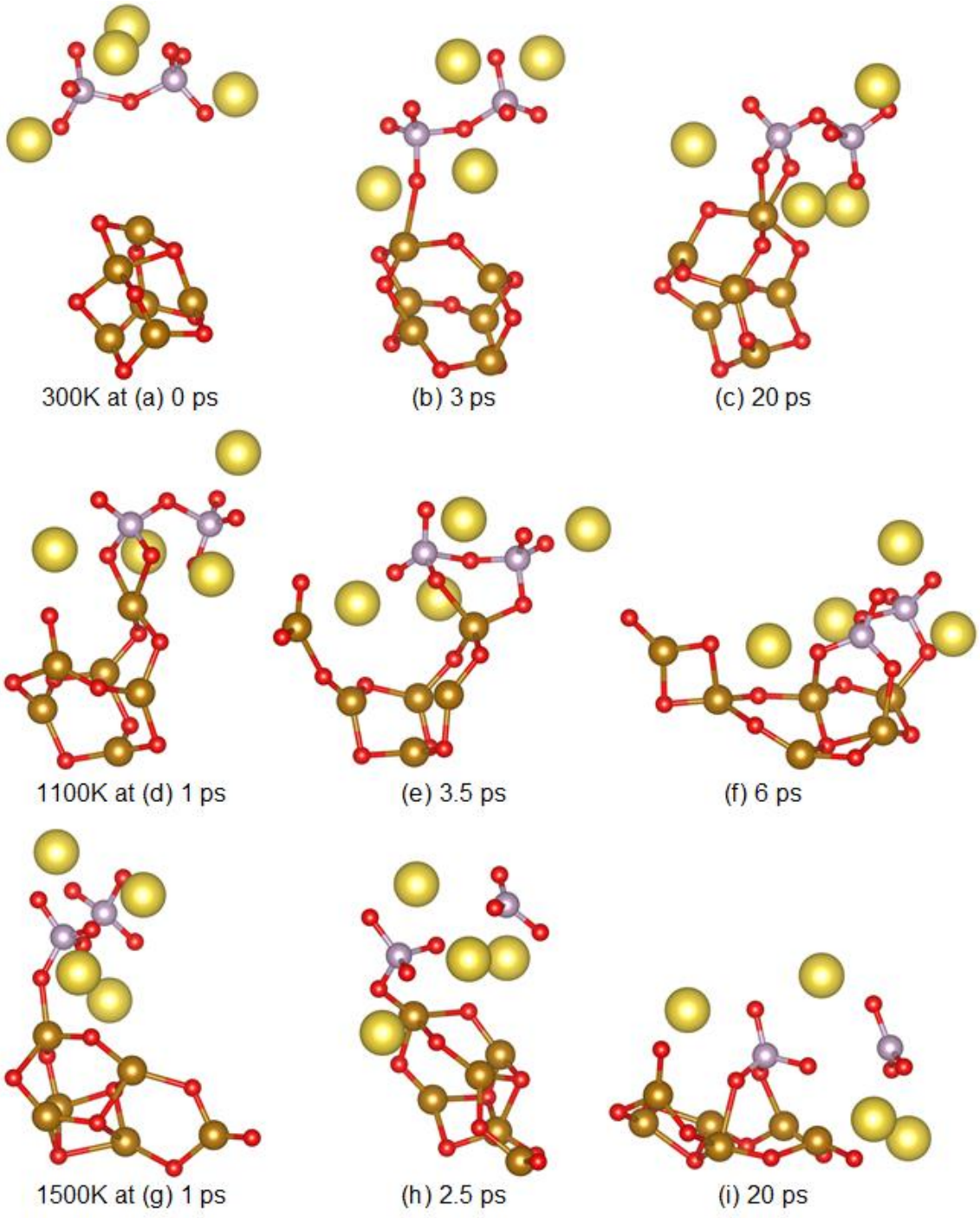

Figure 4-8. Snapshots of AIMD simulations of $Na_4P_2O_7$ cluster on $(Fe_2O_3)_3$ cluster at 300K, at times: (a) 0 ps, (b) 3 ps, (c) 20 ps, at 1100K at (d) 1 ps, (e) 3.5 ps, (f) 6 ps, and at 1500K, at times: (g) 1 ps, (h) 2.5 ps, (i) 20 ps. Red, gold, purple and yellow spheres represent oxygen, iron, phosphorus and sodium atoms, respectively.

Figure 4-8 shows that the pyrophosphate is interacting with the iron oxide cluster. At ambient temperature, the phosphate oxide stabilizes after 20ps adsorption into the iron oxide cluster (Figure 4-8c). The connection between two clusters can be monodentate, mononuclear bidentate, binuclear bidentate, etc. as mentioned in the studies of soil mechanics [184, 185]. The iron oxide is stable at ambient temperature, but this cluster starts deforming at 1ps and continues to deform during the 20-ps simulation (Figure 4-8a) at 1100K. At the end of the simulation, the cage structure of $(Fe_2O_3)_3$ flattens out and makes more connections with the pyrophosphate cluster in the monodentate form, which is consistent with the result from the surface adsorption discussed in the previous section. There is no P-O bond dissociation at this temperature but there is a transformation of the oxide cluster. As the increase of Fe and O exposure due to the effect of high temperature and presence of adsorbate, the attack of the adsorbate and sodium to iron/iron oxide will occur, which can promote the disintegration of oxide particles and incorporate iron atoms into glass network. At a higher temperature of 1500K, the iron oxide also deforms at the start of the simulation and the initial cage structure cannot remain during the simulation. At 2.5ps, the $P\text{-}O_{bridging}$ has been dissociated, which is to be expected at high-temperatures and with the depolymerization effect, as mentioned in Le et al. [245].

To study sodium effects in the system, the rich-Na pyrophosphate cluster was simulated at the same range of temperatures 300-1500K. The obtained result in Figure 4-9 shows that at 300K, and with the clustering of sodium atoms surrounding pyrophosphate, these sodium atoms create a layer which separates pyrophosphate from iron oxide clusters. This layer not only plays a role of separation but, at 2.5ps, also generates an O-terminated interface, which has the same effect on the oxide surface in earlier results of section "Effect of sodium". Moreover, excess sodium atoms can also slightly disrupt the cage-like structure of iron oxide at 300K (Figure 4-9c). At 1100K, the effect of sodium on iron oxide is more severe. In fact, the iron oxide is dissolved and dissociated into small fragments such as FeO_2, and Fe_2O_4, which can separate from or connect to phosphate cluster. The connection to phosphate has been captured in Figure 4-9e while the separation has been shown in Figure 4-9f. For 1500K, in addition to the phenomena observed at 1100K, there is a dissociation of pyrophosphate structure into smaller fragments which is similar to the normal pyrophosphate case.

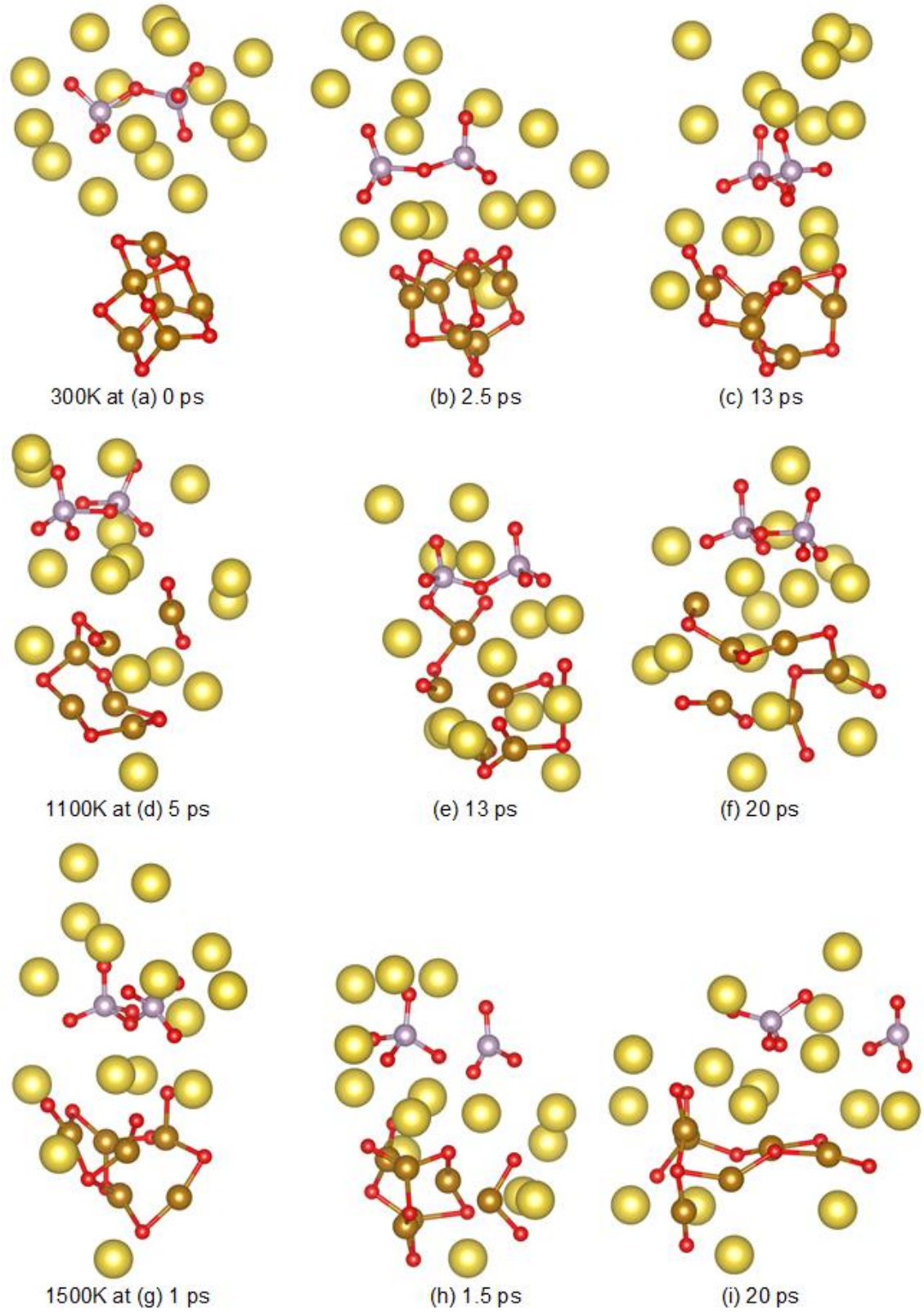

Figure 4-9. Snapshots of AIMD simulations of a $Na_{15}P_2O_7$ cluster on an $(Fe_2O_3)_3$ cluster at 300K, at times: (a) 0 ps, (b) 2.5 ps, (c) 13 ps, at 1100K at (d) 5 ps, (e) 13 ps, (f) 20 ps, and at 1500K, at times: (g) 1 ps, (h) 1.5 ps, (i) 20 ps. Red, gold, purple and yellow spheres represent oxygen, iron, phosphorus and sodium atoms, respectively.

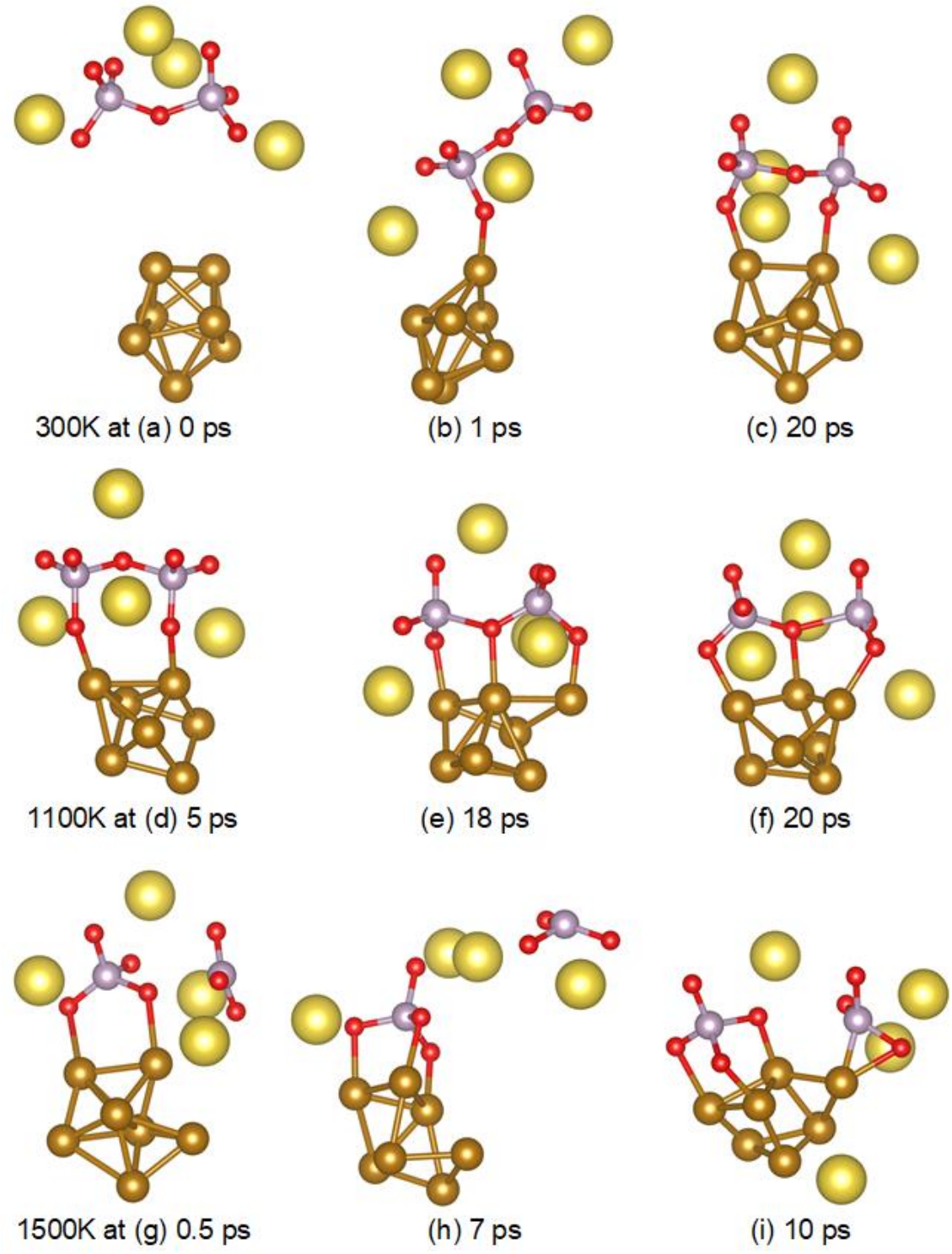

Figure 4-10. Snapshots of AIMD simulations of a $Na_4P_2O_7$ cluster on an Fe_7 cluster at 300K, at times: (a) 0 ps, (b) 1 ps, (c) 20 ps, at 1100K at (d) 5 ps, (e) 18 ps, (f) 20 ps, and at 1500K, at times: (g) 0.5 ps, (h) 7 ps, (i) 10 ps. Red, gold, purple and yellow spheres represent oxygen, iron, phosphorus and sodium atoms, respectively.

The AIMD simulation of an Fe_7 cluster which has more Fe exposure than other cases is also considered and the results shown in Figure 4-10. The stable configuration at ambient temperature is a monodentate complex between pyrophosphate and pure iron (Figure 4-10c). When the temperature is increased from 1100K and 1500K, the iron oxide cluster still maintains its cage-like form even when suffering minor deformation at 1500K. Among the three temperature cases, the Fe-P direct bond was only observed at the later stage of the 1500K case, which indicates that the probability of this bond formation is unlikely. This direct interaction can occur when the system is subjected to severe conditions such as elevated temperature, high exposure to Fe atoms and under-coordinated phosphorus atoms.

According to the dynamic simulation, the effect of adsorbate on the strength of iron oxide surfaces or clusters is similar to the effect of temperature on the normal-Na phosphate. At the working conditions of high temperature metal forming in particular, the iron surface can be deformed. This phenomenon can affect iron oxide areas of high activity, such as a nanoscale cluster. With an excess number of Na atoms in rich-Na pyrophosphate cluster case, the iron oxide deformation can occur at ambient temperature and a higher temperature induces even more intense effect. The Fe-P direct bond will only be observed when the system is subjected to harsh conditions of high temperature.

4.4 Discussion

In this study, all the effects of the alkali phosphate glass adsorbate that have an impact on the stability of the iron oxide layer have been considered. Consequently, of the three connection that may occur between the phosphate network and the iron oxide layer, the -Fe-O_{glass}-P- is the most important linkage that can create the most stable system. The second most important is $O_{surface}$-P bonding which is observed under a high load contact condition. Under more extreme conditions of temperature and glass depolymerization, the rare interaction of Fe-P direct bonding will take place. According to the static and dynamic adsorption, the commonly occurring -Fe-O_{glass}-P- linkage promotes iron oxide structure deformation when under the effect of high temperatures. The attack of the network modifier sodium on the oxide surface is even greater than that of O_{glass} atoms in -Fe-O_{glass}-P- linkages. With a surplus number of sodium aggregate at the oxide surface, the iron oxide is subjected to deformation due to Na-O_{glass} interaction and the mobility of sodium in the system. The deformation of the iron oxide surface has been reported in a previous study [245] and the destruction of the iron oxide cluster has been demonstrated

in this study. Besides the well-known explanation of abrasive particle digestion mechanism for ZDDP tribofilm due to shear, pressure and heat [78, 106, 107], the phosphate-based network itself has an effect on destabilizing of the iron oxide surface through the -Fe-O-P- linkage. The wear debris of iron oxide then can be more easily dissolved into the glass network, which produces a better anti-wear performance. Our phosphate glass lubricant has a similar phosphate network, plus a mobile network modifier cation of sodium has a remarkable performance regarding the reduction of wear, surface roughness and friction for hot rolling processes due to the effect of sodium addition [97, 98, 279].

The Fe-P direct link has been mentioned in the studies of phosphite-based compounds and metallic iron [95, 103, 276]. Our study agrees well with those references in finding Fe-P direct interactions with the presence of under-coordinated phosphorus atoms and extensive iron exposure. The phosphite PR_3 is a π-acceptor ligand that uses phosphorus σ* orbitals. In the case of high metal (M) exposure, more metal atoms are bridged by phosphite ligands, e.g. M_2-PR_3, M_3-PR_3, and more electrons will fill in σ* orbitals which destabilizes the phosphite complex leading to a phosphorus layer on the metallic iron surface. In the context of the phosphate glass lubricant on the iron oxide surface, the Fe-P direct bond may occur, but the phosphorus atoms will achieve the full coordination using oxygen from abrasive particles and incorporate iron oxide into the phosphate network at the end. Rana and Tysoe also pointed out that the friction reduction and tribological performance of phosphite additives correlates with the distribution of full coordinated phosphorus in phosphate tribofilm [280].

With the -Fe-O_{glass}-P- linkage, under temperature, shear and pressure effect, iron or iron oxide will be dissipated into the glass network as high oxidation ions (Fe^{3+}). It is well-known that Fe^{3+} has high cation field strength which creates a strong affinity to oxygen in the glass network and usually plays a role as a network former [281]. However, the gradient composition of Fe in the tribofilm indicates that iron should be in the mobile form that can diffuse inside the molten glass or even penetrate through this layer to migrate to the top of the glass film [97]. Unlike Fe^{3+}, Fe^{2+} can diffuse more easily. The co-existence of Fe multi-valence and its diffusion in the glass has been mentioned in many studies [242, 282-284]. Thus, the diffusion pathway of Fe in our process of using polyphosphate glass lubricant is proposed in a scheme below.

After being removed as Fe^{3+} and immersing into the phosphate glass as a network former, iron will be reduced to Fe^{2+} and diffuse outward. If Fe^{2+} can penetrate through the glass

layer, oxidation will occur, and an oxide scale on top of the glass layer will form. This phenomenon has been experimentally observed [97]. The reduction and oxidation of Fe needs a species to balance electrons on the right side of the scheme. Na could be a potential candidate which can release or receive electron to the Fe processes. This scheme will result in a high concentration of sodium in a glass-oxide interface, which is already reported in the binary borate melt lubrication [39].

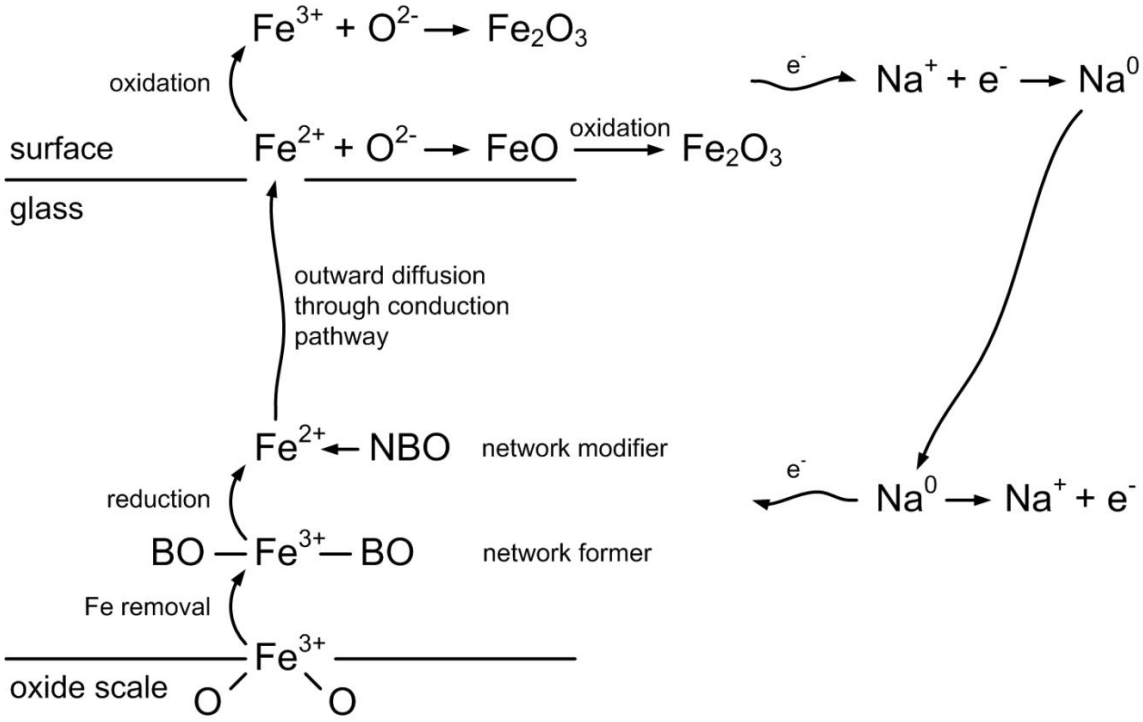

Scheme 4.1. Proposed pathway of Fe removal and diffusion into polyphosphate glass network

With the aim of reducing the oxide scale layer, the removal of Fe should be promoted and the outward diffusion of Fe^{2+} should be controlled, which still ensures Fe dispersion inside the glass network but diminishes the re-oxidation layer. In phosphate glass with high alkali concentration, Greaves [285, 286] proposed the modified random network model in which the structure contains the modifier region or the conduction pathway where network modifiers can be transported in the system. However, this modifier channel will be blocked or hindered and the diffusion of cations will decrease when exposing the glass to other different sized or polarized alkali ions (mixed alkali effect) or non-alkali ions (mixed ion effect) [287, 288].

Table 4.3. Crystal ionic radii (pm) and the optical basicity of some typical ions in glass

Ion	*Fe^{2+}	*Fe^{3+}	Li^{+}	Na^{+}	K^{+}	Be^{2+}	Mg^{2+}	Ca^{2+}	Al^{3+}	B^{3+}	Si^{4+}	P^{5+}
Crystal ionic radii (pm) [289]	75 (92)	69 (78.5)	90	116	152	59	86	114	67.5			
Optical basicity (Λ) [290, 291]	1.0	0.75	1.0	1.15	1.4		0.78	1.0	0.6	0.42	0.48	0.4

* denotes the low spin (high spin)

As mentioning in Table 4.3, we suggest adding smaller radius cations than Na^{+} into the glass composition in order to reduce the volume of the modifier channel, hence reducing Fe^{2+} movement inside the glass. Potential candidates can be Li^{+} and Mg^{2+} which have a small ionic radius and low cation field strength, therefore having low affinity to oxygen while still being as mobile as sodium. Nevertheless, having cations with a smaller radius than Na^{+} leads to a reduction in the optical basicity of glass, and since the optical basicity is related to the Fe^{2+}/Fe^{3+} ratio [290]:

$$\log\frac{[Fe^{2+}]}{[Fe^{3+}]} = 3.2 - 6.5\Lambda \qquad (4.3)$$

Replacing Na^{+} by smaller radius cation (lower optical basicity) will thus increase the equilibrium concentration of Fe^{2+}, which can increase the iron diffusion in phosphate glass. In conclusion, the glass composition can be an important factor that can be used to adjust the tribological performance of the lubricant. However, the study of diffusion of cations Na^{+}, Fe^{2+}, Fe^{3+}, K^{+}, etc. inside the glass and the cation-glass composition should be carefully considered in the future in order to improve the lubricant performance for harsh conditions in general and for hot rolling processes in particular.

4.5 Conclusions

The DFT calculations for the adsorption of full coverage glass and single interactions on an Fe_2O_3 surface, as well as the AIMD for phosphate and iron/iron oxide clusters at various temperatures were performed to determine the iron oxide behavior under glass adsorption at different temperatures. The conclusions are summarized as follows:

- The possible interactions between phosphate networks with iron oxide are Fe-O_{glass}, $O_{surface}$-P and Fe-P. The Fe-O_{glass} interaction is the most stable connection in the system and also has the effect of weakening Fe-O bond of the iron oxide surface. The $O_{surface}$-P interaction is observed under high compression conditions. And lastly, the Fe-P direct bond occurs under severe conditions of high temperature, substantial iron exposure

and with under-coordinated phosphorus atoms present. This bond is less likely to form but it can strengthen the Fe-O bonds of the iron oxide surface. The barrier energy of Fe-$O_{surface}$ dissociation also confirms the effect of adsorbate on surface deformation.

- Additionally, Sodium cations in the glass network reduce the Fe-$O_{surface}$ stability. The iron oxide structure deformation can occur at normal temperatures in excess concentrations of sodium. Sodium adsorption generates O-terminated iron oxide surfaces.
- Phosphate glass itself has the chemical/electronical effect of deforming the iron oxide surface and iron oxide particle.

Chapter 5 Reactive molecular dynamics study of hierarchical tribochemical lubricant films at elevated temperatures [3]

5.1 Introduction

Inorganic alkali polyphosphate (IAP), especially sodium polyphosphate glass has been proposed as a new class of elevated temperature lubricant.[97] The in-situ thermal tests at temperature of 600-800°C indicated that the molten polyphosphate provided excellent lubrication because of the tribochemical reactions at the rubbing surfaces.[27] Most interestingly, this molten lubricant formed a hierarchical structure that was created by the penetration and reaction of polyphosphate and sodium with iron/iron oxides layers because of their affinity with each other under the influences of plastic deformation and thermal effect during the tribo-tests.[12] This hierarchical structure included multifunctional layers and had different functions, such as friction reduction, antiwear, and oxidation reduction.[13] In the molten phase, the polyphosphate glass was made up of cross-linked network formed through covalent bridging oxygens.[13]

However, the fundamental mechanism and chemical insights into this phenomenon have not been revealed by these experiments. In an effort to clarify these chemical insights, several theoretical studies have been carried out to identify the interaction mechanism of sodium phosphate with iron and iron oxide surfaces using density functional theory (DFT).[245] It has been revealed that sodium phosphate chemically adsorbs onto iron and iron oxide surfaces due to the interaction between iron and nonbridging oxygens of polyphosphate to form a medium Fe–O mixing ionic/covalent bond.[188] At high temperature, the dynamic simulations showed that the sodium phosphate were absorbed and then depolymerised onto the iron oxide surface at 1100 K.[245]

Although these theoretical investigations have successfully identified the adsorption of IAP onto iron/iron oxide surface at both static and dynamic conditions with the comprehensive chemical properties of adsorption energy, reaction barrier, electronic structure, and covalent bond order of considered systems, but they are unable to describe

[3] Based on Dinh Thi Ta, **Manh Ha Le,** Anh Kiet Tieu, Hongtao Zhu, Thi Thuy Huong Ta, Van Nam Tran, Shanhong Wan and Adri van Duin, "Reactive molecular dynamics study of hierarchical tribochemical lubricant films at elevated temperatures", *ACS Applied Nano Materials*, 2020, 3(3): p. 2687-2704.

the chemical reactions, as well as the hierarchical structure of tribofilm under lubricated conditions.[188] The accurate electronic description using DFT method exhibits adsorption of a small model of only 200 atoms and short simulation times because of its high computational expense.

In contrast, classical molecular dynamics (MD) approach is able to describe the confined shear systems of several thousands of atoms, making it possible to reach simulation scales that are orders of magnitude beyond what is tractable for QM. This approach utilizes the force fields, which are able to predict the mechanical and structural properties of inorganic materials and organic molecules, to describe the interactions between atoms. Unfortunately, traditional force fields have not been able to describe the chemical reaction because of the nonbreaking harmonic functions for the covalent bonds.[292] To overcome such challenges, researchers continue to develop different potentials, which allow for the formation and breaking of bonds, such as Tersoff, REBO, EDIP, and so on. Unfortunately, these potentials do not include nonbinding contributions like Coulombic and van der Waals interactions.

An advance reactive force field (ReaxFF) has been developed to help bridging this gap using the bond order functions.[144] As pointed out by Wen et al.,[293] an MD approach using ReaxFF seems to be promising pathway taken in theoretical-computational field to answer pertinent questions posed at the current frontier of tribological chemistry sciences. During the last two decades, this force field has been widely used for exploring, developing, and optimizing the materials properties that include the chemical bonding without expensive quantum calculations.[127] From the initial ReaxFF developed for hydrocarbons,[144] this potential has been extended to three common "branches": combustion, aqueous, and other independent systems.[127] However, most of developed ReaxFF parameters are for organic/inorganic molecules rather than solid crystal.[127] In diverse applications of ReaxFF methodology, the heterogeneous catalysis of chemical adsorption of molecules such as hydrocarbon,[294] water,[295] as well as aqueous solution [296] onto the metal and metal oxide surfaces have attracted widespread attention from researchers. Many inorganic systems such as Mo/V/Bi/Te/O,[297] coal/O_2/Mo_3Ni,[298] and organic systems of C/H/O [154] and C/N/B/S/O/H,[298] have been developed. However, the ReaxFF parameters for alkali metal polyphosphate are still missing.

Despite the significant interest of IAP in metal forming at elevated temperature, the available ReaxFF parameters for molecules that containing P elements are still limited.

In their simulation of deoxyribonucleic acid (DNA) and ribonucleic acid (RNA), Zhu et al. have developed the ReaxFF parameters for P.[299] These parameters were then applied for phosphoric acid (H_3PO_4) to investigate its tribochemistry performance between quartz surfaces.[167] The vibration frequencies, charge distribution, dissociation of single and double bond of P–O, and P–O–H angle have been included to optimize ReaxFF for H_3PO_4 acid.[167] In another attempt, Xiao et al. recently developed a new ReaxFF for phosphorus, and this force field was then extended for P/H and P/H/O/C systems.[300] The initial tests prior to this work indicated that these force fields are transferable for phosphorus oxides, but there are still large errors in the prediction of lattice constants, density, and especially the heat of formations (ΔH_f). A similar issue has been found for Na/O and Fe/O systems. In spite of some good predictions in structural properties of iron oxides, the ReaxFF for Fe/O system derived by Aryanpour et al. overestimates ΔH_f.[301]

These developments point out that a ReaxFF developed for a certain system when applied to another could be inaccurate. For instance, the C/H/O combustion force field in 2008 could accurately simulate water as gas phase but it failed to model water as liquid.[154] Moreover, Pahari and Chaturvedi pointed out that the best-fit values of ReaxFF parameters must be determined for specific molecules.[161] In addition, there was an inconsistency in the sources used to train these ReaxFF, that is, using quantum mechanics (QM) or experimental data, which could result in a mismatch when the parameters are combined for a more complex system. Senftle et al. disclosed that transferring parameters between branches requires more extensive refitting.[127] Therefore, the work in this paper will revise these ReaxFF to apply to a new and complex system of Fe/Na/P/O using a consistent reference data from QM calculation as the training set. Moreover, the robust genetic algorithm (GA) will be applied in the current ReaxFF development to obtain a global optimization to overcome the issues with the single-parameter optimization code.[160] Indeed, the newly optimized ReaxFF developed by Larsson et al.[302] using GA for Si–Si bond in $H_3Si–SiH_3$ showed a substantial improvement over the previously published one using conventional algorithm developed by Fogarty et al.[295]

5.2 Computational details

5.2.1 Quantum mechanical calculations

The reference data for the current ReaxFF development was from the ab initio

calculations using the Vienna Ab Initio Simulation Package (VASP) simulation package.[303] The electron-ion interactions using the projector augmented-wave (PAW) method was applied for each atomic species. The Brillouin zone using Monkhorst–Pack scheme with a k-point set of 3×3×3 has been sampled for energy minimization, while a k-point set of 9×9×9 was applied for energy evaluation to obtain an accurate energy value. Furthermore, the generalized gradient approximation (GGA) exchange-correlation functional of Perdew-Burke-Ernzerh (PBE) was utilized. To ensure the convergence of the current ab initio calculations, a convergence criterion of 10^{-4} eV in electronic self-consistent loop and ionic relaxation had been set. A cutoff energy of 520 eV, which implied an increase of 30% with respect to the default value of 400 eV in PBE pseudopotentials, were set to obtain reliable results with precision.

The ab initio MD (AIMD) was performed to simulate the dynamics of $Na_4P_2O_7$ crystal at 1100 K, and the results were used to compare with those obtained from the current ReaxFF to validate the transferability of fitted ReaxFF under severe working conditions. This AIMD simulation using Langevin thermostat for NVT ensemble with the time steps of 0.5 fs during 10 ps with a k-point set of 1×1×1.

5.2.2 ReaxFF method

ReaxFF is an empirical force field that describes the interaction or chemical bonding between two atoms by a function of bond order with relative distance.[144] This force field presents efficiently the bond formation and breakage in a large condensed phase system that is extremely expensive for quantum dynamics simulation. The energy function for ReaxFF is expressed by the following equation:

$$E_{system} = (E_{bond} + E_{over} + E_{under}) + E_{angle} + E_{torsion} + E_{lone-pair} + E_{conj} + E_{H-bonding} + E_{vdW} + E_{Coul} \quad (5.1)$$

where the individual energy terms present the energies of total bond order term (E_{bond}), over coordination (E_{over}), under coordination (E_{under}), bending angle (E_{angle}), torsion ($E_{torsion}$), lone pair electron ($E_{lone\text{-}pair}$), conjugation (E_{conj}), hydrogen bond ($E_{H\text{-}bonding}$), and non-bond interactions of van der Waals (E_{vdW}) and Coulomb (E_{Coul}). The detailed expression of each term can be found in the original work by Duin et al.[144]

5.2.3 Fitting parameters for Fe/Na/P/O system

There were a total of 1320 parameters for the current ReaxFF including 107 trained parameters. A multiparameter optimization technique using an advance GARFfield

package developed by Jaramillo-Botero et al. was utilized in this optimization.[160] Although this technique placed a high demand of calculation due to the large populations and generations, it could find the global optimal value quickly. Compared with stand-alone ReaxFF program in time saving, this algorithm is more effective, especially, for periodic structures. For example, the comparisons were made for Na_3PO_4 molecule and $Na_4P_2O_7$ crystal (52 atoms) with 11 configurations for each compound. The results show that the stand-alone ReaxFF program took only 42.55 s to complete the first optimization using single CPU for Na_3PO_4 molecule, while there was 1430.41 s in real time for GARField using 32 CPUs. However, to obtain the results that were comparable with those obtained from GARField, this stand-alone code needed to run repeatedly several times. In contrast, for $Na_4P_2O_7$ crystal, it took only 188.78 s in real time to finish the job using GARField with 224 CPUs, which was much faster than 3319 s for stand-alone code. However, the cost of GARField in real time depends on the number of CPUs, population size, and crossover ratio.

A population size in range 100-500 and a 2-point crossover probability of 0.85 were employed. The steady-state replacement strategy (SSGA) with the mutation rate is inversely proportional with number of parameters and the maximum number of GA iterations of 400 was used. The optimization strategy in Figure 2-1 includes three stages starting from pure elements and their binary oxides. The obtained parameters were then combined without any change of developed parameters for the relevant binary systems to train the new parameters in ternary oxides. After that the last parameters were fitted for quaternary oxides.

The training set containing the molecular structures, energies, and bond dissociation energies were used to train this ReaxFF. For Fe/Fe_xO_y system, the Fe (bcc), FeO, Fe_3O_4, and Fe_2O_3 crystals and the dissociation of Fe–O bond in $Fe(OH)_6$ cluster were chosen (Figure C-1), while the bcc and hpc Na, NaO_3, NaO_2, Na_2O crystals and the dissociation of Na–O bond in Na_2O cluster (Figure C-2), as well as the crystalline structures of black and white P, P_2O_5, P_2O_3, and P_4O_7 (Figure C-3), were applied for Na/Na_xO_y and P/P_xO_y systems, respectively. For ternary oxides, the crystalline structures of $NaPO_3$, $Na_4P_2O_7$, and $Na_5P_3O_{10}$ were applied for Na/P/O system (Figure C-4), while the $Fe_2P_2O_7$ and $Fe_3P_4O_{14}$ crystals, as well as $NaFeO_2$ were adopted for Fe/P/O and Fe/Na/O systems, respectively (Figure C-5). Finally, the $NaFeP_2O_7$ and $NaFePO_4$ crystals were applied for quaternary oxides (Figure C-5).

The validating process was implemented using the lattice parameters, mass density, ΔH_f,

and atomic charges and compared with previous ReaxFFs, as well as QM calculation. Moreover, the structural relaxation and atomistic charges of Fe_2O_3(0001) surface were considered as it was a critical surface material in this work. Additionally, the molecular properties such as the P–O and P=O bonds, O–P–O and O–P=O angles of H_3PO_4 acid, the P–O_b–P angle, as well as P–O_b–P–O and P–O_b–P=O dihedrals of $H_4P_2O_7$ acid were validated to check the transferability of this force field for molecules. In inorganic compounds, the electrostatic interaction is dominant among various interactions between atoms. The net atomic charges were also evaluated to validate the current ReaxFF. The reference atomic charges were evaluated from QM calculation using a Density Derived Electrostatic and Chemical (DDEC6) method.[251]

The cohesive (E_{coh}) and the energies (E_0) of different crystalline structures,[154] as well as the dissociation energies of Fe–O, Na–O, and P–O bonds were employed as the training sets. E_{coh} was calculated using the expression:

$$E_{coh} = E_{atom} - \frac{E_{bulk}}{N} \qquad (5.2)$$

with E_{bulk} and E_{atom} are the total energies of bulk and individual atom, respectively, and N is the number of atoms in the units cell. In contrast, the energy E_0 was calculated for oxide compounds and imposed as an energy cost function expression with respect to the energy level of their constituent elements. For example, the energy E_0 of Fe_2O_3 was calculated by the following formula:

$$E_0 = E_{Fe_2O_3} - 2E_{Fe} - 3E_O \qquad (5.3)$$

with E_{Fe} and E_O are the energies of isolated Fe and O atoms, respectively. To validate the developed ReaxFF, ΔH_f was evaluated and compared with experimental results. It was imposed as an energy cost function expression with respect to the energy level of zero-ΔH_f compounds such as Fe (bcc), Na (bcc), white P_4 crystals, and O_2 in gas.[301] For instance, ΔH_f of Fe_2O_3 was calculated as following formula:

$$\Delta H_f = E_{Fe_2O_3} - 2E_{Fe(bcc)} - \frac{3}{2}E_{O_2} \qquad (5.4)$$

The initial parameters for Fe/O, Na/O, and P/O systems were taken from the work by Aryanpour et al.,[301] Kim et al.,[304] and Shin et al.[305]

The bulk modulus of crystals was evaluated to consider the mechanical properties of materials. The Birch-Murnaghan function in expression 5.5, which is based on the pressure expansion of bulk modulus, was used to fit the equation of state (EoS).[306]

$$\mathrm{E(V)} = E_0 + \frac{9B_0V_0}{16}\left(\left(\frac{V}{V_0}\right)^2 - 1\right)^2\left(6 + B_0'\left(\left(\frac{V}{V_0}\right)^2 - 1\right) - 4\left(\left(\frac{V}{V_0}\right)^2 - 1\right)^2\right) \quad (5.5)$$

where E_0, B_0, V_0, and B_0' are total energy at ground state, bulk modulus, volume of crystal at ground state, and pressure derivative of B_0, respectively. In this work, the relative energy between a certain state and ground state (E(V) - E_0 or dE) was considered for EoS, so that only the B_0, V_0, and B_0' parameters were fitted. The compressed or extended crystalline structures in ReaxFF calculations were obtained from QM calculations for this EoS calculation. The compressed or extended volume is varied between 0.67 to 1.42 times the equilibrium one; this range corresponds to the change of lattice parameters from 0.875 to 1.125 times of their equilibrium values, and includes 11 volume samples with a scale increment of 0.025 in lattice parameters. Due to the accuracy of the force field development, all energy values are reported in kcal/mol.

5.2.4 MD simulation

An MD simulation using the LAMMPS code was performed to validate the current ReaxFF at 1100 K and apply this force field to confined shear model to investigate the tribological performance of sodium polyphosphate lubricant at elevated temperature. Additionally, this code was also used to validate the lattice cell parameters, density at ground state, and energies for current force field and other references.

NVT at 1100K

In this MD simulation, a lattice structure of 9.23×5.31×13.35 $Å^3$ of $Na_4P_2O_7$ was adopted to validate the transferability of developed ReaxFF at temperature of 1100 K. The temperature was controlled by Nosé-Hoover canonical (NVT) ensemble with a temperature-damping constant of 100 fs and time step of 0.25 fs. The periodic boundary condition was applied in all directions. The radial distribution function g(r) was evaluated to measure the relative distances of atomic pairs in sodium polyphosphate and compared with reference data from our QM calculations.

Confined shear NEMD simulation

The tribo-surfaces of Fe_2O_3(0001) were implemented to investigate the influence of loading pressure on hierarchical structure and tribological performance of IAP lubricant, which was constructed by 72 $Na_4P_2O_7$ molecules. The simulated system had a domain size of approximately 35×35×50 $Å^3$ and was periodic in the lateral directions as shown schematically in Figure 5-1. The system was aperiodic in the normal direction. Each

surface was approximately 10 Å thick, and created by cleaving from its regular crystalline structure. The outer layer of surface was constrained whereas the inner one was relaxed. ReaxFF was applied for considered system, and a bond order cutoff of 0.3 was set to detect the short-lived intermediates and track the reaction phenomena, as well as their products.

The simulation included three stages: i) the system was thermostated at 300K by Nosé-Hoover canonical (NVT) ensemble for 50 ps to relax the structure. After that the temperature was increased up to 1100 K for 75 ps. The outer layer of each surface was constrained during this simulation stage. ii) A load was applied to the top boundary for the next 250 ps to compress the model at 1100 K. A high pressure of 0.5 GPa was applied because it is usually found in practical applications of rolling, metal forming, bearings, and others. The bottom outer surface layer was constrained, while the upper one was allowed to move in the applied-pressure direction. iii) The surfaces moved in opposite directions with a sliding velocity of 10 m/s, while the applied load remained in this shearing stage. Note that only the surfaces were thermostated while the lubricant temperature was free to evolve using an NVE ensemble in the second and third stages.

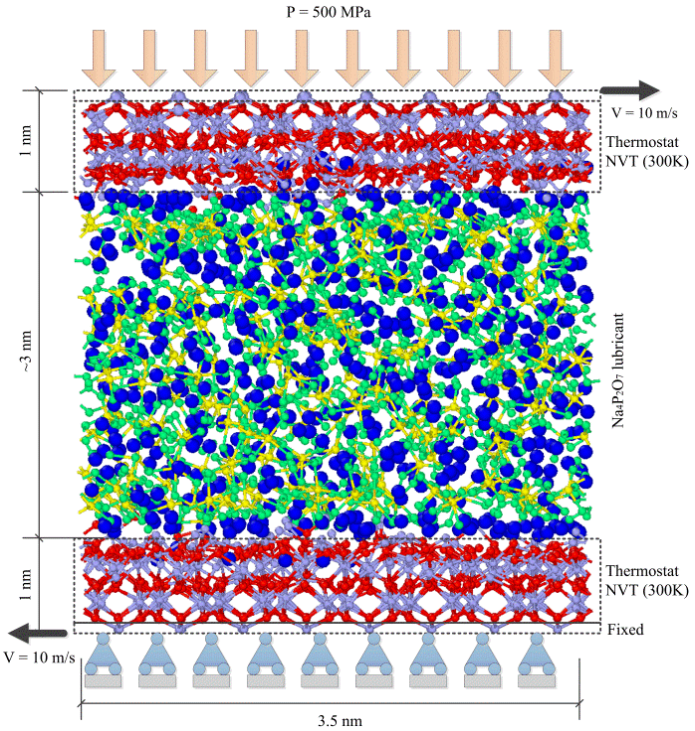

Figure 5-1. Snapshot of molecular model of sodium polyphosphate lubricant confined between Fe_2O_3(0001) surfaces under a pressure of 0.5 GPa at 1100K. Purple, red, green, blue, and yellow colours represent the Fe, O in surface, O in lubricant, Na, and P, respectively.

5.3 Results

5.3.1 Fe/O system

EoS of Fe (bcc) and iron oxides, as well as Fe–O bond dissociation, in Figure 5-2, show the current ReaxFF represents the QM results much better than ReaxFF from Aryanpour et al. which produces significant errors. These errors were calculated from experimental data. Particularly, there are small errors within 2 kcal/mol for cohesive energy of Fe (bcc), and the predicted cohesive energy (E_{coh}) of 117.83 kcal/mol at ground state with the current ReaxFF is close to the value of 115.92 kcal/mol obtained from QM calculation. In contrast, their ReaxFF underestimates this value with the cohesive energy of 103.43 kcal/mol/atom (error -11%).

For iron oxides, the discrepancies between two ReaxFFs can be observed clearly in Figure 5-2a where E_0 of -254.15 kcal/mol is found for FeO for current one, and this value is closer to the QM value of -235.62 kcal/mol than Aryanpour's ReaxFF with -310.75 kcal/mol. Similarly, the respective E_0 values of -851.75 and -586.26 kcal/mol were evaluated for Fe_3O_4 and Fe_2O_3 from current ReaxFF are also closer to the QM values of -848.37 and -604.38 kcal/mol, respectively. These energies are much smaller than the corresponding E_0 values of -1084.65 and -765.03 kcal/mol obtained from their ReaxFF. These data indicates that the current ReaxFF improves significantly E_{coh} of pure iron and the E_0 values of iron oxides.

The overestimation of E_0 obtained from previous ReaxFF developed by Aryanpour et al.[301] could be due to the overestimation of dissociation energy of Fe–O bond presented in Figure 5-2b. In fact the dissociative energy of 30.67 kcal/mol was found for current ReaxFF, which is only 4 kcal/mol larger than the QM calculation of 26.81 kcal/mol. These dissociation energies are much smaller than the value of 50.96 kcal/mol calculated from their ReaxFF. The overestimation of their ReaxFF compared with current QM calculation is as a result of using B3LYP level of theory in Gaussian03, which predicted a larger dissociative energy of Fe–O bond than GGA-PBE function in VASP.[301]

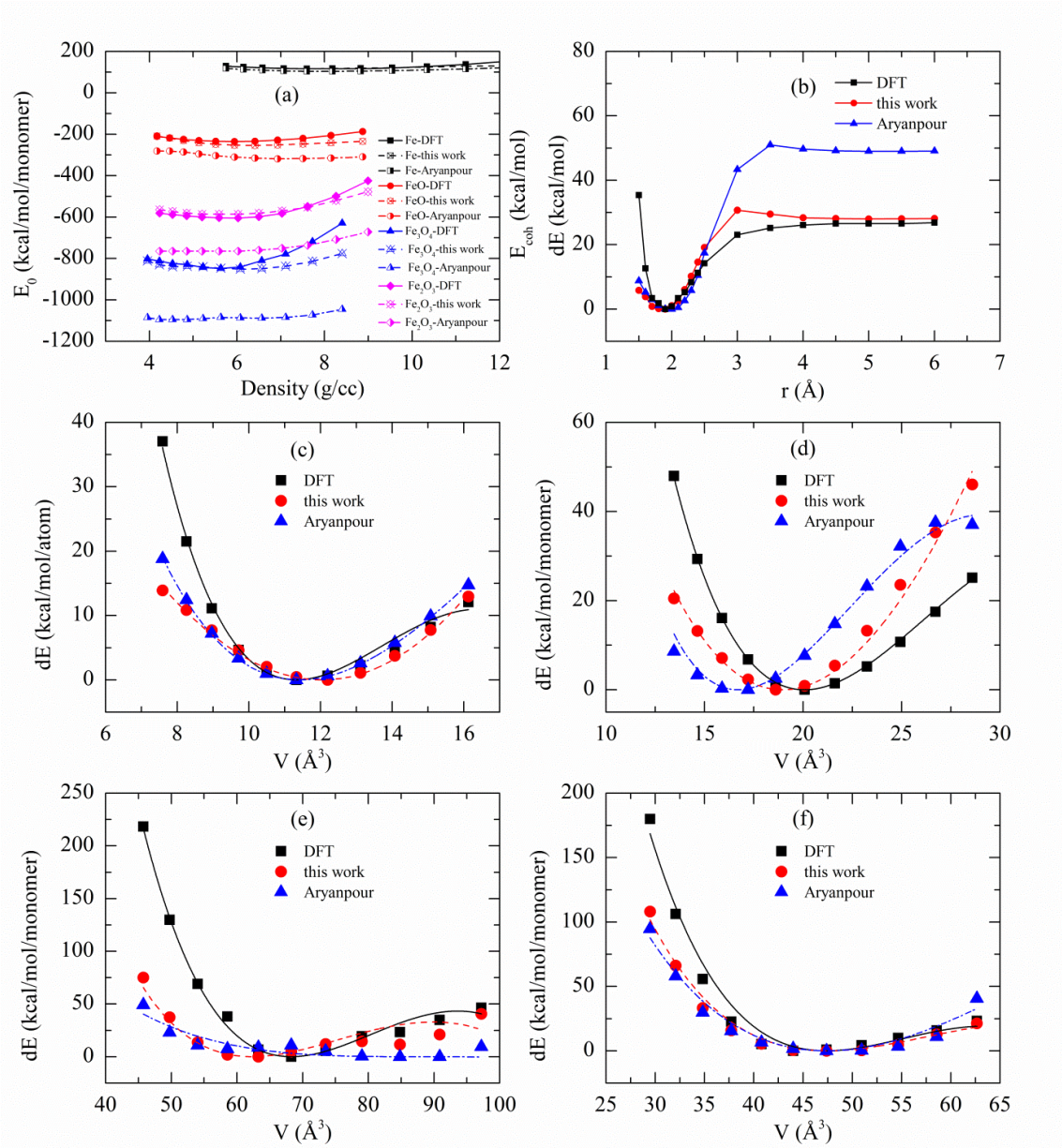

Figure 5-2. (a) E_{coh} of bcc Fe and E_0 of FeO, Fe_3O_4, Fe_2O_3; and (b) dissociation energies of Fe–O bond in $Fe(OH)_6$ cluster; and comparisons EoS of: (c) bcc Fe; (d) FeO; (e) Fe_3O_4; and (f) Fe_2O_3.

The mechanical property of iron and iron oxides has also been considered by evaluating their bulk modulus. The EoS comparison of bcc Fe in Figure 5-2c shows an agreement between the current ReaxFF and QM calculation for equilibrium volume, but the fitted bulk modulus of 129.43 GPa from this work is smaller than the values of 229.82, 152.40, and 171 GPa respectively from QM calculation, Aryanpour's ReaxFF, and experiment.[307] For wüstite, Figure 5-2d shows that the equilibrium volumes obtained from both ReaxFFs are smaller than the QM. Current ReaxFF provides a bulk modulus of 168.40 GPa, which is closer to the experimental value of 154 GPa [308] than QM with

192.35 GPa and Aryanpour's ReaxFF with 215.55 GPa. For magnetite, Figure 5-2e shows a similar trend that both ReaxFFs underestimate the equilibrium volumes of QM calculation, and the bulk modulus of 129.00 GPa from current work is smaller than the values of 185.7 GPa [309] and 214.18 GPa obtained respectively from the experiment and QM calculation. For hematite, Figure 5-2f shows that both ReaxFFs predict properly the equilibrium volume but they underestimate the bulk modulus. The fitted value of 110.17 GPa from the current work is close to the calculated value of 125.27 GPa from the referenced ReaxFF by Aryanpour et al. However, these values are smaller than the values of 230 GPa [310] and 162.16 GPa from the experiment and QM calculation, respectively. To validate this new ReaxFF, ΔH_f and crystalline structure were adopted, and Table 5.3 indicates that the current ReaxFF shows an E_{coh} value of 117.83 kcal/mol for Fe (bcc) with a difference of 19% from experiment. In addition, the current ReaxFF shows a good agreement with current QM calculation with an error of only 2%. Moreover, the current ReaxFF predicts ΔH_f of iron oxides much better than the referenced ones evaluated by Aryanpour's ReaxFF.[301] In fact the errors of 14%, -6%, and -13% were calculated for FeO, Fe_3O_4, and Fe_2O_3 using current ReaxFF, while the much larger errors of 136%, 103%, and 93% have been found for referenced one for these compounds, respectively. The QM calculation overestimates significantly the experimental results with the corresponding errors of -136%, 103%, and 93%.

Table 5.1. Average atomic charge of O and Fe in iron oxides obtained from current ReaxFF and QM calculation

Compounds	Atom	This work (err)	Aryanpour et al. (err)	DFT
		e (%)	e (%)	e (%)
FeO	O	-0.774 (1%)	-0.817 (7%)	-0.763
	Fe	0.774 (1%)	0.817 (7%)	0.763
Fe_3O_4	O	-0.727 (2%)	-0.695 (-2%)	-0.712
	Fe	0.970 (2%)	0.927 (-2%)	0.949
Fe_2O_3	O	-0.642 (-2%)	-0.695 (6%)	-0.655
	Fe	0.963 (-2%)	1.042 (6%)	0.983

For structural properties, the lattice constants in Table 5.1 and density in Table 5.2 show very small errors within 4% from the current ReaxFF, while the larger errors up to 9% have been found for lattice constants and -22% for density of Fe_3O_4 from previous force field.[301] Except for Fe (bcc), which shows a very small error within -1%, the lattice constants and density of other iron oxides obtained from Aryanpour's ReaxFF show much larger errors than those in this paper. The QM calculation tends to underestimate the unit

cells of these crystals; as a consequence, it overestimates their densities with the errors within 10%.

Table 5.2. Average atomic charge of elements in Na and sodium oxides obtained from current ReaxFF and QM calculation

Compounds	Element	This work (err)	Kim et al. (err)	DFT
		e (%)	e (%)	e (%)
Na_2O	Na	0.601 (-23%)	0.648 (-17%)	0.783
	O	-1.202 (-23%)	-1.297 (-17%)	-1.565
NaO_2	Na	1.093 (27%)	1.148 (34%)	0.859
	O	-0.364 (-15%)	-0.383 (-11%)	-0.429
NaO_3	Na	1.068 (34%)	1.207 (52%)	0.796
	O	-0.534 (102%)	-0.603 (128%)	-0.265

Results of atomic charges are presented in Table 5.1, which shows the respective charges of 0.774 and -0.774 for each Fe and O element in relaxed FeO crystal. These values are only 1% larger than the QM calculations, while a larger error of 7% has been found for ReaxFF from Aryanpour et al. For Fe_3O_4, both ReaxFFs show similar small errors of 2%, but there is an overestimation for current ReaxFF, while this is an underestimation of their force field. Similar with FeO, the current ReaxFF also shows a better prediction of atomic charges for Fe_2O_3 with the small error of only 2% compared with 6% obtained from their ReaxFF. These results indicate that the current model predicts properly the Coulombic interaction for different iron oxides.

Table 5.3. Comparison of $E_{coh}/\Delta H_f$ of different compounds

Compounds	This work (err)	Other ReaxFF (err)	References
	kcal/mol	kcal/mol	kcal/mol
Fe (bcc)	117.83 (19%)	103.44 (5%)[a]	98.64[b]
FeO	-74.37 (14%)	-153.24 (136%)[a]	-65.02[c]
Fe_3O_4	-250.77 (-6%)	-543.35 (103%)[a]	-267.90[c]
Fe_2O_3	-172.24 (-13%)	-380.93 (93%)[a]	-197.30[c]
Na (bcc)	25.69 (0%)	23.11 (-10%)[d]	25.57[b]
Na (hpc)	25.44 (1%)	23.97 (-6%)[d]	25.57[b]
NaO_3	-61.42	-50[d]	-
NaO_2	-122.85	-88.68[d]	-
Na_2O	-83.01 (-16%)	-83.55 (-15%)[d]	-98.75[c]
white P	89.95 (12%)	1.47 (-98%)[e]	79.11[c]

black P	102.40 (23%)	1.51 (-98%)[e]	79.11[c]
P_2O_5	-381.02 (7%)	-545.23 (53%)[e]	-356.00[c]
P_2O_3	-367.34	-479.91[e]	-
P_4O_7	-715.26	-1027.53[e]	-
$NaPO_3$	-336.90 (15%)	-	292.87 ± 0.5[f]
$Na_4P_2O_7$	-880.50 (15%)	-	-763.7 ± 1[f]
$Na_5P_3O_{10}$	-1218.18 (16%)	-	-1053.99[g]

[a]Data calculated using ReaxFF by Aryanpour et al.[301]
[b]Data obtained from Kittel.[311]
[c]Data obtained from Chase et al.[312]
[d]Data calculated using ReaxFF by Kim et al.[304]
[e]Data calculated using ReaxFF by Shin et al.[305]
[f]Experimental data by Irving et al.[313]
[g]Experimental data by La Iglesia[314]

As this work aims to investigate the behavior of sodium polyphosphate lubricant on Fe_2O_3(0001) surface, the interfacial properties of this surface was also studied. The oxide-scale structure developed on commercial hot-rolled steel strip at high coiling temperatures in range from 610° to 720° comprised of a thick layer of hematite (3-5 µm) was observed at the edge regions of the strip.[22] In addition, the experiment works revealed that the facet (0001) was the most stable surface configuration of hematite.[219] A static relaxation of Fe_2O_3(0001) surface was carried out and the obtained results are presented in Figure 5-3, which shows a good agreement in the order of atomic layer of Fe-O_3-Fe- at the interface between QM and current ReaxFF calculations. There is an inward relaxation for the first and the third layers, while an outward has been observed for the second and the fourth layers for both current ReaxFF and QM's calculations. The interlayer relaxations of relative distance of nine outer layers of -2%, 22%, -40%, 13%, -15%, 24%, -21%, 10%, and -13% compared with the associated bulk values have been found from current ReaxFF. The larger inward relaxation of -54% was obtained for the first layer in QM calculation, while a smaller outward of 9% was observed for the second layer. Interestingly, the relaxation from reactive MD and QM calculations confirms those obtained from the literature, in particular, there is an inward relaxation of the first, third layers while a distance extension is found for the second and fourth layers.[219, 220, 315, 316]

The surface energy (γ) is defined as the surface excess energy per unit area of a surface, $\gamma = (E_{surf} - E_{bulk})/A$, where E_{surf} and E_{bulk} are the energies of the surface and the bulk containing an equivalent number of ions, respectively, while A is the surface area.[317]

The calculated γ value of 1.719 J/m^2 is close the value of 1.7 J/m^2 from DFT calculation using PW91 functional, GGA and GGA+U by Rohrbach et al.,[318] but the current result is larger than the values of 1.01 and 1.145 J/m^2 from PBE functional calculated by Trainor et al.[219] and Guo et al.,[319] respectively.

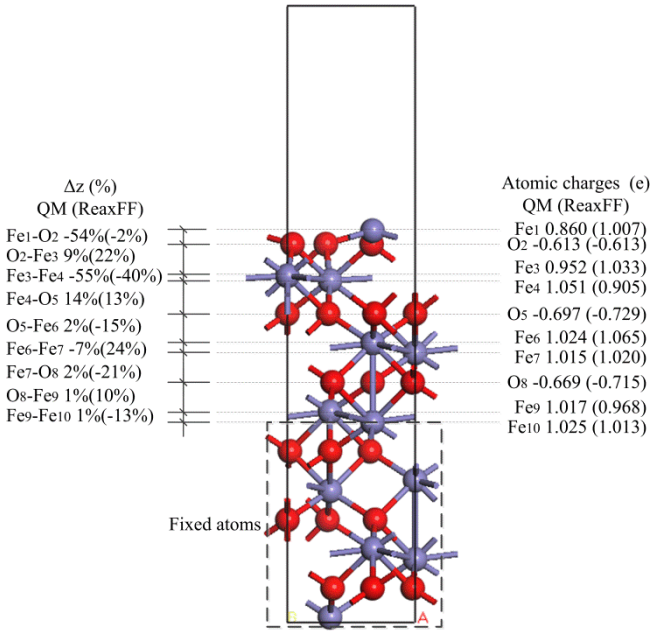

Figure 5-3. Comparisons of relaxed atomic structure and net atomic charges of Fe_2O_3(0001) surface between QM and reactive MD calculations.

Figure 5-3 also reveals that the relaxation not only yields to the changing in atomic structure at the interface but it also leads to the changing in the net atomic charges. There is a reduction of atomic charge for the interfacial atoms compared with that in the inner layers. In particular, the respective charges for Fe in the first layer and O in the second layer are +0.86 e and -0.613 e for QM's calculation, which are smaller than that evaluated from bulk structure in Table 5.1. Note that the current QM calculation of atomic charge shows a good agreement with previous QM calculation by Ta et al.,[220] where the charges of +0.772 e and -0.528 e have been found for outermost iron and oxygen atoms, respectively. A similar observation is found for current ReaxFF in which the corresponding charges of +1.007 e and -0.613 e have been found for these atoms. However, similar with the values given in Table 5.4, the charges obtained from the current ReaxFF are moderately larger than those evaluated from QM calculation. The largest discrepancy between the current reactive MD model and QM calculation is found to be 0.147e for the first Fe layer, but this reactive MD model still achieves a neutral-charge condition. Additionally, Ta et al. showed that a charge reduction of 0.115 e for this Fe

outermost layer resulted in only ~ 10% less adsorption energy of the hydrocarbon.[220] Therefore, the over charge of 0.147e from the current reactive MD model does not affect significantly the interaction between Fe_2O_3(0001) surface and sodium polyphosphate molecules.

Table 5.4. Average atomic charge of P_2O_5

Compounds	Element	This work	DFT	Error (%)
		e	e	e
P_2O_5	O	-0.683	-0.653	0.030 (5%)
	P	1.707	1.632	0.074 (5%)

5.3.2 Na/O system

The ReaxFF parameters for Na element and its oxide compounds were included in the works by Kim et al. for NaCl/water solution systems.[304] Unfortunately, their ReaxFF was unable to predict E_{coh} of bcc Na, and E_0 of some sodium oxides shows a significant underestimation compared with the reference data from QM calculation. In particular, no minimum cohesive energy was found in the considered range of density for bcc Na using this force field. For sodium oxides, the respective E_0 values at ground state of -257.54 and -191.71 kcal/mol for NaO_3 and Na_2O are much smaller than the values of -316.35 and -216.43 kcal/mol from the QM calculation. The underestimations for NaO_3 and Na_2O were -19% and -11%, respectively. In contrast, an overestimation of 15% was found for NaO_2. The underestimation of their ReaxFF could be explained by the shorter equilibrium distance and smaller dissociative energy of Na–O bond as shown in Figure 5-4.

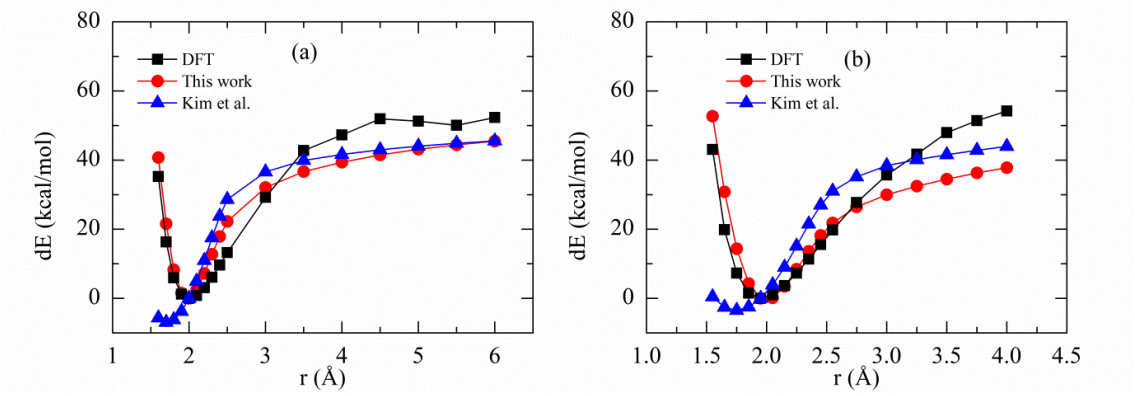

Figure 5-4. Dissociation energies of Na–O bonds in (a) Na_2O and (b) NaOH molecules.

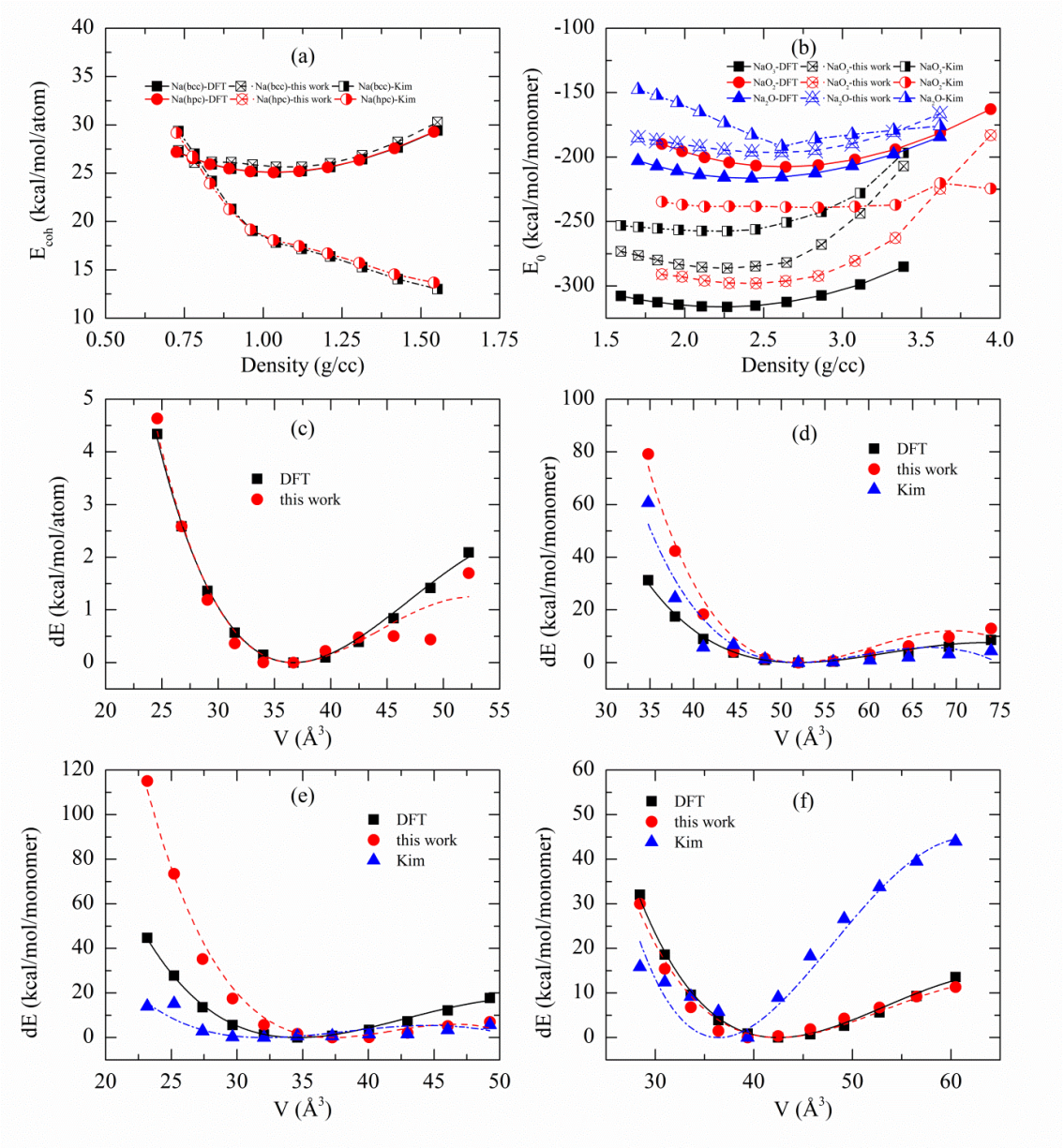

Figure 5-5. (a) Cohesive energy of Na (bcc); (b) E_0 of Na_2O, NaO_2, and NaO_3; EoS comparison of: (c) Na (bcc); (d) NaO_3; (e) NaO_2; and (f) Na_2O.

The better predictions E_{coh} of bcc Na and E_0 of different sodium oxides were observed for current ReaxFF in Figure 5-5a. In fact an E_{coh} value of 25.69 kcal/mol was calculated for bcc Na, which was consistent with the value of 25.07 kcal/mol obtained from QM calculation. For sodium oxides, as shown in Figure 5-5b, the E_0 values of -286.21 and -194.48 kcal/mol which corresponded to -10% and -9% respectively for NaO_3 and Na_2O, have been obtained. The error for NaO_3 is much smaller than aforementioned value from ReaxFF developed by Kim et al.[304] The dissociation energy curves of Na–O bonds in Figure 5-4 reveal that the current ReaxFF predicts very well the equilibrium distances. In

fact, the respective equilibrium bond distances of 2.0 Å and 1.95 Å were found for Na_2O and NaOH molecules using current ReaxFF, which were consistent with QM calculations. These values are larger than the corresponding values of 1.7 Å and 1.75 Å obtained from their ReaxFF. However, the dissociation energy of 45.53 kcal/mol evaluated from the current ReaxFF was 13% smaller than the value of 52.37 kcal/mol from the QM. A similar trend was observed for NaOH molecule where the dissociation energy of 37.81 kcal/mol was predicted by the current ReaxFF compared with 54.23 kcal/mol for QM calculation. The referenced ReaxFF predicted these energies better with 52.49 kcal/mol for Na_2O and 43.98 kcal/mol for NaOH molecules.[304]

A comparison of EoS for Na (bcc) in Figure 5-5c reveals that the current ReaxFF predicts well the energy gradients in compressive and expanding regimes. The fitted bulk modulus of 8.55 GPa is close to the QM result of 9.17 GPa. For NaO_3 and NaO_2, Figure 5-5d and e shows a good prediction of equilibrium volume for current and referenced ReaxFFs, but they overestimate the energy in the compressive regime. For Na_2O, Figure 5-5f shows an excellent prediction with small errors within only 3 kcal/mol by the current ReaxFF, while the referenced ReaxFF from Kim et al.[304] shows steeper descending curves at low and high densities. The calculated bulk modulus of 50.54 GPa obtained from current work is close to the QM value of 56.24 GPa, while their ReaxFF shows a much higher value of 128.06 GPa. These findings reveal that current ReaxFF predict properly the bulk modulus of sodium and disodium oxide. Unfortunately, these is no experimental bulk modulus for these compounds, phosphorus oxides, as well as the ternary oxides of sodium and phosphorus from the literature.

A comparison of lattice constants of different Na and sodium oxides between this work, QM calculation, and ReaxFF from Kim et al.[304] is shown in Table 5.5. There are small errors within 7% between current ReaxFF and QM. The current ReaxFF shows a better prediction of QM values with smaller errors than those obtained from their ReaxFF. In fact larger errors of -15%, -14% and 26% were found for bcc and hpc Na and NaO_2 crystals with Kim's ReaxFF. In addition, in comparison with previous experimental work for sodium by Aruja et al.[320] and Wyckoff et al.,[321] and different sodium oxides by Klein et al.,[322] Carter et al.,[323] and Wyckoff et al.,[321] both current ReaxFF and QM calculation show a good agreement.

The density at ground state is presented in Table 5.6, which shows a better prediction of current ReaxFF for sodium and sodium oxides. For instances, the errors of 11%, 4%, and 11% were calculated for bcc and hpc Na, and NaO_3 which were much smaller than the

corresponding errors of 75%, 63%, and 14% with ReaxFF from Kim et al.[304] However, an underestimate of density of -19% for NaO_2 predicted by current ReaxFF was larger than previous one (-10%). Both force fields predict very well the equilibrium density of Na_2O with an error of 5% and ~0% for this new and referenced ReaxFFs, respectively.

Moreover, Table 5.6 shows that the current ReaxFF predicts very well E_{coh} from experiments. The E_{coh} energies of 25.69 and 25.44 kcal/mol with respective small errors of 0% and 1% have been evaluated. These errors are significantly smaller than the values of -10% and -6% calculated with ReaxFF from Kim et al.[304] This table also indicates that current ReaxFF provides the ΔH_f of -83.01 kcal/mol for Na_2O, which is slightly smaller than the value of -83.55 kcal/mol using their ReaxFF. These values are -16% and -15% smaller than the experimental value of -98.75 kcal/mol.[312] Similar to Fe_xO_y system, ΔH_f calculated from QM using Equation 5.4 overestimated significantly the experimental values for sodium oxides.

Table 5.2 indicates that both current and referenced ReaxFFs underestimate the atomic charges of Na and O. Particularly, the corresponding charges of 0.601 e and -1.202 e have been evaluated for relaxed Na_2O crystal. These values are 23% smaller than the respective charges of 0.783 e and -1.565 e obtained from QM calculation, while Kim's ReaxFF predicts better with smaller errors of 17%. However, the current reactive model predicts the atomic charges of other oxide better than the reference force field. In fact the current ReaxFF provides the charges of 1.093 e and -0.364 e for Na and O in NaO_2 crystal with the corresponding errors of 27% and -15% compared with QM's results of 0.859 e and -0.429 e respectively. Larger errors up to 34% have been found for referenced force field. A similar observation was found for NaO_3, which show larger errors than the current ReaxFF.

Table 5.5. Comparison of lattice properties of different crystalline structures obtained from experiments, QM, and ReaxFF optimization

Crystal	a (Å)				b (Å)				c (Å)				α/β/γ (°)
	Expt.	QM	This work (err)	Other ReaxFF (err)	Expt.	QM	This work (err)	Other ReaxFF (err)	Expt.	QM	This work (err)	Other ReaxFF (err)	
[a] Fe (bcc)	2.86	2.83 (-1%)	2.89 (2%)	[e] 2.84 (0%)	2.86	2.83 (-1%)	2.89 (2%)	[e] 2.84 (0%)	2.86	2.8 (-1%)	2.89 (2%)	[e] 2.84 (0%)	90
[b] FeO	4.33	4.31 (0%)	4.23 (-2%)	[e] 4.06 (-6%)	4.33	4.31 (0%)	4.23 (-2%)	[e] 4.06 (-6%)	4.33	4.31 (0%)	4.23 (-2%)	[e] 4.06 (-6%)	90
[c] Fe_3O_4	8.32	8.17 (-2%)	7.93 (-3%)	[e] 8.87 (9%)	8.32	8.17 (-2%)	7.93 (-3%)	[e] 8.87 (9%)	8.32	8.1 (-2%)	7.93 (-3%)	[e] 8.87 (9%)	90
[d] Fe_2O_3	4.99	4.83 (-3%)	4.89 (-3%)	[e] 4.82 (-4%)	4.99	4.83 (-3%)	4.89 (-3%)	[e] 4.82 (4%)	13.5	13.34 (-1%)	13.33 (-3%)	[e] 13.14 (-4%)	90
[f] Na (bcc)	4.28	4.19 (-2%)	4.13 (-3%)	[k] 3.55 (-15%)	4.28	4.19 (-2%)	4.13 (-3%)	[k] 3.5 (-15%)	4.28	4.19 (-2%)	4.13 (-3%)	[k] 3.55 (-15%)	90
[g] Na (hcp)	3.77	3.70 (-2%)	3.69 (-2%)	[k] 3.17 (-14%)	3.77	3.70 (-2%)	3.69 (-2%)	[k] 3.17 (-14%)	6.15	6.22 (1%)	6.16 (0%)	[k] 5.33 (-14%)	90/90/120
[h] NaO_3	3.51	3.77 (7%)	3.39 (-3%)	[k] 3.36 (-11%)	5.77	5.22 (-10%)	5.58 (-3%)	[k] 5.52 (6%)	5.27	5.29 (0%)	5.10 (-3%)	[k] 5.05 (-5%)	90
[i] NaO_2	3.44	3.49 (1%)	3.70 (7%)	[k] 4.41 (26%)	5.54	5.54 (0%)	5.95 (7%)	[k] 5.73 (4%)	4.26	3.5 (-16%)	4.58 (7%)	[k] 3.56 (-1%)	90
[j] Na_2O	5.55	5.40 (3%)	5.44 (-2%)	[k] 5.40 (0%)	5.55	5.40 (-3%)	5.44 (-2%)	[k] 5.40 (0%)	5.55	5.40 (-3%)	5.44 (-2%)	[k] 5.40 (0%)	90
[l] white P	11.45	12.56 (10%)	12.56 (10%)	[q] 16.21 (42%)	5.5	5.93 (8%)	5.93 (8%)	[q] 7.65 (39%)	11.26	12.30 (9%)	12.30 (9%)	[q] 15.88 (41%)	71.7/90/71.3
[m] black P	3.32	3.37 (2%)	3.38 (2%)	[q] 4.26 (29%)	10.48	11.42 (9%)	10.67 (2%)	[q] 17.17 (64%)	4.38	4.58 (5%)	4.46 (2%)	[q] 8.17 (87%)	90/90/90
[n] P_2O_5	9.19	9.40 (2%)	9.51 (3%)	[q] 9.90 (8%)	4.89	5.07 (4%)	5.06 (3%)	[q] 5.27 (8%)	7.16	7.20 (0%)	7.41 (3%)	[q] 7.71 (8%)	90/90/90
[o] P_2O_3	6.43	6.84 (6%)	5.74 (-11%)	[q] 6.48 (1%)	7.89	8.74 (11%)	7.04 (-11%)	[q] 7.94 (1%)	6.81	7.02 (3%)	5.84 (-14%)	[q] 6.86 (1%)	90/105/90
[p] P_4O_7	9.81	10.16 (4%)	9.98 (2%)	[q] 9.95 (1%)	9.97	10.14 (2%)	10.14 (2%)	[q] 10.11 (1%)	6.85	7.88 (15%)	6.92 (1%)	[q] 6.95 (1%)	90/96/90
[r] $NaPO_3$	12.12	12.26 (1%)	12.54 (3%)	-	6.20	6.22 (0%)	6.29 (1%)	-	7.63	7.04 (-8%)	7.08 (-7%)	-	90/92/90
[s] $Na_4P_2O_7$	9.37	9.34 (0%)	9.45 (1%)	-	5.39	5.43 (1%)	5.44 (1%)	-	13.48	13.61 (1%)	13.59 (1%)	-	90
[t] $Na_5P_3O_{10}$	16.00	16.31 (2%)	16.90 (6%)	-	5.24	5.23 (0%)	5.34 (2%)	-	11.25	11.23 (0%)	11.44 (2%)	-	90/93/90
[u] $Fe_2P_2O_7$	4.47	4.40 (-2%)	5.63 (26%)	-	9.9	9.83 (-1%)	10.81 (9%)	-	5.21	5.18 (-1%)	5.64 (8%)	-	90/96.8/90
[v] $Fe_3P_4O_{14}$	8.95	8.87 (-1%)	9.94 (11%)	-	12.24	12.09 (-1%)	13.59 (11%)	-	10.17	9.89 (-3%)	11.30 (11%)	-	90
[w] $NaFeO_2$	3.06	2.96 (-3%)	3.19 (4%)	-	3.06	2.96 (-3%)	3.19 (4%)	-	16.24	15.34 (-5%)	16.56 (2%)	-	90/90/120

[x]$NaFeP_2O_7$	7.32	7.27 (-1%)	8.05 (10%)	-	7.90	7.76 (-2%)	8.65 (9%)	-	9.57	9.40 (-2%)	9.73 (2%)	-	90/111.5/90
[y]$NaFePO_4$	8.99	8.73 (-3%)	9.34 (4%)	-	6.87	6.58 (-4%)	7.14 (4%)	-	5.04	4.97 (-1%)	5.24 (4%)	-	90

[a] Experimental data by Wood et al.[324]
[b] Experimental data by Jette et al.[325]
[c] Experimental data by Bragg et al.[326]
[d] Experimental data by Rozenberg et al.[327]
[e] Data calculated using ReaxFF by Aryanpour et al.[301]
[f] Experimental data by Aruja et al.[320]
[g] Experimental data by Wyckoff et al.[321]
[h] Experimental data by Klein et al.[322]
[i] Experimental data by Carter et al.[323]
[j] Experimental data by Zintl et al.[328]
[k] Data calculated using ReaxFF by Kim et al[304]
[l] Experimental data by Simon et al.[329]
[m] Experimental data by Lange et al.[330]
[n] Experimental data by Stachel et al.[331]
[o] Experimental data by Jansen et al.[332]
[p] Experimental data by Jost et al.[333]
[q] Data calculated using ReaxFF by Shin et al.[305]
[r] Experimental data by Jost[259]
[s] Experimental data by Leung and Calvo [334]
[t] Experimental data by Cruickshank [209]
[u] Experimental data by Parada et al.[335]
[v] Experimental data by Ijjaali et al.[336]
[w] Experimental data by Persson [337]
[x] Experimental data by Gabelica-Robert et al.[338]
[y] Experimental data by Barpanda [339]

Table 5.6. Comparison of density of different crystalline structures obtained from experiments, QM, and ReaxFF optimization

Crystal	ρ (g/cc)			
	Expt.	QM	This work (err)	Other ReaxFF (err)
[a] Fe (bcc)	7.949	8.208 (3%)	7.728 (-6%)	[e]8.150 (-1%)
[b] FeO	5.888	5.960 (1%)	6.310 (6%)	[e]7.169 (20%)
[c] Fe_3O_4	5.357	5.649 (5%)	6.189 (10%)	[e]4.416 (-22%)
[d] Fe_2O_3	5.539	5.347 (-3%)	5.827 (9%)	[e]6.089 (14%)
[f] Na (bbc)	0.972	1.04 (7%)	1.079 (11%)	[k]1.700 (75%)
[g] Na (hcp)	1.010	1.033 (2%)	1.055 (4%)	[k]1.647 (63%)
[h] NaO_3	2.209	2.269 (3%)	2.448 (11%)	[k]2.520 (14%)
[i] NaO_2	2.249	2.536 (13%)	1.815 (-19%)	[k]2.031 (-10%)
[j] Na_2O	2.408	2.424 (1%)	2.557 (6%)	[k]2.424 (1%)
[l] white P	1.947	1.509 (-22%)	1.509 (-23%)	[q]0.701 (-64%)
[m] black P	2.703	2.335 (-14%)	2.563 (-5%)	[q]0.687 (-75%)
[n] P_2O_5	2.928	2.751 (-6%)	2.644 (-10%)	[q]2.345 (-20%)
[o] P_2O_3	2.185	1.800 (-18%)	3.200 (46%)	[q]2.138 (-2%)
[p] P_4O_7	2.350	1.938 (-18%)	2.249 (-4%)	[q]2.250 (-4%)
[r] $NaPO_3$	2.540	2.526 (-1%)	2.427 (-4%)	-
[s] $Na_4P_2O_7$	2.595	2.558 (-1%)	2.531 (-2%)	-
[t] $Na_5P_3O_{10}$	2.596	2.559 (-1%)	2.374 (-9%)	-
[u] $Fe_2P_2O_7$	4.150	4.265 (3%)	2.783 (-33%)	-
[v] $Fe_3P_4O_{14}$	3.073	3.225 (5%)	2.244 (-27%)	-
[w] $NaFeO_2$	4.199	4.757 (1%)	3.778 (-10%)	-
[x] $NaFeP_2O_7$	3.257	3.401 (4%)	2.665 (-18%)	-
[y] $NaFePO_4$	3.706	4.046 (9%)	3.302 (-11%)	-

[a] Experimental data by Wood et al.[324], [b] Experimental data by Jette et al.[325]
[c] Experimental data by Bragg et al.[326], [d] Experimental data by Rozenberg et al.[327]
[e] Data calculated using ReaxFF by Aryanpour et al.[301]
[f] Experimental data by Aruja et al.[320], [g] Experimental data by Wyckoff et al.[321]
[h] Experimental data by Klein et al.[322], [i] Experimental data by Carter et al.[323]
[j] Experimental data by Zintl et al.[328], [k] Data calculated using ReaxFF by Kim et al[304]
[l] Experimental data by Simon et al.[329], [m] Experimental data by Lange et al.[330]
[n] Experimental data by Stachel et al.[331], [o] Experimental data by Jansen et al.[332]
[p] Experimental data by Jost et al.[333], [q] Data calculated using ReaxFF by Shin et al.[305]
[r] Experimental data by Jost [259], [s] Experimental data by Leung and Calvo [334]
[t] Experimental data by Cruickshank [209], [u] Experimental data by Parada et al.[335]
[v] Experimental data by Ijjaali et al.[336], [w] Experimental data by Persson [337]
[x] Experimental data by Gabelica-Robert et al.[338], [y] Experimental data by Barpanda [339]

5.3.3 P/O system

Before applying the available ReaxFFs for P/O systems, a test was carried out to check their transferability for phosphorus oxide crystals. To the best of our knowledge from literature, there were two available ReaxFFs for this system which were developed by Zhu et al.[299] in 2008 and Shin et al.[305] in 2018. The bond dissociation, bending angle, and dihedral energies of H_3PO_4, $H_4P_2O_7$, P_4O_{10}, and EoS of black and white P and P_xO_y crystals were calculated and presented in Figures 5-6, 5-7 and 5-8 in which the properties of phosphorus acids predicted by Zhu's ReaxFF were better than those obtained from Shin's ReaxFF. In contrast, Zhu's work predicted improperly the EoS of phosphorus oxides, while the other showed a better prediction. Unfortunately, Shin's ReaxFF was unable to predict E_{coh} of white P, which has zero-ΔH_f in practice. As the cohesive energy of white P is the referenced compound for calculating of ΔH_f of phosphorus compounds using Equation 5.4, the parameters of current ReaxFF for P/O were retrained to improve this property and updated the properties of phosphorus oxides as well as phosphorus acids.

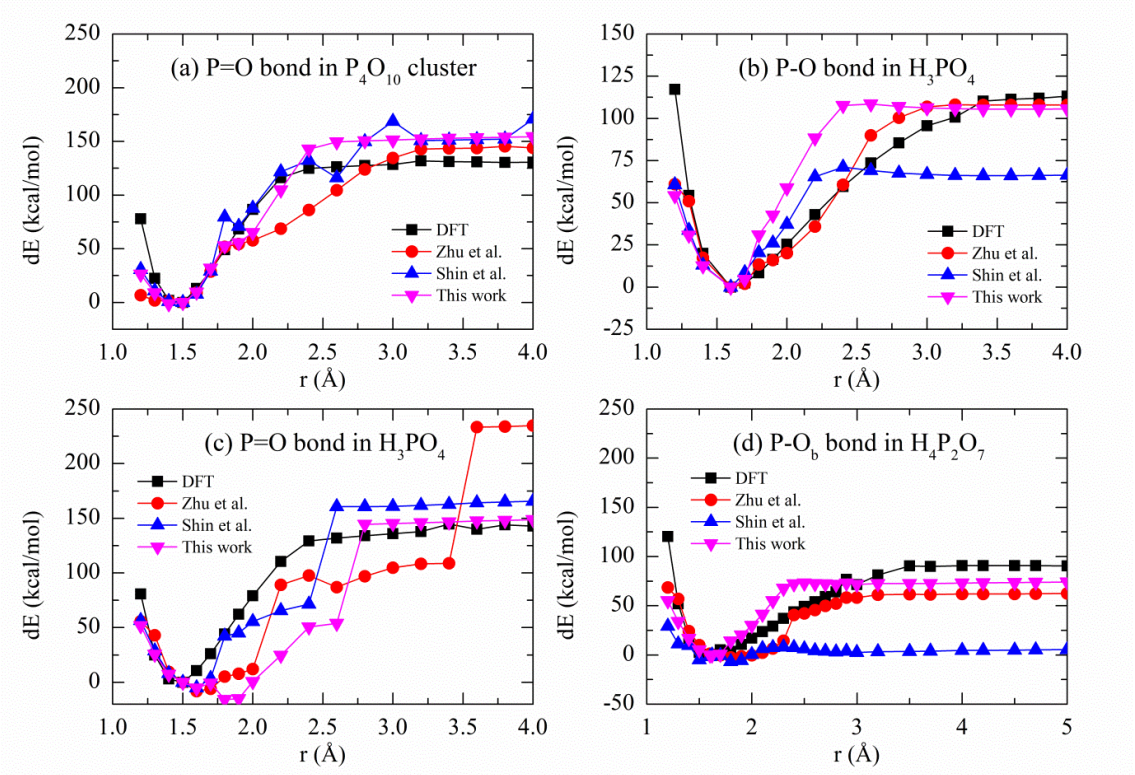

Figure 5-6. Comparisons of bond dissociation of energies of (c) P=O bond in P_4O_{10} cluster; (d) P–O and (e) P=O bonds in H_3PO_4; and (f) P–O bond in $H_4P_2O_7$ between QM calculation and different ReaxFFs.

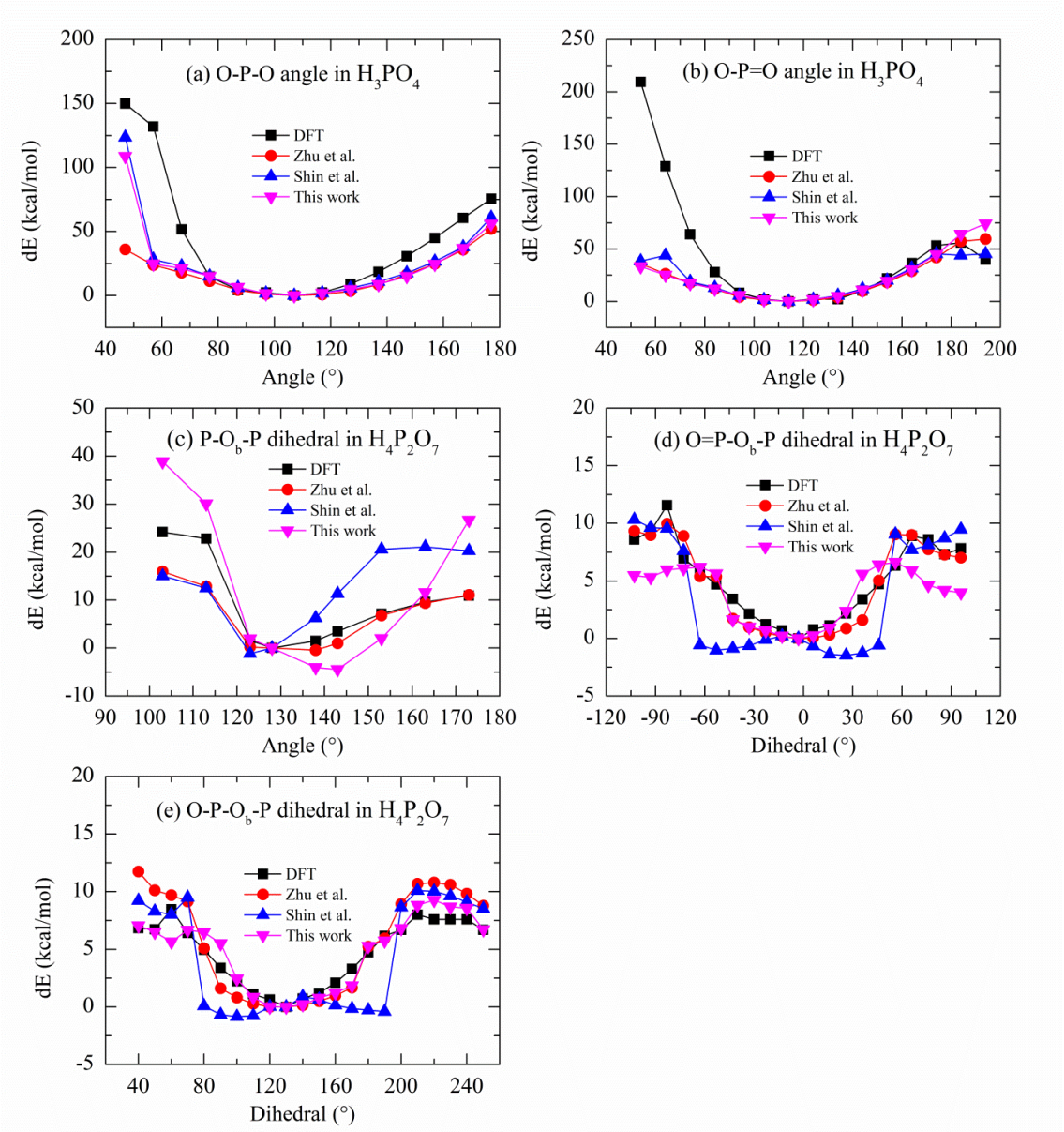

Figure 5-7. Comparisons of energies of (a) O–P–O and (b) O–P=O angles in H_3PO_4; (c) P–O_b–P angle, (d) O=P–O_b–P, and (e) O–P–O_b–P dihedrals in $H_4P_2O_7$

The comparisons of E_{coh} for white P and E_0 for phosphorus oxides between fitted results and those obtained by using referenced ReaxFF with QM calculation are presented in Figure 5-8 which shows the consistent curves of cohesive energies of current ReaxFF and QM. Table 5.3 shows that the respective cohesive energies for white and black P are 91.85 and 102.40 kcal/mol from the current force field at ground state. These values are 16% and 29% larger than the QM value of 79.11 kcal/mol. In contrast, the referenced ReaxFF from Shin et al.[305] provides the corresponding cohesive energies of 1.47 and 1.51 kcal/mol, which underestimate significantly the QM data, and there is no ground state observed for white P using this ReaxFF.

For phosphorus oxides, Figure 5-8 indicate that the current potential shows a better prediction of E_0 and dE for P_2O_5, but it overestimates these energies larger than ReaxFF developed by Shin et al.[305] for other oxides. Figure 5-8a shows P_2O_5 has a minimum energy value of -862.51 kcal/mol at density of 2.56 g/cm^3, which is only -1% different from -869.60 kcal/mol obtained from QM calculation. This error is much smaller than that of -13% evaluated from their force field. However, the respective minimum energies of -685.35 kcal/mol and -1463.04 kcal/mol calculated from current potential for P_2O_3 and P_4O_7 are 19% and 12% larger than those evaluated from QM. The corresponding errors 9% and 5% from their force field are smaller than the current work.

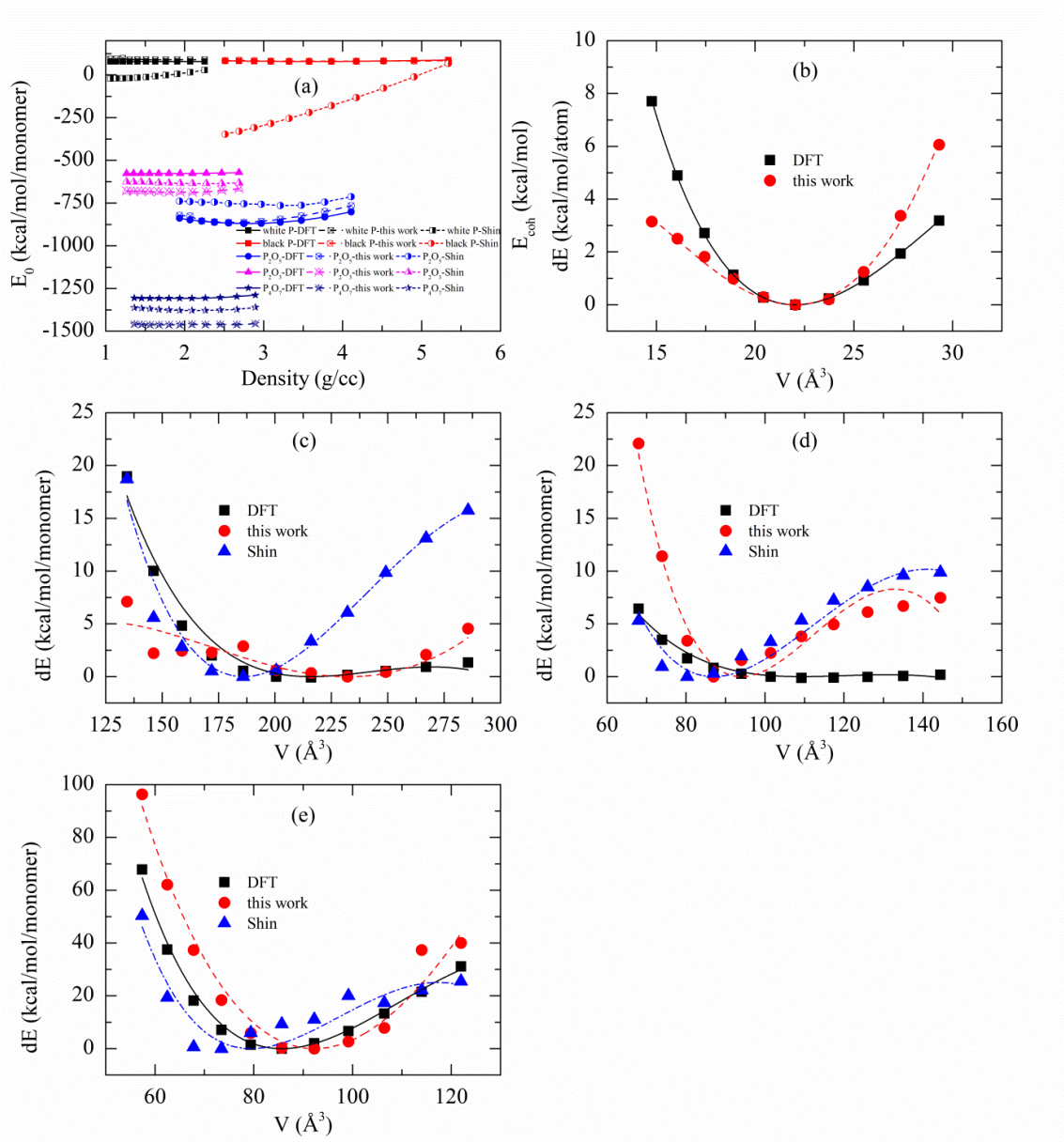

Figure 5-8. E_{coh} of white P and E_0 of different phosphorous oxides; and EoS comparisons of: (b) black P; (c) P_4O_7; (d) P_2O_3; and (e) P_2O_5.

Figure 5-8b indicates that the current ReaxFF is able to predict the EoS of black P. However, it provides higher energy gradients in expanding regime and smaller energy gradients in a compressing regime. The calculated bulk modulus of 28.68 GPa from developed ReaxFF is close to the current QM calculation with 29.39 and 28 GPa from the theoretical work by Chihi et al.[340]. For phosphorus oxides, Figures 5-8c-e show that both current and referenced ReaxFFs show a better prediction for P_2O_5 and P_4O_7 than P_2O_3. In fact, the bulk modulus of 3.48 GPa for P_4O_7 from the current ReaxFF is close to the QM calculation of 3.12 GPa, while the force field from Shin et al.[305] shows an overestimation with 10.99 GPa. These ReaxFFs show a better prediction for P_2O_5 with the bulk modulus of 75.73 and 65.95 GPa calculated respectively for current and referenced ReaxFFs. These values are close to the QM result of 59.44 GPa. The results show that current ReaxFF can predict properly the mechanical property of black P, P_4O_7, and P_2O_5.

For crystalline structure, Table 5.5 reveals that the current force field predicts the lattice constants of white and black P much better than the referenced one[305] with respective errors within 10% and 2% compared with experiment, while ReaxFF developed by Shin et al.[305] predicted larger errors up to 42% and 29%. Consequently, as shown in Table 5.6, the larger errors of density of -64% and -75% have been found for these P crystals. The current ReaxFF improves these values with smaller errors of -23% and -5% for white and black P, respectively.

For phosphorus oxides, current work predicts the lattice parameters of P_2O_5 better than ReaxFF developed by Shin et al.[305] In fact, Table 5.5 shows the small errors within 3% for this oxide, which has larger errors up to 8% with their ReaxFF. However, the current force field shows smaller lattice parameters for P_2O_3 (-14%) than the referenced model (1%). Consequently, the density of this oxide is 46% higher than that in the literature,[332] while there is only -2% from Shin's ReaxFF. For P_4O_7, both ReaxFFs show an excellent prediction with the respective errors of lattice constants within 2% and 1% for current ReaxFF and the referenced one. As a result, there are small errors within -4% for both these force fields.

Interestingly, as shown in Table 5.3, the current ReaxFF shows an excellent prediction of E_{coh} for P and ΔH_f for phosphorus oxides. The errors of 12% and 23% have also been found for E_{coh} for white and black P, respectively. These values are much smaller than the -98% error calculated from Shin's ReaxFF [305]. Importantly, this table shows a small error of 7% for the heat of formation of P_2O_5 using current ReaxFF, while the referenced

one overestimated by 53%. To the best of our knowledge from literature, there is no ΔH_f for P_2O_3 and P_4O_7, but both ReaxFFs show a similar trend that ΔH_f of P_2O_3 is smaller than P_4O_7. This table also indicates that the current force field shows smaller ΔH_f and closer to experiment than ReaxFF developed by Shin et al.[305]

The average atomic charges for P and O elements in P_2O_5 were calculated to check the ability of prediction the electrostatic property of current ReaxFF for P/O system. Table 5.4 discloses that there are insignificant differences of atomic charge evaluated from this ReaxFF compared with QM calculation. These findings indicate that the developed ReaxFF for P/O system not only preserve the structural and electrostatic properties of phosphorus oxides, but it can also predict the cohesive energies and crystalline structure of pure P, as well as improve the heat of formation for P_2O_5 compared with Zhu's and Shin's ReaxFF s.[299, 305]

More importantly, to ensure that this new ReaxFF still preserves the chemical properties of acids molecules, the dissociations of P=O and P–O bonds, angles, and dihedrals were calculated and compared with QM data. Figure 5-6 shows all ReaxFFs provide the same equilibrium bond distance of 1.5 Å for P=O bond in P_4O_{10} (Figure 5-6a), but Zhu's results[299] shows the best prediction with dissociation energy of 144.07 kcal/mol and close to the QM calculation with 130.62 kcal/mol. Both current and Shin's ReaxFFs overestimate this dissociation energy with ~152.6 and ~156.4 kcal/mol, respectively. For P–O bond in H_3PO_4, Figure 5-6b reveals a similar order. However, all ReaxFFs underestimate the dissociation energy of this bond, but Zhu's potential still shows the best prediction with a dissociative energy of 108.0 kcal/mol, a little smaller than the value of 113.12 kcal/mol obtained from QM calculation. For other force fields, the current work shows a much better prediction with the dissociative energy of ~105.7 kcal/mol, which underestimates only -7% from QM result, compared with -41% for ReaxFF developed by Shin et al.[305] For P=O bond, Figure 5-6c shows that Zhu's force field provides the dissociation energy of 234.70 kcal/mol, which overestimates significantly the QM value of 142.9 kcal/mol. In contrast, other ReaxFFs show a better prediction with the dissociative energies of 165.7 (16%) and 146.6 kcal/mol (3%) for Shin's and current ReaxFFs, respectively. Finally, the bond between P and bridging O (O_b) in $H_4P_2O_7$ was considered, Figure 5-6d indicates that all ReaxFF underestimates the dissociation energy of this bond. In particular, the dissociation energies of 62.52 (-31%), 5.56 (-94%), and 72.8 kcal/mol (-19%) were evaluated for potentials obtained from Zhu et al.,[299] Shin et al.,[305] and in this work, respectively. These values are smaller than the QM result of

90.46 kcal/mol. These observations indicate that the current work predicts well the P=O bond in P_4O_{10}, as well as P–O and P=O bonds in H_3PO_4 and $H_4P_2O_7$.

The angle bending and torsion energies are also considered for these acids molecules and they are presented in Figure 5-7, which shows a good prediction of O–P–O (Figure 5-7a) and O–P=O (Figure 5-7b) angles in H_3PO_4 with all ReaxFFs. For P–O_b–P (Figure 5-7c), all ReaxFFs show a similar trend with QM calculation, but only Zhu's ReaxFF provides the best prediction with errors less than 5 kcal/mol. The similar observations are also found in Figure 5-7d-e for O=P–O–P and O–P–O–P dihedrals in $H_4P_2O_7$. It is noted that the current and Zhu's ReaxFFs predict properly the equilibrium angles and dihedrals of the acid molecules. Particularly, these ReaxFFs provided similar equilibrium angles of 107°, 114°, and 128° for O–P–O, O–P=O, and P–O–P angles, respectively, which show a good agreement with QM calculations.

5.3.4 Na/P/O system

Additional off-diagonal parameters for interaction between Na and P, as well as the Na–O–P angle were included in this system. Figure 5-9a shows that the current ReaxFF underestimates E_0 of sodium phosphorus oxides at low densities and overestimates it at high densities. The respective minimum E_0 values for $NaPO_3$, $Na_4P_2O_7$, and $Na_5P_3O_{10}$, crystals are -635.73, -1587.63, and -2220.13 kcal/mol which is within 6% larger than the corresponding values of -601.24, -1495.01, -2098.88, and -1806.71 kcal/mol obtained from QM calculation. This comparison shows that current ReaxFF predicts properly the energies of sodium phosphorus oxides.

Figures 5-9b-d shows that current ReaxFF overestimate the volumes at ground state of these sodium phosphorus oxides. The energy gradients obtained from current ReaxFF are larger than the QM calculation at small volume. To validate the new ReaxFF for Na/P/O system, ΔH_f was calculated and presented in Table 5.3, which shows a good agreement between the values from the current ReaxFF and experiments with the respective differences of 15%, 15%, and 16% for $NaPO_3$, $Na_4P_2O_7$, and $Na_5P_3O_{10}$ crystals. Note that the small differences of ΔH_f between current ReaxFF and experiments, as well as previous theoretical calculation show that this ReaxFF predicts very well the heat of formation of sodium phosphorus oxide crystals.

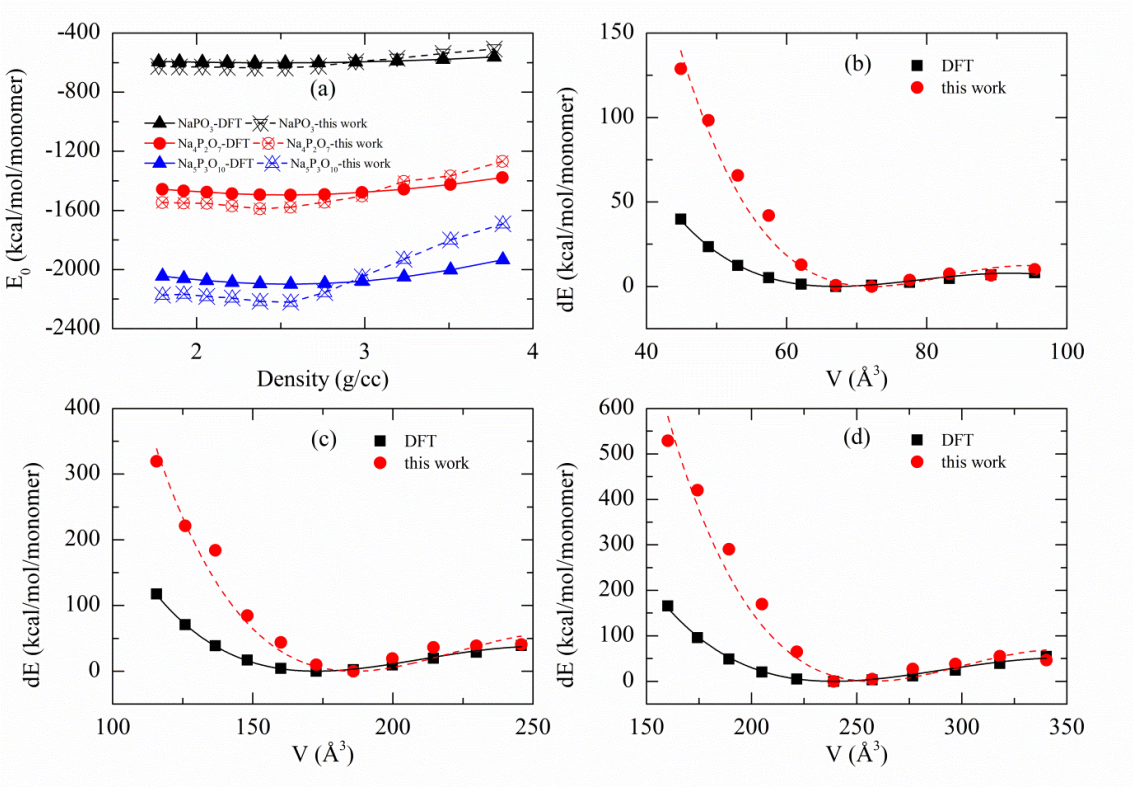

Figure 5-9. (a) Comparison of E_0 of different sodium phosphorous oxides, and EoS comparison of (b) $NaPO_3$; (c) $Na_4P_2O_7$; and (d) $Na_5P_3O_{10}$ between current ReaxFF and QM calculation

Tables 5.2 and 5.3 compare the density and lattice parameters at ground state obtained from current ReaxFF and QM calculations of different sodium phosphorus oxides. The densities obtained from QM calculation show small discrepancies within 1% compared with experiments, while the slightly larger differences up to 9% have been found for current ReaxFF. The smaller densities predicted from current ReaxFF are due to an overestimation of lattice constants. In fact this table indicates that all lattice parameters obtained from current ReaxFF are larger than those obtained from experiment and QM calculation with the errors within 3%, 1%, and 6% compared with experiment for $NaPO_3$, $Na_4P_2O_7$, and $Na_5P_3O_{10}$ crystals, respectively. Note that among of sodium phosphorus oxides, $Na_4P_2O_7$ shows the best prediction with smallest errors in lattice constants and density at equilibrium state.

Different dissociation paths of $Na_4P_2O_7$ molecule calculated previously by Le et al.[245] were also used to validate the current ReaxFF. Note that the energies were re-evaluated using geometry relaxation with the constraints of O_b–P bond between bridging oxygen with P in $–PO_x$ group and O–Na–O angles created by sharing Na ions between $–PO_x$ groups. Figure 5-10b indicates that the energy of 42.00 kcal/mol was obtained from

current ReaxFF when the P–O bond of isolated $Na_4P_2O_7$ cluster is extended to a distance of 2.717 Å and forms two PO_3 and PO_4 units sharing two Na ions, while the energy of 40.59 kcal/mol was calculated from previous QM calculation. A discrepancy of only 2% was found for this configuration. For configurations in Figure 5-10e where $Na_4P_2O_7$ is dissociated completely into two $NaPO_3$ and Na_3PO_4 structures, the current ReaxFF underestimates 24% the binding energies of this structure. An underestimations of -34% was found for $Na_4P_2O_7$ formed from two separate Na_3PO_3 and $NaPO_4$ structures in Figure 5-10c. When $Na_4P_2O_7$ is dissociated into two Na_2PO_3 and Na_2PO_4 structures (Figure 5-10d), an underestimation of -39% was found. Importantly, Figure 5-10 shows a good agreement of order of energy-paths, for example, Figure 5-10e has lowest energy difference compared with other dissociation paths in Figure 5-10c and d for both QM and ReaxFF.

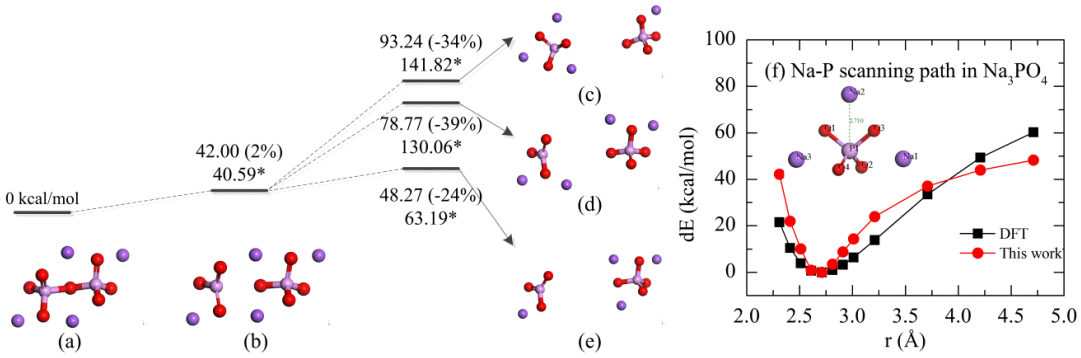

Figure 5-10. Comparison of dissociation energies of $Na_4P_2O_7$ molecule obtained from the current ReaxFF and previous QM results in units of kcal/mol. Asterisk (*) denoted the data obtained by Le et al.[245]. (a) $Na_4P_2O_7$ cluster, (b) PO_3 and PO_4 units sharing two Na ions, (c) Na_3PO_3 and $NaPO_4$ structures, (d) Na_2PO_3 and Na_2PO_4 structures, (e) $NaPO_3$ and Na_3PO_4 structures, and (f) scanning energy along Na-P path in Na_3PO_4 cluster. The energies are in kcal/mol.

A scanning energy along Na–P path in Na_3PO4 cluster was carried out and the results were presented in Figure 5-10f in which the trained ReaxFF shows a good prediction of equilibrium distance of 2.71 Å, but this force field overestimates the repulsive energies and underestimates the attraction between Na^+ cation and Na_2PO_4- anion. In fact the dissociation energy of 48.27 kcal/mol was found for this path from current ReaxFF; this value was 20% lower than the dissociation energy of 60.32 kcal/mol calculated from QM. This is the rationale behind the significant overestimation of dE for the Na/P/O systems for large densities.

5.3.5 Fe/P/O and Fe/Na/P/O systems

Finally, only the off-diagonal parameters for the interactions between Fe-P and Fe-Na pairwise, as well as the parameters for angles of Fe–O–P and Fe–O–Na were missing for Fe/Na/P/O system. The ternary oxides of $Fe_2P_2O_7$ and $Fe_3P_4O_{14}$ were used to train the P-Fe off-diagonal and Fe–O–P angular parameters, while a ternary oxide of $NaFeO_2$ was used to train the Na-Fe off-diagonal and Fe–O–Na angular parameters. Different EoS of quaternary oxides such as $NaFeP_2O_7$ and $NaFePO_4$ crystals were utilized to validate the transferability of parameters derived from previous binary and ternary oxides.

For $Fe_xP_yO_z$ ternary oxides, Figure 5-11a shows that the current ReaxFF predicts very well the energies of $Fe_xP_yO_z$ oxides with E_0 of -1182.97 and -2404.71 kcal/mol for $Fe_2P_2O_7$ and $Fe_3P_4O_{14}$, respectively. The corresponding small underestimations of -11% and -7% have been found for these compounds when compared with the respective values of -1324.12 and -2581.70 kcal/mol obtained from QM calculations. For $NaFeO_2$, this energy value is -494.03 kcal/mol, which is 17% larger than QM result. Similarly, the small discrepancies are also found quaternary oxides of $NaFeP_2O_7$ and $NaFePO_4$, particularly, E_0 of -1296.34 and -786.52 kcal/mol were calculated for $NaFeP_2O_7$ and $NaFePO_4$ crystals, respectively, which were only -4% and -9% smaller than the values of -1343.36 and -863.44 kcal/mol evaluated from QM. The discrepancies within 9% indicate that the developed ReaxFF predicts well the energies of $Fe_xP_yO_z$ and $Fe_xNa_yP_zO_h$ crystals. However, Figure 5-11b and d show that the current ReaxFF overestimates the volumes at ground state for these compounds. These figures also show that the gradient of energy obtained from current ReaxFF is close to that observed from QM. The bulk modulus of 135.88 and 172.73 GPa respectively for $Fe_2P_2O_7$ and $NaFeO_2$ are close to the corresponding QM results of 149.37 and 164.92 GPa.

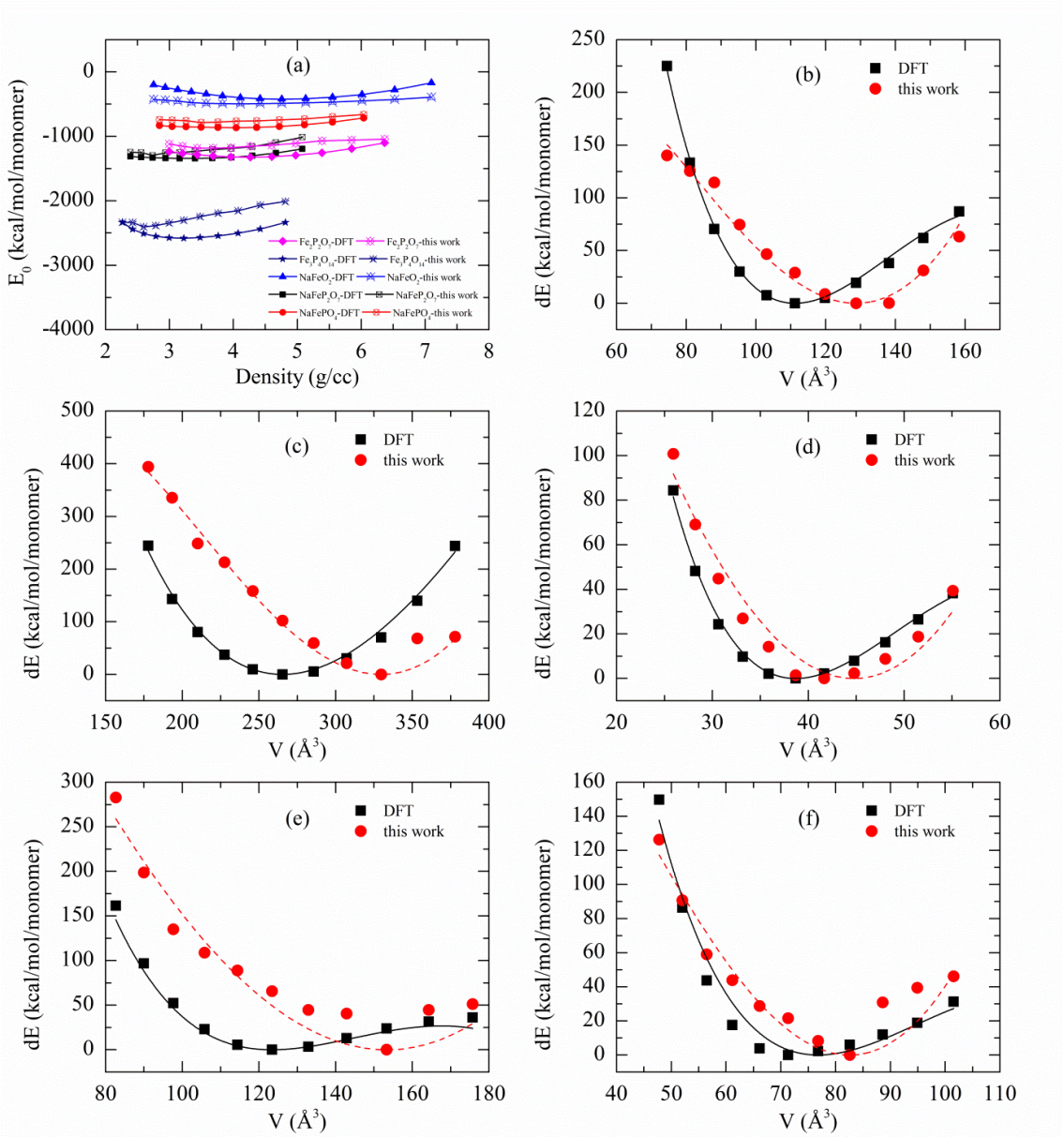

Figure 5-11. Comparison of: (a) E_0 of different $Fe_xP_yO_z$, $NaFeO_2$, and $Fe_xNa_yP_zO_h$ oxides; EoS of (b) $Fe_2P_2O_7$; (c) $Fe_3P_4O_{14}$; (d) $NaFeO_2$; (e) $NaFeP_2O_7$; and (f) $NaFePO_4$ oxides between the current ReaxFF and QM calculation.

The structural properties of $Fe_xP_yO_z$, $NaFeO_2$, and $Fe_xNa_yP_zO_h$ oxides were presented in Table 5.5, which show the overestimates of lattice constants obtained from both QM and current ReaxFF calculations in comparison with referenced data. The errors within 5% were found for QM calculation. Similar with observations in Figure 5-11b and d, for $Fe_xP_yO_z$ and $Fe_xNa_yP_zO_h$ oxides, this table shows the underestimation of -10% to -33% for density at equilibrium state. This is the consequence of the overestimation in lattice parameters, which have discrepancies of 2-26%. A good prediction in both density and lattice constants has been found for $NaFeO_2$ with the corresponding errors of only -10%

and 4%.

Currently, to the best of our knowledge from literature, the heat of formations of $Fe_xP_yO_z$, $NaFeO_2$, and $Fe_xNa_yP_zO_h$ oxides are not available. For the first time ever, this work predicts ΔH_f of these compounds based on the currently developed ReaxFF using Equation 5.4, which provides the respective values of -471.22, -1067.56, -186.76, -633.92, and -374.73 kcal/mol for $Fe_2P_2O_7$, $Fe_3P_4O_{14}$, $NaFeO_2$, $NaFeP_2O_7$, and $NaFePO_4$. Interestingly, the order of ΔH_f depends on the order of number of atoms in each compound. For instance, ΔH_f of $Fe_3P_4O_{14}$ with 21 atoms is nearly 2-fold larger than $Fe_2P_2O_7$ with 11 atoms, or ΔH_f of $NaFeP_2O_7$ with 11 atoms is 1.6 times larger than $NaFePO_4$ with 7 atoms, which has the number of atoms ~1.6 times smaller than $NaFeP_2O_7$.

5.3.6 MD simulation of thin film lubrication of $Na_4P_2O_7$ lubricant confined between Fe_2O_3 surfaces

The ability to model the dynamics of AIMD at elevated temperature will be the first step toward modelling the thin film lubrication of this lubricant. A key application of this force field involves the simulation of alkaline polyphosphate tribofilm, where not only the chemical dissociation is important, but the mechanical properties are also crucial for successful simulations. The AIMD simulations of one periodic cell were carried out using NPT and NVT ensembles to validate the fitted force field at high pressure and elevated temperature. The snapshots of $Na_4P_2O_7$ at 1100 K obtained at 20000 fs in Figure 5-12 show the discrepancies in crystalline structure between the reactive MD simulation using the current ReaxFF and AIMD using QM. This figure shows that the $P–O_b$ is still retained at 1100 K for QM and reactive MD calculations.

Additionally, the developed REAXFF was also validated by considering the relative distance between different pairwise of elements in sodium polyphosphate lubricant through the radial distribution function g(r) for each pair of interaction. This figure indicates that a good prediction of relative distance is found for all pairs of elements in $Na_4P_2O_7$ crystal at 1100 K. In fact Figure 5-12b provides the corresponding peaks of g(r) function at 2.55, 2.35, 1.55, 3.45, 3.05, and 3.05 Å for O-O, O-Na, O-P, Na-Na, Na-P, and P-P pairwise which are respectively only -2%, 5%, -2%, 2%, -3%, and 2% compared with the relevant distances of 2.51, 2.23, 1.58, 3.38, 3.15, and 2.99 Å from AIMD simulation in Figure 5-12a. This reveals that current ReaxFF predicts very well the

molecular structure of sodium phosphorus oxide crystal at high temperature.

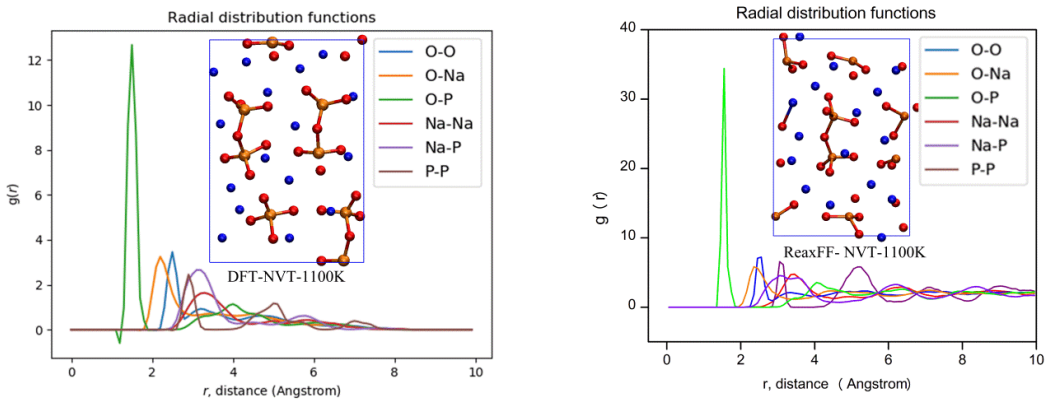

(a) AIMD (b) Reactive MD

Figure 5-12. Snapshots of crystalline structure of $Na_4P_2O_7$ at 1100K obtained at 20,000 fs, and radial distribution functions of: O-O (blue), O-Na (orange), O-P (green), Na-Na (red), Na-P (violet), and P-P (brown) using NVT ensemble with: (a) AIMD; and (b) reactive MD simulation. Red, orange, and blue colours are for O, P, and Na elements, respectively.

The transformation of sodium polyphosphate lubricant during the confined shear simulation is presented in Figure 5-13, which shows an aggregation of different $Na_4P_2O_7$ molecules to form an amorphous structure at 100 ps. When the load of 0.5 GPa was applied onto the upper surface, a layer of sodium has been observed at Fe_2O_3-$Na_4P_2O_7$ interface. Additionally, there are a few Na atoms diffuse into the surface during compressing stage; this diffusion behavior becomes stronger under the sliding of surfaces.

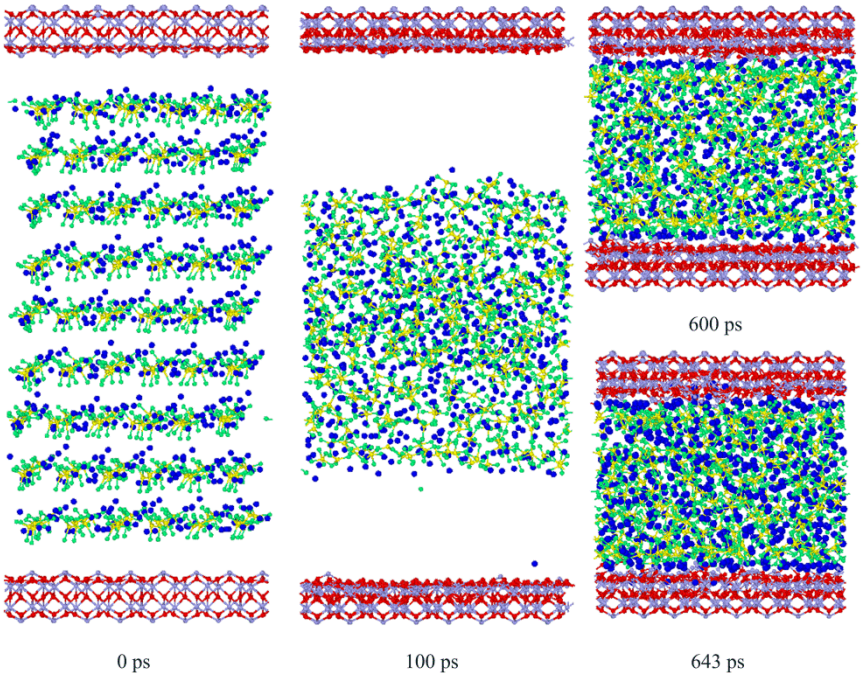

Figure 5-13. Snap-shots of sodium polyphosphate lubricant and Fe_2O_3(0001) surfaces at different simulation time of 0, 100, 600, and 643 ps.

The density profiles of sodium polyphosphate were calculated to determine the distribution of each element across the thin lubricant film. Figure 5-14 shows that there is a layering structure at Fe_2O_3-$Na_4P_2O_7$ interface. This layering structure was found for all lubricant elements, but there are differences in the location of the peaks of these density profiles. In fact this figure reveals that Na layer is closer to the oxide surface than O and P. This figure also indicates that there is a penetration of surface atoms of Fe and O into the lubricant, and vice versa the lubricant's Na atoms into the surfaces while the P and O elements of the PO_4 group remain in the lubricant film. The statistical calculation in Figure 5-12a showed that there are 14 Fe and 5 O atoms that were diffused into the lubricant, and 49 Na atoms penetrated into the surfaces. However, Figure 5-12c shows that the majority of Na atoms are located at Fe_2O_3-sodium polyphosphate interfaces.

To explain for this interesting phenomenon the mean square displacement (MSD) of each element was evaluated and presented in Figure 5-15, which indicates that the MSD of Na is significantly higher than P and O. It is also noted that the MSD of P and O are nearly equal. The differences in chemical interactions result in discrepancies in MSD of these elements. In fact there is an ionic interaction between Na atoms with O of $–PO_4^{-1}$ group, and this interaction is weak due to the small dissociation energy for Na–O bond of 45.53 kcal/mol. This value is lower than the σ bond of P–O with dissociation energies in the range 90-110 kcal/mol and the P=O π bond with dissociation energy of 142 kcal/mol in Figure 5-6. The stronger covalent bonds between P and O cause these elements to stay in the lubricant and tend not to diffuse into the oxide surface as compared with Na. Moreover, Figure 5-10 shows that the dissociation pathways of $Na_4P_2O_7$ molecule provide lower dissociation energies than QM's results, thus they could promote the depolymerization of IAP molecules in current reactive MD model at a lower temperature and strain rate than the QM simulation.

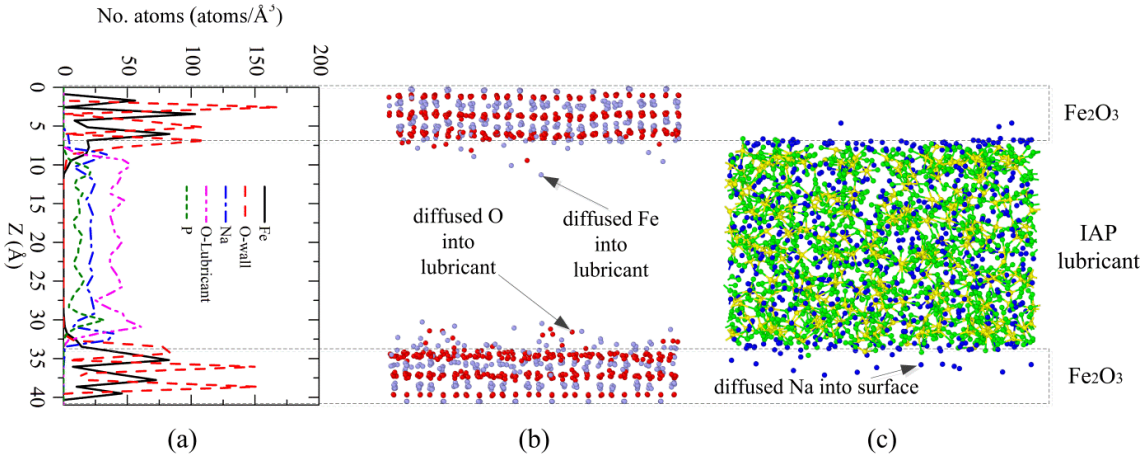

Figure 5-14. (a) Atomic density of different elements across the thin lubricant film thickness of IAP confined between Fe_2O_3(0001) surfaces; (b) Snapshot of Fe_2O_3(0001) surfaces; and (c) IAP lubricant sodium polyphosphate at 643 ps.

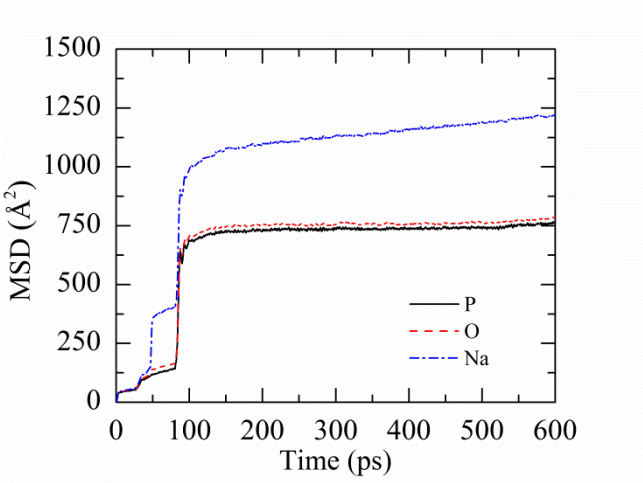

Figure 5-15. Time-evolution of mean square displacement of Na, P, and O elements in sodium polyphosphate lubricant

5.4 Discussion

This work develops a new ReaxFF potential for a system of sodium polyphosphate lubricant confined between hematite substrates with the major attentions focus on the chemical and mechanical properties of sodium polyphosphate lubricant and Fe_2O_3 substrate. The crystalline structures such a lattice constants, EoS, and ΔH_f of iron oxides, sodium oxides, and phosphorus oxides were improved compared with previous works by others. For organic molecules, the current ReaxFF did not provide the best prediction compared with previous work by Zhu et al.[299] However, this new ReaxFF can still represent quantitatively some major bonds of P–O and P=O, P–O–P and O–P–O angles, as well as the O–P–O–P and O–P–O=P dihedrals of phosphoric acids and provides a

better prediction of ΔH_f and mechanical properties of P_2O_5 crystal.

This new ReaxFF does not only predicts properly the molecular structure and atomic charges of Fe_2O_3 in the bulk material, but it also predict well these properties of Fe_2O_3(0001) surface with the error comparable with QM calculation as well as the others from literature. Additionally, the validations for Fe_2O_3 and sodium polyphosphate lubricant at high temperature indicate that this new ReaxFF can be applied at elevated temperature and high pressure. Moreover, the static validation of different dissociation paths of $Na_4P_2O_7$ shows a good agreement in the order of energy differences with previous work carried out by Le et al.[245]

The interactions between lubricant and substrates were optimized using the potential glassy crystals of $Fe_xNa_yP_zO_n$ created by Fe and O elements of surfaces and Na, P, and O elements of lubricant. The EoS of $Fe_2P_2O_7$, $Fe_3P_4O_{14}$, $NaFeO_2$, $NaFeP_2O_7$, and $NaFePO_4$ had been used to train these interactions, and other structural properties were utilized to validate the developed ReaxFF. Although this new potential can represent well the energy of these compounds, it underestimates the equilibrium density and overestimates the lattice constants. However, these limitations do not affect to the current confined shear system because the major constituent materials in this model are Fe_2O_3 and $Na_4P_2O_7$ rather than these glassy crystals.

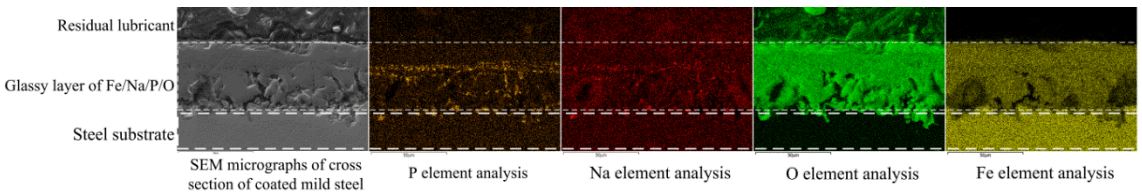

Figure 5-16. SEM and EDX analysis of cross section of hot rolled sample lubricated by sodium metaphosphate in our recent experiment.

The application of the current developed ReaxFF for confined shear system show an interesting phenomenon is that sodium plays a vital role in tribochemistry at surface-lubricant interfaces. The obtained molecular structure reveals that $–PO_4$ group was retained in the lubricant, while there were the inward diffusions of Na into the substrates and Fe from the oxide substrates into the lubricant. Additionally, these diffusive behaviors occurred rapidly with sliding velocity, which indicates that the high friction might cause a rise in local temperature, which helps to accelerate this tribochemical process. The high diffusion of Na element was explained by its weaker ionic bond with O than the covalent

bond between P and O in $Na_4P_2O_7$ molecule.

Interestingly, the diffusion Na atoms into Fe_2O_3 surfaces and the moving of some Fe atoms toward sodium polyphosphate lubricant create a glassy layer of $Fe_xNa_yP_zO_n$. This observation is consistent with our previous experiment presented in Figure 5-16, where the glassy layer including Fe, Na, P, and O elements with thickness up to 5 μm was found by Cui et al.[97] They proposed the formation of a new compound of $NaFePO_4$ due to the reaction of iron oxide and $(NaPO_3)_3$.[97] However, the current simulation show that this is not the exact compound, instead, it is a random combination of these elements to form a complex $Fe_xNa_yP_zO_n$ oxide with the ratio of each element depending on the simulation time and local location. There is a significant difference in the thickness of the glassy layer between the current MD simulation (a few ångström) and previous experiment (a few micrometers). This could be justified by the scale of current MD model, as well as the ideal condition of smooth surfaces. Additionally, there is a larger roughness of 1.0 μm for mild steel at ambient condition, this roughness increased up to 8.88 μm at high temperature.[97] Along with the chemical reactions, the mechanical effects with sliding and high pressure help to form this glassy layer easier and thicker due to the reduction of the roughness. This mechanism is not similar to the current ReaxFF where the roughness is not available and the chemical reaction plays the major role on the formation of this layer.

Obviously, the sliding velocity and applied pressure can contribute to this interesting phenomenon. The insight into the mechanisms of each factor will be investigated in depth in the near future. Additionally, there are rough surface of substrate at macroscale rather than a smooth surface used in this work. Therefore, the unrevealed question of how this diffusion of Na occurs between roughness contacts and the formation of hierarchical tribochemical layers will be studied in future work.

5.5 Conclusions

A new ReaxFF has been developed for Fe/Na/P/O system using a robust GA algorithm and a consistent reference data from QM calculation. This force field show a significant improvement in heat of formation, mechanical properties, lattice constants, bulk modulus, and density of Fe, Na, and P, as well as their binary oxides compared with previous ReaxFFs. Additionally, the new parameters of ternary and quaternary oxides of $Na_xP_yO_z$, $Fe_xP_yO_z$, and $Na_xFe_yP_zO_n$ were also developed and validated against QM calculation at static and elevated-temperature dynamic conditions. This new ReaxFF predicts not only

well the crystalline properties of these oxides, but it also predicts the most stable configuration and the order of energies at intermediate states.

The application of the new developed ReaxFF for the system of $Na_4P_2O_7$ lubricant confined between Fe_2O_3(0001) surface reveals a hierarchical tribochemical layers in which a sodium layer was formed at lubricant-surface interface to improve the tribological performance of this tribo-system. This observation is in agreement with our experiments.

Chapter 6 Conclusions & Future Work

Inorganic sodium phosphate glass has been proposed as potential lubricant in hot rolling processes. Previous experimental works have exposed the outstanding tribological performance of this glass lubricant under the extreme condition of temperature, load and shear. The lubricity mechanism of sodium phosphate glass has also been revealed in the laboratory tests. However, the detailed picture of the mechano-tribochemical reaction of sodium phosphate glass lubricant on iron oxide surfaces is still not complete due to a number of missing pieces, for example, how the role of elements/compounds in reducing friction, lubrication and wear. This thesis applies various theoretical methods to unveil the tribochemical behavior of different sodium phosphate compounds with iron-based interfaces at the atomistic scale and the resulting lubrication effect of this inorganic glass. Firstly, the bond nature of the system, effect of surface and effect of chain length on depolymerization of phosphate-based lubricant have been analyzed with DFT calculations and AIMD simulations at 1100K. In general, the tribo-system contains medium covalent P-O bond, pure ionic Na-O interaction and moderate Fe-O ionic/covalent bond. The bridging P-O_b is the weakest bond targeted for the depolymerization which is induced by sodium - bridging oxygens interaction.

The iron oxide surface plays a dual role in promoting/inhibiting the phosphate depolymerization. On one hand, the phosphate adsorption of oxide surface generates stable configurations and the partial anchoring of phosphate chain on substrates supports P-O_b depolymerization due to the effect of temperature. On the other hand, the oxide surface captures sodium cation which reduces the sodium attack on P-O_b bond and obstructs the depolymerization.

The monodentate complex structures is dominant in all adsorption cases regardless of the chain length. The chain length of phosphate has little effect on the P-O bridging dissociation. The monodentate structures create the deformed FeO_4 tetrahedra on the oxide surface which allow the flexibility of phosphate network but still maintains the strong adherence lubricant film. Moreover, the small chain length structure is preferable at the lubricant-surface interfaces for the full phosphate coverage and all linkages are monodentate, which are associated with the good lubricity of short-chain Na_3PO_4 and the depolymerized products of long-chain $NaPO_3$ in some experimental studies.

Secondly, DFT calculations and AIMD simulations have also been used to investigate the

surface transformation and interactions of iron oxide in glassy lubricant. Among three main interlayer interactions between phosphate networks with iron oxide, Fe-O_{glass} is the most stable linkage which can weaken the outermost Fe-O layer of oxide surface. $O_{surface}$-P interaction is observed under high compression conditions and Fe-P direct bond occurs under severe conditions of high temperature, with an exposure of considerable number of iron atoms and a presence of under-coordinated phosphorus atoms. The Fe-P linkage can strengthen the Fe-O bonds of the iron oxide surface but has a low probability to form in the system. Sodium cations in the glass network also reduce the Fe-$O_{surface}$ stability through generated O-terminated iron oxide surfaces. The iron oxide structure deformation can occur at normal temperatures with an excess concentrations of sodium. In addition to thermal and mechanical factors, phosphate glass itself has a combined chemical/electronical effect on the deformation of the iron oxide surface, which supports the abrasive particle digestion theory in anti-wear mechanism of phosphate lubricant.

Last but not least, a comprehensive ReaxFF has been developed for the sodium phosphate/iron oxide system using a robust GA algorithm and a consistent reference data from QM calculation. This force field show a significant improvement in predicting the heat of formation, mechanical properties, lattice constants, bulk modulus, and density of Fe, Na, and P, as well as their binary oxides compared to previous ReaxFFs. Additionally, the new parameters of ternary and quaternary oxides of $Na_xP_yO_z$, $Fe_xP_yO_z$, and $Na_xFe_yP_zO_n$ have also been developed and validated against QM calculation at static and elevated-temperature dynamic conditions. This new ReaxFF not only predicts well the crystalline properties of these oxides, but it also predicts the most stable configuration and the order of energies of the intermediate states. The application of the newly developed ReaxFF for the system of $Na_4P_2O_7$ lubricant confined between Fe_2O_3(0001) surface reveals a hierarchical tribochemical layers in which a sodium layer was formed at the lubricant-surface interface to improve the system tribological performance in agreement with previous experimental work.

In the future work, different glass composition should be the main focus in relation to the tribological performance of inorganic glass lubricants such as alkali phosphates, borates and silicates. When combined with polyphosphates, the roles of alkali metals such as potassium, calcium, lithium on the lubricity of the tribofilm can reveal more insights into the friction and wear performance. The investigation of cation diffusion inside the glass network can also reveal not only the tribofilm behavior but also the friction and wear rate during hot rolling processes. The optimum inorganic glass lubricant can be proposed

based on the friction, wear or oxidation performance in different fields over a wide range of pressure/shear and temperatures.

For the reactive MD simulation, more realistic factors should be coupled into system such as roughness, multi-valence of the element such as Fe(II), Fe(III), P(III), P(V), etc. in order to simulate the tribological processes in the context of thermal, mechanical and chemical effects. The new ReaxFF can pave the way for the development of different multi-composition glass lubricant force fields for high temperature metal forming processes.

List of References

1. Holmberg, K. and A. Erdemir, *Influence of tribology on global energy consumption, costs and emissions.* Friction, 2017. **5**(3): p. 263-284.
2. Urbakh, M., et al., *The nonlinear nature of friction.* Nature, 2004. **430**(6999): p. 525-528.
3. Saito, K. and S. Iida, *Lubricant for hot working and method for producing seamless steel pipe*. 2011, Google Patents.
4. Altan, T., G. Ngaile, and G. Shen, *Cold and Hot Forging: Fundamentals and Applications*. 2005: A S M International.
5. Davis, J.R., *Surface Engineering for Corrosion and Wear Resistance*. 2001: ASM International.
6. Dohda, K., et al., *Tribology in metal forming at elevated temperatures.* Friction, 2015. **3**(1): p. 1-27.
7. Boccaccini, A.R., D.S. Brauer, and L. Hupa, *Bioactive Glasses: Fundamentals, Technology and Applications*. 2016: Royal Society of Chemistry.
8. Sengupta, P., *A review on immobilization of phosphate containing high level nuclear wastes within glass matrix – Present status and future challenges.* Journal of Hazardous Materials, 2012. **235-236**: p. 17-28.
9. Seshadri, M., et al., *Spectroscopic and laser properties of Sm3+ doped different phosphate glasses.* Journal of Alloys and Compounds, 2009. **476**(1): p. 263-270.
10. Brow, R.K., *Review: the structure of simple phosphate glasses.* Journal of Non-Crystalline Solids, 2000. **263–264**: p. 1-28.
11. Wei, T.Y., Y. Hu, and L.G. Hwa, *Structure and elastic properties of low-temperature sealing phosphate glasses.* Journal of Non-Crystalline Solids, 2001. **288**(1): p. 140-147.
12. Tieu, A.K., et al., *Excellent melt lubrication of alkali metal polyphosphate glass for high temperature applications.* RSC Advances, 2015. **5**(3): p. 1796-1800.
13. Tieu, A.K., et al., *The Influence of Alkali Metal Polyphosphate on the Tribological Properties of Heavily Loaded Steel on Steel Contacts at Elevated Temperatures.* Advanced Materials Interfaces, 2015. **2**(6): p. 1500032.
14. Kong, N., et al., *Tribofilms generated from bulk polyphosphate glasses at elevated temperatures.* Wear, 2015. **330–331**: p. 230-238.
15. Watkins, R.C., *The antiwear mechanism of zddp's. Part II.* Tribology International, 1982. **15**(1): p. 13-15.
16. Spedding, H. and R.C. Watkins, *The antiwear mechanism of zddp's. Part I.* Tribology International, 1982. **15**(1): p. 9-12.
17. Spikes, H., *The history and mechanisms of ZDDP.* Tribology Letters, 2004. **17**(3): p. 469-489.
18. Martin, J., *Antiwear mechanisms of zinc dithiophosphate: a chemical hardness approach.* Tribology Letters, 1999. **6**(1): p. 1-8.
19. Spikes, H., *Stress-augmented thermal activation: Tribology feels the force.* Friction, 2018. **6**(1): p. 1-31.
20. Zhang, J. and H. Spikes, *On the Mechanism of ZDDP Antiwear Film Formation.* Tribology Letters, 2016. **63**(2): p. 24.
21. Beynon, J.H., *Tribology of hot metal forming.* Tribology International, 1998. **31**(1): p. 73-77.
22. Chen, R.Y. and W.Y.D. Yuen, *Oxide-Scale Structures Formed on Commercial Hot-Rolled Steel Strip and Their Formation Mechanisms.* Oxidation of Metals, 2001. **56**(1): p. 89-118.
23. Black, J.T. and R.A. Kohser, *DeGarmo's Materials and Processes in Manufacturing*. 2019: Wiley.
24. Kovalev, L.K. and V.A. Ryabov, *Glass lubricants in metallurgy.* Glass and Ceramics, 1958. **15**(7): p. 352-357.
25. Lopes, M. and J.E. Shelby, *Introduction to Glass Science and Technology*. 2007: Royal Society of Chemistry.
26. Wan, S., et al., *An overview of inorganic polymer as potential lubricant additive for high temperature tribology.* Tribology International, 2016. **102**: p. 620-635.
27. Wan, S., et al., *Chemical nature of alkaline polyphosphate boundary film at heated rubbing surfaces.* Scientific Reports, 2016. **6**: p. 26008.
28. Wang, L., et al., *Lubrication mechanism of sodium metasilicate at elevated temperatures through tribo-interface observation.* Tribology International, 2020. **142**: p. 105972.
29. Tran, B.H., et al., *Multifunctional Bi-Layered Tribofilm Generated on Steel Contact Interfaces under High-Temperature Melt Lubrication.* The Journal of Physical Chemistry C, 2017. **121**(45): p. 25092-25103.

30. Shah, F.U., S. Glavatskih, and O.N. Antzutkin, *Boron in Tribology: From Borates to Ionic Liquids.* Tribology Letters, 2013. **51**(3): p. 281-301.
31. Walsh, R.H., *Aqueous systems containing organo-borate compounds*. 1986, Google Patents.
32. Baş, H. and Y.E. Karabacak, *Investigation of the Effects of Boron Additives on the Performance of Engine Oil.* Tribology Transactions, 2014. **57**(4): p. 740-748.
33. Johnsson, E., *Investigation of tribological mechanisms of a boron additive in lubricants and fuel enhancer*. 2015, Uppsala University, Sweden.
34. Erdemir, A., G.R. Fenske, and R.A. Erck, *A Study of the Formation and Self-lubrication Mechanisms of Boric Acid Films on Boric Oxide Coatings*, in *Metallurgical Coatings and Thin Films 1990*. 1990, Elsevier. p. 588-596.
35. Sawyer, W.G., et al., *In Situ Lubrication with Boric Acid: Powder Delivery of an Environmentally Benign Solid Lubricant.* Tribology Transactions, 2006. **49**(2): p. 284-290.
36. Peeler, R.L., *Alkali metal borate e.p. lubricants*. 1967, Google Patents.
37. Georg, G. and L. Werner, *Metal treating process employing a heat-resistant lubricant composed of alkali metalborate and alkali metal phosphate*. 1961, Google Patents.
38. Henricks, J.A. and G.H. Orozco, *Lubricant composition composed of high-titre soap, borax, and an inorganic compound*. 1950, Google Patents.
39. Tran, B.H., et al., *Understanding the tribological impacts of alkali element on lubrication of binary borate melt.* RSC Advances, 2018. **8**(51): p. 28847-28860.
40. Choudhary, R.B. and P.P. Pande, *Lubrication potential of boron compounds: An overview.* Lubrication Science, 2002. **14**(2): p. 211-222.
41. Kreuz, K.L., R.S. Fein, and M. Dundy, *EP Films from Borate Lubricants.* A S L E Transactions, 1967. **10**(1): p. 67-76.
42. Qiao, Y., et al., *The tribochemical mechanism of the borate modified by N-containing compound as oil additive.* Wear, 1998. **215**(1): p. 165-169.
43. Hao, L., et al., *Preparation and tribological properties of a kind of lubricant containing calcium borate nanoparticles as additives.* Industrial Lubrication and Tribology, 2012. **64**(1): p. 16-22.
44. Ta, H.T.T., et al., *Ab initio study on physical and chemical interactions at borates and iron oxide interface at high temperature.* Chemical Physics, 2020. **529**: p. 110548.
45. Ta, H.T.T., et al., *Mechanisms of Pressure-Induced Structural Transformation in Confined Sodium Borate Glasses.* The Journal of Physical Chemistry B, 2020. **124**(1): p. 277-287.
46. Dong, J.X. and Z.S. Hu, *A study of the anti-wear and friction-reducing properties of the lubricant additive, nanometer zinc borate.* Tribology International, 1998. **31**(5): p. 219-223.
47. Jia, Z., et al., *Synthesis, Characterization, and Tribological Behavior of Oleic Acid–Capped Calcium Borate Hydrate.* Tribology Transactions, 2013. **56**(3): p. 521-529.
48. de Oliveira, L.A., et al., *Effect of silicate-based films on the corrosion behavior of the API 5L X80 pipeline steel.* Corrosion Science, 2018. **139**: p. 21-34.
49. Salasi, M., et al., *The electrochemical behaviour of environment-friendly inhibitors of silicate and phosphonate in corrosion control of carbon steel in soft water media.* Materials Chemistry and Physics, 2007. **104**(1): p. 183-190.
50. Calas, G., G.S. Henderson, and J.F. Stebbins, *Glasses and Melts: Linking Geochemistry and Materials Science.* Elements, 2006. **2**(5): p. 265-268.
51. Navrotsky, A., et al., *The tetrahedral framework in glasses and melts — inferences from molecular orbital calculations and implications for structure, thermodynamics, and physical properties.* Physics and Chemistry of Minerals, 1985. **11**(6): p. 284-298.
52. Silver, L. and E. Stolper, *A Thermodynamic Model for Hydrous Silicate Melts.* The Journal of Geology, 1985. **93**(2): p. 161-177.
53. Potužák, M., *Physico-chemical properties of silicate melts*. 2006, Ludwig-Maximilians-Universität München.
54. Alexander, B. and W.H. John, *Lubricants*. 1968, Google Patents.
55. Zhang, J., B. Tian, and C. Wang, *Long-term surface restoration effect introduced by advanced silicate based lubricant additive.* Tribology International, 2013. **57**: p. 31-37.
56. Yue, W., et al., *Study of the Regenerated Layer on the Worn Surface of a Cylinder Liner Lubricated by a Novel Silicate Additive in Lubricating Oil.* Tribology Transactions, 2010. **53**(2): p. 288-295.
57. Cochain, B., et al., *Effects of the Iron Content and Redox State on the Structure of Sodium Borosilicate Glasses: A Raman, Mössbauer and Boron K-Edge XANES Spectroscopy Study.* Journal of the American Ceramic Society, 2012. **95**(3): p. 962-971.
58. Magnien, V., et al., *Kinetics and mechanisms of iron redox reactions in silicate melts: The effects of temperature and alkali cations.* Geochimica et Cosmochimica Acta, 2008. **72**(8): p. 2157-2168.
59. Tran, N.V., et al., *First-Principles Study of the Adsorption and Depolymerization Mechanisms of*

Sodium Silicate on Iron Surfaces at High Temperature. The Journal of Physical Chemistry C, 2018. **122**(36): p. 20827-20840.
60. Matsumoto, K., et al., *Tribological Properties of Water Glass Lubricant for Hot Metalworking.* Tribology Transactions, 2009. **52**(4): p. 553-559.
61. Talley, S.K., S.J. Beaubien, and L.P. Richardson, *Metal-working lubricant*. 1954, Google Patents.
62. Gililland, M.E., *Transparent metal working lubricant composition*. 1961, Google Patents.
63. De Barros-Bouchet, M.I., et al., *Tribochemistry of phosphorus additives: experiments and first-principles calculations.* RSC Advances, 2015. **5**(61): p. 49270-49279.
64. Pawlak, Z., et al., *The mechanical characteristics of phosphate glasses under high temperature and friction-induced cross-linking processes.* Journal of Achievements in Materials and Manufacturing Engineering, 2009. **37**(2): p. 458-465.
65. Zachariasen, W.H., *The Atomic Arrangement in Glass.* Journal of the American Chemical Society, 1932. **54**(10): p. 3841-3851.
66. Shelby, J.E., *Introduction to Glass Science and Technology*. 2015: Royal Society of Chemistry.
67. Lippmaa, E., et al., *Structural studies of silicates by solid-state high-resolution silicon-29 NMR.* Journal of the American Chemical Society, 1980. **102**(15): p. 4889-4893.
68. Van Wazer, J.R., *Phosphorus and Its Compounds*. 1958: Interscience Pubs.
69. Mitchell, K.A.R., *Use of outer d orbitals in bonding.* Chemical Reviews, 1969. **69**(2): p. 157-178.
70. Cruickshank, D.W.J., *The rôle of 3d-orbitals in π-bonds between (a) silicon, phosphorus, sulphur, or chlorine and (b) oxygen or nitrogen.* Journal of the Chemical Society (Resumed), 1961(0): p. 5486-5504.
71. Nelson, B.N. and G.J. Exarhos, *Vibrational spectroscopy of cation-site interactions in phosphate glasses.* The Journal of Chemical Physics, 1979. **71**(7): p. 2739-2747.
72. Rouse, G.B., P.J. Miller, and W.M. Risen, *Mixed alkali glass spectra and structure.* Journal of Non-Crystalline Solids, 1978. **28**(2): p. 193-207.
73. So, H. and Y.C. Lin, *The theory of antiwear for ZDDP at elevated temperature in boundary lubrication condition.* Wear, 1994. **177**(2): p. 105-115.
74. Yin, Z., et al., *Application of soft X-ray absorption spectroscopy in chemical characterization of antiwear films generated by ZDDP Part I: the effects of physical parameters.* Wear, 1997. **202**(2): p. 172-191.
75. Bird, R.J. and G.D. Galvin, *The application of photoelectron spectroscopy to the study of e. p. films on lubricated surfaces.* Wear, 1976. **37**(1): p. 143-167.
76. Bennett, P.A., *A Surface Effect Associated with the Use of Oils Containing Zinc Dialkyl Dithiophosphate.* A S L E Transactions, 1959. **2**(1): p. 78-90.
77. Wan, Y., L. Cao, and Q. Xue, *Friction and wear characteristics of ZDDP in the sliding of steel against aluminum alloy.* Tribology International, 1997. **30**(10): p. 767-772.
78. Martin, J.M., et al., *The origin of anti-wear chemistry of ZDDP*. Faraday Discussions, 2012. **156**(0): p. 311-323.
79. Nicholls, M.A., et al., *Review of the lubrication of metallic surfaces by zinc dialkyl-dithiophosphates.* Tribology International, 2005. **38**(1): p. 15-39.
80. Mosey, N.J., et al., *Interpretation of experiments on ZDDP anti-wear films through pressure-induced cross-linking.* Tribology Letters, 2006. **24**(2): p. 105-114.
81. Mosey, N.J., M.H. Muser, and T.K. Woo, *Molecular mechanisms for the functionality of lubricant additives.* Science, 2005. **307**(5715): p. 1612-5.
82. Kato, O., et al., *Mechanisms of Surface Deterioration of Roll for Hot Strip Rolling.* ISIJ International, 1992. **32**(11): p. 1216-1220.
83. Wu, H., T. Ren, and G. Zuo, *The Tribological Chemistry of the Oil Blends of Zinc Dialkyldithiophosphate with 2-Mercaptobenzothiazole Derivatives.* Tribology Letters, 2009. **35**(3): p. 171-179.
84. Shakhvorostov, D., et al., *Smart materials behavior in phosphates: Role of hydroxyl groups and relevance to antiwear films.* The Journal of Chemical Physics, 2009. **131**(4): p. 044704.
85. Gauvin, M., et al., *Boundary Lubrication by Pure Crystalline Zinc Orthophosphate Powder in Oil.* Tribology Letters, 2008. **31**(3): p. 139-148.
86. Crobu, M., A. Rossi, and N.D. Spencer, *Effect of Chain-Length and Countersurface on the Tribochemistry of Bulk Zinc Polyphosphate Glasses.* Tribology Letters, 2012. **48**(3): p. 393-406.
87. Wan, Y., et al., *Effects of detergent on the chemistry of tribofilms from ZDDP: studied by X-ray absorption spectroscopy and XPS*, in *Tribology Series*, M.P.G.D. D. Dowson and A.A. Lubrecht, Editors. 2002, Elsevier. p. 155-166.
88. Heuberger, R., A. Rossi, and N.D. Spencer, *Pressure Dependence of ZnDTP Tribochemical Film Formation: A Combinatorial Approach.* Tribology Letters, 2007. **28**(2): p. 209-222.

89. Gosvami, N.N., et al., *Mechanisms of antiwear tribofilm growth revealed in situ by single-asperity sliding contacts.* Science, 2015. **348**(6230): p. 102.
90. Zhang, J., et al., *Mechanochemistry of Zinc Dialkyldithiophosphate on Steel Surfaces under Elastohydrodynamic Lubrication Conditions.* ACS Applied Materials & Interfaces, 2020. **12**(5): p. 6662-6676.
91. Holbert, A.W., et al., *Passivation of Fe(110) via phosphorus deposition: the reactions of trimethylphosphite.* Surface Science, 1998. **401**(3): p. L437-L443.
92. Philippon, D., et al., *A multi-technique approach to the characterization of iron phosphide tribofilm.* Thin Solid Films, 2012. **524**: p. 191-196.
93. Philippon, D., et al., *Role of nascent metallic surfaces on the tribochemistry of phosphite lubricant additives.* Tribology International, 2011. **44**(6): p. 684-691.
94. Righi, M.C., et al., *A comparative study on the functionality of S- and P-based lubricant additives by combined first principles and experimental analysis.* RSC Advances, 2016. **6**(53): p. 47753-47760.
95. Righi, M.C., et al., *Trimethyl-phosphite dissociative adsorption on iron by combined first-principle calculations and XPS experiments.* RSC Advances, 2015. **5**(122): p. 101162-101168.
96. Cui, S., et al., *Tribochemical Behavior of Phosphate Compounds at an Elevated Temperature.* The Journal of Physical Chemistry C, 2016. **120**(45): p. 25742-25751.
97. Cui, S., et al., *Investigation of different inorganic chemical compounds as hot metal forming lubricant by pin-on-disc and hot rolling.* Tribology International, 2018. **125**: p. 110-120.
98. Cui, S., et al., *Effect of loading on the friction and interface microstructure of lubricated steel tribopairs.* Tribology International, 2017. **116**: p. 180-191.
99. Mosey, N.J. and T.K. Woo, *Finite Temperature Structure and Dynamics of Zinc Dialkyldithiophosphate Wear Inhibitors: A Density Functional Theory and ab Initio Molecular Dynamics Study.* The Journal of Physical Chemistry A, 2003. **107**(25): p. 5058-5070.
100. Mosey, N.J. and T.K. Woo, *A Quantum Chemical Study of the Unimolecular Decomposition Mechanisms of Zinc Dialkyldithiophosphate Antiwear Additives.* The Journal of Physical Chemistry A, 2004. **108**(28): p. 6001-6016.
101. Mosey, N.J. and T.K. Woo, *Insights into the chemical behavior of zinc dialkyldithiophosphate anti-wear additives in their isomeric and decomposed forms through molecular simulation.* Tribology International, 2006. **39**(9): p. 979-993.
102. Mosey, N.J. and T.K. Woo, *An ab Initio Molecular Dynamics and Density Functional Theory Study of the Formation of Phosphate Chains from Metathiophosphates.* Inorganic Chemistry, 2006. **45**(18): p. 7464-7479.
103. Loehlé, S. and M.C. Righi, *Ab Initio Molecular Dynamics Simulation of Tribochemical Reactions Involving Phosphorus Additives at Sliding Iron Interfaces.* Lubricants, 2018. **6**(2): p. 31.
104. Osei-Agyemang, E., S. Berkebile, and A. Martini, *Decomposition Mechanisms of Anti-wear Lubricant Additive Tricresyl Phosphate on Iron Surfaces Using DFT and Atomistic Thermodynamic Studies.* Tribology Letters, 2018. **66**(1): p. 48.
105. Koyama, M., et al., *Tribochemical Reaction Dynamics of Phosphoric Ester Lubricant Additive by Using a Hybrid Tight-Binding Quantum Chemical Molecular Dynamics Method.* The Journal of Physical Chemistry B, 2006. **110**(35): p. 17507-17511.
106. Onodera, T., et al., *Antiwear Chemistry of ZDDP: Coupling Classical MD and Tight-Binding Quantum Chemical MD Methods (TB-QCMD).* Tribology Letters, 2013. **50**(1): p. 31-39.
107. Onodera, T., et al., *A theoretical investigation on the abrasive wear prevention mechanism of ZDDP and ZP tribofilms.* Applied Surface Science, 2008. **254**(23): p. 7976-7979.
108. Selvam, P., et al., *Tight-binding quantum chemical molecular dynamics method: a novel approach to the understanding and design of new materials and catalysts.* Catalysis Today, 2005. **100**(1–2): p. 11-25.
109. Wolloch, M., et al., *Interfacial Charge Density and Its Connection to Adhesion and Frictional Forces.* Physical Review Letters, 2018. **121**(2): p. 026804.
110. Adams, H.L., et al., *Shear-Induced Mechanochemistry: Pushing Molecules Around.* The Journal of Physical Chemistry C, 2015. **119**(13): p. 7115-7123.
111. Atkins, P.W. and R.S. Friedman, *Molecular Quantum Mechanics*. 2011: OUP Oxford.
112. Szabo, A. and N.S. Ostlund, *Modern Quantum Chemistry: Introduction to Advanced Electronic Structure Theory*. 1989: Dover Publications.
113. Jensen, F., *Introduction to Computational Chemistry*. 2007: Wiley.
114. Parr, R.G. and Y. Weitao, *Density-Functional Theory of Atoms and Molecules*. 1994: Oxford University Press.
115. Hohenberg, P. and W. Kohn, *Inhomogeneous Electron Gas.* Physical Review, 1964. **136**(3B): p.

B864-B871.
116. Kohn, W. and L.J. Sham, *Self-Consistent Equations Including Exchange and Correlation Effects.* Physical Review, 1965. **140**(4A): p. A1133-A1138.
117. Slater, J.C., *A Simplification of the Hartree-Fock Method.* Physical Review, 1951. **81**(3): p. 385-390.
118. Vosko, S.H., L. Wilk, and M. Nusair, *Accurate spin-dependent electron liquid correlation energies for local spin density calculations: a critical analysis.* Canadian Journal of Physics, 1980. **58**(8): p. 1200-1211.
119. Perdew, J.P., K. Burke, and M. Ernzerhof, *Generalized Gradient Approximation Made Simple.* Physical Review Letters, 1996. **77**(18): p. 3865-3868.
120. Becke, A.D., *Density-functional thermochemistry. III. The role of exact exchange.* The Journal of Chemical Physics, 1993. **98**(7): p. 5648-5652.
121. Lee, C., W. Yang, and R.G. Parr, *Development of the Colle-Salvetti correlation-energy formula into a functional of the electron density.* Physical Review B, 1988. **37**(2): p. 785-789.
122. Shakhvorostov, D., et al., *On the pressure-induced loss of crystallinity in orthophosphates of zinc and calcium.* The Journal of Chemical Physics, 2008. **128**(7): p. 074706.
123. Mosey, N.J., T.K. Woo, and M.H. Müser, *Energy dissipation via quantum chemical hysteresis during high-pressure compression: A first-principles molecular dynamics study of phosphates.* Physical Review B, 2005. **72**(5): p. 054124.
124. Onodera, T., et al., *Development of a quantum chemical molecular dynamics tribochemical simulator and its application to tribochemical reaction dynamics of lubricant additives.* Modelling and Simulation in Materials Science and Engineering, 2010. **18**(3).
125. Russo Jr, M.F. and A.C.T. van Duin, *Atomistic-scale simulations of chemical reactions: Bridging from quantum chemistry to engineering.* Nuclear Instruments and Methods in Physics Research Section B: Beam Interactions with Materials and Atoms, 2011. **269**(14): p. 1549-1554.
126. Bhushan, B., J.N. Israelachvili, and U. Landman, *Nanotribology: friction, wear and lubrication at the atomic scale.* Nature, 1995. **374**(6523): p. 607-616.
127. Senftle, T.P., et al., *The ReaxFF reactive force-field: development, applications and future directions.* Npj Computational Materials, 2016. **2**: p. 15011.
128. Rapaport, D.C., *The Art of Molecular Dynamics Simulation*. 2004: Cambridge University Press.
129. Allen, M.P. and D.J. Tildesley, *Computer Simulation of Liquids*. 1989: Clarendon Press.
130. Swope, W.C., et al., *A computer simulation method for the calculation of equilibrium constants for the formation of physical clusters of molecules: Application to small water clusters.* The Journal of Chemical Physics, 1982. **76**(1): p. 637-649.
131. Verlet, L., *Computer "Experiments" on Classical Fluids. I. Thermodynamical Properties of Lennard-Jones Molecules.* Physical Review, 1967. **159**(1): p. 98-103.
132. Frenkel, D. and B. Smit, *Understanding Molecular Simulation: From Algorithms to Applications*. 2001: Elsevier Science.
133. Andersen, H.C., *Molecular dynamics simulations at constant pressure and/or temperature.* The Journal of Chemical Physics, 1980. **72**(4): p. 2384-2393.
134. Parrinello, M. and A. Rahman, *Polymorphic transitions in single crystals: A new molecular dynamics method.* Journal of Applied Physics, 1981. **52**(12): p. 7182-7190.
135. Berendsen, H.J.C., et al., *Molecular dynamics with coupling to an external bath.* The Journal of Chemical Physics, 1984. **81**(8): p. 3684-3690.
136. Hoover, W.G., *Constant-pressure equations of motion.* Physical Review A, 1986. **34**(3): p. 2499-2500.
137. Hoover, W.G., *Canonical dynamics: Equilibrium phase-space distributions.* Physical Review A, 1985. **31**(3): p. 1695-1697.
138. Nosé, S., *A molecular dynamics method for simulations in the canonical ensemble.* Molecular Physics, 1984. **52**(2): p. 255-268.
139. Yong, X. and L.T. Zhang, *Thermostats and thermostat strategies for molecular dynamics simulations of nanofluidics.* The Journal of Chemical Physics, 2013. **138**(8): p. 084503.
140. Khare, R., J. de Pablo, and A. Yethiraj, *Molecular simulation and continuum mechanics study of simple fluids in non-isothermal planar couette flows.* The Journal of Chemical Physics, 1997. **107**(7): p. 2589-2596.
141. Liang, T., et al., *Reactive Potentials for Advanced Atomistic Simulations.* Annual Review of Materials Research, 2013. **43**(1): p. 109-129.
142. Brenner, D.W., *Empirical potential for hydrocarbons for use in simulating the chemical vapor deposition of diamond films.* Physical Review B, 1990. **42**(15): p. 9458-9471.
143. Jianwei, C., Ç. Tahir, and A.G. William, III, *Studies of fullerenes and carbon nanotubes by an*

extended bond order potential. Nanotechnology, 1999. **10**(3): p. 263.
144. van Duin, A.C.T., et al., *ReaxFF: A Reactive Force Field for Hydrocarbons.* The Journal of Physical Chemistry A, 2001. **105**(41): p. 9396-9409.
145. Plimpton, S., *Fast Parallel Algorithms for Short-Range Molecular Dynamics.* Journal of Computational Physics, 1995. **117**(1): p. 1-19.
146. Humphrey, W., A. Dalke, and K. Schulten, *VMD: Visual molecular dynamics.* Journal of Molecular Graphics, 1996. **14**(1): p. 33-38.
147. Alexander, S., *Visualization and analysis of atomistic simulation data with OVITO–the Open Visualization Tool.* Modelling and Simulation in Materials Science and Engineering, 2010. **18**(1): p. 015012.
148. Szlufarska, I., M. Chandross, and R.W. Carpick, *Recent advances in single-asperity nanotribology.* Journal of Physics D: Applied Physics, 2008. **41**(12): p. 123001.
149. Vanossi, A., et al., *Colloquium: Modeling friction: From nanoscale to mesoscale.* Reviews of Modern Physics, 2013. **85**(2): p. 529-552.
150. Dong, Y., Q. Li, and A. Martini, *Molecular dynamics simulation of atomic friction: A review and guide.* Journal of Vacuum Science & Technology A, 2013. **31**(3): p. 030801.
151. Sawyer, W.G., et al., *Mechanistic Studies in Friction and Wear of Bulk Materials.* Annual Review of Materials Research, 2014. **44**(1): p. 395-427.
152. Ewen, J.P., D.M. Heyes, and D. Dini, *Advances in nonequilibrium molecular dynamics simulations of lubricants and additives.* Friction, 2018. **6**(4): p. 349-386.
153. van Duin, A.C.T., *ReaxFF User Manual (privately provided)*. 2013.
154. Chenoweth, K., A.C.T. van Duin, and W.A. Goddard, *ReaxFF Reactive Force Field for Molecular Dynamics Simulations of Hydrocarbon Oxidation.* The Journal of Physical Chemistry A, 2008. **112**(5): p. 1040-1053.
155. Janssens, G.O.A., et al., *Comparison of Cluster and Infinite Crystal Calculations on Zeolites with the Electronegativity Equalization Method (EEM).* The Journal of Physical Chemistry, 1995. **99**(10): p. 3251-3258.
156. van Duin, A.C.T., J.M.A. Baas, and B. van de Graaf, *Delft molecular mechanics: a new approach to hydrocarbon force fields. Inclusion of a geometry-dependent charge calculation.* Journal of the Chemical Society, Faraday Transactions, 1994. **90**(19): p. 2881-2895.
157. Dittner, M., et al., *Efficient global optimization of reactive force-field parameters.* Journal of Computational Chemistry, 2015. **36**(20): p. 1550-1561.
158. Iype, E., et al., *Parameterization of a reactive force field using a Monte Carlo algorithm.* Journal of Computational Chemistry, 2013. **34**(13): p. 1143-1154.
159. Müller, J. and B. Hartke, *reaxFF Reactive Force Field for Disulfide Mechanochemistry, Fitted to Multireference ab Initio Data.* Journal of Chemical Theory and Computation, 2016. **12**(8): p. 3913-3925.
160. Jaramillo-Botero, A., S. Naserifar, and W.A. Goddard, *General Multiobjective Force Field Optimization Framework, with Application to Reactive Force Fields for Silicon Carbide.* Journal of Chemical Theory and Computation, 2014. **10**(4): p. 1426-1439.
161. Pahari, P. and S. Chaturvedi, *Determination of best-fit potential parameters for a reactive force field using a genetic algorithm.* Journal of Molecular Modeling, 2012. **18**(3): p. 1049-1061.
162. Larentzos, J.P., et al., *Parameterizing Complex Reactive Force Fields Using Multiple Objective Evolutionary Strategies (MOES). Part 1: ReaxFF Models for Cyclotrimethylene Trinitramine (RDX) and 1,1-Diamino-2,2-dinitroethene (FOX-7).* Journal of Chemical Theory and Computation, 2015. **11**(2): p. 381-391.
163. Trnka, T., I. Tvaroška, and J. Koča, *Automated Training of ReaxFF Reactive Force Fields for Energetics of Enzymatic Reactions.* Journal of Chemical Theory and Computation, 2018. **14**(1): p. 291-302.
164. Shchygol, G., et al., *ReaxFF Parameter Optimization with Monte-Carlo and Evolutionary Algorithms: Guidelines and Insights.* Journal of Chemical Theory and Computation, 2019. **15**(12): p. 6799-6812.
165. Martini, A., J.S. Eder, and N. Dörr, *Tribochemistry: A Review of Reactive Molecular Dynamics Simulations.* Lubricants, 2020. **8**(4).
166. Yue, D.-C., et al., *Tribochemical Mechanism of Amorphous Silica Asperities in Aqueous Environment: A Reactive Molecular Dynamics Study.* Langmuir, 2015. **31**(4): p. 1429-1436.
167. Yue, D.-C., et al., *Tribochemistry of Phosphoric Acid Sheared between Quartz Surfaces: A Reactive Molecular Dynamics Study.* The Journal of Physical Chemistry C, 2013. **117**(48): p. 25604-25614.
168. Wen, J., et al., *Atomic insight into tribochemical wear mechanism of silicon at the Si/SiO2*

interface in aqueous environment: Molecular dynamics simulations using ReaxFF reactive force field. Applied Surface Science, 2016. **390**: p. 216-223.
169. Yeon, J., et al., *Mechanochemistry at Solid Surfaces: Polymerization of Adsorbed Molecules by Mechanical Shear at Tribological Interfaces.* ACS Applied Materials & Interfaces, 2017. **9**(3): p. 3142-3148.
170. Mohammadtabar, K., et al., *Heat-, Load-, and Shear-Driven Reactions of Di-tert-butyl Disulfide on Fe(100).* The Journal of Physical Chemistry C, 2019. **123**(32): p. 19688-19692.
171. Mohammadtabar, K., et al., *Reactive Molecular Dynamics Simulations of Thermal Film Growth from Di-tert-butyl Disulfide on an Fe(100) surface.* Langmuir, 2018. **34**(51): p. 15681-15688.
172. Hahn, S.H., et al., *Atomistic understanding of surface wear process of sodium silicate glass in dry versus humid environments.* Journal of the American Ceramic Society, 2020. **103**(5): p. 3060-3069.
173. Khajeh, A., et al., *Statistical Analysis of Tri-Cresyl Phosphate Conversion on an Iron Oxide Surface Using Reactive Molecular Dynamics Simulations.* The Journal of Physical Chemistry C, 2019. **123**(20): p. 12886-12893.
174. Ewen, J.P., et al., *Substituent Effects on the Thermal Decomposition of Phosphate Esters on Ferrous Surfaces.* The Journal of Physical Chemistry C, 2020. **124**(18): p. 9852-9865.
175. Ito, K., et al., *Formation Mechanism of a Low Friction ZDDP Tribofilm on Iron Oxide.* Tribology Transactions, 2007. **50**(2): p. 211-216.
176. Abdala, D.B., et al., *Residence time and pH effects on the bonding configuration of orthophosphate surface complexes at the goethite/water interface as examined by Extended X-ray Absorption Fine Structure (EXAFS) spectroscopy.* Journal of Colloid and Interface Science, 2015. **442**: p. 15-21.
177. Abdala, D.B., et al., *Surface loading effects on orthophosphate surface complexation at the goethite/water interface as examined by extended X-ray Absorption Fine Structure (EXAFS) spectroscopy.* Journal of Colloid and Interface Science, 2015. **437**: p. 297-303.
178. Harvey, O.R. and R.D. Rhue, *Kinetics and energetics of phosphate sorption in a multi-component Al(III)–Fe(III) hydr(oxide) sorbent system.* Journal of Colloid and Interface Science, 2008. **322**(2): p. 384-393.
179. Elzinga, E.J. and D.L. Sparks, *Phosphate adsorption onto hematite: An in situ ATR-FTIR investigation of the effects of pH and loading level on the mode of phosphate surface complexation.* Journal of Colloid and Interface Science, 2007. **308**(1): p. 53-70.
180. Atkinson, R.J., A.M. Posner, and J.P. Quirk, *Kinetics of isotopic exchange of phosphate at the α-FeOOH-aqueous solution interface.* Journal of Inorganic and Nuclear Chemistry, 1972. **34**(7): p. 2201-2211.
181. Belelli, P.G., S.A. Fuente, and N.J. Castellani, *Phosphate adsorption on goethite and Al-rich goethite.* Computational Materials Science, 2014. **85**: p. 59-66.
182. Acelas, N.Y., et al., *Density functional theory characterization of phosphate and sulfate adsorption on Fe-(hydr)oxide: Reactivity, pH effect, estimation of Gibbs free energies, and topological analysis of hydrogen bonds.* Computational and Theoretical Chemistry, 2013. **1005**: p. 16-24.
183. Kubicki, J.D., et al., *ATR–FTIR and Density Functional Theory Study of the Structures, Energetics, and Vibrational Spectra of Phosphate Adsorbed onto Goethite.* Langmuir, 2012. **28**(41): p. 14573-14587.
184. Kubicki, J.D., et al., *Surface complex structures modelled with quantum chemical calculations: carbonate, phosphate, sulphate, arsenate and arsenite.* European Journal of Soil Science, 2007. **58**(4): p. 932-944.
185. Kwon, K.D. and J.D. Kubicki, *Molecular Orbital Theory Study on Surface Complex Structures of Phosphates to Iron Hydroxides: Calculation of Vibrational Frequencies and Adsorption Energies.* Langmuir, 2004. **20**(21): p. 9249-9254.
186. Arai, Y. and D.L. Sparks, *ATR–FTIR Spectroscopic Investigation on Phosphate Adsorption Mechanisms at the Ferrihydrite–Water Interface.* Journal of Colloid and Interface Science, 2001. **241**(2): p. 317-326.
187. Hoang, K. and M.D. Johannes, *First-principles studies of the effects of impurities on the ionic and electronic conduction in LiFePO4.* Journal of Power Sources, 2012. **206**(Supplement C): p. 274-281.
188. Ta, H.T.T., et al., *Chemical Origin of Sodium Phosphate Interactions on Iron and Iron Oxide Surfaces by First Principle Calculations.* The Journal of Physical Chemistry C, 2018. **122**(1): p. 635-647.
189. Haw, S.M. and N.J. Mosey, *Tribochemistry of Aldehydes Sheared between (0001) Surfaces of α-Alumina from First-Principles Molecular Dynamics.* The Journal of Physical Chemistry C, 2012.

116(3): p. 2132-2145.
190. Kresse, G. and J. Furthmüller, *Efficient iterative schemes for ab initio total-energy calculations using a plane-wave basis set.* Physical Review B, 1996. **54**(16): p. 11169-11186.
191. Blöchl, P.E., *Projector augmented-wave method.* Physical Review B, 1994. **50**(24): p. 17953-17979.
192. Zhong, J., L.G. Hector, and J.B. Adams, *Dynamic decomposition of aliphatic molecules on Al(111) from ab initio molecular dynamics.* Physical Review B, 2009. **79**(12): p. 125419.
193. Monkhorst, H.J. and J.D. Pack, *Special points for Brillouin-zone integrations.* Physical Review B, 1976. **13**(12): p. 5188-5192.
194. Methfessel, M. and A.T. Paxton, *High-precision sampling for Brillouin-zone integration in metals.* Physical Review B, 1989. **40**(6): p. 3616-3621.
195. Alavi, A., et al., *CO Oxidation on Pt(111): An Ab Initio Density Functional Theory Study.* Physical Review Letters, 1998. **80**(16): p. 3650-3653.
196. Zhang, C.J. and P. Hu, *CO Oxidation on Pd(100) and Pd(111): A Comparative Study of Reaction Pathways and Reactivity at Low and Medium Coverages.* Journal of the American Chemical Society, 2001. **123**(6): p. 1166-1172.
197. Michaelides, A. and P. Hu, *Catalytic Water Formation on Platinum: A First-Principles Study.* Journal of the American Chemical Society, 2001. **123**(18): p. 4235-4242.
198. Feynman, R.P., *Forces in Molecules.* Physical Review, 1939. **56**(4): p. 340-343.
199. Bučko, T., J. Hafner, and J.G. Ángyán, *Geometry optimization of periodic systems using internal coordinates.* The Journal of Chemical Physics, 2005. **122**(12): p. 124508.
200. Silvi, B. and A. Savin, *Classification of chemical bonds based on topological analysis of electron localization functions.* Nature, 1994. **371**(6499): p. 683-686.
201. Becke, A.D. and K.E. Edgecombe, *A simple measure of electron localization in atomic and molecular systems.* The Journal of Chemical Physics, 1990. **92**(9): p. 5397-5403.
202. Savin, A., et al., *ELF: The Electron Localization Function.* Angewandte Chemie International Edition in English, 1997. **36**(17): p. 1808-1832.
203. Maintz, S., et al., *LOBSTER: A tool to extract chemical bonding from plane-wave based DFT.* Journal of Computational Chemistry, 2016. **37**(11): p. 1030-1035.
204. Segall, M.D., et al., *Population analysis of plane-wave electronic structure calculations of bulk materials.* Physical Review B, 1996. **54**(23): p. 16317-16320.
205. Delle Site, L., et al., *Polymers near Metal Surfaces: Selective Adsorption and Global Conformations.* Physical Review Letters, 2002. **89**(15): p. 156103.
206. Banach, M. and A. Makara, *Thermal Decomposition of Sodium Phosphates.* Journal of Chemical & Engineering Data, 2011. **56**(7): p. 3095-3099.
207. Larsen, M., R. Willett, and R.G. Yount, *Imidodiphosphate and Pyrophosphate: Possible Biological Significance of Similar Structures.* Science, 1969. **166**(3912): p. 1510-1511.
208. MacArthur, D.M. and C.A. Beevers, *The crystal structure of sodium pyrophosphate decahydrate, Na4P2O7.10H2O.* Acta Crystallographica, 1957. **10**(6): p. 428-432.
209. Cruickshank, D., *Refinements of structures containing bonds between Si, P, S or Cl and O or N. III. Na5P3O10, phase II.* Acta Crystallographica, 1964. **17**(6): p. 674-675.
210. Hoppe, U., et al., *Neutron and X-ray Diffraction Study on the Structure of Ultraphosphate Glasses.* Zeitschrift für Naturforschung A, 1997. **52**(3): p. 259.
211. Le Beuze, A., et al., *Comprehensive study of the valence band of standard alkali-metal and indium phosphorus oxide salts through x-ray photoemission spectroscopy and extended H\"uckel theory tight-binding analysis: A contribution towards the elucidation of local order in oxides on InP surfaces.* Physical Review B, 1989. **39**(15): p. 11055-11065.
212. Hoppe, U., et al., *Structural specifics of phosphate glasses probed by diffraction methods: a review.* Journal of Non-Crystalline Solids, 2000. **263-264**(Supplement C): p. 29-47.
213. Hoppe, U., et al., *Variation in P-O Bonding in Phosphate Glasses - A Neutron Diffraction Study.* Zeitschrift fur Naturforschung - Section A Journal of Physical Sciences, 2000. **55**(3-4): p. 369-380.
214. Uchino, T. and Y. Ogata, *Ab initio molecular orbital calculations on the electronic structure of phosphate glasses. Binary alkali metaphosphate glasses.* Journal of Non-Crystalline Solids, 1995. **191**(1): p. 56-70.
215. Musinu, A., G. Piccaluga, and G. Pinna, *X-ray Diffraction Investigation of Iron in Sodium Phosphate Glasses.* The Journal of Physical Chemistry, 1996. **100**(30): p. 12462-12466.
216. Uchino, T. and Y. Ogata, *Ab initio molecular orbital calculations on the electronic structure of phosphate glasses. Sodium phosphate glasses.* Journal of Non-Crystalline Solids, 1995. **181**(1–2): p. 175-188.

217. Bingham, P.A. and E.R. Barney, *Structure of iron phosphate glasses modified by alkali and alkaline earth additions: neutron and x-ray diffraction studies.* Journal of Physics: Condensed Matter, 2012. **24**(17): p. 175403.
218. Tang, J.-J. and B. Liu, *Reactivity of the Fe2O3(0001) Surface for Methane Oxidation: A GGA + U Study.* The Journal of Physical Chemistry C, 2016. **120**(12): p. 6642-6650.
219. Trainor, T.P., et al., *Structure and reactivity of the hydrated hematite (0 0 0 1) surface.* Surface Science, 2004. **573**(2): p. 204-224.
220. Ta, T.D., et al., *Adsorption of Normal-Alkanes on Fe(110), FeO(110), and Fe2O3(0001): Influence of Iron Oxide Surfaces.* The Journal of Physical Chemistry C, 2015. **119**(23): p. 12999-13010.
221. Luengo, C.V., N.J. Castellani, and R.M. Ferullo, *Quantum chemical study on surface complex structures of phosphate on gibbsite.* Spectrochimica Acta Part A: Molecular and Biomolecular Spectroscopy, 2015. **147**: p. 193-199.
222. Hoppe, U., et al., *The Fe–O coordination in iron phosphate glasses by x-ray diffraction with high energy photons.* Journal of Physics: Condensed Matter, 2003. **15**(36): p. 6143.
223. Zhang, Z., et al., *Tribofilms generated from ZDDP and DDP on steel surfaces:Part 2, chemistry.* Tribology Letters, 2005. **19**(3): p. 221-229.
224. Bay, N., et al., *Environmentally benign tribo-systems for metal forming.* CIRP Annals, 2010. **59**(2): p. 760-780.
225. Stoch, P., et al., *Structural properties of iron-phosphate glasses: spectroscopic studies and ab initio simulations.* Physical Chemistry Chemical Physics, 2014. **16**(37): p. 19917-19927.
226. Yang, T., et al., *Interaction of alkali metals with the Fe3O4(1 1 1) Surface.* Surface Science, 2009. **603**(1): p. 78-83.
227. Greaves, G.N. and S. Sen, *Inorganic glasses, glass-forming liquids and amorphizing solids.* Advances in Physics, 2007. **56**(1): p. 1-166.
228. Boyd, D.B., *Topography of the electron density in pyrophosphate bonds.* Theoretica chimica acta, 1970. **18**(3): p. 184-192.
229. de Groot, F.M.F., et al., *Oxygen 1s x-ray-absorption edges of transition-metal oxides.* Physical Review B, 1989. **40**(8): p. 5715-5723.
230. Ringwood, A.E., *Composition of the core and implications for origin of the earth.* GEOCHEMICAL JOURNAL, 1977. **11**(3): p. 111-135.
231. Evans, R.C., *An Introduction to Crystal Chemistry*. 1964: Cambridge University Press.
232. Wang, C., et al., *Morphology and Electronic Structure of the Oxide Shell on the Surface of Iron Nanoparticles.* Journal of the American Chemical Society, 2009. **131**(25): p. 8824-8832.
233. Hudgens, J.J. and S.W. Martin, *Glass Transition and Infrared Spectra of Low-Alkali, Anhydrous Lithium Phosphate Glasses.* Journal of the American Ceramic Society, 1993. **76**(7): p. 1691-1696.
234. Al-Hasni, B. and G. Mountjoy, *Structural investigation of iron phosphate glasses using molecular dynamics simulation.* Journal of Non-Crystalline Solids, 2011. **357**(15): p. 2775-2779.
235. Knowles, J.C., *Phosphate based glasses for biomedical applications.* Journal of Materials Chemistry, 2003. **13**(10): p. 2395-2401.
236. Musinu, A., G. Piccaluga, and G. Pinna, *Structural properties of lead-iron phosphate glasses by X-ray diffraction.* Journal of Non-Crystalline Solids, 1990. **122**(1): p. 52-58.
237. Yu, D., et al., *Structural and Catalytic Investigation of Mesoporous Iron Phosphate.* The Journal of Physical Chemistry C, 2007. **111**(39): p. 14394-14399.
238. Song, Y., et al., *New Iron(III) Phosphate Phases: Crystal Structure and Electrochemical and Magnetic Properties.* Inorganic Chemistry, 2002. **41**(22): p. 5778-5786.
239. Berkani, S., et al., *Model formation of ZDDP tribofilm from a mixture of zinc metaphosphate and goethite.* Tribology International, 2014. **79**: p. 197-203.
240. Cooper, R.F., J.B. Fanselow, and D.B. Poker, *The mechanism of oxidation of a basaltic glass: Chemical diffusion of network-modifying cations.* Geochimica et Cosmochimica Acta, 1996. **60**(17): p. 3253-3265.
241. Moguš-Milanković, A., et al., *Mixed ion–polaron transport in Na2O–PbO–Fe2O3–P2O5 glasses.* Journal of Non-Crystalline Solids, 2004. **342**(1): p. 97-109.
242. Smedskjaer, M.M., et al., *Modifying glass surfaces via internal diffusion.* Journal of Non-Crystalline Solids, 2010. **356**(6): p. 290-298.
243. Malki, M., et al., *Electrical conductivity of iron-bearing silicate glasses and melts. Implications for the mechanisms of iron redox reactions.* Geochimica et Cosmochimica Acta, 2015. **165**: p. 137-147.
244. Fatti, G., et al., *Phosphorus Adsorption on Fe(110): An ab Initio Comparative Study of Iron Passivation by Different Adsorbates.* The Journal of Physical Chemistry C, 2018. **122**(49): p.

28105-28112.
245. Le, M.H., et al., *Depolymerization of sodium polyphosphates on an iron oxide surface at high temperature.* Physical Chemistry Chemical Physics, 2018. **20**(11): p. 7819-7835.
246. Dudarev, S.L., et al., *Electron-energy-loss spectra and the structural stability of nickel oxide: An LSDA+U study.* Physical Review B, 1998. **57**(3): p. 1505-1509.
247. Huang, X., S.K. Ramadugu, and S.E. Mason, *Surface-Specific DFT + U Approach Applied to α-Fe2O3(0001).* The Journal of Physical Chemistry C, 2016. **120**(9): p. 4919-4930.
248. Parkinson, G.S., *Iron oxide surfaces.* Surface Science Reports, 2016. **71**(1): p. 272-365.
249. Kiejna, A. and T. Pabisiak, *Mixed Termination of Hematite (α-Fe2O3)(0001) Surface.* The Journal of Physical Chemistry C, 2013. **117**(46): p. 24339-24344.
250. Manz, T.A., *Introducing DDEC6 atomic population analysis: part 3. Comprehensive method to compute bond orders.* RSC Advances, 2017. **7**(72): p. 45552-45581.
251. Manz, T.A. and N.G. Limas, *Introducing DDEC6 atomic population analysis: part 1. Charge partitioning theory and methodology.* RSC Advances, 2016. **6**(53): p. 47771-47801.
252. Limas, N.G. and T.A. Manz, *Introducing DDEC6 atomic population analysis: part 2. Computed results for a wide range of periodic and nonperiodic materials.* RSC Advances, 2016. **6**(51): p. 45727-45747.
253. Rohling, R.Y., et al., *Correlations between Density-Based Bond Orders and Orbital-Based Bond Energies for Chemical Bonding Analysis.* The Journal of Physical Chemistry C, 2019. **123**(5): p. 2843-2854.
254. van Santen, R.A., I. Tranca, and E.J.M. Hensen, *Theory of surface chemistry and reactivity of reducible oxides.* Catalysis Today, 2015. **244**: p. 63-84.
255. Christie, J.K., et al., *Structures and properties of phosphate-based bioactive glasses from computer simulation: a review.* Journal of Materials Chemistry B, 2017. **5**(27): p. 5297-5306.
256. Di Tommaso, D., et al., *Modelling the structural evolution of ternary phosphate glasses from melts to solid amorphous materials.* Journal of Materials Chemistry B, 2013. **1**(38): p. 5054-5066.
257. Speghini, A., et al., *Structural investigation of NaPO3 glass using molecular dynamics simulation.* Physical Chemistry Chemical Physics, 1999. **1**(1): p. 173-177.
258. Jost, K., *Die Struktur des Kurrol'schen Na-Salzes (NaPO3)x, Typ B.* Acta Crystallographica, 1963. **16**(7): p. 640-642.
259. Jost, K., *Die Struktur des Kurrol'schen Na-Salzes (NaPO3)x Typ A.* Acta Crystallographica, 1961. **14**(8): p. 844-847.
260. Callis, C.F., J.R. Van Wazer, and J.S. Metcalf, *Structure and Properties of the Condensed Phosphates. VIII. Density and Surface Tension of Molten Sodium Phosphates.* Journal of the American Chemical Society, 1955. **77**(6): p. 1468-1470.
261. Kraka, E., D. Setiawan, and D. Cremer, *Re-evaluation of the bond length–bond strength rule: The stronger bond is not always the shorter bond.* Journal of Computational Chemistry, 2016. **37**(1): p. 130-142.
262. Seifitokaldani, A., et al., *Important Variation in Vibrational Properties of LiFePO4 and FePO4 Induced by Magnetism.* Scientific Reports, 2016. **6**(1): p. 33033.
263. Lee, K., et al., *Measurement of Diphosphine σ-Donor and π-Acceptor Properties in d0 Titanium Complexes Using Ligand K-Edge XAS and TDDFT.* Inorganic Chemistry, 2018. **57**(16): p. 10277-10286.
264. Ardizzoia, G.A. and S. Brenna, *Interpretation of Tolman electronic parameters in the light of natural orbitals for chemical valence.* Physical Chemistry Chemical Physics, 2017. **19**(8): p. 5971-5978.
265. Setiawan, D., et al., *Direct Measure of Metal–Ligand Bonding Replacing the Tolman Electronic Parameter.* Inorganic Chemistry, 2016. **55**(5): p. 2332-2344.
266. Mitoraj, M.P. and A. Michalak, *σ-Donor and π-Acceptor Properties of Phosphorus Ligands: An Insight from the Natural Orbitals for Chemical Valence.* Inorganic Chemistry, 2010. **49**(2): p. 578-582.
267. Leyssens, T., et al., *Insight into metal–phosphorus bonding from analysis of the electronic structure of redox pairs of metal–phosphine complexes.* New Journal of Chemistry, 2005. **29**(11): p. 1424-1430.
268. Tolman, C.A., *Electron donor-acceptor properties of phosphorus ligands. Substituent additivity.* Journal of the American Chemical Society, 1970. **92**(10): p. 2953-2956.
269. Harrison, J.F., *Electronic Structure of Diatomic Molecules Composed of a First-Row Transition Metal and Main-Group Element (H−F).* Chemical Reviews, 2000. **100**(2): p. 679-716.
270. Tang, P., N.A.W. Holzwarth, and Y.A. Du, *Comparison of the electronic structures of four crystalline phases of FePO4.* Physical Review B, 2007. **76**(17): p. 174118.

271. Piccinin, S., *The band structure and optical absorption of hematite (α-Fe2O3): a first-principles GW-BSE study.* Physical Chemistry Chemical Physics, 2019. **21**(6): p. 2957-2967.
272. Novotny, Z., et al., *Probing the surface phase diagram of Fe3O4(001) towards the Fe-rich limit: Evidence for progressive reduction of the surface.* Physical Review B, 2013. **87**(19): p. 195410.
273. Mulakaluri, N., et al., *Partial Dissociation of Water on Fe3O4(001): Adsorbate Induced Charge and Orbital Order.* Physical Review Letters, 2009. **103**(17): p. 176102.
274. Parkinson, G.S., et al., *Antiphase domain boundaries at the Fe3O4(001) surface.* Physical Review B, 2012. **85**(19): p. 195450.
275. Persson, P., N. Nilsson, and S. Sjöberg, *Structure and Bonding of Orthophosphate Ions at the Iron Oxide–Aqueous Interface.* Journal of Colloid and Interface Science, 1996. **177**(1): p. 263-275.
276. Philippon, D., et al., *Experimental simulation of phosphites additives tribochemical reactions by gas phase lubrication.* Tribology - Materials, Surfaces & Interfaces, 2007. **1**(3): p. 113-123.
277. Erlebach, A., et al., *Structure evolution of nanoparticulate Fe2O3.* Nanoscale, 2015. **7**(7): p. 2960-2969.
278. Gutsev, G.L., et al., *Structure and Properties of Fen, Fen–, and Fen+ Clusters, n = 7–20.* The Journal of Physical Chemistry A, 2012. **116**(41): p. 10218-10228.
279. Tran, N.V., et al., *An ab initio study on the effects of Na passivation on friction reduction of an iron oxide surface.* Journal of Applied Physics, 2020. **127**(6): p. 065305.
280. Rana, R. and W. Tysoe, *Tribochemical Mechanisms of Trimethyl and Triethyl Phosphite on Oxidized Iron in Ultrahigh Vacuum.* Tribology Letters, 2019. **67**(3): p. 93.
281. Lesher, C.E., *Self-diffusion in Silicate Melts: Theory, Observations and Applications to Magmatic Systems.* Reviews in Mineralogy and Geochemistry, 2010. **72**(1): p. 269-309.
282. Cochain, B., O. Pinet, and P. Richet, *Diffusion of sodium ions driven by charge compensation as the rate-limiting step of internal redox reactions.* Journal of Non-Crystalline Solids, 2013. **365**: p. 23-26.
283. Rao, P.R., et al., *Electrical and spectroscopic properties of Fe2O3 doped Na2SO4–BaO–P2O5 glass system.* Journal of Non-Crystalline Solids, 2012. **358**(23): p. 3255-3267.
284. Smedskjær, M.M., *Structural and Topological Basis of Glass Properties and Diffusion*. 2011: Institut for Kemi, Miljø og Bioteknologi, Aalborg Universitet.
285. Greaves, G.N., *EXAFS, glass structure and diffusion.* Philosophical Magazine B, 1989. **60**(6): p. 793-800.
286. Greaves, G.N., *EXAFS and the structure of glass.* Journal of Non-Crystalline Solids, 1985. **71**(1): p. 203-217.
287. Swenson, J. and S. Adams, *Mixed Alkali Effect in Glasses.* Physical Review Letters, 2003. **90**(15): p. 155507.
288. Tsuchida, J.E., et al., *Ionic conductivity and mixed-ion effect in mixed alkali metaphosphate glasses.* Physical Chemistry Chemical Physics, 2017. **19**(9): p. 6594-6600.
289. Shannon, R.D., *Revised effective ionic radii and systematic studies of interatomic distances in halides and chalcogenides.* Acta Crystallographica Section A, 1976. **32**(5): p. 751-767.
290. Duffy, J.A., *A review of optical basicity and its applications to oxidic systems.* Geochimica et Cosmochimica Acta, 1993. **57**(16): p. 3961-3970.
291. Mills, K.C., *The Influence of Structure on the Physico-chemical Properties of Slags.* ISIJ International, 1993. **33**(1): p. 148-155.
292. Sun, H., *COMPASS: An ab Initio Force-Field Optimized for Condensed-Phase ApplicationsOverview with Details on Alkane and Benzene Compounds.* Journal of Physical Chemistry B, 1998. **102**(38): p. 7338-7364.
293. Wen, J., et al., *Atomistic mechanisms of Si chemical mechanical polishing in aqueous H2O2: ReaxFF reactive molecular dynamics simulations.* Computational Materials Science, 2017. **131**: p. 230-238.
294. Mueller, J.E., A.C.T. van Duin, and W.A. Goddard, *Development and Validation of ReaxFF Reactive Force Field for Hydrocarbon Chemistry Catalyzed by Nickel.* The Journal of Physical Chemistry C, 2010. **114**(11): p. 4939-4949.
295. Fogarty, J.C., et al., *A reactive molecular dynamics simulation of the silica-water interface.* The Journal of Chemical Physics, 2010. **132**(17): p. 174704.
296. Monti, S., et al., *Exploration of the Conformational and Reactive Dynamics of Glycine and Diglycine on TiO2: Computational Investigations in the Gas Phase and in Solution.* The Journal of Physical Chemistry C, 2012. **116**(8): p. 5141-5150.
297. Chenoweth, K., A.C.T. van Duin, and W.A. Goddard Iii, *The ReaxFF Monte Carlo Reactive Dynamics Method for Predicting Atomistic Structures of Disordered Ceramics: Application to the Mo3VOx Catalyst.* Angewandte Chemie International Edition, 2009. **48**(41): p. 7630-7634.

298. Vasenkov, A., et al., *Reactive molecular dynamics study of Mo-based alloys under high-pressure, high-temperature conditions.* Journal of Applied Physics, 2012. **112**(1): p. 013511.
299. Zhu, R., et al., *Characterization of the active site of yeast RNA polymerase II by DFT and ReaxFF calculations.* Theoretical Chemistry Accounts, 2008. **120**(4-6): p. 479-489.
300. Xiao, H., et al., *Development of a Transferable Reactive Force Field of P/H Systems: Application to the Chemical and Mechanical Properties of Phosphorene.* The Journal of Physical Chemistry A, 2017. **121**(32): p. 6135-6149.
301. Aryanpour, M., A.C.T. van Duin, and J.D. Kubicki, *Development of a Reactive Force Field for Iron−Oxyhydroxide Systems.* The Journal of Physical Chemistry A, 2010. **114**(21): p. 6298-6307.
302. Larsson, H.R., A.C.T. van Duin, and B. Hartke, *Global optimization of parameters in the reactive force field ReaxFF for SiOH.* Journal of Computational Chemistry, 2013. **34**(25): p. 2178-2189.
303. Kresse, G. and D. Joubert, *From ultrasoft pseudopotentials to the projector augmented-wave method.* Physical Review B, 1999. **59**(3): p. 1758-1775.
304. Kim, S.-Y., A.C.T. van Duin, and J.D. Kubicki, *Molecular dynamics simulations of the interactions between TiO2 nanoparticles and water with Na+ and Cl−, methanol, and formic acid using a reactive force field.* Journal of Materials Research, 2013. **28**(3): p. 513-520.
305. Shin, Y.K., et al., *Development of a ReaxFF reactive force field for lithium ion conducting solid electrolyte Li1+xAlxTi2−x(PO4)3 (LATP).* Physical Chemistry Chemical Physics, 2018. **20**(34): p. 22134-22147.
306. Birch, F., *Finite Elastic Strain of Cubic Crystals.* Physical Review, 1947. **71**(11): p. 809-824.
307. Rayne, J.A. and B.S. Chandrasekhar, *Elastic Constants of Iron from 4.2 to 300°K.* Physical Review, 1961. **122**(6): p. 1714-1716.
308. Liu, M. and L.-g. Liu, *Bulk moduli of wüstite and periclase: a comparative study.* Physics of the Earth and Planetary Interiors, 1987. **45**(3): p. 273-279.
309. Reichmann, H.J. and S.D. Jacobsen, *High-pressure elasticity of a natural magnetite crystal.* American Mineralogist, 2004. **89**(7): p. 1061-1066.
310. Olsen, J.S., et al., *A study of the crystal structure of Fe2O3in the pressure range up to 65 GPa using synchrotron radiation.* Physica Scripta, 1991. **43**(3): p. 327-330.
311. Kittel, C., *Introduction to Solid State Physics*. 8 ed. 2005: Hoboken, NJ: John Wiley & Sons.
312. Chase, M.W.J., *NIST-JANAF Thermochemical Tables*. 4th ed. 1998: American Institute of Physics.
313. Irving, R.J. and H. McKerrell, *Standard heats of formation of two sodium pyrophosphates, sodium trimetaphosphate, and sodium tetrametaphosphate.* Transactions of the Faraday Society, 1968. **64**(0): p. 879-882.
314. La Iglesia, A., *Estimating the thermodynamic properties of phosphate minerals at high and low temperature from the sum of constituent units.* Estudios Geologicos (Madrid), 2009. **65**(2): p. 109-119.
315. Chambers, S.A. and S.I. Yi, *Fe termination for α-Fe2O3(0001) as grown by oxygen-plasma-assisted molecular beam epitaxy.* Surface Science, 1999. **439**(1–3): p. L785-L791.
316. Wasserman, E., et al., *Ewald methods for polarizable surfaces with application to hydroxylation and hydrogen bonding on the (012) and (001) surfaces of α-Fe2O3.* Surface Science, 1997. **385**(2–3): p. 217-239.
317. Cooke, D.J., S.E. Redfern, and S.C. Parker, *Atomistic simulation of the structure and segregation to the (0001) and surfaces of Fe2O3.* Physics and Chemistry of Minerals, 2004. **31**(8): p. 507-517.
318. Rohrbach, A., J. Hafner, and G. Kresse, *Ab initio study of the (0001) surfaces of hematite and chromia: Influence of strong electronic correlations.* Physical Review B, 2004. **70**(12): p. 125426.
319. Guo, H. and A.S. Barnard, *Thermodynamic modelling of nanomorphologies of hematite and goethite.* Journal of Materials Chemistry, 2011. **21**(31): p. 11566-11577.
320. Aruja, E. and H. Perlitz, *Neubestimmung der Gitterkonstante von Natrium*, in *Zeitschrift für Kristallographie - Crystalline Materials*. 1939. p. 195.
321. Wyckoff, R.W.G., *Second edition. Interscience Publishers, New York, New York Sample at T = 5 K Hexagonal closest packed, hcp, structure.* Crystal Structures, 1963. **1**: p. 7-76.
322. Klein, W., K. Armbruster, and M. Jansen, *Synthesis and crystal structure determination of sodium ozonide.* Chemical Communications, 1998(6): p. 707-708.
323. Carter, G.F. and D.H. Templeton, *Polymorphism of Sodium Superoxide.* Journal of the American Chemical Society, 1953. **75**(21): p. 5247-5249.
324. Wood, I.G., et al., *Thermoelastic properties of magnesiowustite, (Mg1-xFex)O: determination of the Anderson-Gruneisen parameter by time-of-flight neutron powder diffraction at simultaneous high pressures and temperatures.* Journal of Applied Crystallography, 2008. **41**(5): p. 886-896.
325. Jette, E.R. and F. Foote, *An X-Ray Study of the Wüstite (FeO) Solid Solutions.* Journal of Chemical

Physics, 1933. **1**(1): p. 29-36.
326. Bragg, W.H., *The Structure of Magnetite and the Spinels.* Nature, 1915. **95**(2386): p. 561-561.
327. Rozenberg, G.K., et al., *High-pressure structural studies of hematite Fe2O3.* Physical Review B, 2002. **65**(6): p. 064112.
328. Zintl, E., A. Harder, and B. Dauth, *Gitterstruktur der Oxyde, Sulfide, Selenide und Telluride des Lithiums, Natriums und Kaliums.* Zeitschrift für Elektrochemie und angewandte physikalische Chemie, 1934. **40**(8): p. 588-593.
329. Simon, A.B., H.; Craubner, H., *Crystal structure of ordered white phosphorus (beta-P) Locality: synthetic Sample: at T = 158.15 K Note: beta phase; transforms from alpha phase at T = 196.75 K.* Phosphorus and Sulfur and the Related Elements, 1987. **30**: p. 507 - 510.
330. Lange, S., P. Schmidt, and T. Nilges, *Au3SnP7@Black Phosphorus: An Easy Access to Black Phosphorus.* Inorganic Chemistry, 2007. **46**(10): p. 4028-4035.
331. Stachel, D., I. Svoboda, and H. Fuess, *Phosphorus Pentoxide at 233 K.* Acta Crystallographica Section C, 1995. **51**(6): p. 1049-1050.
332. Jansen, M., M. Voss, and H.-J. Deiseroth, *Struktureigenschaften der Phosphoroxide im festen Aggregatzustand.* Angewandte Chemie, 1981. **93**(11): p. 1023-1024.
333. Jost, K.H.S., M., *Structure of Phosphorus(III, V) Oxide P4O7.* Acta Crystallographica B (24,1968-38,1982), 1981. **37**: p. 222 - 224.
334. Leung, K.Y. and C. Calvo, *The Structure of Na4P2O7 at 22 °C.* Canadian Journal of Chemistry, 1972. **50**(16): p. 2519-2526.
335. Parada, C., et al., *Crystal Growth, Structure, and Magnetic Properties of a New Polymorph of Fe2P2O7.* Chemistry of Materials, 2003. **15**(17): p. 3347-3351.
336. Ijjaali, M., et al., *ChemInform Abstract: Synthesis, Structure and Physical Properties of a Mixed-Valence Iron Diphosphate Fe3(P2O7)2: First Example of Trigonal Prismatic Fe2+ with O2-Ligands.* ChemInform, 1991. **22**(45): p. 983-998.
337. Persson, K., *Materials Data on NaFeO2 (SG:166) by Materials Project*. 2014: ; LBNL Materials Project; Lawrence Berkeley National Lab. (LBNL), Berkeley, CA (United States).
338. Gabelica-Robert, M., et al., *The pyrophosphate NaFeP2O7: A cage structure.* Journal of Solid State Chemistry, 1982. **45**(3): p. 389-395.
339. Barpanda, P., et al., *Na2FeP2O7: A Safe Cathode for Rechargeable Sodium-ion Batteries.* Chemistry of Materials, 2013. **25**(17): p. 3480-3487.
340. Chihi, T. and M. Fatmi, *Structural, elastic, electronic and optical properties of black phosphorus, TiP and VP; ab initio study.* Chinese Journal of Physics, 2016. **54**(5): p. 734-743.

Appendix A Supporting material for chapter 3

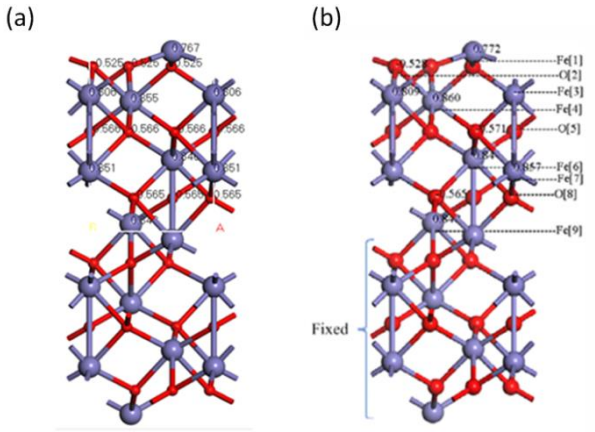

Figure A-1. Partial charges of nine top layers of Fe_2O_3(0001) surface of (a) current work and (b) Ta et al.[220]

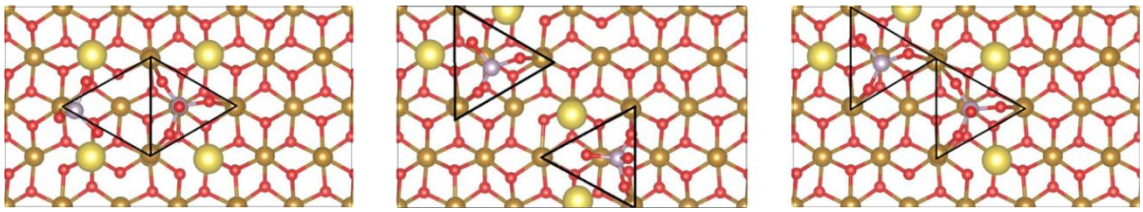

Figure A-2: Different relative position of Fe adsorption sites triangles for PO_4 or PO_3 units. The triangles can share one edge (left), be separate (middle) and share one vertex (right). Red, gold, purple and yellow spheres represent oxygen, iron, phosphorus and sodium atoms, respectively.

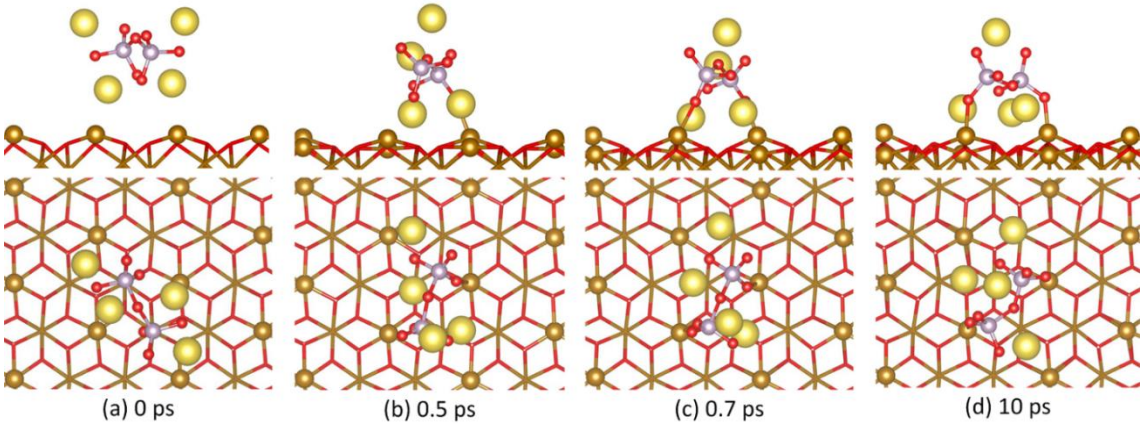

Figure A-3: Snapshots of AIMD at 300K of $Na_4P_2O_7$ cluster on Fe_2O_3 surface for 0 ps (a), 0.5 ps (b), 0.7 ps (c), and 10 ps (d). Structures have been displayed in side view (upper) and top view (lower). Red, gold, purple and yellow spheres represent oxygen, iron on top surface, phosphorus and sodium atoms, respectively. Surface oxygen and lower-layered iron atoms have been removed for apparent visualization.

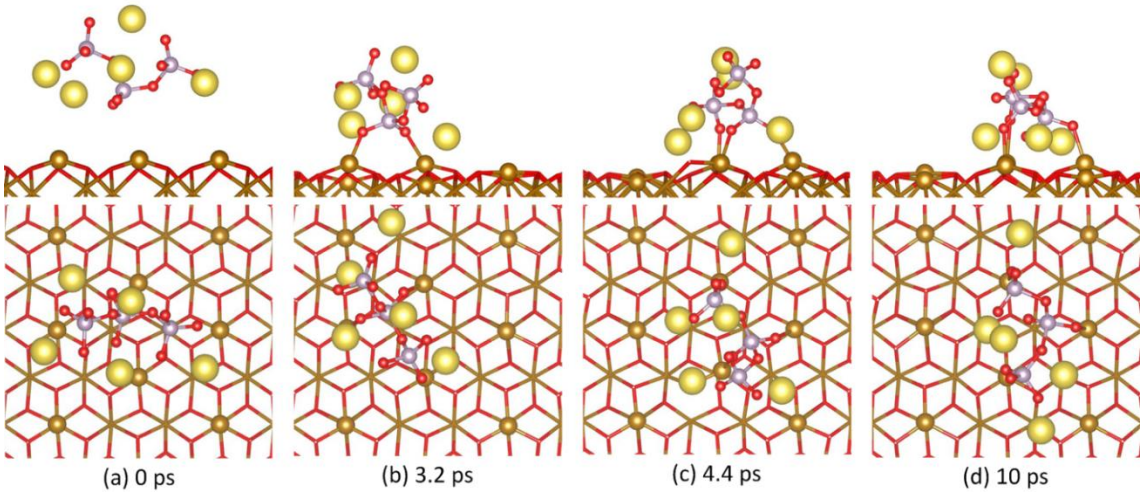

Figure A-4: Snapshots of AIMD at 300K of $Na_5P_3O_{10}$ cluster on Fe_2O_3 surface for 0 ps (a), 3.2 ps (b), 4.4 ps (c), and 10 ps (d). Structures have been displayed in side view (upper) and top view (lower). Red, gold, purple and yellow spheres represent oxygen, iron on top surface, phosphorus and sodium atoms, respectively. Surface oxygen and lower-layered iron atoms have been removed for apparent visualization.

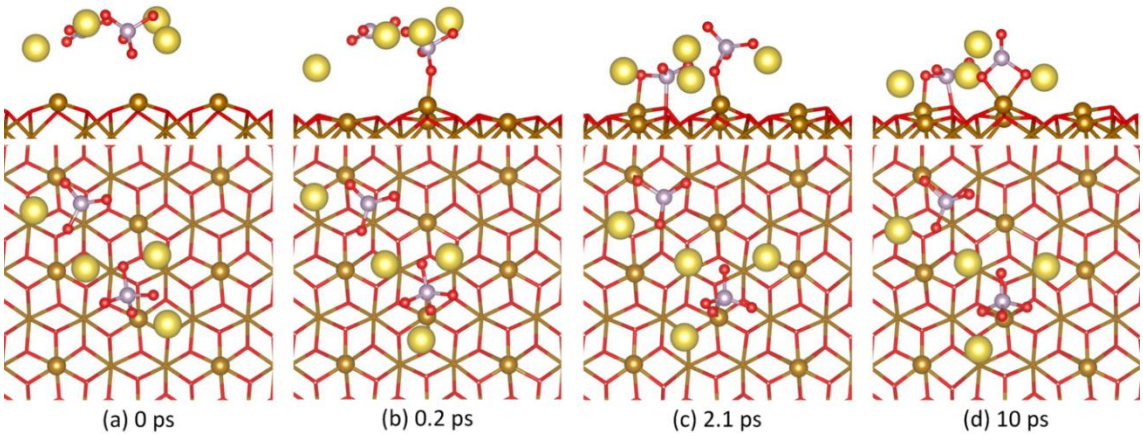

Figure A-5: Snapshots of AIMD at 300K of PO_3 and PO_4 units on Fe_2O_3 surface for 0 ps (a), 0.2 ps (b), 2.1 ps (c), and 10 ps (d). Structures have been displayed in side view (upper) and top view (lower). Red, gold, purple and yellow spheres represent oxygen, iron on top surface, phosphorus and sodium atoms, respectively. Surface oxygen and lower-layered iron atoms have been removed for apparent visualization.

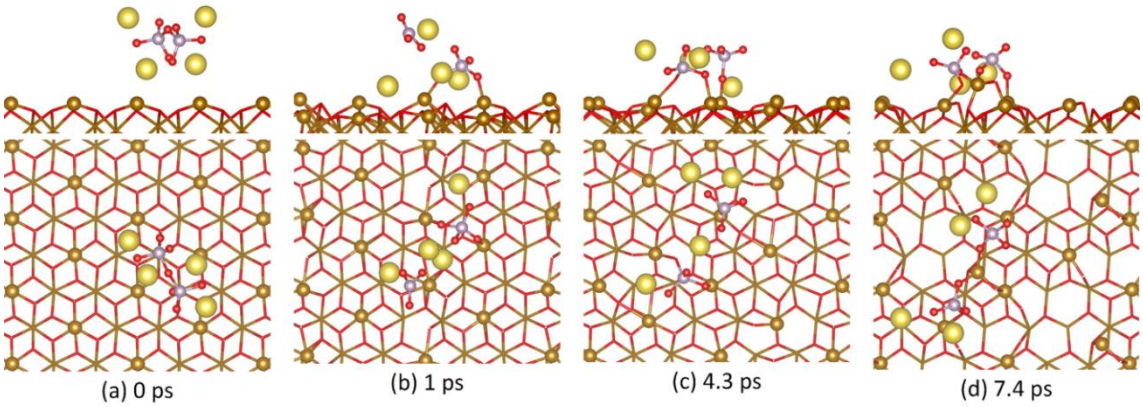

Figure A-6: Snapshots of AIMD at 1500K of $Na_4P_2O_7$ cluster on Fe_2O_3 surface for 0 ps (a), 1 ps (b), 4.3 ps (c), and 7.4 ps (d). Structures have been displayed in side view (upper) and top view (lower). Red, gold, purple and yellow spheres represent oxygen, iron on top surface, phosphorus and sodium atoms, respectively. Surface oxygen and lower-layered iron atoms have been removed for apparent visualization.

Appendix B Supporting material for chapter 4

Table B.1. Surface relaxation percentage for the interlayer spacing of Fe_2O_3(0001) surface

	This work (%)	Tang et al.[218]	Huang et al.[247]	Adam et al.[249]	Trainor et al.[219]	Exp [315]
Fe1 – O2	-68.92	-51	-61.48	-66.6	-65	-59
O2 – Fe3	11.53	13	6.95	7.2	7	17
Fe3 – Fe4	-41.44	-40	-40.05	-38	-26	-17
Fe4 – O5	18.24	20	15.91	16.3	13	41
O5 – Fe6	10.47	10	6.04	3.7	5	
Fe6 – Fe7	-13.33	-10	-4.66	-3.7	-4	

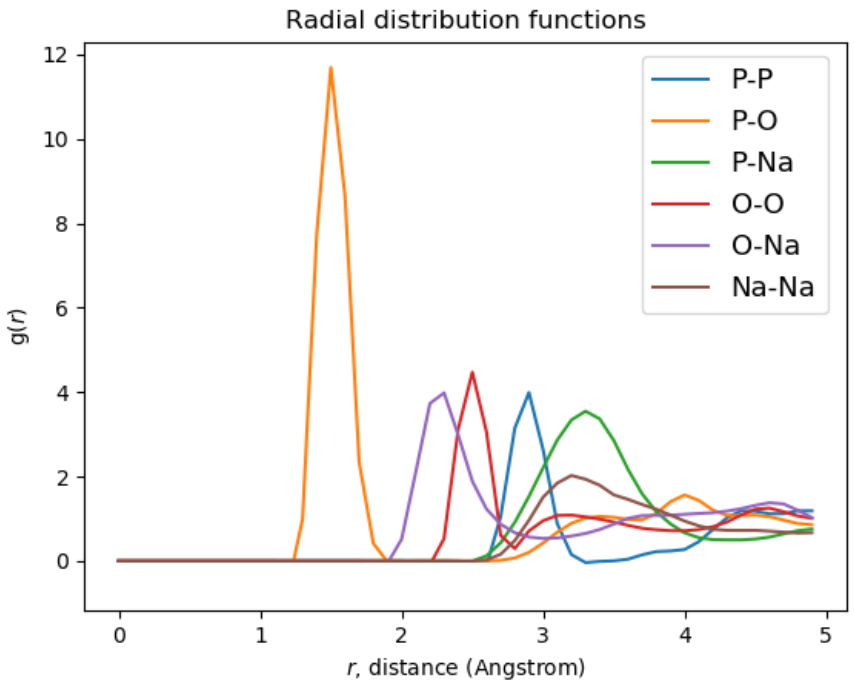

Figure B-1. Radial distribution functions of all interaction pairs in $NaPO_3$ glass state

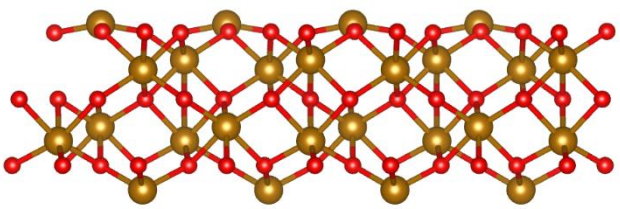

Figure B-2. The optimized Fe_2O_3(0001) surface

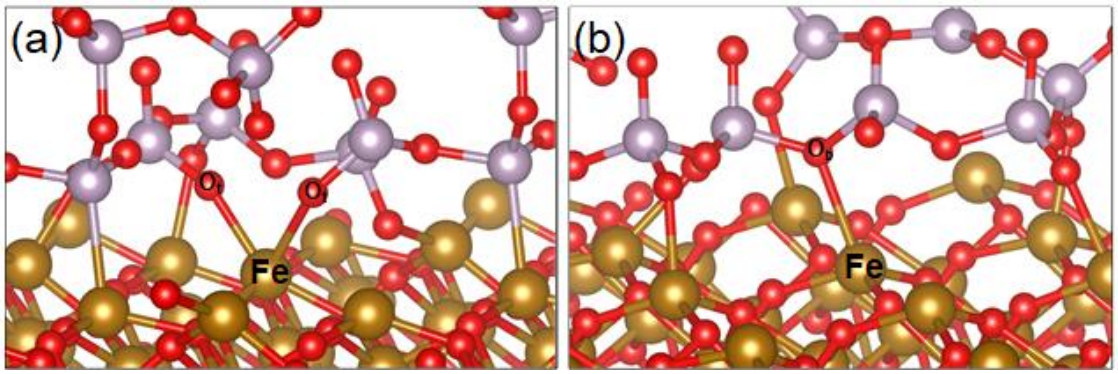

Figure B-3. Mononuclear bidentate complex (a) and bridging oxygen linkage structure (b). Na atoms have been removed for clear visualization.

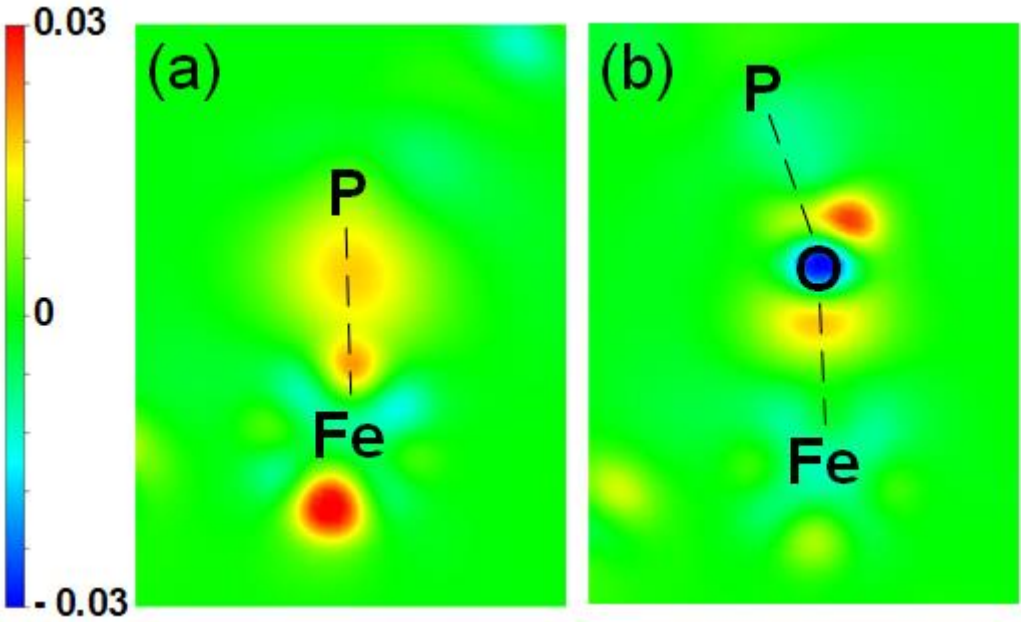

Figure B-4. Charge density different contours of (a) Fe_P – P bond and (b) Fe_O – O – P linkage. The red areas depict the electron accumulation and blue areas depict electron depletion regions, respectively.

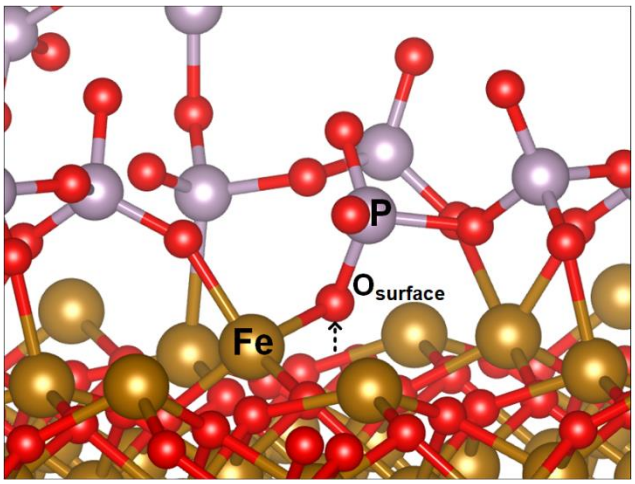

Figure B-5. Adsorption configuration for narrow gap case. $O_{surface}$ has been pulled up and bonded to P atom. Na atoms have been removed for clear visualization.

Appendix C Supporting material for chapter 5

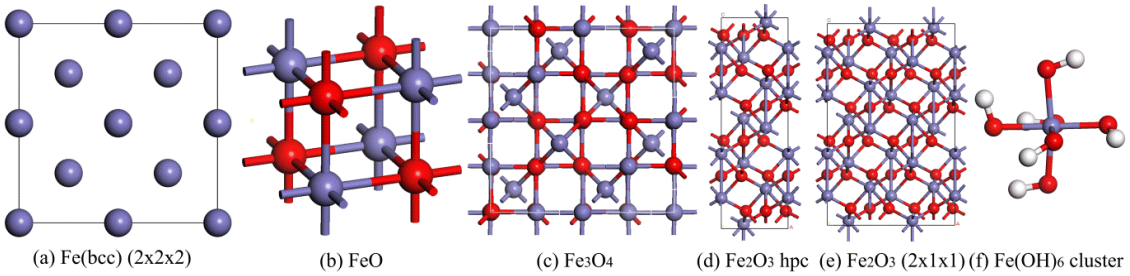

Figure C-1. Iron and iron oxides crystals and $Fe(OH)_6$ cluster.

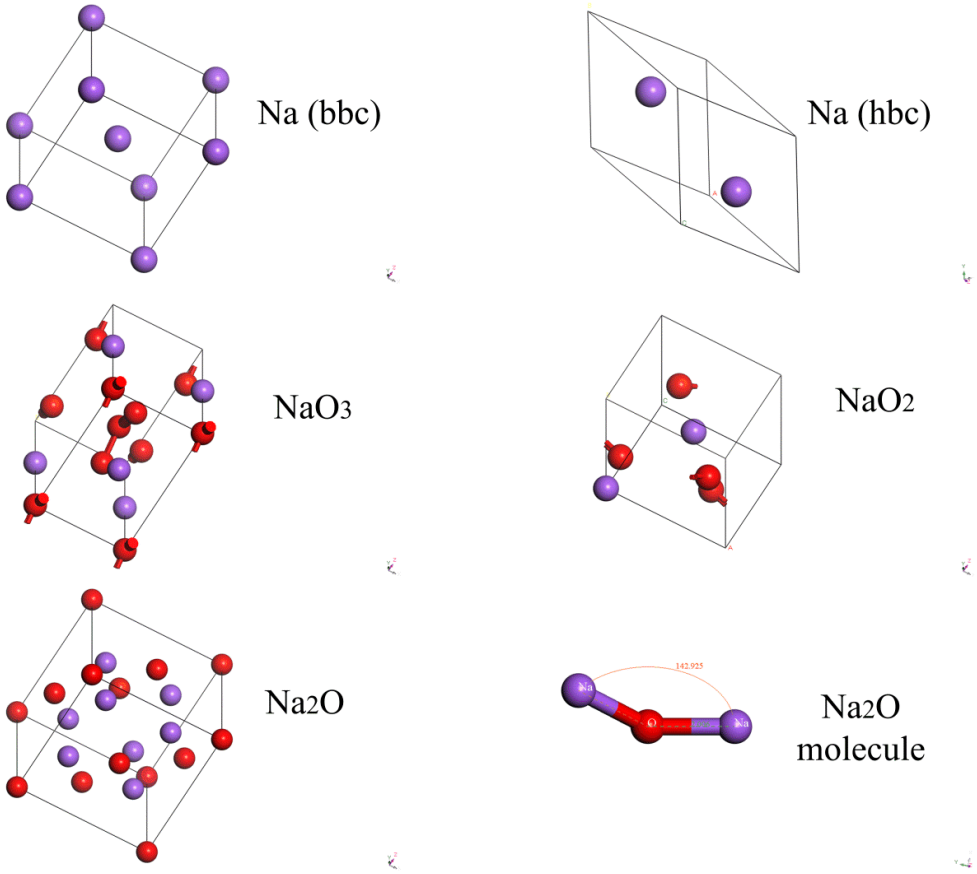

Figure C-2. Sodium and sodium oxide crystals, and Na_2O molecule.

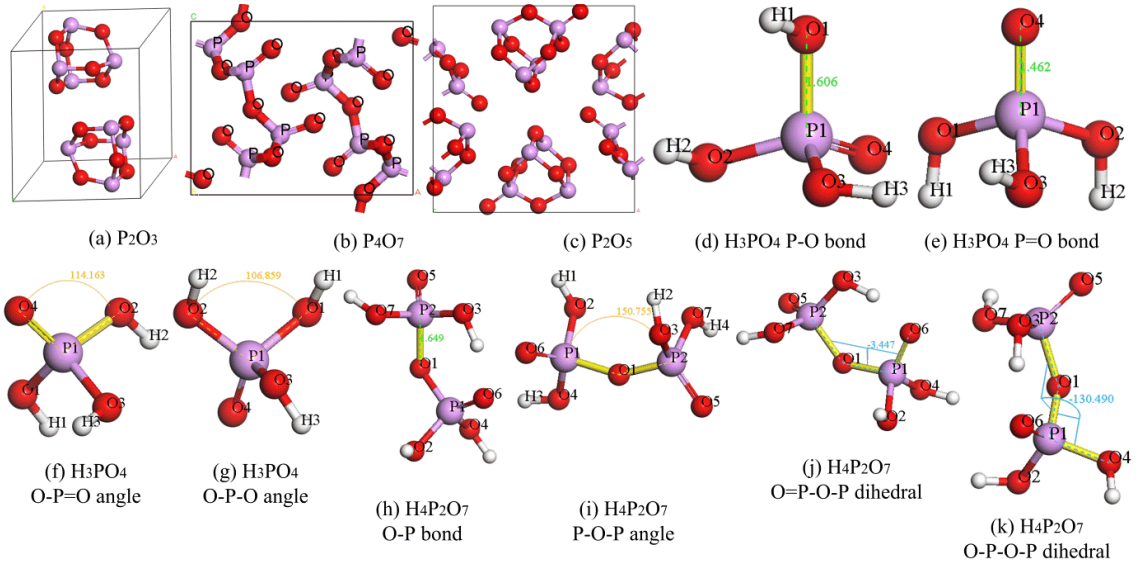

Figure C-3. Phosphorous oxides crystals and phosphorous acid molecules with different bonds, angles, and dihedrals.

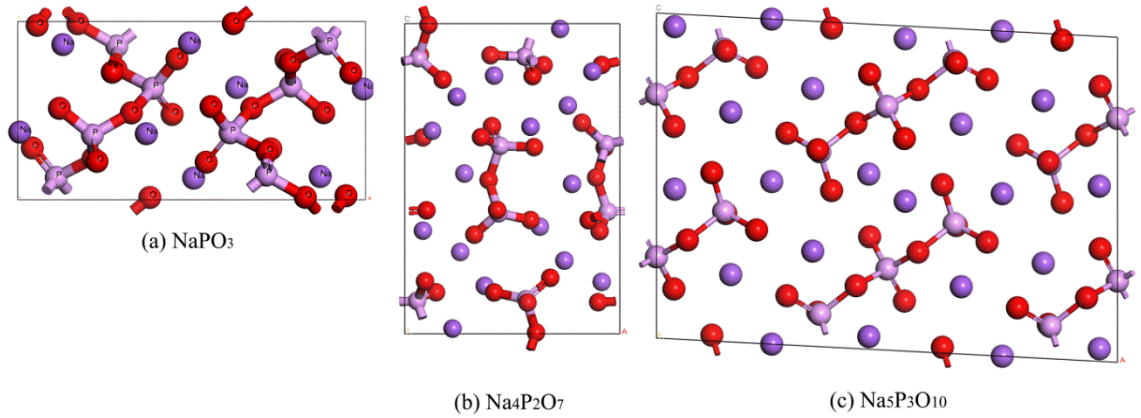

Figure C-4. Sodium phosphorous oxides crystals.

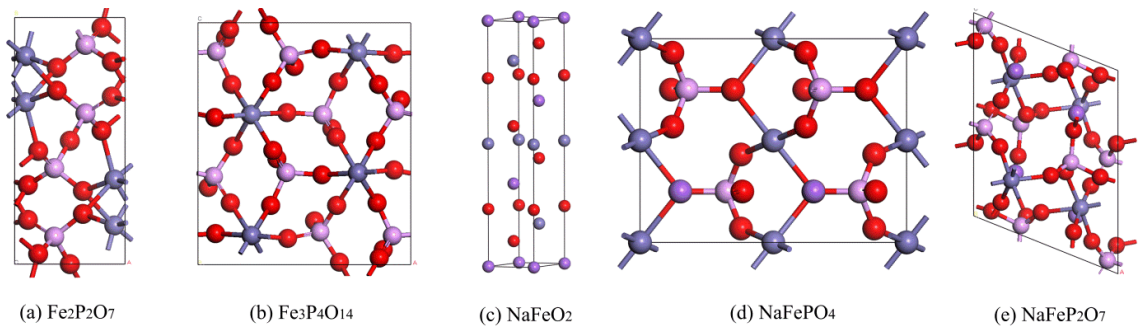

Figure C-5. Trinary oxides of $Fe_xP_yO_z$, $NaFeO_2$, and quaternary oxides of $Na_xFe_yP_zO_n$.

Parallel performance of GA method:

A. The influence of number of core (CPU):

CPU	Real time	CPU Time	Memory	Total Error
	hour:min:sec	Service Unit (SU)	GB	
16	0:23:53	6:55:13	38.8	11.6944
32	0:26:15	12:31:12	37.78	11.6944
64	0:25:03	25:58:49	41.2	11.6944
128	0:25:15	52:18:34	42.52	11.6944

For the same mutation rate of 10% and population of 100, the total error has not changed, while the memory increases insignificantly.

B. The influence of percent replacement (-z) with SSGA:
'SSGA' is a population replacement strategy.

Percent replacement	Real time	CPU Time	Memory	Total Error
(128 cores)	hour:min:sec	SU	GB	
10	0:25:15	52:18:34	42.52	11.6944
20	0:30:39	62:56:28	72.96	10.9978
30	0:40:58	80:50:01	104.14	11.3142
40	0:27:44	56:06:07	129.16	11.2609
50	0:43:46	79:39:10	162.74	11.1316

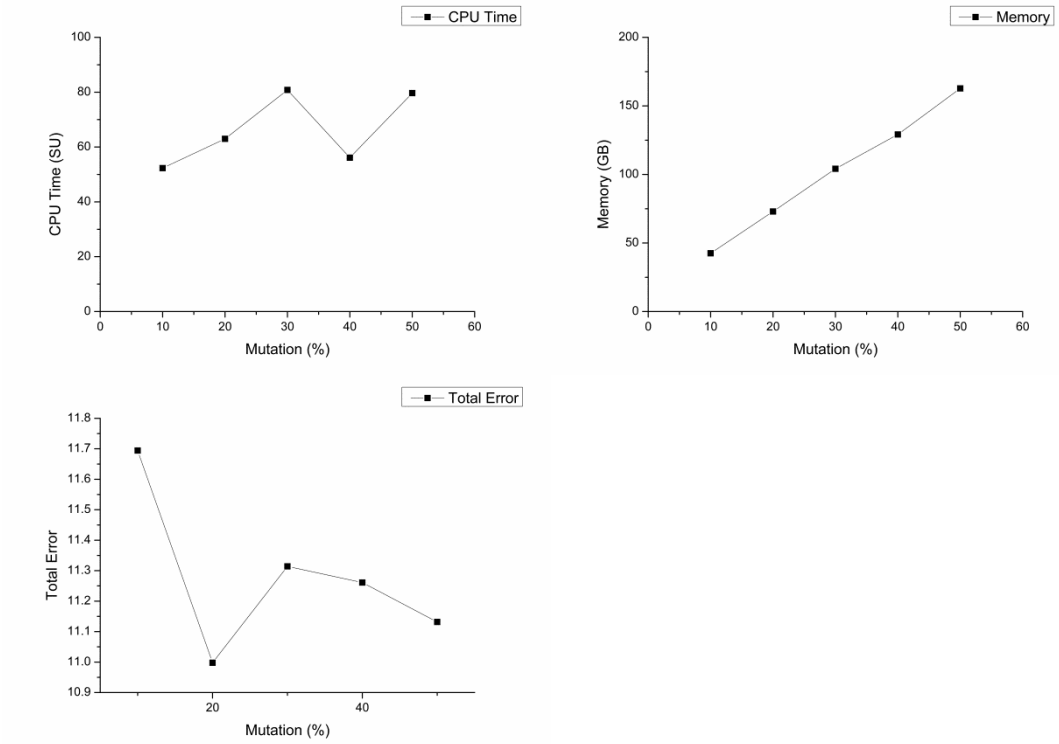

An increase of percent replacement results in an increase of calculating time and memory, and a small reduction of total error. Notably, the memory increase linearly with the mutation rate.

C. The influence of population (-p):

Population	Real time	CPU Time	Memory	Total Error
(128 cores)	hour:min:sec	SU	GB	
100	0:25:15	52:18:34	42.52	11.6944
150	0:26:32	53:32:25	59.67	11.5176
200 (128)	2:01:14	255:38:30	79.98	5.9007
200 (64)	2:23:20	150:07:22	87.67	4.9307
300(128)	2:01:20	256:16:04	120.46	6.5283
300(64)	2:14:59	141:44:07	125.42	6.5698

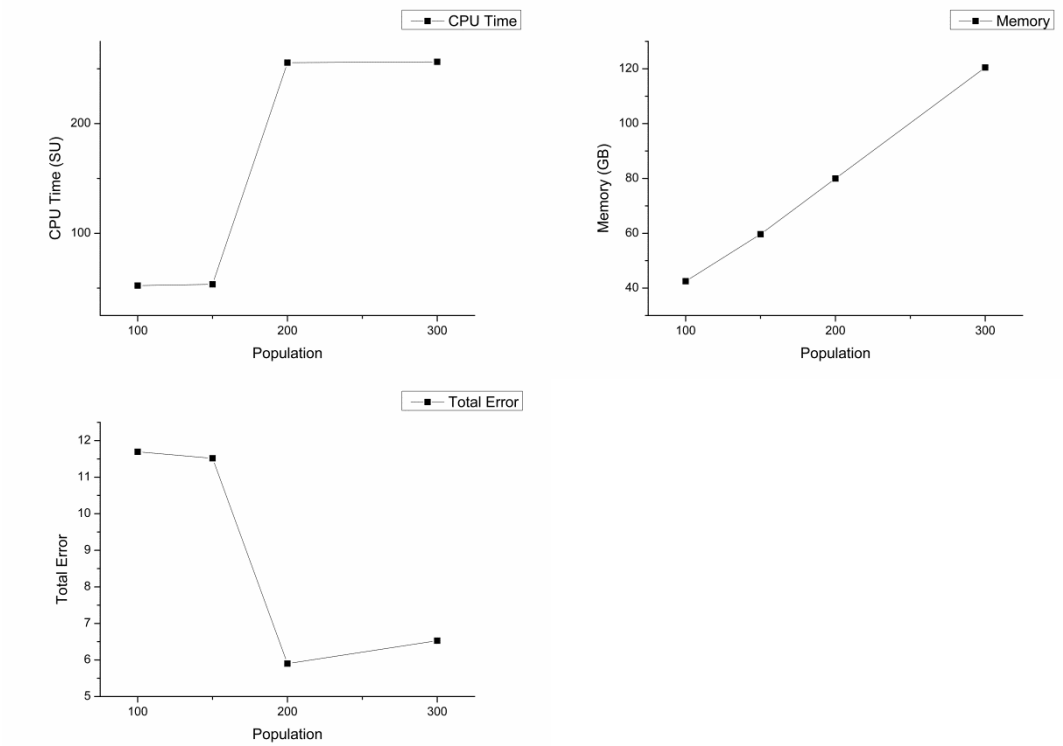

An increase of population results in a significant increase of calculating time and memory, but it also yields a significant reduction of total error. The increase of memory with population is a linear function. The increase in population size will result in a decrease of total error but it yields a linear increase of required memory. The increase of number of cores does not improve the simulation times.

D. The influence of conjugation gradient (-j):

Conjugate	Real time	CPU Time	Memory	Total Error
(32 cores)	hour:min:sec	SU	GB	
No	0:26:15	12:31:12	37.78	11.6944
Yes	0:31:13	16:34:22	12.66	14.4051

E. The influence of crossover rate (-o):

Crossover	Real time	CPU Time	Memory	Total Error

(32 cores)	hour:min:sec	SU	GB	
0.5	0:24:39	12:46:05	35.31	11.1507
0.6	0:25:51	13:29:10	35.66	11.6057
0.7	0:27:24	14:03:39	37.22	12.1249
0.85	0:26:15	12:31:12	37.78	11.6944
0.95	0:24:34	12:49:07	39.45	11.0353

The crossover rate does not influence the CPU time, memory, and total error.

F. The influence of climb hill parameters (-c):

Climb hill	Real time	CPU Time	Memory	Total Error
(32 cores)	hour:min:sec	SU	GB	
100	0:24:25	12:48:35	34.75	11.5675
150	00:22:50	11:52:17	34.92	11.6561
200	0:22:41	11:52:51	34.64	11.5501
300	0:22:40	11:52:38	32.06	11:52:38
500	0:22:50	12:03:01	32.77	11.6498

The clime hill parameter does not influence the simulation time, memory, and total error.

G. Conclusion:

In order to avoid segmentation error, the memory usage should be reduced. The memory is the core requirement as each node of the Raijin supercomputer of National Computational Infrastructure - Australian National University only allows maximum 128 GB. For the current setting of 100 population, percent replacement of 10%, and crossover 0.85 the maximum required memory is ~43 GB. Therefore, only 1 node (16 cores) can be used for this task. Initially, the short time job should be tested to determine the required memory then setting up the number of cores. In the case the number of core is larger than necessary; it does not help the job run quicker, whereas it consumes a larger amount of simulation time.

ReaxFF files

A. Structure for Iron and Iron Oxides and Their Geometry Files

```
BIOGRF 200
DESCRP Fe2x2x2
CRYSTX     5.65900    5.65900    5.65900   90.00000    90.00000    90.00000
FORMAT ATOM   (a6,1x,i5,1x,a5,1x,a3,1x,a1,1x,a5,3f10.5,1x,a5,i3,i2,1x,f8.5)
HETATM     1 Fe                  0.00000   0.00000   0.00000 Fe     1 0  0.00000
HETATM     2 Fe                  1.41495   1.41495   1.41495 Fe     1 0  0.00000
HETATM     3 Fe                  2.82991   0.00000   0.00000 Fe     1 0  0.00000
HETATM     4 Fe                  4.24386   1.41495   1.41495 Fe     1 0  0.00000
HETATM     5 Fe                  0.00000   2.82991   0.00000 Fe     1 0  0.00000
HETATM     6 Fe                  1.41495   4.24386   1.41495 Fe     1 0  0.00000
HETATM     7 Fe                  2.82991   2.82991   0.00000 Fe     1 0  0.00000
HETATM     8 Fe                  4.24386   4.24386   1.41495 Fe     1 0  0.00000
HETATM     9 Fe                  0.00000   0.00000   2.82991 Fe     1 0  0.00000
HETATM    10 Fe                  1.41495   1.41495   4.24386 Fe     1 0  0.00000
HETATM    11 Fe                  2.82991   0.00000   2.82991 Fe     1 0  0.00000
```

```
HETATM    12 Fe                  4.24386   1.41495   4.24386 Fe     1 0  0.00000
HETATM    13 Fe                  0.00000   2.82991   2.82991 Fe     1 0  0.00000
HETATM    14 Fe                  1.41495   4.24386   4.24386 Fe     1 0  0.00000
HETATM    15 Fe                  2.82991   2.82991   2.82991 Fe     1 0  0.00000
HETATM    16 Fe                  4.24386   4.24386   4.24386 Fe     1 0  0.00000
END

BIOGRF 200
DESCRP FeO
CRYSTX     4.31435    4.31435    4.31435   90.00000    90.00000    90.00000
FORMAT ATOM   (a6,1x,i5,1x,a5,1x,a3,1x,a1,1x,a5,3f10.5,1x,a5,i3,i2,1x,f8.5)
HETATM     1 Fe                  0.00000   0.00000   0.00000 Fe     1 0  0.00000
HETATM     2 Fe                  0.00000   2.15717   2.15717 Fe     1 0  0.00000
HETATM     3 Fe                  2.15717   0.00000   2.15717 Fe     1 0  0.00000
HETATM     4 Fe                  2.15717   2.15717   0.00000 Fe     1 0  0.00000
HETATM     5 O                   2.15717   2.15717   2.15717 O      2 0  0.00000
HETATM     6 O                   2.15717   0.00000   0.00000 O      2 0  0.00000
HETATM     7 O                   0.00000   2.15717   0.00000 O      2 0  0.00000
HETATM     8 O                   0.00000   0.00000   2.15717 O      2 0  0.00000
END

BIOGRF 200
DESCRP Fe3O4
CRYSTX     8.17423    8.17423    8.17423   90.00247    90.00247    90.00247
FORMAT ATOM   (a6,1x,i5,1x,a5,1x,a3,1x,a1,1x,a5,3f10.5,1x,a5,i3,i2,1x,f8.5)
HETATM     1 Fe                  1.02167   1.02167   1.02167 Fe     1 0  0.00000
HETATM     2 Fe                  1.02149   5.10868   5.10868 Fe     1 0  0.00000
HETATM     3 Fe                  5.10868   1.02149   5.10868 Fe     1 0  0.00000
HETATM     4 Fe                  5.10868   5.10868   1.02149 Fe     1 0  0.00000
HETATM     5 Fe                  7.15251   3.06526   3.06526 Fe     1 0  0.00000
HETATM     6 Fe                  7.15230   7.15230   7.15230 Fe     1 0  0.00000
HETATM     7 Fe                  3.06526   3.06526   7.15251 Fe     1 0  0.00000
HETATM     8 Fe                  3.06526   7.15251   3.06526 Fe     1 0  0.00000
HETATM     9 Fe                  4.08707   4.08707   4.08707 Fe     1 0  0.00000
HETATM    10 Fe                  4.08731   0.00009   0.00009 Fe     1 0  0.00000
HETATM    11 Fe                  0.00009   4.08731   0.00009 Fe     1 0  0.00000
HETATM    12 Fe                  0.00009   0.00009   4.08731 Fe     1 0  0.00000
HETATM    13 Fe                  2.04352   6.13075  -0.00011 Fe     1 0  0.00000
HETATM    14 Fe                  2.04356   2.04356   4.08706 Fe     1 0  0.00000
HETATM    15 Fe                  6.13075  -0.00011   2.04352 Fe     1 0  0.00000
HETATM    16 Fe                  6.13062   4.08691   6.13062 Fe     1 0  0.00000
HETATM    17 Fe                 -0.00011   2.04352   6.13075 Fe     1 0  0.00000
HETATM    18 Fe                  4.08706   2.04356   2.04356 Fe     1 0  0.00000
HETATM    19 Fe                  2.04356   4.08706   2.04356 Fe     1 0  0.00000
HETATM    20 Fe                  6.13075   2.04352  -0.00011 Fe     1 0  0.00000
HETATM    21 Fe                  6.13062   6.13062   4.08691 Fe     1 0  0.00000
HETATM    22 Fe                  2.04352  -0.00011   6.13075 Fe     1 0  0.00000
HETATM    23 Fe                 -0.00011   6.13075   2.04352 Fe     1 0  0.00000
HETATM    24 Fe                  4.08691   6.13062   6.13062 Fe     1 0  0.00000
HETATM    25 O                   2.13693   2.13693   2.13693 O      2 0  0.00000
HETATM    26 O                   2.13668   6.22396   6.22396 O      2 0  0.00000
HETATM    27 O                   6.22396   2.13668   6.22396 O      2 0  0.00000
HETATM    28 O                   6.22396   6.22396   2.13668 O      2 0  0.00000
HETATM    29 O                   3.99339   8.08063   6.22395 O      2 0  0.00000
HETATM    30 O                   3.99352   3.99352   2.13684 O      2 0  0.00000
HETATM    31 O                   8.08063   6.22395   3.99339 O      2 0  0.00000
HETATM    32 O                   8.08055   2.13674   8.08055 O      2 0  0.00000
HETATM    33 O                   3.99352   2.13684   3.99352 O      2 0  0.00000
HETATM    34 O                   6.22395   3.99339   8.08063 O      2 0  0.00000
HETATM    35 O                   2.13684   3.99352   3.99352 O      2 0  0.00000
HETATM    36 O                   0.09347   4.18066   1.95012 O      2 0  0.00000
HETATM    37 O                   0.09341   0.09341   6.03732 O      2 0  0.00000
HETATM    38 O                   6.03707   6.03707   6.03707 O      2 0  0.00000
HETATM    39 O                   6.03718   1.95001   1.95001 O      2 0  0.00000
HETATM    40 O                   1.95001   6.03718   1.95001 O      2 0  0.00000
HETATM    41 O                   1.95001   1.95001   6.03718 O      2 0  0.00000
HETATM    42 O                   4.18066   1.95012   0.09347 O      2 0  0.00000
HETATM    43 O                   4.18046   6.03720   4.18046 O      2 0  0.00000
HETATM    44 O                   0.09341   6.03732   0.09341 O      2 0  0.00000
HETATM    45 O                   1.95012   0.09347   4.18066 O      2 0  0.00000
HETATM    46 O                   6.03732   0.09341   0.09341 O      2 0  0.00000
HETATM    47 O                   4.18066   0.09347   1.95012 O      2 0  0.00000
HETATM    48 O                   4.18046   4.18046   6.03720 O      2 0  0.00000
HETATM    49 O                   0.09347   1.95012   4.18066 O      2 0  0.00000
HETATM    50 O                   1.95012   4.18066   0.09347 O      2 0  0.00000
HETATM    51 O                   6.03720   4.18046   4.18046 O      2 0  0.00000
HETATM    52 O                   8.08063   3.99339   6.22395 O      2 0  0.00000
```

```
HETATM    53 O                   8.08055   8.08055   2.13674 O      2 0  0.00000
HETATM    54 O                   3.99339   6.22395   8.08063 O      2 0  0.00000
HETATM    55 O                   6.22395   8.08063   3.99339 O      2 0  0.00000
HETATM    56 O                   2.13674   8.08055   8.08055 O      2 0  0.00000
END

BIOGRF 200
DESCRP Fe2O3_2x1x1
CRYSTX     8.20264    4.82508   13.34192   90.01346    90.73387    89.99976
FORMAT ATOM   (a6,1x,i5,1x,a5,1x,a3,1x,a1,1x,a5,3f10.5,1x,a5,i3,i2,1x,f8.5)
HETATM     1 O                   1.27040   4.06752   3.35043 O      2 0  0.00000
HETATM     2 O                   5.37113   1.65524   3.32311 O      2 0  0.00000
HETATM     3 O                   3.97232   4.06922   7.78126 O      2 0  0.00000
HETATM     4 O                   8.07630   1.65774   7.75755 O      2 0  0.00000
HETATM     5 O                   2.58175   1.65597  12.24146 O      2 0  0.00000
HETATM     6 O                   6.68369   4.06842  12.21385 O      2 0  0.00000
HETATM     7 O                  -0.02212   1.50256   3.33730 O      2 0  0.00000
HETATM     8 O                   4.08175   3.91057   3.30897 O      2 0  0.00000
HETATM     9 O                   2.68687   1.49263   7.76163 O      2 0  0.00000
HETATM    10 O                   6.78779   3.90423   7.73408 O      2 0  0.00000
HETATM    11 O                   1.28846   3.90516  12.22323 O      2 0  0.00000
HETATM    12 O                   5.38988   1.49219  12.19715 O      2 0  0.00000
HETATM    13 O                   2.78909   1.65476   3.29353 O      2 0  0.00000
HETATM    14 O                   6.89097   4.06756   3.26600 O      2 0  0.00000
HETATM    15 O                   1.39261   4.06901   7.74398 O      2 0  0.00000
HETATM    16 O                   5.49360   1.65641   7.71789 O      2 0  0.00000
HETATM    17 O                  -0.00145   1.65646  12.20095 O      2 0  0.00000
HETATM    18 O                   4.09989   4.06865  12.17361 O      2 0  0.00000
HETATM    19 O                   2.74730   3.16876   9.96368 O      2 0  0.00000
HETATM    20 O                   6.84850   0.75574   9.93762 O      2 0  0.00000
HETATM    21 O                   1.43393   0.75490   1.07449 O      2 0  0.00000
HETATM    22 O                   5.53598   3.16735   1.04742 O      2 0  0.00000
HETATM    23 O                   0.04029   3.16624   5.52974 O      2 0  0.00000
HETATM    24 O                   4.14111   0.75364   5.50343 O      2 0  0.00000
HETATM    25 O                  -0.06178   3.32437  10.00545 O      2 0  0.00000
HETATM    26 O                   4.03880   0.91250   9.98019 O      2 0  0.00000
HETATM    27 O                   2.72875   3.33106   1.09175 O      2 0  0.00000
HETATM    28 O                   6.83027   0.91925   1.06517 O      2 0  0.00000
HETATM    29 O                   1.33051   0.91826   5.55268 O      2 0  0.00000
HETATM    30 O                   5.43132   3.33040   5.52757 O      2 0  0.00000
HETATM    31 O                   1.22778   0.75544  10.02154 O      2 0  0.00000
HETATM    32 O                   5.32873   3.16887   9.99462 O      2 0  0.00000
HETATM    33 O                   4.01605   0.75545   1.11217 O      2 0  0.00000
HETATM    34 O                   8.11991   3.16754   1.08767 O      2 0  0.00000
HETATM    35 O                   2.62494   3.16803   5.56992 O      2 0  0.00000
HETATM    36 O                   6.72546   0.75448   5.54380 O      2 0  0.00000
HETATM    37 Fe                  8.14932  -0.00175   4.56263 Fe     1 0  0.00000
HETATM    38 Fe                  4.04828   2.41074   4.58860 Fe     1 0  0.00000
HETATM    39 Fe                  2.65182  -0.00350   9.04448 Fe     1 0  0.00000
HETATM    40 Fe                  6.75376   2.40881   9.01700 Fe     1 0  0.00000
HETATM    41 Fe                  1.34080   2.41024   0.15938 Fe     1 0  0.00000
HETATM    42 Fe                  5.44165  -0.00224   0.13308 Fe     1 0  0.00000
HETATM    43 Fe                  0.01080  -0.00154   2.05518 Fe     1 0  0.00000
HETATM    44 Fe                  4.11181   2.41077   2.02777 Fe     1 0  0.00000
HETATM    45 Fe                  2.71768  -0.00267   6.48383 Fe     1 0  0.00000
HETATM    46 Fe                  6.81923   2.41007   6.45690 Fe     1 0  0.00000
HETATM    47 Fe                  1.32275   2.40892  10.94189 Fe     1 0  0.00000
HETATM    48 Fe                  5.42402  -0.00410  10.91574 Fe     1 0  0.00000
HETATM    49 Fe                 -0.03127   0.00029   8.72648 Fe     1 0  0.00000
HETATM    50 Fe                  4.06956   2.41255   8.69969 Fe     1 0  0.00000
HETATM    51 Fe                  2.67570   0.00035  13.15439 Fe     1 0  0.00000
HETATM    52 Fe                  6.77727   2.41280  13.12788 Fe     1 0  0.00000
HETATM    53 Fe                  1.36432   2.41522   4.27065 Fe     1 0  0.00000
HETATM    54 Fe                  5.46606   0.00218   4.24414 Fe     1 0  0.00000
HETATM    55 Fe                  8.10707  -0.00021  11.23265 Fe     1 0  0.00000
HETATM    56 Fe                  4.00582   2.41231  11.25905 Fe     1 0  0.00000
HETATM    57 Fe                  2.69470   0.00239   2.37300 Fe     1 0  0.00000
HETATM    58 Fe                  6.79537   2.41470   2.34657 Fe     1 0  0.00000
HETATM    59 Fe                  1.29852   2.41378   6.83091 Fe     1 0  0.00000
HETATM    60 Fe                  5.39943   0.00097   6.80474 Fe     1 0  0.00000
END

BIOGRF 200
DESCRP FeO6H6
REMARK .bgf-file generated by xtob-script
#       At1 At2 R12 Force1 Force2 dR12/dIteration(MD only)
BOND RESTRAINT 1 4 1.80 7500.00 0.25000 0.0000000
```

```
CRYSTX    15.00000   15.00000   15.00000   90.00000    90.00000    90.00000
FORMAT ATOM   (a6,1x,i5,1x,a5,1x,a3,1x,a1,1x,a5,3f10.5,1x,a5,i3,i2,1x,f8.5)
HETATM     1 Fe                 7.55804   7.47104   7.40204 Fe     1 0  0.00000
HETATM     2 O                  7.40628   9.29786   7.62016 O      2 0  0.00000
HETATM     3 O                  5.71862   7.45080   7.32544 O      2 0  0.00000
HETATM     4 O                  7.45604   5.73903   6.92203 O      2 0  0.00000
HETATM     5 O                  7.68880   7.56381   5.49548 O      2 0  0.00000
HETATM     6 O                  7.63282   6.98850   9.19298 O      2 0  0.00000
HETATM     7 O                  9.36017   7.52459   7.46885 O      2 0  0.00000
HETATM     8 H                  8.31567   9.61285   7.78522 H      1 0  0.00000
HETATM     9 H                  5.42215   8.33826   7.60869 H      1 0  0.00000
HETATM    10 H                  6.49522   5.55828   6.80842 H      1 0  0.00000
HETATM    11 H                  6.75261   7.62942   5.19824 H      1 0  0.00000
HETATM    12 H                  6.80831   6.49809   9.38370 H      1 0  0.00000
HETATM    13 H                  9.61016   7.08563   8.30983 H      1 0  0.00000
END
```

B. Sodium and Sodium Oxides and Their Geometry Files

```
BIOGRF 200
DESCRP Na_bcc
CRYSTX     4.18681    4.18681    4.18681   90.00000    90.00000    90.00000
FORMAT ATOM   (a6,1x,i5,1x,a5,1x,a3,1x,a1,1x,a5,3f10.5,1x,a5,i3,i2,1x,f8.5)
HETATM     1 Na                 0.00000   0.00000   0.00000 Na     1 0  0.00000
HETATM     2 Na                 2.09341   2.09341   2.09341 Na     1 0  0.00000
END


BIOGRF 200
DESCRP Na_hpc
CRYSTX     3.70408    3.70385    6.22332   90.00000    90.00000   119.99742
FORMAT ATOM   (a6,1x,i5,1x,a5,1x,a3,1x,a1,1x,a5,3f10.5,1x,a5,i3,i2,1x,f8.5)
HETATM     1 Na                -0.00044   2.13819   1.55533 Na     1 0  0.00000
HETATM     2 Na                 1.85211   1.06929   4.66699 Na     1 0  0.00000
END

BIOGRF 200
DESCRP NaO3
CRYSTX     3.76596    5.21671    5.28876   89.99919   90.00152   90.00100
FORMAT ATOM   (a6,1x,i5,1x,a5,1x,a3,1x,a1,1x,a5,3f10.5,1x,a5,i3,i2,1x,f8.5)
HETATM     1 Na                 0.94149   2.33792   4.56257    Na  1 0  0.00000
HETATM     2 Na                 2.82446   4.94617   1.91818    Na  1 0  0.00000
HETATM     3 O                  0.94144  -0.34838   4.56253    O   2 0  0.00000
HETATM     4 O                  2.82464   2.25988   1.91817    O   2 0  0.00000
HETATM     5 O                  0.94142   3.99619   0.37708    O   2 0  0.00000
HETATM     6 O                  2.82441   1.38774   3.02140    O   2 0  0.00000
HETATM     7 O                  0.94150   3.99621   3.45934    O   2 0  0.00000
HETATM     8 O                  2.82449   1.38776   0.81491    O   2 0  0.00000
END

BIOGRF 200
DESCRP NaO2
CRYSTX     3.49302    5.53694    3.57775   90.00000   90.00000   90.00000
FORMAT ATOM   (a6,1x,i5,1x,a5,1x,a3,1x,a1,1x,a5,3f10.5,1x,a5,i3,i2,1x,f8.5)
HETATM     1 Na                 0.33717   0.62184   0.89391    Na  1 0  0.00000
HETATM     2 Na                 2.08367   3.30409   2.68384    Na  1 0  0.00000
HETATM     3 O                  0.61591   2.71361   0.86588    O   2 0  0.00000
HETATM     4 O                  3.64744   3.95881   0.92269    O   2 0  0.00000
HETATM     5 O                  1.90094   5.50407   2.65506    O   2 0  0.00000
HETATM     6 O                  2.36242   1.21233   2.71187    O   2 0  0.00000
END

BIOGRF 200
DESCRP Na2O
CRYSTX     5.53819    5.53819    5.53819   90.00000    90.00000    90.00000
FORMAT ATOM   (a6,1x,i5,1x,a5,1x,a3,1x,a1,1x,a5,3f10.5,1x,a5,i3,i2,1x,f8.5)
HETATM     1 O                  0.00000   0.00000   0.00000 O_3    2 0  0.00000
HETATM     2 O                  0.00000   2.76909   2.76909 O_3    2 0  0.00000
HETATM     3 O                  2.76909   0.00000   2.76909 O_3    2 0  0.00000
HETATM     4 O                  2.76909   2.76909   0.00000 O_3    2 0  0.00000
HETATM     5 Na                 1.38455   1.38455   1.38455 Na     1 0  0.00000
HETATM     6 Na                 4.15364   4.15364   1.38455 Na     1 0  0.00000
HETATM     7 Na                 4.15364   1.38455   4.15364 Na     1 0  0.00000
HETATM     8 Na                 1.38455   4.15364   4.15364 Na     1 0  0.00000
HETATM     9 Na                 1.38455   1.38455   4.15364 Na     1 0  0.00000
```

```
HETATM    10 Na                  4.15364   4.15364   4.15364 Na     1 0  0.00000
HETATM    11 Na                  4.15364   1.38455   1.38455 Na     1 0  0.00000
HETATM    12 Na                  1.38455   4.15364   1.38455 Na     1 0  0.00000
END

BIOGRF 200
DESCRP Na2O_Na-O_Bond
#       At1 At2 R12 Force1 Force2 dR12/dIteration(MD only)
BOND RESTRAINT 1 2 2.00 7500.00 0.25000 0.0000000
CRYSTX    20.00000   20.00000   20.00000   90.00000    90.00000    90.00000
FORMAT ATOM   (a6,1x,i5,1x,a5,1x,a3,1x,a1,1x,a5,3f10.5,1x,a5,i3,i2,1x,f8.5)
HETATM     1 O                10.62416  10.44614  10.73000 O_3    2 0  0.00000
HETATM     2 Na               11.07437  12.34543  11.18098 Na     1 0  0.00000
HETATM     3 Na               11.07547   8.54443  11.18003 Na     1 0  0.00000
END

BIOGRF 200
DESCRP NaOH_Na-O_bond
#       At1 At2 R12 Force1 Force2 dR12/dIteration(MD only)
BOND RESTRAINT 2 3 1.95 7500.00 0.25000 0.0000000
CRYSTX    15.00000   15.00000   15.00000   90.00000    90.00000    90.00000
FORMAT ATOM   (a6,1x,i5,1x,a5,1x,a3,1x,a1,1x,a5,3f10.5,1x,a5,i3,i2,1x,f8.5)
HETATM     1 H                7.86704   7.38604   8.95405 H_HB   1 0  0.00000
HETATM     2 O                7.51504   7.50204   8.06204 O_3    2 0  0.00000
HETATM     3 Na               7.00404   7.98904   6.24303 Na     1 0  0.00000
END
```

C. Phosphorous Oxides Crystals and Phosphorous Acid Molecules and Their Geometry Files

```
BIOGRF 200
DESCRP P2O3
CRYSTX     6.83607    8.73596    7.02207   90.15432   104.65702    90.05429
FORMAT ATOM   (a6,1x,i5,1x,a5,1x,a3,1x,a1,1x,a5,3f10.5,1x,a5,i3,i2,1x,f8.5)
HETATM     1 O                1.91020   3.46318   5.39446 O_3    2 0 -0.23674
HETATM     2 O                4.20650   3.45897   4.27426 O_3    2 0 -0.23674
HETATM     3 O                3.03390   7.81930   1.46125 O_3    2 0 -0.23674
HETATM     4 O                0.73790   7.82078   2.58184 O_3    2 0 -0.23674
HETATM     5 O                3.03458   5.26017   1.46740 O_3    2 0 -0.23674
HETATM     6 O                0.73840   5.26447   2.58790 O_3    2 0 -0.23674
HETATM     7 O                1.91078   0.90392   5.39913 O_3    2 0 -0.23674
HETATM     8 O                4.20673   0.90261   4.27858 O_3    2 0 -0.23674
HETATM     9 O                3.85031   2.18568   6.45934 O_3    2 0 -0.23674
HETATM    10 O                2.26294   2.17904   3.21253 O_3    2 0 -0.23674
HETATM    11 O                1.09441   6.53680   0.40195 O_3    2 0 -0.23674
HETATM    12 O                2.68193   6.54542   3.64850 O_3    2 0 -0.23674
HETATM    13 P                3.52235   3.66831   5.77980 P_3    1 0  0.35510
HETATM    14 P                1.42141   8.02270   1.07568 P_3    1 0  0.35510
HETATM    15 P                1.42235   5.05442   1.08220 P_3    1 0  0.35510
HETATM    16 P                3.52312   0.70001   5.78479 P_3    1 0  0.35510
HETATM    17 P                3.93312   2.17950   3.24208 P_3    1 0  0.35510
HETATM    18 P                1.26157   2.18179   4.54733 P_3    1 0  0.35510
HETATM    19 P                1.01172   6.54459   3.61908 P_3    1 0  0.35510
HETATM    20 P                3.68306   6.54210   2.31379 P_3    1 0  0.35510
END

BIOGRF 200
DESCRP P4O7
CRYSTX    10.15542   10.14449    7.88222   90.00174    95.52281    90.00620
FORMAT ATOM   (a6,1x,i5,1x,a5,1x,a3,1x,a1,1x,a5,3f10.5,1x,a5,i3,i2,1x,f8.5)
HETATM     1 O               -0.59114   1.17448   6.31827 O_3    2 0 -0.16761
HETATM     2 O                1.20854   2.70283   5.33604 O_3    2 0 -0.22747
HETATM     3 O                0.19899   3.22952   7.62199 O_2    1 0 -0.22690
HETATM     4 O                8.02095   3.17914   6.66170 O_3    2 0 -0.25102
HETATM     5 O                9.01692   2.66369   4.38709 O_2    1 0 -0.22696
HETATM     6 O                7.42193   4.67995   4.64022 O_2    1 0 -0.22696
```

```
HETATM     7 O                  -0.36650   4.69639   5.62421 O_2    1 0 -0.22690
HETATM     8 O                   4.46632   6.24658   5.47153 O_3    2 0 -0.23665
HETATM     9 O                   2.66601   7.77385   6.45394 O_3    2 0 -0.23665
HETATM    10 O                   3.67521   8.30123   4.16792 O_3    2 0 -0.23665
HETATM    11 O                   6.00868   8.25241   5.18478 O_3    2 0 -0.21080
HETATM    12 O                   5.01299   7.73714   7.45923 O_3    2 0 -0.21080
HETATM    13 O                   6.60684   9.75446   7.20557 O_2    1 0 -0.22602
HETATM    14 O                   4.23998   9.76845   6.16540 O_3    2 0 -0.21080
HETATM    15 O                   9.94389   8.96974   1.57843 O_3    2 0 -0.16761
HETATM    16 O                   8.14429   7.44138   2.56124 O_3    2 0 -0.22747
HETATM    17 O                   9.15280   6.91490   0.27473 O_2    1 0 -0.22690
HETATM    18 O                   1.33134   6.96475   1.23419 O_3    2 0 -0.25102
HETATM    19 O                   0.33609   7.48012   3.50920 O_2    1 0 -0.22696
HETATM    20 O                   1.93080   5.46376   3.25600 O_2    1 0 -0.22696
HETATM    21 O                   9.71862   5.44737   2.27233 O_2    1 0 -0.22690
HETATM    22 O                   4.88624   3.89698   2.42669 O_3    2 0 -0.23665
HETATM    23 O                   6.68619   2.36926   1.44364 O_3    2 0 -0.23665
HETATM    24 O                   5.67746   1.84192   3.72987 O_3    2 0 -0.23665
HETATM    25 O                   3.34382   1.89150   2.71362 O_3    2 0 -0.21080
HETATM    26 O                   4.33936   2.40682   0.43903 O_3    2 0 -0.21080
HETATM    27 O                   2.74495   0.38967   0.69206 O_2    1 0 -0.22602
HETATM    28 O                   5.11204   0.37504   1.73247 O_3    2 0 -0.21080
HETATM    29 P                   8.46088   3.87961   5.28440 P_3    1 0  0.54422
HETATM    30 P                   9.05390   2.18805   7.58206 P_3    1 0  0.16070
HETATM    31 P                   0.97739   3.98125   6.36590 P_3    1 0  0.54575
HETATM    32 P                   0.06867   1.59437   4.86137 P_3    1 0  0.30314
HETATM    33 P                   5.56786   8.95287   6.56152 P_3    1 0  0.49710
HETATM    34 P                   4.97584   7.26062   4.26440 P_3    1 0  0.35709
HETATM    35 P                   2.89644   9.05246   5.42409 P_3    1 0  0.35709
HETATM    36 P                   3.80661   6.66637   6.92843 P_3    1 0  0.35709
HETATM    37 P                   0.89133   6.26444   2.61140 P_3    1 0  0.54422
HETATM    38 P                   0.29800   7.95643   0.31434 P_3    1 0  0.16070
HETATM    39 P                   8.37479   6.16286   1.53110 P_3    1 0  0.54575
HETATM    40 P                   9.28426   8.54962   3.03535 P_3    1 0  0.30314
HETATM    41 P                   3.78444   1.19112   1.33675 P_3    1 0  0.49710
HETATM    42 P                   4.37692   2.88304   3.63394 P_3    1 0  0.35709
HETATM    43 P                   6.45579   1.09059   2.47370 P_3    1 0  0.35709
HETATM    44 P                   5.54602   3.47718   0.96960 P_3    1 0  0.35709
END

BIOGRF 200
DESCRP P2O5
CRYSTX     9.39680    5.06807    7.19560   90.00000    90.02086    90.00000
FORMAT ATOM   (a6,1x,i5,1x,a5,1x,a3,1x,a1,1x,a5,3f10.5,1x,a5,i3,i2,1x,f8.5)
HETATM     1 O                   3.40608   0.00333   1.52737 O_2    1 0 -0.51681
HETATM     2 O                   1.28982   5.06532   5.12719 O_2    1 0 -0.22686
HETATM     3 O                   5.98938   2.53736   5.66654 O_3    2 0 -0.25663
HETATM     4 O                   8.10564   2.53128   2.06671 O_3    2 0 -0.21191
HETATM     5 O                   5.98898   5.06463   5.66489 O_3    2 0 -0.43688
HETATM     6 O                   8.10362   0.00376   2.06916 O_2    1 0 -0.22686
HETATM     7 O                   3.40647   2.53059   1.52901 O_3    2 0 -0.25663
HETATM     8 O                   1.29184   2.53780   5.12474 O_3    2 0 -0.21191
HETATM     9 O                   2.54301   1.26579   3.48505 O_3    2 0 -0.25223
HETATM    10 O                   5.12073   1.26612   2.90305 O_3    2 0 -0.43688
HETATM    11 O                   3.36217   1.26662   5.99561 O_3    2 0 -0.14394
HETATM    12 O                   2.15367   3.80005   7.08292 O_2    1 0 -0.22686
HETATM    13 O                   8.97310   3.79968   6.49939 O_3    2 0  0.00000
HETATM    14 O                   1.33454   3.80107   2.39754 O_2    1 0 -0.26897
HETATM    15 O                   6.85244   3.79982   3.70885 O_3    2 0 -0.25223
HETATM    16 O                   4.27472   3.80015   4.29085 O_2    1 0 -0.51681
HETATM    17 O                   6.03329   3.80065   1.19829 O_3    2 0 -0.14394
HETATM    18 O                   7.24178   1.26601   0.11098 O_2    1 0 -0.22686
HETATM    19 O                   0.42236   1.26565   0.69451 O_3    2 0  0.00000
HETATM    20 O                   8.06091   1.26703   4.79636 O_2    1 0 -0.26897
HETATM    21 P                   3.73595   1.26651   2.43033 P_3    1 0  0.22578
HETATM    22 P                   2.25283   1.26690   5.05483 P_3    1 0  0.37851
HETATM    23 P                   0.96130   3.80067   6.02797 P_3    1 0  0.54693
HETATM    24 P                   2.44463   3.80085   1.45691 P_3    1 0  0.38987
HETATM    25 P                   5.65950   3.80054   4.76358 P_3    1 0  0.22578
HETATM    26 P                   7.14262   3.80093   2.13907 P_3    1 0  0.37851
HETATM    27 P                   8.43415   1.26664   1.16594 P_3    1 0  0.54693
HETATM    28 P                   6.95082   1.26681   5.73700 P_3    1 0  0.38987
END

BIOGRF 200
DESCRP H3PO4
REMARK .bgf-file generated by xtob-script
```

```
FORCEFIELD DREIDING
CRYSTX    20.00000   20.00000   20.00000   90.00000    90.00000    90.00000
FORMAT ATOM   (a6,1x,i5,1x,a5,1x,a3,1x,a1,1x,a5,3f10.5,1x,a5,i3,i2,1x,f8.5)
HETATM     1 P                  10.08393   9.98530   9.98940 P_3    1 0  0.46982
HETATM     2 O                   9.39229   9.09453   8.84475 O_3    2 0 -0.30272
HETATM     3 O                   9.48412   9.49256  11.38489 O_3    2 0 -0.30272
HETATM     4 O                   9.39513  11.43846   9.85518 O_3    2 0 -0.30272
HETATM     5 O                  11.54337   9.93031   9.91192 O_2    1 0 -0.22772
HETATM     6 H                   8.42277   9.18582   8.78623 H_HB   1 0  0.22202
HETATM     7 H                   8.51414   9.52961  11.45729 H_HB   1 0  0.22202
HETATM     8 H                   9.88426  11.99241   9.21734 H_HB   1 0  0.22202
END

BIOGRF 200
DESCRP H4P2O7
REMARK .bgf-file generated by xtob-script
FORCEFIELD DREIDING
CRYSTX    20.00000   20.00000   20.00000   90.00000    90.00000    90.00000
FORMAT ATOM   (a6,1x,i5,1x,a5,1x,a3,1x,a1,1x,a5,3f10.5,1x,a5,i3,i2,1x,f8.5)
HETATM     1 P                  13.80786  15.33485  10.05790 P_3    1 0  0.48082
HETATM     2 P                  16.89315  15.81420  10.11633 P_3    1 0  0.48082
HETATM     3 O                  15.37385  15.52084   9.68390 O_3    2 0 -0.18630
HETATM     4 O                  13.49133  16.55956  11.05330 O_3    2 0 -0.30233
HETATM     5 O                  17.22640  14.77207  11.26789 O_3    2 0 -0.30233
HETATM     6 O                  13.21820  15.82511   8.66201 O_3    2 0 -0.30233
HETATM     7 O                  17.78451  15.76755   8.95770 O_2    1 0 -0.22709
HETATM     8 O                  13.39863  14.02026  10.57035 O_2    1 0 -0.22709
HETATM     9 O                  16.81179  17.18805  10.94340 O_3    2 0 -0.30233
HETATM    10 H                  13.24787  16.20809  11.93046 H_HB   1 0  0.22203
HETATM    11 H                  16.94906  15.04235  12.16204 H_HB   1 0  0.22203
HETATM    12 H                  12.26683  15.62392   8.56973 H_HB   1 0  0.22203
HETATM    13 H                  16.88257  17.96505  10.35784 H_HB   1 0  0.22203
END

BIOGRF 200
DESCRP P4O10
REMARK .bgf-file generated by xtob-script
#       At1 At2 R12 Force1 Force2 dR12/dIteration(MD only)
BOND RESTRAINT    2  12  1.5000  7500.00 7500.00 0.0000000
CRYSTX    20.00000   20.00000   20.00000   90.00000    90.00000    90.00000
FORMAT ATOM   (a6,1x,i5,1x,a5,1x,a3,1x,a1,1x,a5,3f10.5,1x,a5,i3,i2,1x,f8.5)
HETATM     1 P                   9.10410   8.50048   9.91136 P_3    1 0  0.50287
HETATM     2 P                  11.70720   9.67062   9.81267 P_3    1 0  0.50287
HETATM     3 P                   9.71880  10.75711  11.55094 P_3    1 0  0.50287
HETATM     4 P                   9.46945  11.07075   8.72502 P_3    1 0  0.50287
HETATM     5 O                  10.71786   8.38236   9.75784 O_3    2 0 -0.18470
HETATM     6 O                   8.95931   9.34363  11.29327 O_3    2 0 -0.18470
HETATM     7 O                   8.73924   9.62166   8.79266 O_3    2 0 -0.18470
HETATM     8 O                  11.26186  10.37895  11.20682 O_3    2 0 -0.18470
HETATM     9 O                  11.04063  10.65639   8.70675 O_3    2 0 -0.18470
HETATM    10 O                   9.28265  11.61751  10.24331 O_3    2 0 -0.18470
HETATM    11 O                   8.36321   7.26032   9.83783 O_2    1 0 -0.22582
HETATM    12 O                  13.11914   9.39820   9.65661 O_2    1 0 -0.22582
HETATM    13 O                   9.48638  11.38327  12.83408 O_2    1 0 -0.22582
HETATM    14 O                   9.03017  11.95875   7.66884 O_2    1 0 -0.22582
END
```

D. Sodium Phosphorous Oxides ($Na_xP_yO_z$) and Their Geometry Files

```
BIOGRF 200
DESCRP NaPO3
CRYSTX    12.26254    6.21608    7.03907   90.00005    91.80447    89.99994
FORMAT ATOM   (a6,1x,i5,1x,a5,1x,a3,1x,a1,1x,a5,3f10.5,1x,a5,i3,i2,1x,f8.5)
HETATM     1 O                   0.58455   6.07435   2.21707 O      2 0  0.00000
HETATM     2 O                   2.63156   1.32665   4.61191 O      1 0  0.00000
HETATM     3 O                   1.35512   3.25656   3.48365 O      2 0  0.00000
HETATM     4 O                   2.09215   6.18602   0.14698 O      2 0  0.00000
HETATM     5 O                   2.55628   1.48885   2.05352 O      2 0  0.00000
HETATM     6 O                   0.48447   1.85179   0.58978 O      2 0  0.00000
HETATM     7 O                   5.42956   2.96632   1.31153 O      1 0  0.00000
HETATM     8 O                   3.14834   4.43462   5.95193 O      2 0  0.00000
HETATM     9 O                   4.65904   0.14842   0.04498 O      2 0  0.00000
HETATM    10 O                   3.92200   3.07801   3.38168 O      2 0  0.00000
HETATM    11 O                   3.45782   4.59692   1.47515 O      2 0  0.00000
HETATM    12 O                   5.52970   4.95985   2.93879 O      2 0  0.00000
```

```
HETATM    13 O                 11.44364   0.14173   4.84006 O      2 0  0.00000
HETATM    14 O                  9.39672   4.88948   2.44523 O      1 0  0.00000
HETATM    15 O                 10.67325   2.95962   3.57349 O      2 0  0.00000
HETATM    16 O                  9.93616   0.02996   6.91024 O      2 0  0.00000
HETATM    17 O                  9.47197   4.72719   5.00364 O      2 0  0.00000
HETATM    18 O                 11.54388   4.36427   6.46729 O      2 0  0.00000
HETATM    19 O                  6.59876   3.24972   5.74552 O      1 0  0.00000
HETATM    20 O                  8.88012   1.78150   1.10522 O      2 0  0.00000
HETATM    21 O                  7.36932   6.06766   7.01225 O      2 0  0.00000
HETATM    22 O                  8.10637   3.13804   3.67546 O      2 0  0.00000
HETATM    23 O                  8.57050   1.61916   5.58201 O      2 0  0.00000
HETATM    24 O                  6.49866   1.25618   4.11827 O      2 0  0.00000
HETATM    25 P                  2.51009   2.29237   3.47064 P      1 0  0.00000
HETATM    26 P                  1.29422   0.80183   1.28204 P      1 0  0.00000
HETATM    27 P                  3.50406   5.40033   0.05797 P      1 0  0.00000
HETATM    28 P                  4.71991   3.90986   2.24655 P      1 0  0.00000
HETATM    29 P                  9.51826   3.92376   3.58646 P      1 0  0.00000
HETATM    30 P                 10.73406   5.41424   5.77506 P      1 0  0.00000
HETATM    31 P                  8.52431   0.81575   6.99916 P      1 0  0.00000
HETATM    32 P                  7.30842   2.30617   4.81057 P      1 0  0.00000
HETATM    33 Na                -0.12472   2.35911   5.36967 Na     1 0  0.00000
HETATM    34 Na                 1.46496   5.44666   4.41552 Na     1 0  0.00000
HETATM    35 Na                 5.90476   5.46715   5.19417 Na     1 0  0.00000
HETATM    36 Na                 4.31497   2.33858   6.14834 Na     1 0  0.00000
HETATM    37 Na                12.15304   3.85696   1.68747 Na     1 0  0.00000
HETATM    38 Na                10.56333   0.76944   2.64168 Na     1 0  0.00000
HETATM    39 Na                 6.12360   0.74890   1.86301 Na     1 0  0.00000
HETATM    40 Na                 7.71333   3.87750   0.90887 Na     1 0  0.00000
END

BIOGRF 200
DESCRP Na4P2O7
CRYSTX     9.33985    5.43171   13.61135   90.00011    90.00001    89.99997
FORMAT ATOM   (a6,1x,i5,1x,a5,1x,a3,1x,a1,1x,a5,3f10.5,1x,a5,i3,i2,1x,f8.5)
HETATM     1 O                  5.32771   3.95568   1.35130 O      2 0  0.00000
HETATM     2 O                  5.32938   1.21154  11.16275 O      2 0  0.00000
HETATM     3 O                  3.80050   0.52364   1.82800 O      2 0  0.00000
HETATM     4 O                  5.57818   0.71739   0.00434 O      2 0  0.00000
HETATM     5 O                  3.74984   4.96732  12.23677 O      2 0  0.00000
HETATM     6 O                  6.22617   4.37483  11.90829 O      2 0  0.00000
HETATM     7 O                  6.29107   0.63421   2.41590 O      2 0  0.00000
HETATM     8 O                  8.68251   1.47572   8.15719 O      1 0  0.00000
HETATM     9 O                  8.68034   4.22039   4.35699 O      2 0  0.00000
HETATM    10 O                  0.86927   4.90705   8.63325 O      2 0  0.00000
HETATM    11 O                  8.43091   4.71454   6.80993 O      2 0  0.00000
HETATM    12 O                  0.92004   0.46424   5.43140 O      2 0  0.00000
HETATM    13 O                  7.78400   1.05723   5.10222 O      2 0  0.00000
HETATM    14 O                  7.71869   4.79742   9.22167 O      2 0  0.00000
HETATM    15 O                  4.01263   1.24015   5.45434 O      2 0  0.00000
HETATM    16 O                  4.01059   3.92719   9.25444 O      2 0  0.00000
HETATM    17 O                  5.53908   3.24034   4.97797 O      2 0  0.00000
HETATM    18 O                  3.76126   3.43317   6.80142 O      2 0  0.00000
HETATM    19 O                  5.59002   2.25163   8.18001 O      2 0  0.00000
HETATM    20 O                  3.11421   1.65868   8.50896 O      2 0  0.00000
HETATM    21 O                  3.04864   3.34988   4.38971 O      1 0  0.00000
HETATM    22 O                  0.65800   4.19174  12.25972 O      2 0  0.00000
HETATM    23 O                  0.65957   1.50476   2.44855 O      2 0  0.00000
HETATM    24 O                  8.47033   2.19202  11.78303 O      2 0  0.00000
HETATM    25 O                  0.90792   1.99867  13.60698 O      2 0  0.00000
HETATM    26 O                  8.41942   3.18032   1.37471 O      2 0  0.00000
HETATM    27 O                  1.55575   3.77323   1.70311 O      2 0  0.00000
HETATM    28 O                  1.62109   2.08116  11.19536 O      2 0  0.00000
HETATM    29 Na                 7.08216   2.64604   3.32109 Na     1 0  0.00000
HETATM    30 Na                 6.76907   2.80302  13.47695 Na     1 0  0.00000
HETATM    31 Na                 3.58104   2.78373   2.17050 Na     1 0  0.00000
HETATM    32 Na                 8.45420   5.27571   2.26712 Na     1 0  0.00000
HETATM    33 Na                 6.92756   2.78567  10.12661 Na     1 0  0.00000
HETATM    34 Na                 7.24091   2.62850   6.67144 Na     1 0  0.00000
HETATM    35 Na                 1.08904   2.64783   8.97633 Na     1 0  0.00000
HETATM    36 Na                 5.55605   0.15611   9.07268 Na     1 0  0.00000
HETATM    37 Na                 2.25788   5.36206   3.48494 Na     1 0  0.00000
HETATM    38 Na                 2.57083   0.08698   6.94033 Na     1 0  0.00000
HETATM    39 Na                 5.75886   0.06787   4.63496 Na     1 0  0.00000
HETATM    40 Na                 0.88581   2.55981   4.53866 Na     1 0  0.00000
HETATM    41 Na                 2.41234   0.06970  10.29018 Na     1 0  0.00000
HETATM    42 Na                 2.09916   5.34485   0.13453 Na     1 0  0.00000
HETATM    43 Na                 8.25131   5.36374  11.44091 Na     1 0  0.00000
```

```
HETATM    44 Na                  3.78382   2.87190  11.34440 Na     1 0  0.00000
HETATM    45 P                   5.21757   5.46836   1.49406 P      1 0  0.00000
HETATM    46 P                   5.18979   0.04466  12.15349 P      1 0  0.00000
HETATM    47 P                   8.79207  -0.03714   8.29967 P      1 0  0.00000
HETATM    48 P                   8.81996   5.38742   5.34770 P      1 0  0.00000
HETATM    49 P                   4.12225   2.75272   5.31162 P      1 0  0.00000
HETATM    50 P                   4.15027   2.76024   8.26357 P      1 0  0.00000
HETATM    51 P                   0.54769   2.67892  12.11723 P      1 0  0.00000
HETATM    52 P                   0.51972   2.67155   1.45794 P      1 0  0.00000
END

BIOGRF 200
DESCRP Na5P3O10
CRYSTX    16.31025    5.22660   11.22637   89.99990    93.92777    90.00016
FORMAT ATOM   (a6,1x,i5,1x,a5,1x,a3,1x,a1,1x,a5,3f10.5,1x,a5,i3,i2,1x,f8.5)
HETATM     1 O                   0.87218   0.53308   3.42255 O      2 0  0.00000
HETATM     2 O                   2.17831   2.53548   4.39590 O      2 0  0.00000
HETATM     3 O                   0.49805   2.38375   1.69186 O      2 0  0.00000
HETATM     4 O                   1.65863   0.43626   5.80475 O      1 0  0.00000
HETATM     5 O                   3.34160   0.28307   3.88111 O      2 0  0.00000
HETATM     6 O                   9.02694   3.14639   3.36250 O      2 0  0.00000
HETATM     7 O                  10.33319   5.14878   4.33563 O      2 0  0.00000
HETATM     8 O                   8.65299   4.99706   1.63156 O      1 0 -0.50000
HETATM     9 O                   9.81363   3.04961   5.74459 O      2 0  0.00000
HETATM    10 O                  11.49643   2.89638   3.82083 O      2 0  0.00000
HETATM    11 O                  15.09462   0.53305   2.05924 O      2 0  0.00000
HETATM    12 O                  13.78842   2.53544   1.08610 O      2 0  0.00000
HETATM    13 O                  15.46862   2.38380   3.79018 O      2 0  0.00000
HETATM    14 O                  13.62170   0.43626  10.88256 O      2 0  0.00000
HETATM    15 O                  12.62515   0.28306   1.60094 O      2 0  0.00000
HETATM    16 O                   6.93970   3.14636   2.11957 O      2 0  0.00000
HETATM    17 O                   5.63353   5.14879   1.14641 O      1 0  0.00000
HETATM    18 O                   7.31368   4.99712   3.85043 O      2 0 -0.50000
HETATM    19 O                   5.46682   3.04960  10.94283 O      2 0  0.00000
HETATM    20 O                   4.47024   2.89640   1.66120 O      2 0  0.00000
HETATM    21 O                  14.75153   4.69355   7.66198 O      2 0  0.00000
HETATM    22 O                  13.44533   2.69112   6.68881 O      2 0  0.00000
HETATM    23 O                  15.12552   2.84281   9.39282 O      2 0  0.00000
HETATM    24 O                  13.96483   4.79030   5.27985 O      1 0  0.00000
HETATM    25 O                  12.28207   4.94349   7.20363 O      2 0  0.00000
HETATM    26 O                   6.59663   2.08024   7.72227 O      2 0  0.00000
HETATM    27 O                   5.29044   0.07780   6.74910 O      2 0  0.00000
HETATM    28 O                   6.97062   0.22951   9.45312 O      2 0 -0.50000
HETATM    29 O                   5.80991   2.17699   5.34016 O      2 0  0.00000
HETATM    30 O                   4.12714   2.33016   7.26390 O      2 0  0.00000
HETATM    31 O                   0.52895   4.69358   9.02548 O      2 0  0.00000
HETATM    32 O                   1.83517   2.69118   9.99864 O      2 0  0.00000
HETATM    33 O                   0.15501   2.84288   7.29454 O      2 0  0.00000
HETATM    34 O                   2.00192   4.79037   0.20218 O      2 0  0.00000
HETATM    35 O                   2.99846   4.94355   9.48375 O      2 0  0.00000
HETATM    36 O                   8.68387   2.08025   8.96520 O      2 0  0.00000
HETATM    37 O                   9.99013   0.07785   9.93833 O      2 0  0.00000
HETATM    38 O                   8.30992   0.22956   7.23428 O      1 0 -0.50000
HETATM    39 O                  10.15682   2.17701   0.14190 O      2 0  0.00000
HETATM    40 O                  11.15336   2.33024   9.42349 O      2 0  0.00000
HETATM    41 Na                  0.39659   3.83696   5.17709 Na     1 0  0.00000
HETATM    42 Na                  2.46905   3.80988   2.29600 Na     1 0  0.00000
HETATM    43 Na                  8.55148   1.22368   5.11683 Na     1 0  0.00000
HETATM    44 Na                 10.62396   1.19658   2.23573 Na     1 0  0.00000
HETATM    45 Na                 15.57014   3.83698   0.30488 Na     1 0  0.00000
HETATM    46 Na                 13.49765   3.80985   3.18598 Na     1 0  0.00000
HETATM    47 Na                  7.41525   1.22368   0.36518 Na     1 0  0.00000
HETATM    48 Na                  5.34279   1.19657   3.24627 Na     1 0  0.00000
HETATM    49 Na                 15.22708   1.38958   5.90761 Na     1 0  0.00000
HETATM    50 Na                 13.15458   1.41673   8.78866 Na     1 0  0.00000
HETATM    51 Na                  7.07217   4.00290   5.96790 Na     1 0  0.00000
HETATM    52 Na                  4.99968   4.03004   8.84896 Na     1 0  0.00000
HETATM    53 Na                  0.05349   1.38962  10.77975 Na     1 0  0.00000
HETATM    54 Na                  2.12595   1.41673   7.89867 Na     1 0  0.00000
HETATM    55 Na                  8.20839   4.00289  10.71950 Na     1 0  0.00000
HETATM    56 Na                 10.28086   4.03001   7.83843 Na     1 0  0.00000
HETATM    57 Na                  3.73449   3.91985   5.57234 Na     1 0  0.00000
HETATM    58 Na                 11.54628   3.92000  11.11477 Na     1 0  0.00000
HETATM    59 Na                 11.88939   1.30658   5.51205 Na     1 0  0.00000
HETATM    60 Na                  3.39135   1.30671  11.17506 Na     1 0  0.00000
HETATM    61 P                   2.14082   1.01758   4.46927 P      1 0  0.00000
HETATM    62 P                  10.29573   3.63091   4.40909 P      1 0  0.00000
```

```
HETATM    63 P                  13.82584   1.01760   1.01264 P      1 0  0.00000
HETATM    64 P                   5.67093   3.63092   1.07297 P      1 0  0.00000
HETATM    65 P                  13.48275   4.20897   6.61537 P      1 0  0.00000
HETATM    66 P                   5.32787   1.59566   6.67565 P      1 0  0.00000
HETATM    67 P                   1.79768   4.20902  10.07210 P      1 0  0.00000
HETATM    68 P                   9.95269   1.59568  10.01176 P      1 0  0.00000
HETATM    69 P                  -0.17141   1.59831   2.80105 P      1 0  0.00000
HETATM    70 P                   7.98330   4.21161   2.74102 P      1 0  0.00000
HETATM    71 P                  15.79515   3.62830   8.28342 P      1 0  0.00000
HETATM    72 P                   7.64027   1.01500   8.34370 P      1 0  0.00000
END
```

E. Iron Phosphorous Oxides ($Fe_xP_yO_z$), Trinary Sodium Iron Oxides ($NaFeO_2$), and Sodium Iron Phosphorous Oxides ($Na_xFe_yP_zO_n$) and Their Geometry Files

```
BIOGRF 200
DESCRP Fe2P2O7
CRYSTX     4.39638    9.83202    5.18156   90.00035    96.77265    89.99971
FORMAT ATOM   (a6,1x,i5,1x,a5,1x,a3,1x,a1,1x,a5,3f10.5,1x,a5,i3,i2,1x,f8.5)
HETATM     1 Fe                   3.96197   1.57817   0.43840 Fe     1 0  0.00000
HETATM     2 Fe                   0.11364   6.49407   2.15832 Fe     1 0  0.00000
HETATM     3 Fe                  -0.20711   8.25376   4.72925 Fe     1 0  0.00000
HETATM     4 Fe                   3.64128   3.33778   3.00921 Fe     1 0  0.00000
HETATM     5 P                    1.14328   1.10180   3.40526 P_3    1 0  0.00000
HETATM     6 P                    2.29075   6.01755   4.33286 P_3    1 0  0.00000
HETATM     7 P                    2.61169   8.73017   1.76251 P_3    1 0  0.00000
HETATM     8 P                    1.46392   3.81424   0.83434 P_3    1 0  0.00000
HETATM     9 O                    2.29333   2.00473   3.90906 O_3    2 0  0.00000
HETATM    10 O                    3.39801   9.42020   0.63959 O_2    1 0  0.00000
HETATM    11 O                   -0.17978   3.21227   4.96246 O_3    2 0  0.00000
HETATM    12 O                    1.14076   6.92067   3.82928 O_3    2 0  0.00000
HETATM    13 O                    0.67769   4.50427   1.95721 O_3    2 0  0.00000
HETATM    14 O                    3.61394   8.12822   2.77609 O_3    2 0  0.00000
HETATM    15 O                    1.46154   7.82732   1.25859 O_3    2 0  0.00000
HETATM    16 O                    0.35699   0.41177   4.52811 O_2    1 0  0.00000
HETATM    17 O                    3.93409   6.61960   0.20462 O_3    2 0  0.00000
HETATM    18 O                    2.61404   2.91133   1.33818 O_3    2 0  0.00000
HETATM    19 O                    3.07731   5.32772   3.21023 O_3    2 0  0.00000
HETATM    20 O                    0.14099   1.70372   2.39162 O_2    1 0  0.00000
HETATM    21 O                    1.87751   9.83205   2.58383 O_3    2 0  0.00000
HETATM    22 O                    1.55670   4.91594   5.15463 O_3    2 0  0.00000
END

BIOGRF 200
DESCRP Fe3P4O14
CRYSTX     8.87435   12.09148    9.89281   90.00000    90.00000    90.23121
FORMAT ATOM   (a6,1x,i5,1x,a5,1x,a3,1x,a1,1x,a5,3f10.5,1x,a5,i3,i2,1x,f8.5)
HETATM     1 Fe                   2.21303   0.31113   1.15238 Fe     1 0  0.00000
HETATM     2 Fe                   2.19970  11.77143   6.09879 Fe     1 0  0.00000
HETATM     3 Fe                   6.64439   6.35517   8.73907 Fe     1 0  0.00000
HETATM     4 Fe                   6.64268   5.70952   3.79265 Fe     1 0  0.00000
HETATM     5 Fe                   6.63687  11.76249   8.74046 Fe     1 0  0.00000
HETATM     6 Fe                   6.65020   0.30220   3.79404 Fe     1 0  0.00000
HETATM     7 Fe                   2.20551   5.71845   1.15377 Fe     1 0  0.00000
HETATM     8 Fe                   2.20722   6.36411   6.10019 Fe     1 0  0.00000
HETATM     9 Fe                   2.82741   3.00380   1.15318 Fe     1 0  0.00000
HETATM    10 Fe                   1.58531   9.07875   6.09960 Fe     1 0  0.00000
HETATM    11 Fe                   6.02248   9.06982   8.73965 Fe     1 0  0.00000
HETATM    12 Fe                   7.26458   2.99487   3.79324 Fe     1 0  0.00000
HETATM    13 P                    8.16018   1.57027   1.11542 P_3    1 0  0.00000
HETATM    14 P                    8.34023   1.46626   6.36876 P_3    1 0  0.00000
HETATM    15 P                    5.12689  10.49441   6.06184 P_3    1 0  0.00000
HETATM    16 P                    4.94684  10.59843   1.42234 P_3    1 0  0.00000
HETATM    17 P                    0.71276   7.63065   8.77637 P_3    1 0  0.00000
HETATM    18 P                    0.54205   7.53079   3.52269 P_3    1 0  0.00000
HETATM    19 P                    3.69996   4.45191   3.82995 P_3    1 0  0.00000
HETATM    20 P                    3.87068   4.55177   8.46911 P_3    1 0  0.00000
HETATM    21 P                    0.68972  10.50335   8.77741 P_3    1 0  0.00000
HETATM    22 P                    0.50967  10.60736   3.52408 P_3    1 0  0.00000
HETATM    23 P                    3.72301   1.57921   3.83099 P_3    1 0  0.00000
HETATM    24 P                    3.90306   1.47520   8.47050 P_3    1 0  0.00000
HETATM    25 P                    8.13713   4.44297   1.11647 P_3    1 0  0.00000
HETATM    26 P                    8.30785   4.54283   6.37014 P_3    1 0  0.00000
HETATM    27 P                    5.14993   7.62172   6.06288 P_3    1 0  0.00000
HETATM    28 P                    4.97922   7.52185   1.42373 P_3    1 0  0.00000
```

```
HETATM    29 O                   5.25586   5.02882   8.81639 O_3    2 0  0.00000
HETATM    30 O                   3.17439   0.69470   7.42994 O_2    1 0  0.00000
HETATM    31 O                   0.80577   1.65415   1.19213 O_3    2 0  0.00000
HETATM    32 O                   7.49730   1.57008   5.01817 O_3    2 0  0.00000
HETATM    33 O                   3.11257   1.55469   2.37095 O_3    2 0  0.00000
HETATM    34 O                   3.10860   0.49287   4.63279 O_2    1 0  0.00000
HETATM    35 O                   8.03121   7.03587   3.86997 O_3    2 0  0.00000
HETATM    36 O                   1.23834  11.38786   2.48352 O_3    2 0  0.00000
HETATM    37 O                   3.60696  10.42841   6.13854 O_3    2 0  0.00000
HETATM    38 O                   5.78977  10.49461   0.07175 O_2    1 0  0.00000
HETATM    39 O                   1.30016  10.52787   7.31736 O_3    2 0  0.00000
HETATM    40 O                   1.30412  11.58969   9.57921 O_3    2 0  0.00000
HETATM    41 O                   3.54794  11.04352   1.07554 O_3    2 0  0.00000
HETATM    42 O                   5.73510   6.76846   2.46452 O_3    2 0  0.00000
HETATM    43 O                   8.07033   7.65999   8.69126 O_3    2 0  0.00000
HETATM    44 O                   1.37860   7.65121   4.87660 O_3    2 0  0.00000
HETATM    45 O                   5.76706   7.61252   7.52105 O_3    2 0  0.00000
HETATM    46 O                   5.77615   6.54454   5.25864 O_3    2 0  0.00000
HETATM    47 O                   0.86479   1.03904   6.02195 O_3    2 0  0.00000
HETATM    48 O                   7.55197   5.29623   7.41094 O_3    2 0  0.00000
HETATM    49 O                   5.21674   4.40470   3.74484 O_3    2 0  0.00000
HETATM    50 O                   3.03413   4.43135   9.82302 O_2    1 0  0.00000
HETATM    51 O                   7.52001   4.45216   2.57463 O_3    2 0  0.00000
HETATM    52 O                   7.51092   5.52015   0.31222 O_3    2 0  0.00000
HETATM    53 O                   3.59404   7.04480   1.07645 O_3    2 0  0.00000
HETATM    54 O                   5.67551  11.37893   2.46290 O_3    2 0  0.00000
HETATM    55 O                   8.04413  10.41947   8.70071 O_3    2 0  0.00000
HETATM    56 O                   1.35260  10.50354   4.87467 O_3    2 0  0.00000
HETATM    57 O                   5.73733  10.51893   7.52189 O_3    2 0  0.00000
HETATM    58 O                   5.74129  11.58076   5.26004 O_2    1 0  0.00000
HETATM    59 O                   0.81869   5.03776   6.02287 O_3    2 0  0.00000
HETATM    60 O                   7.61156   0.68576   7.40931 O_3    2 0  0.00000
HETATM    61 O                   5.24294   1.64522   3.75429 O_3    2 0  0.00000
HETATM    62 O                   3.06013   1.57901   9.82109 O_3    2 0  0.00000
HETATM    63 O                   7.54974   1.54576   2.57547 O_3    2 0  0.00000
HETATM    64 O                   7.54577   0.48393   0.31363 O_3    2 0  0.00000
HETATM    65 O                   5.30196   1.03010   8.81730 O_3    2 0  0.00000
HETATM    66 O                   3.11480   5.30516   7.42832 O_3    2 0  0.00000
HETATM    67 O                   0.77957   4.41363   1.20158 O_3    2 0  0.00000
HETATM    68 O                   7.47130   4.42242   5.01623 O_3    2 0  0.00000
HETATM    69 O                   3.08284   4.46110   2.37179 O_3    2 0  0.00000
HETATM    70 O                   3.07375   5.52908   4.63420 O_3    2 0  0.00000
HETATM    71 O                   7.98511  11.03459   3.87088 O_3    2 0  0.00000
HETATM    72 O                   1.29793   6.77740   2.48190 O_3    2 0  0.00000
HETATM    73 O                   3.63316   7.66892   6.14799 O_3    2 0  0.00000
HETATM    74 O                   5.81577   7.64227   0.06981 O_2    1 0  0.00000
HETATM    75 O                   1.32989   7.62146   7.31820 O_3    2 0  0.00000
HETATM    76 O                   1.33898   6.55347   9.58061 O_3    2 0  0.00000
HETATM    77 O                   3.25294   3.01157   4.40186 O_3    2 0  0.00000
HETATM    78 O                   3.97333   3.01331   7.98359 O_3    2 0  0.00000
HETATM    79 O                   1.15978   9.07099   9.34828 O_3    2 0  0.00000
HETATM    80 O                   0.43940   9.06925   3.03718 O_3    2 0  0.00000
HETATM    81 O                   5.59696   9.06205   5.49098 O_3    2 0  0.00000
HETATM    82 O                   4.87657   9.06031   1.90924 O_3    2 0  0.00000
HETATM    83 O                   7.69011   3.00264   0.54456 O_3    2 0  0.00000
HETATM    84 O                   8.41050   3.00437   6.85566 O_3    2 0  0.00000
END

BIOGRF 200
DESCRP NaFeO2
FORCEFIELD DREIDING
CRYSTX     5.11900    2.95500   15.34500   89.99000    89.99000    90.02000
FORMAT ATOM   (a6,1x,i5,1x,a5,1x,a3,1x,a1,1x,a5,3f10.5,1x,a5,i3,i2,1x,f8.5)
HETATM     1 Na                  0.85300   1.47800   2.55600 Na     1 0  0.00000
HETATM     2 Na                  3.41300  -0.00000   2.55600 Na     1 0  0.00000
HETATM     3 Na                  0.00100   0.00100   7.66700 Na     1 0  0.00000
HETATM     4 Na                  2.56000   1.47800   7.66800 Na     1 0  0.00000
HETATM     5 Na                  1.70500   2.95400  12.79600 Na     1 0  0.00000
HETATM     6 Na                  4.26500   1.47600  12.79600 Na     1 0  0.00000
HETATM     7 Fe                  0.85300   1.47600  10.23200 Fe     1 0  0.00000
HETATM     8 Fe                  3.41200   2.95300  10.23300 Fe     1 0  0.00000
HETATM     9 Fe                  2.55800   1.47500   0.00300 Fe     1 0  0.00000
HETATM    10 Fe                  5.11700   2.95200   0.00300 Fe     1 0  0.00000
HETATM    11 Fe                  1.70800   0.00200   5.11100 Fe     1 0  0.00000
HETATM    12 Fe                  4.26800   1.47900   5.11200 Fe     1 0  0.00000
HETATM    13 O                   0.00200   0.00200   4.14400 O_3    2 0  0.00000
HETATM    14 O                   2.56100   1.47900   4.14500 O_3    2 0  0.00000
```

```
HETATM    15 O                   1.70600   2.95400   9.26400 O_3    2 0  0.00000
HETATM    16 O                   4.26500   1.47600   9.26400 O_3    2 0  0.00000
HETATM    17 O                   0.85200   1.47600  -0.96500 O_3    2 0  0.00000
HETATM    18 O                   3.41200   2.95300  -0.96500 O_3    2 0  0.00000
HETATM    19 O                   2.55900   1.47600  11.20000 O_3    2 0  0.00000
HETATM    20 O                   5.11800   2.95300  11.20100 O_3    2 0  0.00000
HETATM    21 O                   1.70500   2.95300   0.96800 O_3    2 0  0.00000
HETATM    22 O                   4.26400   1.47500   0.96800 O_3    2 0  0.00000
HETATM    23 O                   0.85400   1.47800   6.08000 O_3    2 0  0.00000
HETATM    24 O                   3.41300  -0.00000   6.08000 O_3    2 0  0.00000
END

BIOGRF 200
DESCRP NaFeP2O7
CRYSTX     7.27357    7.76386    9.40006   90.00216   111.56205    90.00051
FORMAT ATOM   (a6,1x,i5,1x,a5,1x,a3,1x,a1,1x,a5,3f10.5,1x,a5,i3,i2,1x,f8.5)
HETATM     1 Na                  1.09713   3.67911   2.59758 Na     1 0  0.00000
HETATM     2 Na                  4.42778   7.56077   1.80101 Na     1 0  0.00000
HETATM     3 Na                  2.67891   4.08445   6.16327 Na     1 0  0.00000
HETATM     4 Na                 -0.65175   0.20212   6.96062 Na     1 0  0.00000
HETATM     5 Fe                  1.03560   0.05435   2.16321 Fe     1 0  0.00000
HETATM     6 Fe                  4.48919   3.93622   2.23496 Fe     1 0  0.00000
HETATM     7 Fe                  2.74047   7.70934   6.59735 Fe     1 0  0.00000
HETATM     8 Fe                 -0.71336   3.82742   6.52577 Fe     1 0  0.00000
HETATM     9 P                  -1.04928   1.99522   3.94792 P_3    1 0  0.00000
HETATM    10 P                   3.28673   1.61620   3.99195 P_3    1 0  0.00000
HETATM    11 P                   6.57401   5.87734   0.45018 P_3    1 0  0.00000
HETATM    12 P                   2.23813   5.49822   0.40629 P_3    1 0  0.00000
HETATM    13 P                   4.82517   5.76834   4.81291 P_3    1 0  0.00000
HETATM    14 P                   0.48932   6.14739   4.76863 P_3    1 0  0.00000
HETATM    15 P                  -2.79806   1.88608   8.31026 P_3    1 0  0.00000
HETATM    16 P                   1.53794   2.26511   8.35459 P_3    1 0  0.00000
HETATM    17 O                   4.84203   1.15561   3.88170 O_2    1 0 -0.50000
HETATM    18 O                  -0.77838   2.24649   5.43345 O_3    2 0  0.00000
HETATM    19 O                  -1.20300   3.27456   3.10182 O_3    2 0  0.00000
HETATM    20 O                   0.02290   1.07347   3.42206 O_3    2 0  0.00000
HETATM    21 O                   2.65179   0.63615   3.01301 O_3    2 0  0.00000
HETATM    22 O                   2.81025   1.54105   5.44744 O_3    2 0 -0.50000
HETATM    23 O                   3.24188   3.08899   3.53345 O_3    2 0  0.00000
HETATM    24 O                   0.68271   5.03789   0.51657 O_2    1 0  0.00000
HETATM    25 O                   2.80544   6.12852   7.68972 O_3    2 0  0.00000
HETATM    26 O                   6.72769   7.15664   1.29639 O_3    2 0  0.00000
HETATM    27 O                   5.50181   4.95550   0.97605 O_3    2 0  0.00000
HETATM    28 O                   2.87291   4.51819   1.38509 O_3    2 0  0.00000
HETATM    29 O                  -0.78313   5.42291   7.67584 O_3    2 0  0.00000
HETATM    30 O                   2.28292   6.97098   0.86469 O_2    1 0  0.00000
HETATM    31 O                  -1.06627   6.60792   4.87920 O_3    2 0 -0.50000
HETATM    32 O                   4.55448   5.51698   3.32700 O_3    2 0  0.00000
HETATM    33 O                   4.97931   4.48902   5.65892 O_3    2 0  0.00000
HETATM    34 O                   3.75264   6.68983   5.33847 O_3    2 0  0.00000
HETATM    35 O                   1.12385   7.12811   5.74754 O_3    2 0  0.00000
HETATM    36 O                   0.96549   6.22260   3.31326 O_2    1 0 -0.50000
HETATM    37 O                   0.53430   4.67491   5.22735 O_3    2 0  0.00000
HETATM    38 O                   3.09322   2.72565   8.24409 O_2    1 0  0.00000
HETATM    39 O                   0.97032   1.63495   1.07105 O_3    2 0  0.00000
HETATM    40 O                  -2.95186   0.60680   7.46421 O_3    2 0  0.00000
HETATM    41 O                  -1.72578   2.80804   7.78446 O_3    2 0  0.00000
HETATM    42 O                   0.90314   3.24544   7.37555 O_3    2 0  0.00000
HETATM    43 O                   4.55915   2.34056   1.08488 O_3    2 0  0.00000
HETATM    44 O                   1.49316   0.79257   7.89615 O_2    1 0  0.00000
END

BIOGRF 200
DESCRP NaFePO4
CRYSTX     8.72758    6.57867    4.96905   90.00892    89.98629    89.99674
FORMAT ATOM   (a6,1x,i5,1x,a5,1x,a3,1x,a1,1x,a5,3f10.5,1x,a5,i3,i2,1x,f8.5)
HETATM     1 O                   3.20940   2.91281   0.91685 O_3    2 0  0.00000
HETATM     2 O                   1.15375   3.66052   3.39936 O_3    2 0  0.00000
HETATM     3 O                   5.52017   6.20395   4.05298 O_3    2 0  0.00000
HETATM     4 O                   7.57696   0.37942   1.57096 O_2    1 0  0.00000
HETATM     5 O                   5.51988   3.66726   4.05265 O_3    2 0  0.00000
HETATM     6 O                   7.57317   2.91654   1.56902 O_3    2 0  0.00000
HETATM     7 O                   3.20925   0.37558   0.91739 O_3    2 0  0.00000
HETATM     8 O                   1.15038   6.19766   3.39828 O_3    2 0  0.00000
HETATM     9 O                   3.39689   1.64315   3.68830 O_3    2 0  0.00000
HETATM    10 O                   1.18490   1.64384   0.21607 O_3    2 0  0.00000
HETATM    11 O                   0.96783   4.92842   1.20094 O_3    2 0  0.00000
```

```
HETATM    12 O                3.17754   4.93285   2.70069 O_3    2 0  0.00000
HETATM    13 O                5.33155   4.93606   1.28174 O_3    2 0  0.00000
HETATM    14 O                7.54399   4.93466   4.75405 O_3    2 0  0.00000
HETATM    15 O                7.76120   1.64914   3.76782 O_3    2 0  0.00000
HETATM    16 O                5.55040   1.64525   2.26950 O_3    2 0  0.00000
HETATM    17 Fe               4.36414   3.28930   2.48512 Fe     1 0  0.00000
HETATM    18 Fe               0.00015   3.28918  -0.00008 Fe     1 0  0.00000
HETATM    19 Fe               4.36442   6.57861   2.48496 Fe     1 0  0.00000
HETATM    20 Fe               0.00026   6.57841  -0.00040 Fe     1 0  0.00000
HETATM    21 P                2.78159   1.64414   0.16798 P_3    1 0  0.00000
HETATM    22 P                1.58045   4.92978   2.65034 P_3    1 0  0.00000
HETATM    23 P                5.94724   4.93512   4.80247 P_3    1 0  0.00000
HETATM    24 P                7.14743   1.64785   2.31892 P_3    1 0  0.00000
HETATM    25 Na               5.68204   1.64688   4.90578 Na     1 0  0.00000
HETATM    26 Na               7.40698   4.93731   2.42151 Na     1 0  0.00000
HETATM    27 Na               3.04702   4.93353   0.06378 Na     1 0  0.00000
HETATM    28 Na               1.32072   1.63961   2.54877 Na     1 0  0.00000
END
```

F. ReaxFF

```
Reactive MD-force field: Fe/Na/P/O crystals developed by Thi Ta and Manh Ha Le
in Oct 2019
 39       ! Number of general parameters
   50.0000 !Overcoordination parameter
    9.5469 !Overcoordination parameter
    1.6725 !Valency angle conjugation parameter
    1.7224 !Triple bond stabilisation parameter
    6.8702 !Triple bond stabilisation parameter
   60.4850 !C2-correction
    1.0588 !Undercoordination parameter
    4.6000 !Triple bond stabilisation parameter
   12.1176 !Undercoordination parameter
   13.3056 !Undercoordination parameter
  -40.0000 !Triple bond stabilization energy
    0.0000 !Lower Taper-radius
   10.0000 !Upper Taper-radius
    2.8793 !Not used
   33.8667 !Valency undercoordination
    6.0891 !Valency angle/lone pair parameter
    1.0563 !Valency angle
    2.0384 !Valency angle parameter
    6.1431 !Not used
    6.9290 !Double bond/angle parameter
    0.3989 !Double bond/angle parameter: overcoord
    3.9954 !Double bond/angle parameter: overcoord
   -2.4837 !Not used
    5.7796 !Torsion/BO parameter
   10.0000 !Torsion overcoordination
    1.9487 !Torsion overcoordination
   -1.2327 !Conjugation 0 (not used)
    2.1645 !Conjugation
    1.5591 !vdWaals shielding
    0.1000 !Cutoff for bond order (*100)
    1.7602 !Valency angle conjugation parameter
    0.6991 !Overcoordination parameter
   50.0000 !Overcoordination parameter
    1.8512 !Valency/lone pair parameter
    0.5000 !Not used
   20.0000 !Not used
    5.0000 !Molecular energy (not used)
    0.0000 !Molecular energy (not used)
    0.7903 !Valency angle conjugation parameter
  6    !Nr of atoms; cov.r; valency;a.m;Rvdw;Evdw;gammaEEM;cov.r2;
           alfa;gammavdW;valency;Eunder;Eover;chiEEM;etaEEM;n.u.
           cov r3;Elp;Heat inc.;n.u.;n.u.;n.u.;n.u.
           ov/un;val1;n.u.;val3,vval4
 C    1.3817   4.0000  12.0000   1.8903   0.1838   0.9100   1.1341   4.0000
      9.7559   2.1346   4.0000  34.9350  79.5548   5.9666   7.0000   0.0000
```

```
     1.2114   0.0000 202.2908   8.9539  34.9289  13.5366   0.8563   0.0000
    -2.8983   2.5000   1.0564   4.0000   2.9663   0.0000   0.0000   0.0000
H    0.8930   1.0000   1.0080   1.3550   0.0930   0.8203  -0.1000   1.0000
     8.2230  33.2894   1.0000   0.0000 121.1250   3.7248   9.6093   1.0000
    -0.1000   0.0000  55.1878   3.0408   2.4197   0.0003   1.0698   0.0000
   -19.4571   4.2733   1.0338   1.0000   2.8793   0.0000   0.0000   0.0000
O    1.2450   2.0000  15.9990   2.3890   0.1000   1.0898   1.0548   6.0000
     9.7300  13.8449   4.0000  37.5000 116.0768   8.5000   8.3122   2.0000
     0.9049   0.4056  59.0626   3.5027   0.7640   0.0021   0.9745   0.0000
    -3.5500   2.9000   1.0493   4.0000   2.9225   0.0000   0.0000   0.0000
Na   1.7986   1.0000  22.9898   2.7586   0.3000   0.8476  -1.0000   1.0000
     9.0003   2.5000   1.0000   0.0000   0.0000  -3.4731   8.1298   0.0000
    -1.0000   0.0000  23.0445 100.0000   1.0000   0.0000   0.8563   0.0000
    -4.1479   3.9900   1.0338   8.0000   2.5791   0.0000   0.0000   0.0000
P    1.5994   3.0000  30.9738   1.5770   0.1983   0.4655   1.3000   5.0000
    10.7864   2.7884   5.0000   0.0000   0.0000   3.4186   5.3855   0.0000
    -1.0000   3.3786 125.6300   0.5475  11.9674  17.3824   0.0000   0.0000
   -13.7379   2.8674   1.0338   5.0000   2.8793   0.0000   0.0000   0.0000
Fe   2.0843   3.0000  55.8450   1.8993   0.1873   0.7264  -1.0000   3.0000
    11.0534   2.2637   3.0000   0.0000  18.3725   1.2457   7.3021   0.0000
    -1.2000   0.0000  66.4838  30.0000   1.0000   0.0000   0.8563   0.0000
   -16.2040   2.7917   1.0338   6.0000   2.5791   0.0000   0.0000   0.0000
20      ! Nr of bonds; Edis1;LPpen;n.u.;pbe1;pbo5;13corr;pbo6
                       pbe2;pbo3;pbo4;n.u.;pbo1;pbo2;ovcorr
 1  1 158.2004  99.1897  78.0000  -0.7738  -0.4550   1.0000  37.6117   0.4147
       0.4590  -0.1000   9.1628   1.0000  -0.0777   6.7268   1.0000   0.0000
 1  2 169.4760   0.0000   0.0000  -0.6083   0.0000   1.0000   6.0000   0.7652
       5.2290   1.0000   0.0000   1.0000  -0.0500   6.9136   0.0000   0.0000
 1  3 164.4303  82.6772  60.8077  -0.3739  -0.2351   1.0000  10.5036   1.0000
       0.4475  -0.2288   7.0250   1.0000  -0.1363   4.8734   0.0000   0.0000
 1  5   0.0000   0.0000   0.0000   0.2171  -0.1418   1.0000  13.1260   0.6000
       0.3601  -0.2500  20.0000   1.0000  -0.2000  10.0000   1.0000   0.0000
 1  6 109.5214   0.0000   0.0000   0.6663  -0.3000   1.0000  36.0000   0.0100
       1.0648  -0.3500  15.0000   1.0000  -0.1512   4.1708   1.0000   0.0000
 2  2 153.3934   0.0000   0.0000  -0.4600   0.0000   1.0000   6.0000   0.7300
       6.2500   1.0000   0.0000   1.0000  -0.0790   6.0552   0.0000   0.0000
 2  3 160.0000   0.0000   0.0000  -0.5725   0.0000   1.0000   6.0000   0.5626
       1.1150   1.0000   0.0000   0.0000  -0.0920   4.2790   0.0000   0.0000
 2  4   0.0000   0.0000   0.0000  -1.0000  -0.3000   1.0000  36.0000   0.7000
      10.1151  -0.3500  25.0000   1.0000  -0.1053   8.2003   1.0000   0.0000
 2  5   0.0000   0.0000   0.0000   0.2250  -0.1418   1.0000  13.1260   0.6000
       0.3912  -0.1310   0.0000   1.0000  -0.2000  10.0000   0.0000   0.0000
 2  6  78.2669   0.0000   0.0000   0.4668   0.0000   1.0000   6.0000   0.1164
       0.5673   1.0000   0.0000   1.0000  -0.1543   5.4965   0.0000   0.0000
 3  3 142.2858 145.0000  50.8293   0.2506  -0.1000   1.0000  29.7503   0.6051
       0.3451  -0.1055   9.0000   1.0000  -0.1225   5.5000   1.0000   0.0000
 3  4  31.0064   0.0000   0.0000   0.1816  -0.3000   1.0000  36.0000   0.4059
      19.1117  -0.3500  25.0000   1.0000  -0.1974   6.5386   1.0000   0.0000
 3  5  81.3817 119.8068   0.0000   0.8652  -0.5000   1.0000  25.0000   0.2000
       3.5797  -0.2067  16.0316   1.0000  -0.2491   7.9507   1.0000   0.0000
 3  6  70.6636   0.0000   0.0000   0.2110  -0.4469   1.0000  36.0000   0.0148
       1.0000  -0.2842  15.0000   1.0000  -0.2077   6.2250   1.0000   0.0000
 4  4 104.6461   0.0000   0.0000  -0.7273   0.3000   0.0000  25.0000   0.1919
       6.6441  -0.4000  12.0000   1.0000  -0.0345   5.0063   0.0000   0.0000
 4  5   0.0000   0.0000   0.0000  -0.1228   0.2190   1.0000  35.0000   0.8100
       3.2849   1.0000   0.9636   1.0000  -0.9038   1.3783   1.0000   0.0000
 4  6   0.0000   0.0000   0.0000   0.2500  -0.5000   1.0000  35.0000   0.6000
       0.5000  -0.5000  20.0000   1.0000  -0.0001  10.0000   1.0000   0.0000
 5  5  77.6075  23.0652   9.0151   0.3170  -0.5000   1.0000  35.0000   0.0402
      13.4229  -0.4110  22.3594   1.0000  -0.0279   9.1607   1.0000   0.0000
 5  6   0.0000   0.0000   0.0000  -0.6998  -0.5924   0.0000  36.0000   0.2723
      -0.2496  -0.6423  17.4444   1.0000  -0.0691   4.9408   0.0000   0.0000
 6  6  27.0485   0.0000   0.0000   0.7994  -0.2469   0.0000  16.0000   0.1520
       1.0000  -0.2770  15.0000   1.0000  -0.0880   6.6348   0.0000   0.0000
12    ! Nr of off-diagonal terms; Ediss;Ro;gamma;rsigma;rpi;rpi2
 1  2   0.1239   1.4004   9.8467   1.1210  -1.0000  -1.0000
 1  3   0.1345   1.8422   9.7725   1.2835   1.1576   1.0637
 1  6   0.1380   1.8365   9.9369   1.6095  -1.0000  -1.0000
```

```
 2  3   0.0283   1.2885  10.9190   0.9215  -1.0000  -1.0000
 2  5   0.1744   1.7715  10.4931   0.0100   0.0100  -1.0000
 2  6   0.0374   1.6774  11.5143   1.3523  -1.0000  -1.0000
 3  4   0.2000   1.3405  17.0045   1.6861  -1.0000  -1.0000
 3  5   0.0450   1.7136  11.6409   1.7097   1.4401  -1.0000
 3  6   0.1114   1.2653  12.0394   1.9221  -1.0000  -1.0000
 4  5   0.1682   1.1937   8.1129   0.9312  -1.0000  -1.0000
 4  6   0.2053   1.5393   5.8090   1.1111  -1.0000  -1.0000
 5  6   0.3080   1.0117  13.6865   1.0230  -1.0000  -1.0000
64    ! Nr of angles;at1;at2;at3;Thetao,o;ka;kb;pv1;pv2
 1  1  1  59.0573  30.7029   0.7606   0.0000   0.7180   6.2933   1.1244
 1  1  2  65.7758  14.5234   6.2481   0.0000   0.5665   0.0000   1.6255
 1  1  3  53.9517   7.8968   2.6122   0.0000   3.0000  58.6562   1.0338
 1  1  6  59.8697   2.8115   1.9262   0.0000   0.7602   0.0000   1.4056
 1  2  1   0.0000   3.4110   7.7350   0.0000   0.0000   0.0000   1.0400
 1  2  2   0.0000   0.0000   6.0000   0.0000   0.0000   0.0000   1.0400
 1  2  3   0.0000  25.0000   3.0000   0.0000   1.0000   0.0000   1.0400
 1  3  1  72.6199  42.5510   0.7205   0.0000   2.9294   0.0000   1.3096
 1  3  2  70.1101  13.1217   4.4734   0.0000   0.8433   0.0000   3.0000
 1  3  3  81.9029  32.2258   1.7397   0.0000   0.9888  68.1072   1.7777
 1  3  5  53.2386  27.6683   3.5448   0.0000   0.9129   0.0000   1.2759
 1  3  6  85.7539  12.4507   1.7016   0.0000   0.7773   0.0000   1.0072
 1  5  1  56.0196  40.1896   1.0567   0.0000   0.7180   6.2933   1.1983
 1  5  3  82.8511  35.1702   2.2155   0.0000   1.0000   0.0000   1.0400
 1  6  1  29.1655   3.3035   0.2000   0.0000   1.1221   0.0000   1.0562
 1  6  6  23.1289  17.1960   0.9080   0.0000   2.1592   0.0000   1.1284
 2  1  2  70.2607  25.2202   3.7312   0.0000   0.0050   0.0000   2.7500
 2  1  3  65.0000  16.3141   5.2730   0.0000   0.4448   0.0000   1.4077
 2  1  6  47.7440  17.2406   4.2409   0.0000   0.1189   0.0000   1.0000
 2  2  2   0.0000  27.9213   5.8635   0.0000   0.0000   0.0000   1.0400
 2  2  3   0.0000   8.5744   3.0000   0.0000   0.0000   0.0000   1.0421
 2  2  6   0.1000  30.0000   3.4094   0.0000   2.4379   0.0000   1.5166
 2  3  2  85.8000   9.8453   2.2720   0.0000   2.8635   0.0000   1.5800
 2  3  3  75.6935  50.0000   2.0000   0.0000   1.0000   0.0000   1.1680
 2  3  4  79.5256   0.0000   3.4651   0.0000   1.1304   0.0000   1.1392
 2  3  5  99.9653  44.2516   0.1000   0.0000   3.0722   0.0000   1.0400
 2  3  6  58.9778   6.8975   0.3755   0.0000   1.2323   0.0000   1.0000
 2  5  3  75.0000  25.0000   2.0000   0.0000   1.0000   0.0000   1.2500
 2  6  2  34.1965   6.6782   6.5943   0.0000   1.3895   0.0000   1.5365
 2  6  3  31.9418  20.2787   3.3430   0.0000   0.1776   0.0000   1.6699
 2  6  6  15.4956   8.5450   1.5223   0.0000   2.8058   0.0000   1.0000
 3  1  3  82.1309  19.2307   3.4337  -2.7509   1.5183   0.0000   2.9248
 3  1  5  50.2929  41.6249   2.8868   0.0000   1.0000   0.0000   1.0400
 3  1  6  19.3842  24.1157   4.0634   0.0000   0.1048   0.0000   1.5118
 3  2  3   0.0000  15.0000   2.8900   0.0000   0.0000   0.0000   2.8774
 3  2  5   0.0000  10.0000   1.0000   0.0000   1.0000   0.0000   1.0400
 3  2  6   0.0000   2.8412   2.9329   0.0000   0.9527   0.0000   1.3664
 3  3  3  89.9934  17.9465   1.7798   0.0000   2.9881   0.0000   1.0538
 3  3  4   0.0000   0.0000   1.0000   0.0000   1.6743   0.0000   2.4009
 3  3  5  60.0000  40.0000   4.0000   0.0000   1.0000   0.0000   1.0400
 3  3  6  62.0924   3.5446   8.5573   0.0000   1.9458   0.0000   2.5867
 3  4  3   8.0033   8.1164   0.0100   0.0000   1.7673   0.0000   4.9473
 3  4  4   0.0000   0.0000   1.0000   0.0000   1.6743   0.0000   2.4009
 3  5  3  71.7497  16.7048   3.1929 -12.5000   1.3898   0.0000   2.9676
 3  5  5  70.0000  25.0000   2.0000   0.0000   1.0000   0.0000   1.2500
 3  5  6  80.0000  40.7321   4.7609   0.0000   0.0100   0.0000   1.0400
 3  6  3  80.5562   6.1200   1.8307   0.0000   0.5992   0.0000   1.4235
 3  6  5  80.0000  14.6298   2.6578   0.0000   0.5087   0.0000   2.2481
 3  6  6  69.5788   6.3351   8.3746   0.0000   1.7643   0.0000   2.4170
 4  3  4  88.7938   8.3861   4.0760   0.0000   0.0000   0.0000   0.8880
 4  3  5  36.4626   6.7019   5.2274   0.0000   0.2960   0.0000   1.9380
 4  3  6   0.0000   0.0000   1.0000   0.0000   1.0000   0.0000   1.0000
 4  4  4   0.0000   0.0000   1.0000   0.0000   1.6743   0.0000   2.4009
 4  4  5   0.0000   0.0000   1.0000   0.0000   1.6743   0.0000   2.4009
 4  5  5   0.0000   0.0000   1.0000   0.0000   1.6743   0.0000   2.4009
 5  3  5  37.5590  10.7725   9.2578  -1.9090   2.1445   0.0000   1.1963
 5  3  6   0.8587 108.4731  18.6370   0.0000  11.7539   0.0000  10.1359
 5  4  5   0.0000   0.0000   1.0000   0.0000   1.6743   0.0000   2.4009
```

```
 5  5  5  60.0000   7.3367  20.0247   0.0000   4.0137   0.0000   3.0019
 5  6  6   0.0000   0.0000   1.0000   0.0000   0.1741   0.0000   1.0400
 6  1  6  89.6090  27.4283   1.2044   0.0000   0.2760   0.0000   1.9666
 6  2  6   0.0000   8.6047   6.0092   0.0000   2.8424   0.0000   1.7365
 6  3  6  32.2224   3.0545   4.0388   0.0000   0.1291   0.0000   0.9714
 6  5  6  80.0000  19.0562   4.5151   0.0000   0.0100   0.0000   1.4639
34    ! Nr of torsions;at1;at2;at3;at4;;V1;V2;V3;V2(BO);vconj;n.u;n
 0  1  1  0   0.0000  50.0000   0.3000  -4.0000  -2.0000   0.0000   0.0000
 0  1  2  0   0.0000   0.0000   0.0000   0.0000   0.0000   0.0000   0.0000
 0  1  5  0   4.0000  45.8264   0.9000  -4.0000   0.0000   0.0000   0.0000
 0  2  2  0   0.0000   0.0000   0.0000   0.0000   0.0000   0.0000   0.0000
 0  2  3  0   0.0000   0.1000   0.0200  -2.5415   0.0000   0.0000   0.0000
 0  3  3  0   0.5511  25.4150   1.1330  -5.1903  -1.0000   0.0000   0.0000
 1  1  1  1  -0.2500  34.7453   0.0288  -6.3507  -1.6000   0.0000   0.0000
 1  1  1  2  -0.2500  29.2131   0.2945  -4.9581  -2.1802   0.0000   0.0000
 1  1  1  3   1.2799  20.7787  -0.5249  -2.5000  -1.0000   0.0000   0.0000
 1  1  1  5  -0.3232  14.3871   0.1823  -9.8682  -1.7255   0.0000   0.0000
 1  1  3  1   0.4816  19.6316  -0.0057  -2.5000  -1.0000   0.0000   0.0000
 1  1  3  2   1.2044  80.0000  -0.3139  -6.1481  -1.0000   0.0000   0.0000
 1  1  3  3  -0.0002  20.1851   0.1601  -9.0000  -2.0000   0.0000   0.0000
 1  3  3  1   0.0002  80.0000  -1.5000  -4.4848  -2.0000   0.0000   0.0000
 1  3  3  2  -2.1289  12.8382   1.0000  -5.6657  -2.9759   0.0000   0.0000
 1  3  3  3   2.5000 -25.0000   1.0000  -2.5000  -1.0000   0.0000   0.0000
 1  3  5  3  -0.9451   8.2456   0.5757  -5.7138   0.0000   0.0000   0.0000
 2  1  1  2  -0.2500  31.2081   0.4539  -4.8923  -2.2677   0.0000   0.0000
 2  1  1  3   1.9159  19.8113   0.7914  -4.6995  -1.0000   0.0000   0.0000
 2  1  3  1  -2.5000  31.0191   0.6165  -2.7733  -2.9807   0.0000   0.0000
 2  1  3  2  -2.4875  70.8145   0.7582  -4.2274  -3.0000   0.0000   0.0000
 2  1  3  3  -1.4383  80.0000   1.0000  -3.6877  -2.8000   0.0000   0.0000
 2  1  3  5  -0.1220  61.5112   0.3316  -5.4970   0.0000   0.0000   0.0000
 2  3  3  2   2.5000 -22.9397   0.6991  -3.3961  -1.0000   0.0000   0.0000
 2  3  3  3  -2.5000  -2.5103  -1.0000  -2.5000  -1.0000   0.0000   0.0000
 2  3  5  3  -1.5000  -1.0000   0.3045  -2.5000   0.0000   0.0000   0.0000
 3  1  1  3  -1.4477  16.6853   0.6461  -4.9622  -1.0000   0.0000   0.0000
 3  1  3  1  -1.1390  78.0747  -0.0964  -4.5172  -3.0000   0.0000   0.0000
 3  1  3  2  -2.5000  70.3345  -1.0000  -5.5315  -3.0000   0.0000   0.0000
 3  1  3  3  -0.1583  20.0000   1.5000  -9.0000  -2.0000   0.0000   0.0000
 3  3  3  3  -2.5000 -25.0000   1.0000  -2.5000  -1.0000   0.0000   0.0000
 5  1  1  5  -0.1452  50.0000  -0.1915  -8.0773  -1.7255   0.0000   0.0000
 5  3  5  3   0.1946  20.0266  -0.3314  -8.1095   0.0000   0.0000   0.0000
 5  5  5  5   3.5590  23.6453  -0.7307  -4.6741   0.0000   0.0000   0.0000
 1    ! Nr of hydrogen bonds;at1;at2;at3;Rhb;Dehb;vhb1
 3  2  3   2.1200  -3.5800   1.4500   0.1000
```